STUDY ON NONLINEAR WAVE-PARTICLE INTERACTIONS IN SPACE PLASMAS VIA COMPUTER SIMULATIONS

by

Yoshiharu OMURA

March, 1985

Department of Electrical Engineering

Kyoto University, Kyoto, 606 Japan

STUDY ON NONLINEAR WAVE-PARTICLE INTERACTIONS IN SPACE PLASMAS VIA COMPUTER SIMULATIONS

by

Yoshiharu OMURA

March, 1985

Department of Electrical Engineering
Kyoto University, Kyoto, 606 Japan

DOCTORAL THESIS
SUBMITTED TO
THE FACULTY OF ENGINEERING
KYOTO UNIVERSITY

ACKNOWLEDGMENTS

I wish to express my sincere appreciation to my research supervisor, Professor Iwane Kimura for his advice and encouragement during the course of this work and for his careful reading of the manuscript and many suggestions for revision.

I also wish to express my deep appreciation to Dr. Hiroshi Matsumoto for his continual guidance, inspiration and stimulating discussion throughout the present work. I am indebted particularly to him for the physical insights gained during countless stimulating discussion on many aspects of this research and for his careful and critical reading of the manuscript and suitable suggestions for revision.

I am grateful to Professor Susumu Kato for his supervision and guidance in the early stage of this research and to Professor Toru Ogawa for his discussion.

I am also grateful to Professor Tatsuzo Obayashi at ISAS for his encouragement and support.

I am deeply grateful to Dr. Maha Ashour-Abdalla at UCLA (U.S.A.) for her guidance and support during my stay at UCLA and for her stimulating discussion. I am also grateful to Professor Roger Gendrin at CRPE/CNET (France), who was a visiting professor during my stay at UCLA, for his guidance, discussion and co-investigation of the study in Chapter 4.

I would like to thank Dr. Kevin Quest at LANL (U.S.A.) and Dr. John P. Matthews and Mr. Masayoshi Ohashi for their co-investigations and discussion.

I would also like to thank Dr. Kozo Hashimoto and Dr. Minoru Tsutsui for their discussion and stimulating suggestions through seminars.

Thanks are also due to discussion with my colleagues in the Space Plasma Simulation Group at Kyoto University, Messrs. Masaru Nishio, Keisuke Nagai, Koichi Fukuchi, Ichiro Ayukawa, Toru Yamada, Toshinari Kimura, Yukinori Matsumoto and Miss Noriko Terada.

I am indebted to Dr. Masao Kitano for his technical support in formating the text of the present thesis.

I wish to express my thanks to Mrs. Keiko Miwa, Mr. Noriaki Komori and Mr. Takahiko Tanaka for their help in preparing materials concerning the present study.

Finally, I thank my wife Chiaki for her encouragement in completing this thesis.

ABSTRACT

The magnetosphere and the interplanetary space are filled with plasmas in which various kinds of electromagnetic as well as electrostatic waves are excited due to the interaction with high energy particles. Wave-particle interactions and associated wave phenomena such as anomalous resistivities, plasma heatings and wave-wave couplings play important roles in the energy transfer in space.

These natural phenomena observed in space plasmas are often highly nonlinear and too complicated for analytic theories. In order to obtain better understanding of nonlinear wave-particle interactions in space plasmas, we have developed three different computer simulation codes, a full electromagnetic code, a long-time-scale code for whistler interactions and a hybrid electromagnetic code.

Using these codes, we first investigated a whistler mode wave-particle interaction. We clarified basic processes of the interactions and effects of the phase bunchings and trappings associated with VLF triggered emissions. Effects of co-existing electrostatic waves on whistler mode instabilities are also studied.

Secondly, we studied heating of heavy ions in the equatorial magnetosphere in conjunction with electromagnetic ion cyclotron waves generated by anisotropic hot protons. Linear stage of the interaction is studied by computing the linear growth rates for various parameters. Nonlinear stage is studied by the hybrid electromagnetic simulation. The mechanism of the He^+ heating is explained by a two-step process.

Thirdly, we investigated radiation from two types of high energy electron beams. One is the beam injected from a space vehicle, in which we found excitation of two types of electromagnetic waves with k vectors perpendicular to the external magnetic field. The other is the beam modulated by a coherent whistler wave, where we found interesting two-beam jetting as a results of trapping and detrapping process, yielding a strong electrostatic emissions with k vector parallel to the external magnetic field.

CONTENTS

CHAPTER 1
GENERAL INTRODUCTION

1.1 Wave-Particle Interactions in Space Plasmas

Space surrounding our mother planet Earth, which once believed to be a void vacuum, is filled with plasma which is the forth state of matter. Plasma is a fully or partially ionized gas, which is, however, electrically neutral on the average and exhibits collective behavior. It is often said that 99% of the matter in the universe is in the plasma state. The principal origin of the plasma in the vicinity of the earth is a continuous emission of plasma from the sun. This plasma flow which carries away a part of the solar energy and fills up the interplanetary space with the plasma is designated as the solar wind. Since the geomagnetic field around the earth prevents the access of the solar wind toward the earth, a cavity is formed around the earth in the midst of the streaming solar plasma. The cavity, in which field lines of the earth's magnetic field are confined is called the magnetosphere of the earth. Other magnetized planets like Jupiter and Saturn also have magnetospheres.

In the magnetospheres as well as the interplanetary space there exist various kinds of electromagnetic plasma waves. Through interactions with plasma particles, these plasma waves play important roles in the transfer of the solar wind energy into the magnetosphere and further into the ionosphere. Such a transfered energy is evidenced by auroras in the polar regions. The wave-particle interactions in the magnetosphere also control the environment of electromagnetic radiations and would have influences on communication and other human activities in space in the future.

1.2 Significance of Computer Simulations

The space exploration has been achieved by a rapid development of space vehicles and their use for scientific survey of our space environment. In 1960's and 1970's a lot of discoveries of new phenomena were brought from these spacecraft observations. Data analysis-phase followed after the discovery-phase yielding a variety of physical models of our space plasma environment and theories for the related plasma processes taking place therein. However, there still remains a large number of

problems because of too many degrees of freedom in choice of physical models. Natural phenomena in space plasmas are often highly nonlinear and too complicated for analytic theories which usually rely on linearization or weak nonlinearization, symmetry characteristics, homogeneity or simple inhomogeneity and other simplified assumptions. On the other hand, observations by satellite are still too coarse: Measurements are limited in time and in space, so that much ambiguity is left, which causes disputes among related theoretical models. To resolve these uncertainties among various models and theories and to find a hint or clue for understanding the unsolved physics underlying the observed phenomena, computer simulations have been high-lighted as a third promising approach to bridge the traditional two approaches, theory and experiment, among space researchers in late 1970's and in 1980's.

Computer simulations for space physics may be divided into two categories: First is an MHD simulation which follows the nonlinear fluid motion of plasmas in their self-consistent fields (and applied fields if any). This class of simulations is useful in understanding macroscopic global-scale dynamics which cannot be understood by piecewise information from individual satellite observations. Second is a particle simulation which follows the individual nonlinear motions of many particles in their self-consistent fields (or applied fields if any). The particle simulations play a significant role in space physics in interpreting highly nonlinear kinetic effects like wave instabilities and associated plasma scattering, diffusion, heating and particle acceleration.

Complicated and sometimes overlapping phenomena which nature generally exhibits can be decomposed into simpler elements of physics in simulations to obtain a clearer physical picture. One of the advantages of the computer simulation is that one can make as detailed diagnostics of plasma and field quantities as one desires. A precise visualization of the time evolution of the nonlinear micro-dynamics of interest is easily achieved in detail by graphic displays of the results of particle simulations. This could not be realized either by theory nor by satellite observations. Thus particle simulations provide useful data of wave-particle interactions which are currently inaccessible to satellite observations nor to theories. One such example is a rapid variation of the particle distribution function in velocity space. Such detailed information may often provide a hint and inspiration not only for further theoretical development but also for design of new satellite observations.

1.3 Contribution of the Present Work

In Chapter 2, we first give an introductory review and a guide of particle simulations of electromagnetic waves [Matsumoto and Omura, 1984]. The basic concept of particle simulations is not given in detail because it is found in the existing literature [e.g., Hockney and Eastwood, 1981; Birdsall and Langdon, 1984]. We describe one of the important techniques in particle simulations, i.e., cancellation of a self-force of superparticles. We then explain numerical algorithms and techniques of three different simulation codes which have been developed for the study of wave-particle interactions and have been successfully used in the present work. These codes are (1) Full Electromagnetic (FEM) code, (2) Long Time Scale (LTS) code and (3) Hybrid Electromagnetic (HEM) code. The FEM code solves Maxwell's equations and equations of motion for individual particles. Since no approximation is made to the basic equations, the code is applicable to a wide range of problems in plasma physics. We describe several techniques of making the simulation code more efficient and accurate. Especially, a Multiple-Time-Step (MTS) scheme we developed makes the code as efficient as the magnetostatic simulation code (with the Darwin approximation), and makes it more applicable to low frequency wave phenomena. The LTS code is specially designed for application to whistler mode wave-particle interactions. Instead of solving Maxwell's equations, it solves basic equations of wave field deduced from the Maxwell equations under an assumption of a monochromatic whistler mode wave with a slowly varying amplitude and frequency. The LTS code is very efficient for following evolution of a whistler mode wave and motions of resonant particles. The HEM code is developed for low frequency ion mode wave-particle interactions where kinetic effects of electrons are neglegible. Ions are treated as particles, while electrons are treated as a massless fluid. There exist two types of algorithms for this hybrid formulation. One is an explicit scheme which is said to be liable to numerical instability and in which we have to choose the time step very small. The other is an implicit scheme which is numerically stable but suffers from a larger energy loss in the system. We have developed a new explicit scheme whose numerical stability is greatly improved and yet its numerical energy loss is considerably small.

Chapter 3 is devoted to the study of a whistler mode wave-particle interaction which is one of the most fundamental wave-particle interactions

in the magnetosphere and plays an important role in the magnetospheric dynamics. Nonlinear orbits of resonant electrons in a monochromatic whistler mode wave are studied by a test particle simulation [Matsumoto and Omura, 1981]. We show that two types of phase bunching occur in a nonuniform magnetic field, and the importance of phase trapping is examined. Basic processes of the whistler mode interaction are studied using the LTS code with an emphasis on roles of trapped and untrapped electrons in a dipole geomagnetic field [Omura and Matsumoto, 1982]. We discuss frequency variations of whistler emissions generated through an interaction of a triggering whistler packet with an energetic electron beam in a homogeneous medium [Omura and Matsumoto, 1984]. Then we study the effects of a whistler mode wave on a particle velocity distribution in a dipole geomagnetic field. We find that the particle distribution is strongly modified and becomes unstable for whistler mode waves owing to the nonlinear phase trapping and detrapping [Matthews et al., 1984]. Based on this study, we tried a new explanation of VLF triggered emissions [Matsumoto and Omura, 1983]. We also studied an excitation of whistler mode waves by an energetic electron beam using the FEM code where electrostatic waves are also solved [Omura and Matsumoto, 1985]. It is found that the whistler mode instability could be suppressed by an effect of a co-existing electrostatic wave instability. We give a theoretical analysis to this effect of electrostatic waves.

In Chapter 4, we study the heating of heavy ions observed in the magnetosphere in conjunction with ion cyclotron waves (ICW) generated by anisotropic hot protons (i.e., GEOS-1 and 2 and ATS6 results). The ICW has a left-handed polarization, while the whistler mode wave studied in Chapter 3 has a right-handed polarization. However, both waves propagate parallel to the static magnetic field, and resonate with counter-streaming energetic particles. Therefore, characteristics of these wave-particle interactions are basically the same. We first analyze the ion cyclotron interaction in a plasma containing cold H^+ and He^+ ions by computing the linear growth rates (both temporal and spatial) for different plasma parameters: concentration, temperature, and anisotropy of cold He^+ and of hot protons [Gendrin et al., 1984]. Through this linear analysis we find suitable parameters for computer simulations. Then we run the HEM code with these parameters, and find a good agreement between the linear theory and the computer simulation at the linear phase as far as the growth rate of the wave and the frequency of the most amplified wave and the variation of the hot proton anisotropy are concerned [Omura et al., 1984]. The saturation

occurs due to trapping of the helium particles. However, most interesting results concern the heating of cold species. He^+ ions are heated mainly in the perpendicular direction and they are heated more than cold H^+ ions. The heating of He^+ ions is explained by a two-step process : first He^+ ions are set into oscillations (in both $v_\perp$ and $v_\parallel$) by the growing wave until some of the ions attain a parallel velocity of the order of the resonant velocity at which time strong heating occurs owing to the nonlinear trapping.

In Chapter 5, we study a radiation of electromagnetic and electrostatic waves from an electron beam for two different physical models using the FEM code. One of the problems is a quantitative estimation of electromagnetic radiation from an artificially injected electron beam in the Space Experiment with Particle Accelerators (SEPAC) which is an active and interactive experiment in the earth's upper atmosphere and magnetosphere using a high-power electron gun on board the space shuttle [Obayashi, 1982]. We find a strong excitation of slow extraordinary wave around the electron beam and a propagation of a pulselike ordinary wave packet excited as an impulse response to the onset of the beam injection [Omura and Matsumoto, 1984]. We also find that the electron beam initially expands in the transverse direction to the electrostatic field produced by a local excess charge of the beam electrons, and it subsequently oscillates with a frequency of the slow extraordinary wave which is excited around the beam. The other problem is to explain a phenomenon observed by the ISEE satellite which found strong electrostatic bursts often associated with a coherent chorus hook element. The electrostatic bursts that are apparently hook-induced emissions stimulated by the combined action of a coherent whistler-mode wave and a simultaneously observed electron beam with an energy range of the order of 1keV [Reinleitner et al., 1982]. In order to seek a plausible generation mechanism and interpret this nonlinear phenomenon we carried out computer simulations following nonlinear motion of more than a half-million particles in the 128-128 grid space under the self-consistent fields [Matsumoto et al., 1984]. The results show an interesting two-beam jetting as a result of a trapping and subsequent detrapping process, yielding a strong electrostatic emission with k vector parallel to the external magnetic field. The nonlinear evolution of the wave spectra and of particle distribution functions and their phase-space behavior are discussed in connection with the observed ES bursts.

In Chapter 6, we summarize the present study and give conclusions obtained through the present study via computer simulations. We also

clarify problems unsolved or items which need further investigations. Finally, we give suggestions for further works.

CHAPTER 2
COMPUTER SIMULATIONS FOR STUDY OF WAVE-PARTICLE INTERACTIONS

2.1 Introduction

In this chapter, we will give an introductory review and guide for particle simulation of electromagnetic waves in plasmas. The basic concept of particle simulations is not given in detail because it is described excellently in the existing literatures [e.g., Langdon and Lasinski, 1976; Hockney and Eastwood, 1981; Birdsall and Langdon, 1984]. First we will describe important basic concepts of particle simulations such as superparticle, discretization of space and time, and cancellation of self-force in Section 2.2. Section 2.3, 2.4 and 2.5 are devoted to the description of the basic equations and numerical algorithms of three different simulation codes which have been developed for the present study of wave-particle interactions. These codes are (1) Full Electromagnetic (FEM) code, (2) Long Time Scale (LTS) code and (3) Hybrid Electromagnetic (HEM) code. These simulation codes developed at Kyoto University are named "KEMPO" (Kyoto University ElectroMagnetic Particle cOde), "KULTS" (Kyoto University LTS code) and "KEMHO" (Kyoto University ElectroMagnetic Hybrid cOde), respectively.

2.2 Particle Model Simulations

In this section, we will give a short review of the basic concept and models used in particle simulation in general. Readers are recommended to refer to existing textbook and literature for details [Morse and Nielson, 1969; Birdsall and Fuss, 1969; Dawson, 1970; Birdsall, Langdon and Okuda, 1970; Hockney, 1970; Langdon and Birdsall, 1970; Okuda and Birdsall, 1970; Okuda and Dawson, 1973; Langdon and Lasinski, 1976;Nielson and Lewis, 1976; Hockney and Eastwood, 1981; Birdsall and Langdon, 1984].

2.2.1 Superparticles

In particle simulation, plasma dynamics is studied by following a large number of particles in their self-consistent electric and magnetic fields. Naturally, one cannot emulate nature even with the today's super-

computer. Only several orders of magnitude less number of particles are treatable in computer compared with the enormous number of particles in the real plasma of almost any size of interest. Therefore we are obliged to use an artificial model-particle called "superparticle" with a larger mass and charge than the real particle. The superparticle represents many particles in a real plasma, and has a finite size with its charge being distributed over a finite region of space.

The concept of the finite-sized superparticle was introduced historically by two research groups. First one was "Cloud-in-Cell(CIC)" [Birdsall and Fuss, 1969] and the other was "Particle-in-Cell(PIC) [Morse and Nielson, 1969]. Both were introduced as an improved model of zero-sized superparticle (plasma sheet model) to suppress statistical fluctuations and short range collisions caused by a delta-functional nature of the zero-sized superparticles [Hockney,1966; Birdsall and Fuss, 1969; Morse and Nielson,1969; Okuda and Birdsall, 1970; Langdon and Birdsall, 1970]. At the same time the method of assignment of charge and current of the superparticle to its neighboring spatial grids was improved from NGP (Nearest Grid Point) scheme to AS (Area Sharing) scheme [Morse and Nielson,1969], MPE (Multipole Expansion) scheme and SUDS (Subtracted Dipole Scheme) [Kruer et al.,1973]. The theoretical works were developed on the modification of the plasma theory for the finite-size superparticle plasma [Langdon and Birdsall, 1970; Okuda and Birdsall, 1970]. Details such as modification of the dispersion characteristics and of the collisional effects are discussed elsewhere in this book [Okuda] and are not given here.

The shape of the superparticle can be of any form. Normally, however, one of the following three shapes is, for practical codings, hired in the particle simulation. These three shapes for one dimensional case are depicted in Figure 2.1. They are (1) Square-shaped, (2) Triangular-shaped, and (3) Gaussian-shaped. As for the scheme for the charge and current assignment to the neighboring grid points, the AS (area sharing) scheme is most frequently used. A schematic illustration of charge and current assignment for the square-shaped superparticle with a charge $q_{s,i}^{(s)}$ is given in Figure 2.2. In the figure the size of the square-shaped superparticle is assumed to be identical to that of the grid (or cell). Charge and current of a superparticle is shared by grid points where the superparticle is located. The charge and current assignment is made in such a way that the share to each grid is proportional to the overlapped area of that of the superparticle and the cell area of the grid. Other

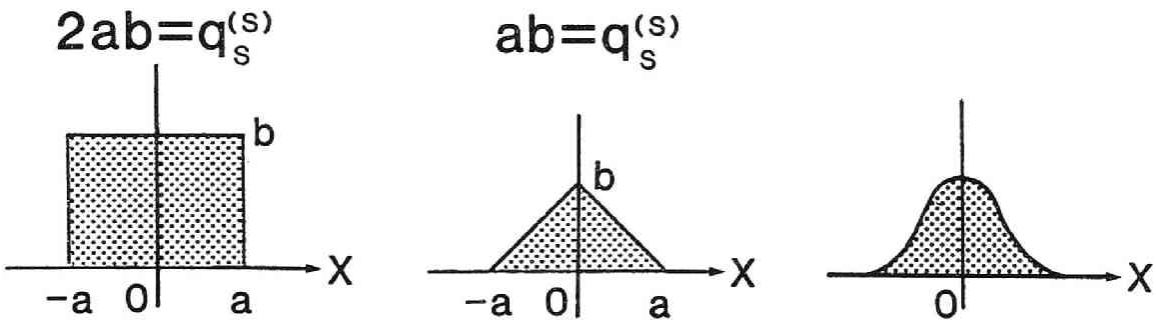

Fig. 2.1 Three shapes of superparticle: (1) Square-shaped, (2) Triangular-shaped, (3) Gaussian-shaped.

methods of the charge and current assignment have been proposed and are described in the literature [e.g., Hockney and Eastwood, 1981; Birdsall and Langdon, 1984; Okuda, 1984].

The charge and mass of the superparticle is much larger than those of the real particle. However the following three densities of the superparticles are taken to be the same as those of the real particles.

(1) Charge Density

$$N_s Q_s = N_r Q_r \tag{2.1}$$

(2) Mass Density

$$N_s M_s = N_r M_r \tag{2.2}$$

(3) Energy Density

$$N_s \kappa T_s = N_r \kappa T_r \tag{2.3}$$

where the subscripts, s and r, mean the quantities of the super- and real-particles, and N, Q, M, κ and T denote number density, charge, mass, Boltzmann's constant and temperature, respectively. Under these equalities, not only the charge to mass ratio but also the basic physical quantities such as the plasma and cyclotron frequencies, the Debye length, and the thermal velocity are kept identical to each other in both

simulational and real plasmas. Thus the most of the physical properties of the plasma are reproduced in the particle simulation.

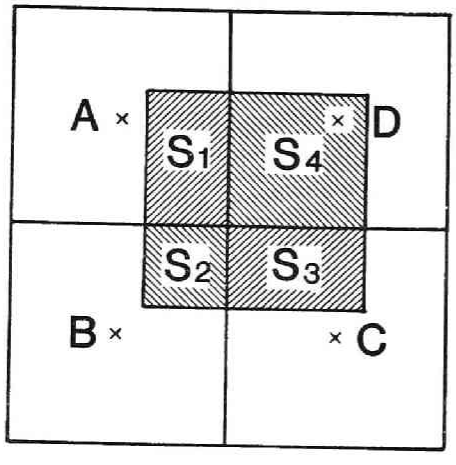

charge current

$$A: \frac{S_1}{S} q_{s,i}^{(s)}, \frac{S_1}{S} q_{s,i}^{(s)} \underset{\sim}{v}_{s,i}$$

$$B: \frac{S_2}{S} q_{s,i}^{(s)}, \frac{S_2}{S} q_{s,i}^{(s)} \underset{\sim}{v}_{s,i}$$

$$C: \frac{S_3}{S} q_{s,i}^{(s)}, \frac{S_3}{S} q_{s,i}^{(s)} \underset{\sim}{v}_{s,i}$$

$$D: \frac{S_4}{S} q_{s,i}^{(s)}, \frac{S_4}{S} q_{s,i}^{(s)} \underset{\sim}{v}_{s,i}$$

Where $S = S_1 + S_2 + S_3 + S_4$

Fig. 2.2 Schematic illustration of charge and current assignment for the square-shaped superparticle.

2.2.2 Discretization of Space and Time

In the particle simulation, both space and time are discretized. Spatial discretization is introduced by two reasons. One is to speed up the calculation of force acting on particles [Buneman, 1959; Dawson,1961]. Instead of calculating all contribution of Coulomb force from all particles, the force acting on a superparticle is calculated by field quantities defined on the grid points nearby the particle. Second reason is that the superparticle has a finite size over a certain region of space so that the spatial resolution smaller than the particle size is

unnecessary and meaningless. Normally, the spatial grid spacing is taken to be from 1 to 3 times the Debye length. Numerical stability related to the choice of the grid size has been studied in detail [Langdon and Birdsall, 1970; Okuda, 1973; Abe et al.,1981].

Time discretization is inevitable in any numerical approach to any partial differential equations. The problem is how large we can choose the time step keeping the numerical stability. To avoid the numerical instability, the Courant-Fredericks-Lewy (CFL) condition should be satisfied. In case of the electromagnetic particle simulation, the CFL condition is

$$\Delta t < \Delta r/(c\sqrt{n}) \tag{2.4}$$

where n is the spatial dimension of the simulation model, and c is the light speed.

Discretization of space and time modifies the dispersion characteristics. This modification comes from digital samplings of continuous quantities in space and time. As is well known from the sampling theorem, the frequency ω and wavenumber k should be replaced by $\Omega = \sin(\omega\Delta t/2)/(\omega\Delta t/2)$ and $K = \sin(k\Delta r/2)/(k\Delta r/2)$, respectively (see Appendix A) Thus the dispersion equation for real plasma, $D(\omega,k) = 0$ is modified to $D(\Omega, K) = 0$. Because of this sampling function nature, high frequency and large k components are folded down in the low and small k domain in the ω-k space as "aliases". This effect should always be taken into account both in designing the model of simulation and in analyzing the simulation data.

2.2.3 Average Field and Self-Force

Since the charge of the superparticle with a finite size smears out in space, the force acting on it is the averaged one. In this sub-section, we will discuss the procedure for the average and its related self-force problem. To this purpose, we will confine ourselves only to the simplest case of the square-shaped superparticle in one-dimensional case. Extension to the case of superparticles with other shapes and/or two-dimensional case is straightforward. We also limit our discussion only to the case of the electrostatic electric field as an example of the self-force. The magnetostatic self-force can be treated in a similar manner.

To guarantee the centered difference scheme for Maxwell's equations (Poisson's equation in this particular example), we normally adopt a staggered dual grid system composed of full-integer- and half-integer grid

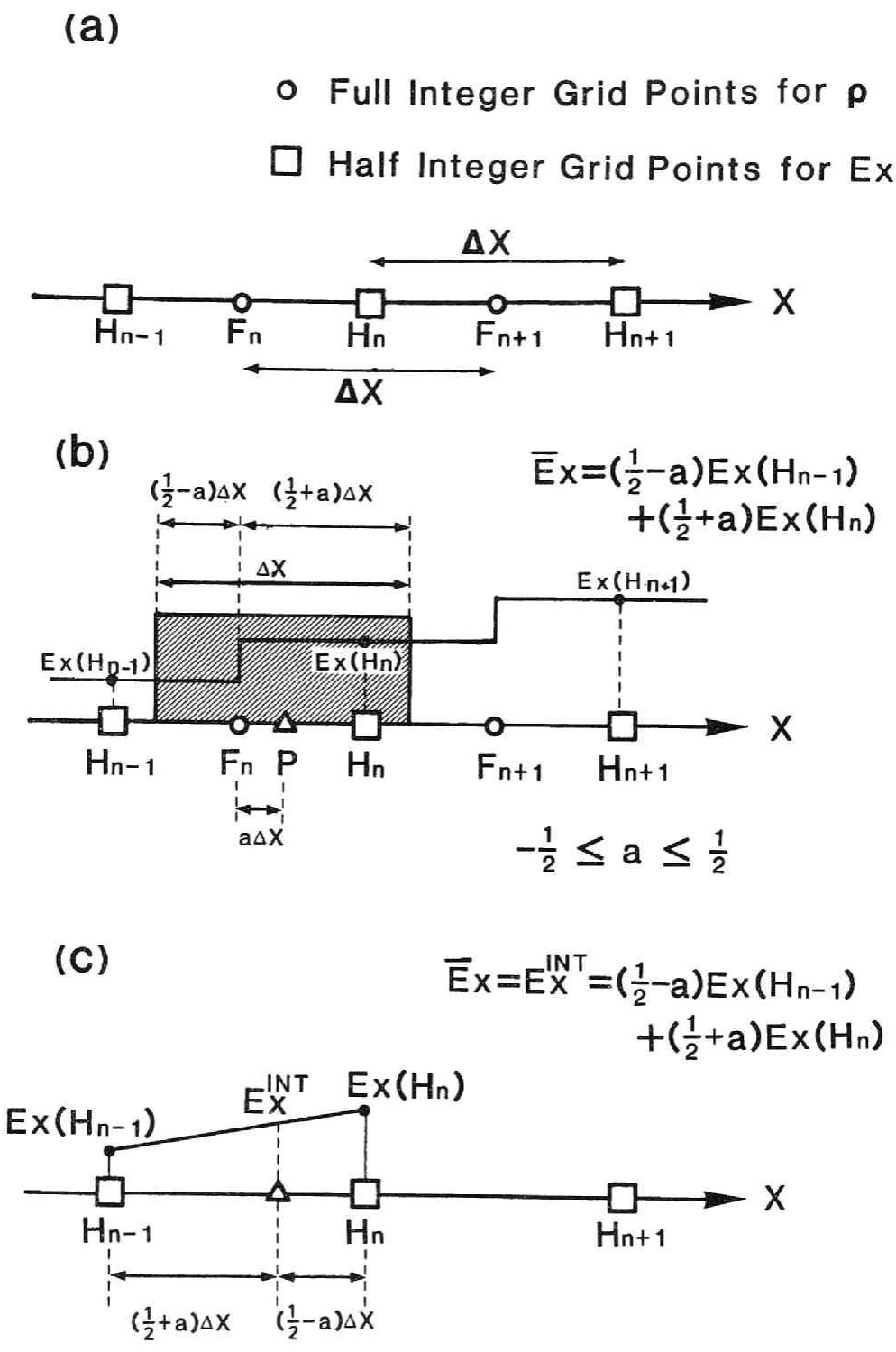

Fig. 2.3 Staggered dual grid system and effective electric field acting on a superparticle.

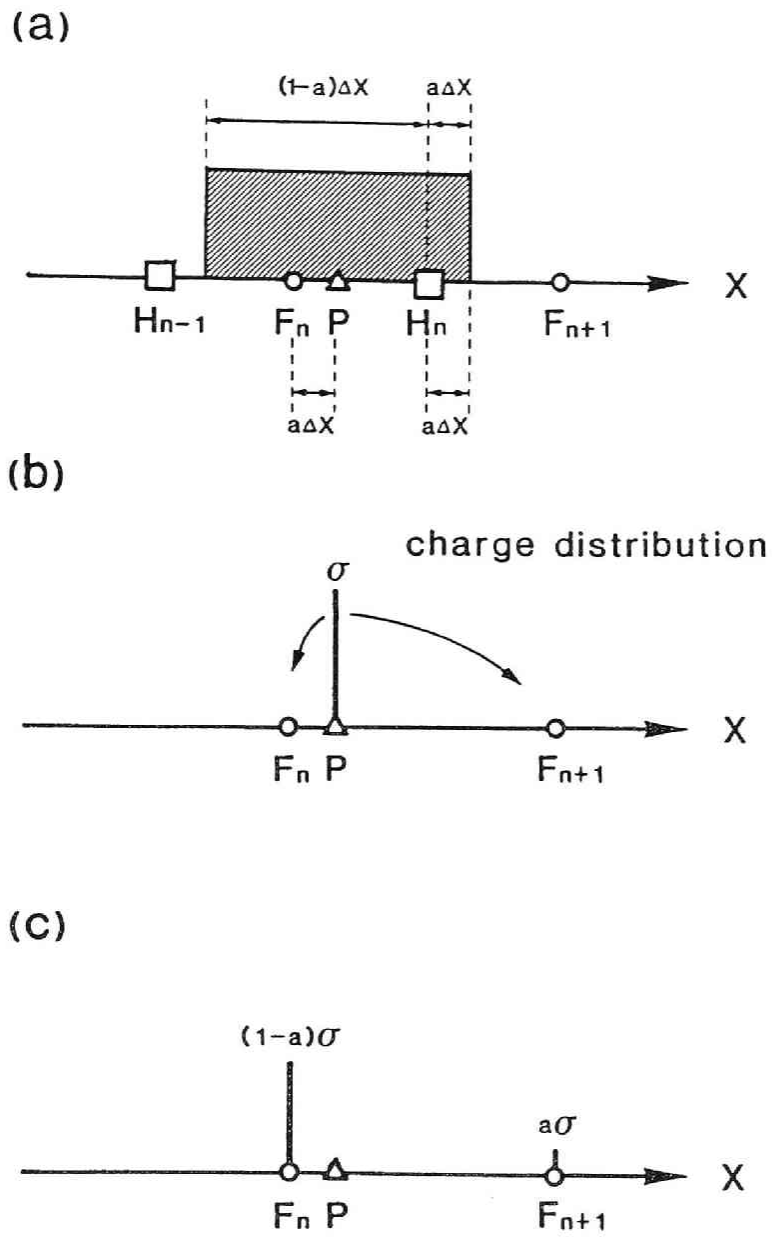

Fig. 2.4 Charge distribution of superparticles to grid points.

points as illustrated in Figure 2.3(a). The open circle points indicate full-integer-grid points on which the charge is defined. The open square symbols along the x-axis are half-integer grid points on which the electric field E_x is defined. Suppose that a superparticle with a size of the grid spacing Δx is located at point P in between F_n and F_{n+1} with a distance $a\Delta x$

from F_n as illustrated in Figure 2.3(b). Then the area-weighted average of the electric field $\bar{E}$ is given by

$$\bar{E} = \left(\frac{1}{2} - a\right)E_x(H_{n-1}) + \left(\frac{1}{2} + a\right)E_x(H_n) \quad . \tag{2.5}$$

The effective electric field which the superparticle feels is this averaged value $\bar{E}$. It is formally computed by a simple linear interpolation from the two values of E_x at two adjacent grid points H_{n-1} and H_n as shown in Figure 2.3(c). However, one should note that the simply interpolated value $E^{INT}(P)$ from $E_x(H_{n-1})$ and $E_x(H_n)$ produces a nonphysical force acting on the superparticle. The nonphysical force is called a "self-force". Physically, the electric or magnetic field produced by a particle should not give any force back to the particle itself.

As far as we adopt the staggered dual grid system together with the area sharing scheme for charge and current distribution to grid points, the self-force comes in automatically and leads to violation of conservation of energy and momentum through the nonphysical acceleration of particles. To demonstrate how the self-force appears, let us consider a case where only one superparticle is placed in the system at a point P as shown in Figure 2.4(a). The charge density σ of the superparticle is distributed to two adjacent grid points F_n and F_{n+1} by the area sharing scheme. This process is identical to divide the concentrated charge density σ at the point P onto F_n and F_{n+1} as illustrated in Figure 2.4(b). The resultant charges at F_n and F_{n+1} are $(1-a)\sigma$ and $a\sigma$, respectively as shown in Figure 2.4(c). The electrostatic field E_x produced by the particle is represented by a step function with a jump of amount of σ/ε_0 as shown in Figure 2.5(a). Due to the symmetry characteristics, $E_x = 0$ at the particle location P. However, in the computer simulation, the electric fields at half-integer grid points are calculated from the charge distribution at full-integer grid points. Thus as illustrated in Figure 2.5(b), the electric field at the half-integer points are

$$\begin{aligned} E_x(H_{n-1}) &= -\frac{1}{2}\frac{\sigma}{\varepsilon_0} \\ E_x(H_n) &= \frac{1}{2}\frac{\sigma}{\varepsilon_0}(1 - 2a) \end{aligned} \quad . \tag{2.6}$$

These values are, in turn, used to compute the effective electric field

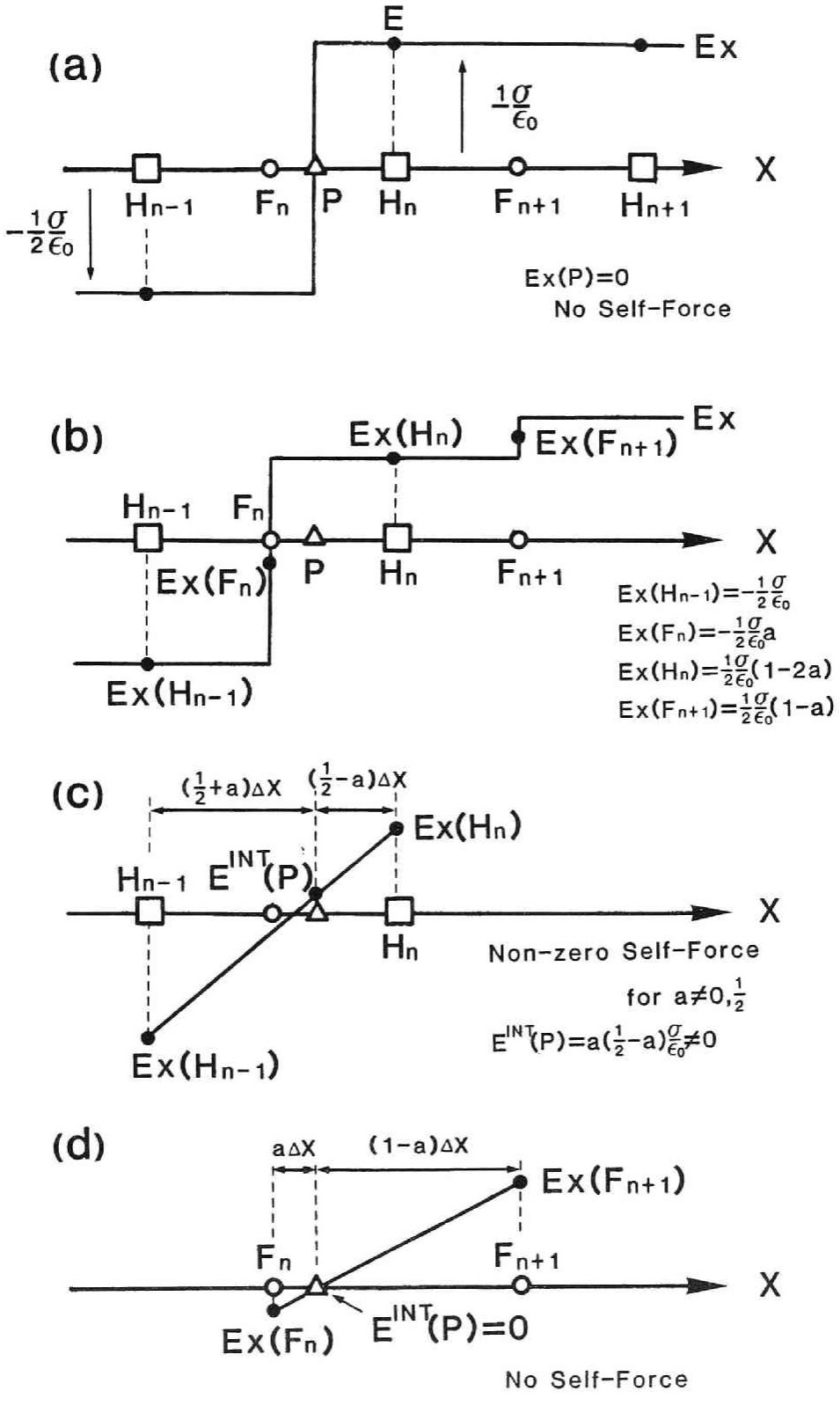

Fig. 2.5 Explanation of self-force and its cancellation.

acting on the superparticle at P using Eq.(2.5). Then, unfortunately, the result is given by

$$\bar{E}_x(P) = E_x^{INT}(P) = a\left(\frac{1}{2} - a\right)\frac{\sigma}{\varepsilon_0} \tag{2.7}$$

which is not zero except for special cases of a = 0 or 1/2 as illustrated by Figure 2.5(c). This non-zero electric field acts on the particle and accelerates it nonphysically. Therefore, we cannot simply estimate the effective electric fields by Eq.(2.5) if we use the E_x values at half-integer points. However, as shown in Figure 2.5(d), the correct value can be computed by the same linear interpolation scheme if we use the electric field values at F_n and F_{n+1}, i.e., at two adjacent full-integer points. The values of E_x at these full-integer points are given by (see Figure 2.5(b))

$$\begin{aligned} E_x(F_n) &= -\frac{1}{2}\frac{\sigma}{\varepsilon_0}a \\ E_x(F_{n+1}) &= \frac{1}{2}\frac{\sigma}{\varepsilon_0}(1 - a) \end{aligned} \tag{2.8}$$

which yields

$$\bar{E}_x(P) = E_x^{INT}(P) = 0 \tag{2.9}$$

Therefore, to avoid the self-force, we need to relocate the values of E_x onto the same grid points where the charge is defined. In the same way, the magnetic field should be relocated onto the grid points where the current is defined. Details of the grid assignment of various physical quantities are described in Section 2.3.3.

2.3 Full Electromagnetic Code

2.3.1 General Features of FEM Code (KEMPO)

We have developed a two-and-half dimensional electromagnetic simulation code which solves Maxwell's equations and equations of motion of electrons and, if necessary, ions explicitly. We assume (x, y, z)-coordinates neglecting variation along the z axis, i.e., $\partial/\partial z = 0$. Three

velocity components v_x, v_y, v_z and all three components of electromagnetic fields E and B are retained. Since no approximation is made to the basic equations except for $\partial/\partial z = 0$, the code is applicable to a wide rage of two-dimensional problems in plasma physics. The algorithm for integration of the field and particles is designed basically after Langdon and Lasinski [1976]. The fields are integrated using Maxwell's equations in a central difference form in space and time. Particles are integrated by the Buneman-Boris method [Buneman, 1967. Boris, 1970] which is accurate to the second order and time-reversible. The current density J and the charge density ρ are calculated using PIC (particle in cell) method which distributes the current and charge of a superparticle to the adjacent four grid points with the area weighting. The electric and magnetic fields acting on the superparticle are interpolated to the particle position from the adjacent four grid points with the same area weighting.

In the following sections we describe several techniques making the simulation code more efficient and accurate. Especially, a Multiple-Time-Step (MTS) scheme we developed makes the code as efficient as the magnetostatic simulation code (with the Darwin approximation), and makes it more applicable to low frequency problems such as in the lower hybrid resonance region and of ion wave modes.

2.3.2 Multiple Time Step Scheme

The time step which satisfies the CFL condition is often too small for the wave modes of interest. Usually the wave frequencies of interest are of the order of the plasma frequency or the cyclotron frequency, while the maximum frequency in the system is $\pi/\Delta t$, and is much higher than these wave frequencies of interest. Since most of the CPU time is used to solve the particle motion rather than the field integration, it is desired to take a larger time step for the particle calculations. Langdon and Lasinski [1976] proposed an algorithm in which the fields are integrated twice as often as the particles. However, they discovered that the algorithm can lead to a numerical instability. We developed a new algorithm where the particles are advanced less often than the field without leading to the numerical instability. A filtering of the field quantities in time is performed to avoid the numerical instability.

The high frequency parts of the fast extraordinary (FE) and ordinary (O) modes, i.e., the light modes, receive little contribution from the particle motion which is expressed as the conduction current density J in

Maxwell's equations. This is justified by taking the ratio of the conduction current J and the displacement current $\varepsilon_0 \partial E/\partial t$ as (see Appendix B)

$$\frac{J}{\varepsilon_0 \partial E/\partial t} \leqslant \left(\frac{\omega_p}{\omega}\right)^2 \left(1 + \frac{v_{th} B_0}{V_p B_w}\right) \tag{2.10}$$

where v_{th} is the thermal velocity of the particles, and V_p is the phase velocity of the wave. B_w is a wave amplitude and B_0 is a static magnetic filed. If $\omega \gg \omega_p$ and $v_{th}/V_p \leqslant B_w/B_0$, the conduction current is negligibly small.

As the particle motion has little effects on the high frequency waves, we may eliminate the high frequency components of the current J, and treat the high frequency waves as the light mode in vacua. Then velocities and positions of particles may not necessarily be updated at as often as for the wave integration. We adopt two different time steps for the field integration and particle integration, respectively. The time step for the field is called "field-time-step" and the time step for the particles is called "particle-time-step". We define the field-time-step as Δt and take the particle-time-step as an integer multiple of the filed-time-step, i.e., $m\Delta t$. We call the algorithm using the particle-time-step of $m\Delta t$ as "Multiple Time Step (MTS) scheme" hereafter.

In order to eliminate the high frequency component of the current density J it is necessary to perform a time-filtering of the electromagnetic force acting on the particles. If the particles are not affected by the high frequency electromagnetic force, the conduction current density J, which is the summation of the particle motion, does not have high frequency components, yielding a consistent simulation. Since the current density J is calculated at each particle-time-step. the current density at each field-time-step is extrapolated and/or interpolated from the values available at the two nearest particle-time-steps.

In Figure 2.6 the algorithm of the MTS scheme is depicted as a time step chart. The time step charts are depicted for the case of m = [even number] in Figure 2.6(a) and for the case of m = [odd number] in Figure 2.6(b), respectively. E_p and B_p are the electric and magnetic fields for particle pushing, which are the sums of the fields E and B at the m time steps indicated by the dashed rectangle in Figure 2.6. This operation automatically gives the averages of the field E and B over the period of $m\Delta t$, and has an effect of the time filtering, which suppresses

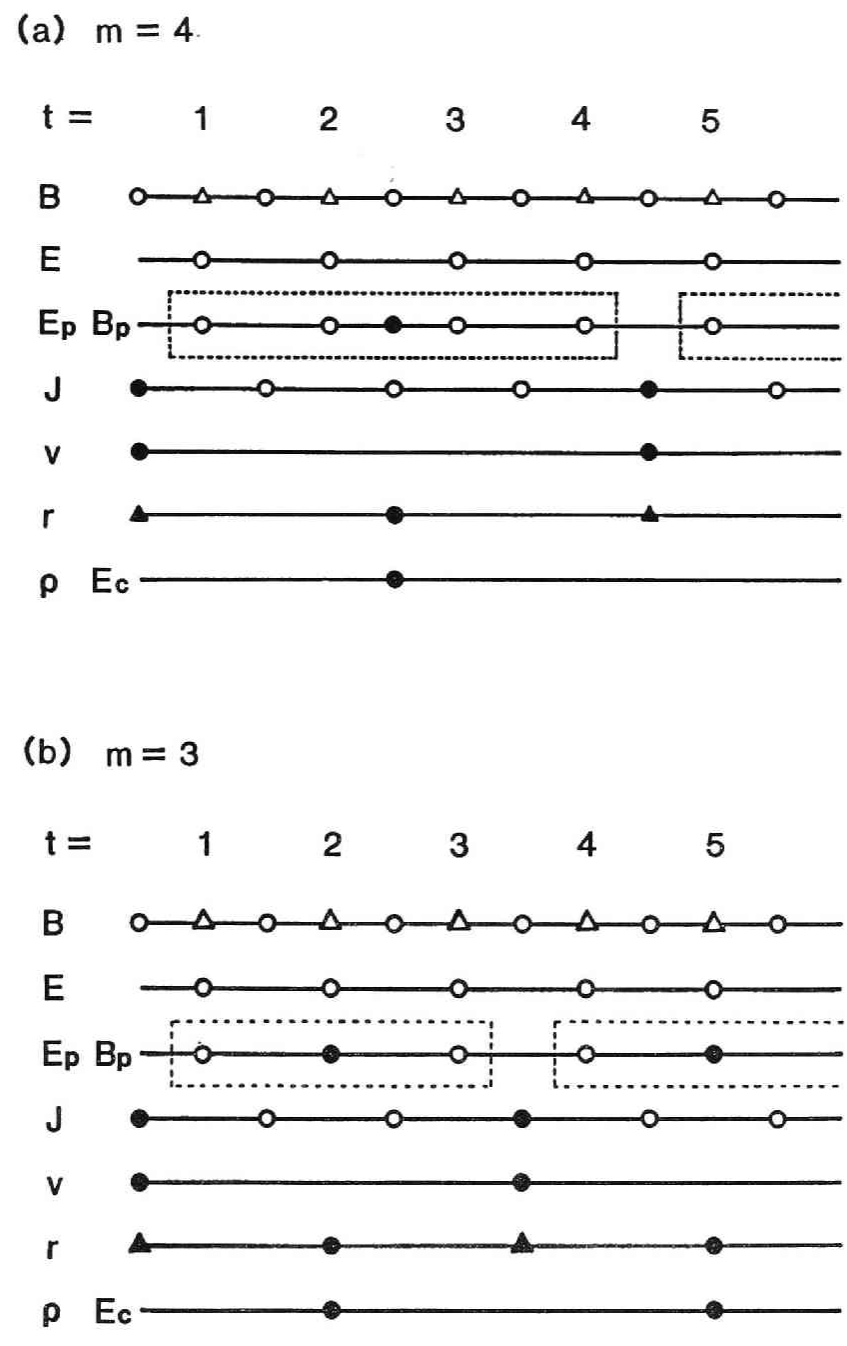

Fig. 2.6 Time step chart of the MTS scheme : (a) m = 4 (b) m = 3.

the high frequency components of the fields. These operations are depicted in the flow chart of the KEMPO as illustrated in Figure 2.7. Using these E_p and B_p, we advance the velocities of particles over the particle-time-step $m\Delta t$. The fields E and B are re-integrated from these E_p and B_p over the period $(m-1)\Delta t/2$ using the field-time-step Δt recursively.

The current density J for the re-integration is interpolated in time from the values at the adjacent particle-time-steps. Then the fields E and B are integrated further over the period of $m\Delta t$ in order to obtain new E_p and B_p, where the current density J is extrapolated from the values at the previous two particle-time-steps.

The MTS scheme has an effect of digital filtering of the electromagnetic fields in time sequence. The digital filtering is an m-point filtering with equal weightings, which is defined by the following equation.

$$\phi_f(T_j) = \frac{1}{m} \sum_{k=-(m-1)/2}^{(m-1)/2} \phi(T_{j+k}) \tag{2.11}$$

High frequency waves are attenuated at every particle-time-step. The attenuation factor A of the wave of a frequency ω is obtained by assuming

$$\phi(\omega) = \frac{1}{N} \sum_{j=1}^{N} \phi(T_j)\, e^{i\omega T_j} \tag{2.12}$$

where N is a number of time steps. From (2.11) and (2.12), we have

$$\phi_f(\omega) = \frac{1}{m} \sum_{k=-(m-1)/2}^{(m-1)/2} e^{-i\omega(k\Delta t)} \phi(\omega) \tag{2.13}$$

which gives the attenuation factor for m = (even number) as

$$A(\omega\Delta t) = \frac{\phi_f(\omega)}{\phi(\omega)} = \frac{2}{m} \left[\sum_{k=1}^{m/2} \cos\left\{ \left(k - \frac{1}{2} \right) \omega\Delta t \right\} \right] \tag{2.14}$$

and for m = (odd number) as

$$A(\omega\Delta t) = \frac{\phi_f(\omega)}{\phi(\omega)} = \frac{1}{m} \left\{ 1 + 2 \sum_{k=1}^{(m-1)/2} \cos(\omega k\Delta t) \right\} \tag{2.15}$$

The attenuation factor A is plotted as a function of $\omega\Delta t$ for m = 2 to 8 in Figure 2.8. Since the maximum frequency of the system is $\pi/\Delta t$, A is calculated in the range of $0 \leqslant \omega\Delta t \leqslant \pi$. As noted from the curves, high frequency modes undergo phase-reversal in the MTS scheme, but they also get damped and disappear from the system.

Electrons undergo oscillation with the plasma frequency ω_p in the direction of the static magnetic field. Since the plasma oscillation is a simple harmonic oscillation, the stability criterion for the leapfrog harmonic oscillator [Hockney and Eastwood, 1981] must be so as to give

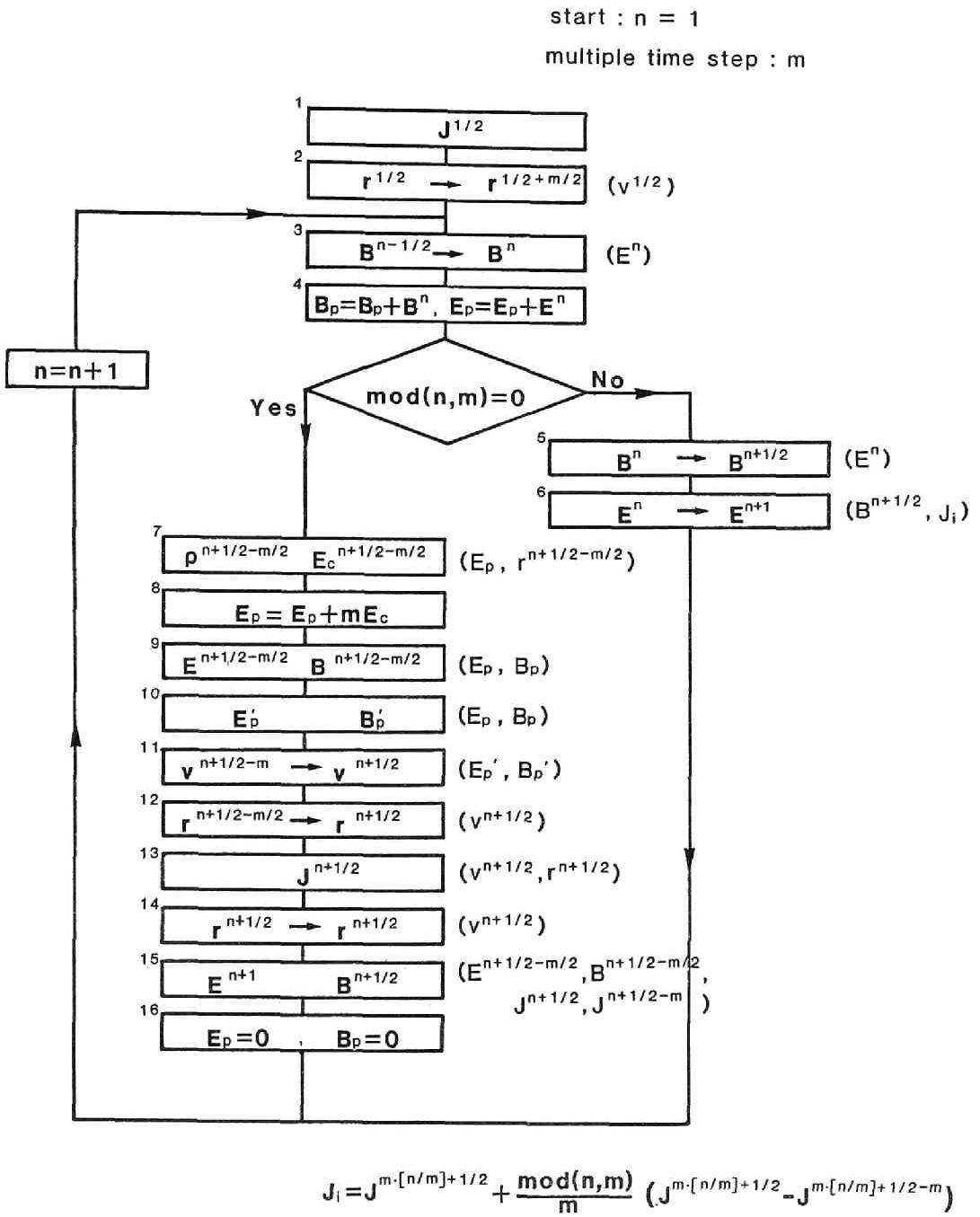

Fig. 2.7 Flow chart of the KEMPO : Quantities in boxes are calculated or advanced in time using quantities in parentheses.

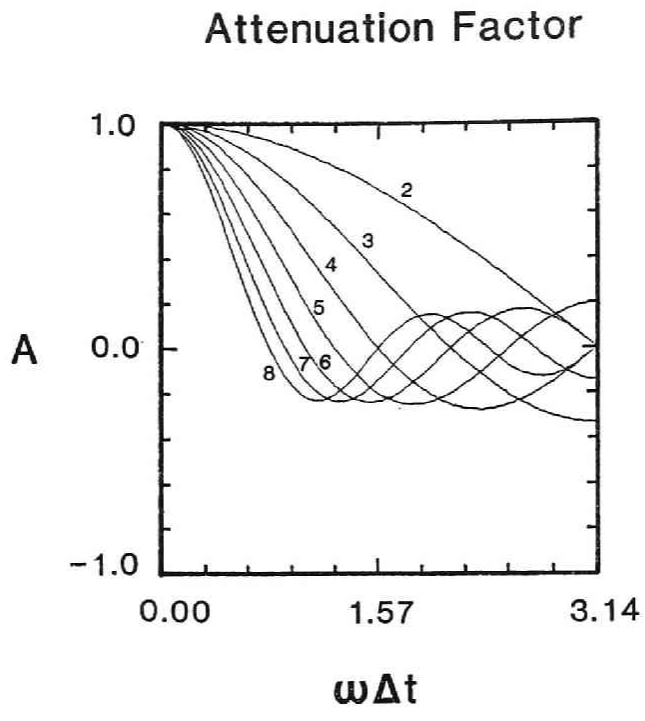

Fig. 2.8 Attenuation factor $A(\omega\Delta t)$ of the MTS scheme for different multiple time steps. The numbers attached to the curves indicate the MTS factor m.

$$\omega_p m\Delta t \leqslant 2 \quad . \tag{2.16}$$

In the transverse plane electrons follow the cyclotron motion with a cyclotron frequency ω_c. The Buneman-Boris method for the particle integration is unconditionally stable for the cyclotron motion. However, if the frequency of the waves of interest are less than or nearly equal to ω_p or ω_c, the following condition is generally satisfied in order to obtain a reasonable resolution and accuracy.

$$\mathrm{Max}(\omega_p,\omega_c)\cdot m\Delta t \leqslant 0.2 \tag{2.17}$$

We define an attenuation rate Γ_A by $\log A(\omega) / (m\Delta t)$. In Figure 2.9 the ratio of the attenuation rate and a wave frequency Γ_A/ω is plotted as a function of $\omega\Delta t$ for m=1~8. The MTS factor m and field-time-step Δt must be chosen so that Γ_A is much less than physical growth/damping rate of electromagnetic waves in the simulation model.

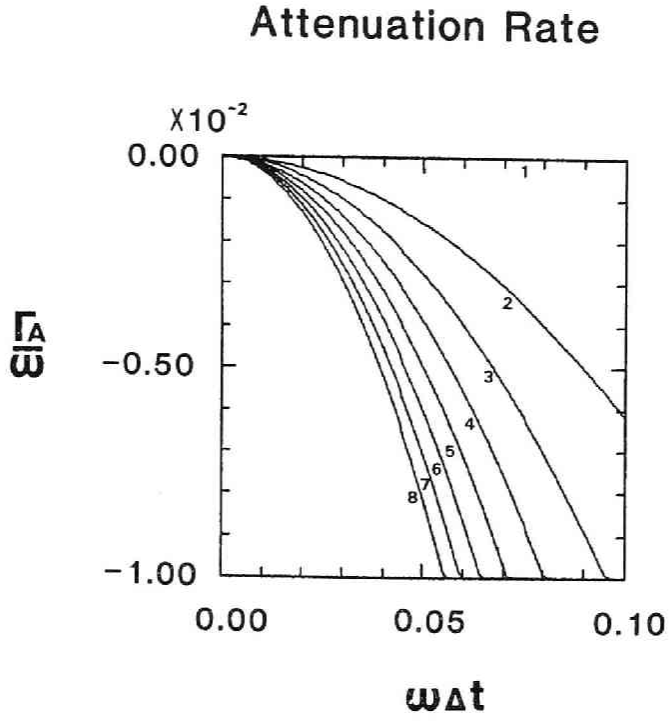

Fig. 2.9 Attenuation rate Γ_A/ω of the MTS scheme for different multiple time steps. The numbers attached to the curves indicate the MTS factor m.

2.3.3 Grid Location for Integration of the Field

For the two dimensional system Maxwell's equations are reduced to the following two independent sets of equations.

(A)

$$\frac{\partial B_z}{\partial t} = -\frac{\partial E_y}{\partial x} + \frac{\partial E_x}{\partial y} \tag{2.18}$$

$$\frac{\partial E_x}{\partial t} = c^2 \left[\frac{\partial B_z}{\partial y} - \mu_0 J_x \right] \tag{2.19}$$

$$\frac{\partial E_y}{\partial t} = c^2 \left[-\frac{\partial B_z}{\partial x} - \mu_0 J_y \right] \tag{2.20}$$

(B)

$$\frac{\partial B_x}{\partial t} = -\frac{\partial E_z}{\partial y} \tag{2.21}$$

$$\frac{\partial B_y}{\partial t} = -\frac{\partial E_z}{\partial x} \tag{2.22}$$

$$\frac{\partial E_z}{\partial t} = c^2 \left[\frac{\partial B_y}{\partial x} - \frac{\partial B_x}{\partial y} - \mu_0 J_z \right] \tag{2.23}$$

These equations (A) and (B) are solved as central difference equations in space and time by defining the E, B and J at the location shown in Figure 2.10-(a) and -(b) [Langdon and Lasinski, 1976]. For further reference we call the grid with label "i" a full grid (F) in x and the grid with label "i+1/2" a half grid (H) in x. Likewise, we call the grid with a label "j" a full grid (F) in y and the grid with label "j+1/2" a half grid (H) in y. Combining x and y locations, we express the locations of the grid points with (i,j), (i+1/2,j), (i,j+1/2) and (i+1/2,j+1/2) by FF, HF, FH and HH.

The grid locations shown in Figure 2.10 are summarized as follows.

E_x	B_x	J_x	:	HF
E_y	B_y	J_y	:	FH
E_z	B_z	J_z	:	HH

The current densities J_x, J_y and J_z are defined at different locations. To assign contributions of particles to the grid points, we have to calculate three different area-weightings. In order to reduce the CPU time in calculating area-weightings, we first calculate all J_x, J_y and J_z at HH grid points, and then relocate J_x and J_y to HF and FH grid points by the following operations, respectively.

$$J'_{x\ i+1/2,\ j} = \frac{1}{2} \left(J_{x\ i+1/2,\ j-1/2} + J_{x\ i+1/2,j+1/2} \right) \tag{2.24}$$

$$J'_{y\ i,\ j+1/2} = \frac{1}{2} \left(J_{y\ i-1/2,\ j+1/2} + J_{y\ i+1/2,j+1/2} \right) \tag{2.25}$$

where the quantities with ' are relocated ones. The relocation procedure has the effect of spatial filtering (see Section 2.3.4). This filtering reduces electromagnetic radiation loss at small wavelengths. As J_z is not

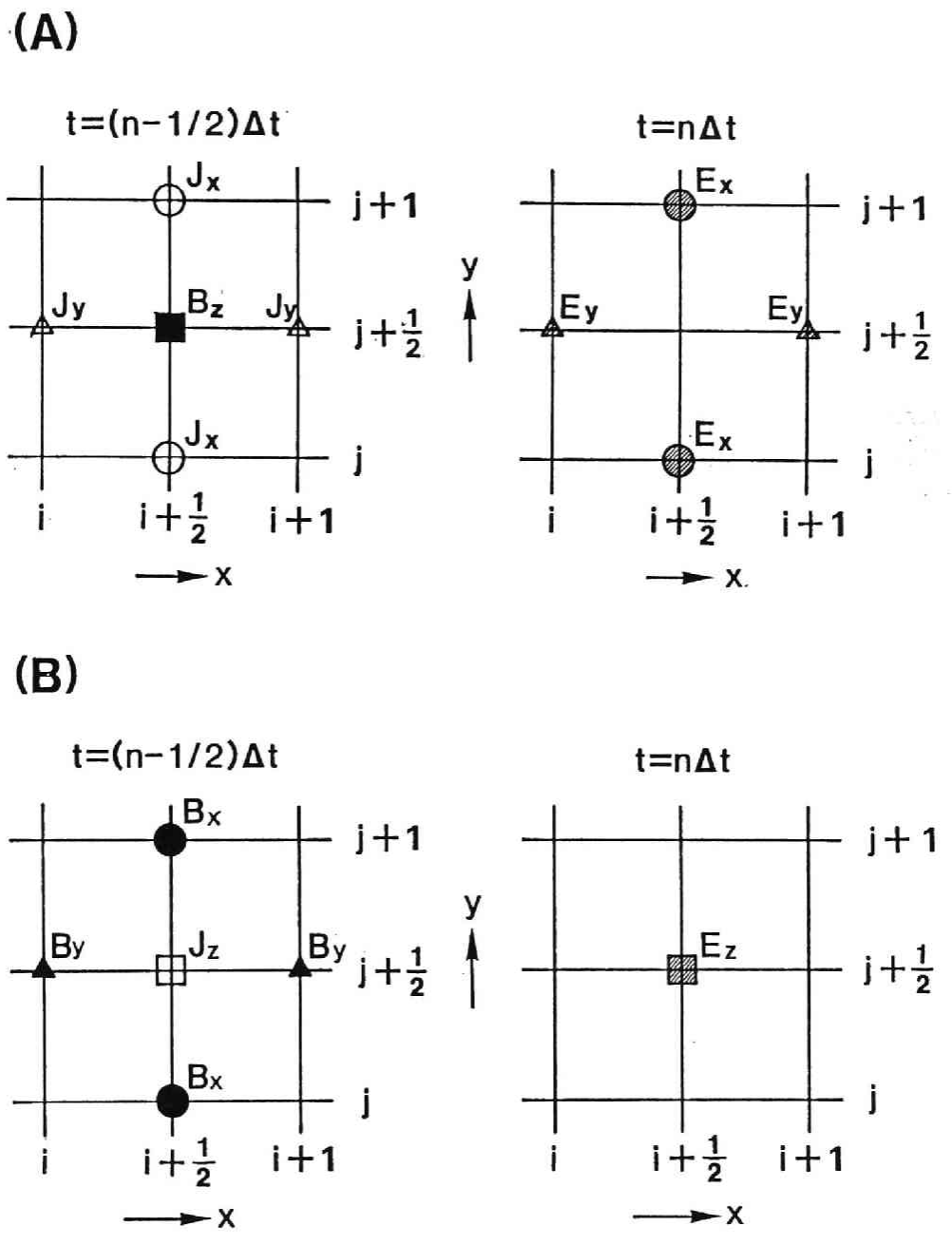

Fig. 2.10 Allocation of field quantities to grid points: (a) E_x, E_y, B_z, J_x, J_y ; (b) E_z, B_x, B_y, J_z.

relocated, it is necessary to apply the three point filtering to J_z both in x and in y directions. It is noted that filtering of J_x in x-direction and J_y in y-direction is not necessary at all, because fluctuations of J_x in x direction and J_y in y direction are not responsible to the electromagnetic radiations. In addition, the current density $\vec{J}$ and $\vec{E}$ must satisfy

$$\mathrm{div}\ \left(\vec{J} + \varepsilon_0 \frac{\partial \vec{E}}{\partial t} \right) = 0 \tag{2.26}$$

Since the electrostatic components E_x and E_y are calculated from the charge distribution via Poisson's equation, the relocation of J_x in x and J_y in y only increases the inconsistency of J_x and J_y with E_x and E_y, respectively.

The electric fields E_x and E_y obtained by integrating Eqs. (2.19) and (2.20) are corrected by solving Poisson's equation using the charge density defined at FF grid points. If we calculate an electric force acting on particles from the electric field E_x and E_y defined at HF and FH grid points, it results in an electrostatic self-force acting on the particle, violating the momentum conservation as discussed in Section 2.1. The area weighting in the calculation of the charge density and that in the calculation of the force acting on particles must be identical and must be done using the quantities defined at the same grid locations. Since the charge density is defined at FF grid points, the electric field E_x and E_y obtained at FH and HF grid points must be relocated to the FF grid points before calculating the particle force. The above discussion of the electrostatic self-force is also applied to the magnetostatic force induce by Ampere's low rot $B = \mu_0 J$, which is rewritten as

$$\frac{\partial B_z}{\partial y} = \mu_0 J_x \tag{2.27}$$

$$-\frac{\partial B_z}{\partial x} = \mu_0 J_y \tag{2.28}$$

$$\frac{\partial B_y}{\partial x} - \frac{\partial B_x}{\partial y} = \mu_0 J_z \tag{2.29}$$

As the B_z is defined at HH grid points where J_x and J_y are also calculated by the area weighting scheme. The relations of Eqs. (2.28) and (2.29) do not produce the self-force. However, B_x and B_y are defined at HF and FH grid points, while J_z is defined at HH grid points. In the calculation of the magnetic force acting on particles, B_x and B_y must be relocated to HH grid points.

Let us summarize the relocation procedure for elimination of the self-force.

E_x : HF → FF
E_y : FH → FF
B_x : HF → HH
B_y : FH → HH

E_z and B_z are not relocated.

Owing to the relocation procedure, computing time for calculating the particle forces is reduced because the area weighting for FH and HF grid points are not computed any more. In calculation of electromagnetic forces acting on particles, E_x and E_y are interpolated from FF grid points, while E_z, B_x, B_y and B_z are interpolated from HH grid points.

2.3.4 Digital Filtering

Spatial filterings of the quantities defined at grid points are generally used in order to eliminate nonphysical noises at short wavelengths, where the finite difference of the fields becomes most inaccurate. Two kinds of digital filtering schemes are used in the KEMPO. One is a filtering of two-point averaging as defined by

$$\phi'_{i+1/2} = \frac{1}{2} (\phi_i + \phi_{i+1}) \tag{2.30}$$

which is implicitly involved in the relocation procedure of the field quantities. The other is three-point digital filter or a binomial digital filter [Birdsall and Langdon, 1984] given as

$$\phi'_i = \frac{1}{4} (\phi_{i-1} + 2\phi_i + \phi_{i+1}) \tag{2.31}$$

which is explicitly used in the code. The attenuation factor of these two filters are given by the following equations.

Two-point digital filter :

$$\phi'(k) = \cos \frac{k\Delta x}{2} \phi(k) \tag{2.32}$$

Three-point digital filter :

$$\phi'(k) = \cos \left(\frac{k\Delta x}{2} \right)^2 \phi(k) \tag{2.33}$$

These filters are used in the following two manners. Firstly they are applied to the particle-pushing fields E_p and B_p in order to eliminate nonphysical random forces which causes stochastic heatings of particles. Since the relocation procedures implicitly involving the two-point filter are different for the components (E_x, E_y, etc.) and for the directions (x and y), it is necessary to apply the three-point filter to the components and directions which are not affected by the relocation procedure. Secondly these filters are applied to the current density calculated from the particles. The current density is the source of electromagnetic radiations. Fluctuations at short wavelengths correspond to high frequency electromagnetic waves which undergo a damping by the time filtering of MTS scheme as time goes on. Due to the electromagnetic radiations which are to be damped by both spatial and time filtering, particles lose their thermal energy. In order to prevent the energy loss, it is necessary to eliminate fluctuations at short wavelength by the digital filters.

2.3.5 Unit System used in the FEM Code

It is noted that there is no necessity to stick to a real unit system like CGS or MKS unit system in simulations. What is important in simulations are ratios of quantities in the system, i.e., a ratio of a wave magnetic field to the static magnetic field, or a ratio of a kinetic energy to the total energy, etc.. In most of simulations physical quantities are normalized to the basic parameters in the system where the basic parameters are assumed to be unity. However, selections of basic parameters are different depending on physical models. In order to make the simulation code applicable to various problems of a wide range of parameters, we do not normalize any quantities, or rather we adopt a relative unit system where all parameters are calculated from a set of independent basic parameters via basic equations. These basic parameters are as follows.

1. Angular frequency (plasma, cyclotron, wave frequency etc.)
   ω_{pi}, ω_{c1}, ω
2. System length L_x, L_y
3. Charge-to-mass ratio $(q/m)_i$
4. Number of superparticles in the system N_i

where the subscript "i" denotes the i-th species of particles. Note that the cyclotron frequency is specified only for species 1. Values of these four quantities are given arbitrarily, except that ratios of quantities in

the same units like ω_{pi}/ω_{c1}, L_y/L_x or $(q/m)_2/(q/m)_1$, are kept the same as those of the real physical quantities. Especially, it is noted that numbers of superparticles have no relation to the real number densities in the plasma, and N_1 and N_2 are independent of each other.

The basic equations are written in the following form which is identical to those in the MKS unit system.

(1) Equations of motion

$$\frac{d\vec{r}}{dt} = \vec{v} \tag{2.34}$$

$$\frac{d\vec{v}}{dt} = \frac{q_i}{m_i} (\vec{E} + \vec{v} \times \vec{B}) \tag{2.35}$$

(2) Maxwell's equations

$$\text{rot } \vec{B} = \mu_0 \vec{J} + \frac{1}{c^2} \frac{\partial \vec{E}}{\partial t} \tag{2.36}$$

$$\text{rot } \vec{E} = - \frac{\partial \vec{B}}{\partial t} \tag{2.37}$$

$$\text{div } \vec{B} = 0 \tag{2.38}$$

$$\text{div } \vec{E} = \frac{\rho}{\varepsilon_0} \tag{2.39}$$

where c, ε_0 and μ_0 are the light speed, electric permittivity and magnetic permeability, respectively.

It is noted that ε_0 and μ_0 may be chosen arbitrarily except that $\varepsilon_0 \mu_0 = 1/c^2$. For simplicity, we define $\varepsilon_0 = 1$ and $\mu_0 = 1/c^2$, and the units of charge, mass, electric and magnetic fields are given based on their definition.

Other physical quantities are calculated via the following relations obtained from the basic equations. The cyclotron frequency of species 1 and the plasma frequencies of species i are given as

$$\omega_{c1} = \frac{q_1}{m_1} B_0 \quad , \quad \omega_{pi} = \left(\frac{n_i q_i^2}{m_i \varepsilon_0} \right)^{1/2} \tag{2.40}$$

where n_i is a particle density of species i defined as a density in the two dimensional system of $L_x \times L_y$. i.e.,

-Particle density

$$n_i = \frac{N_i}{L_x L_y} \tag{2.41}$$

From (2.40) and (2.41) we can calculat the following physical quantities.

-Charge of a particle

$$q_i = \frac{\varepsilon_0 L_x L_y \omega_{pi}^2}{N_i (q/m)_i} \tag{2.42}$$

-Mass of a particle

$$m_i = \frac{\varepsilon_0 L_x L_y \omega_{pi}^2}{N_i (q/m)_i^2} \tag{2.43}$$

-Static magnetic field

$$B_0 = \frac{\omega_{cl}}{(q/m)_1} \tag{2.44}$$

It is noted that the mass m_i and charge q_i have little physical meaning in the relative unit system. What are physically meaningful are the mass density $m_i n_i$ and charge density $q_i n_i$ given as

$$q_i n_i = \frac{\varepsilon_0 \omega_{pi}^2}{(q/m)_i} \quad , \quad m_i n_i = \frac{\varepsilon_0 \omega_{pi}^2}{(q/m)_i^2} \tag{2.45}$$

The values of ω_{pi} and $(q/m)_i$ of different species must be given based on the ratios in the physical model.

2.3.6 Rescaling of Physical Quantities

In order to attain computational efficiency, it is necessary to reduce the number of operations involved in difference equations of fields and particles. Since the operations of multiplication and division by Δr, $\Delta t/2$ and $(q/m)_i$ are frequently used in the difference equations, we rescale the distance, time and charge-to-mass-ratio expressed in the relative unit by Δr, $\Delta t/2$ and $(q/m)_1$, respectively. Other physical quantities are rescaled

as follows.

distance	$r^* = (1/\Delta r)\, r$
time	$t^* = (2/\Delta t)\, t$
velocity	$v^* = (\Delta t/2)(1/\Delta r)\, v$
number density	$n^* = (\Delta r)^2\, n$
charge	$q^* = (q/m)_1 (\Delta t/2)^2 (1/\Delta r)^2\, q$
mass	$m^* = (q/m)_1^2 (\Delta t/2)^2 (1/\Delta r)^2\, m$
Electric field	$E^* = (q/m)_1 (\Delta t/2)^2 (1/\Delta r)\, E$
Magnetic field	$B^* = (q/m)_1 (\Delta t/2)\, B$
Current density	$J^* = (q/m)_1 (\Delta t/2)^3 (1/\Delta r)\, J$
Electric potential	$\phi^* = (q/m)_1 (\Delta t/2)^2 (1/\Delta r)^2\, \phi$
Charge density	$\rho^* = (q/m)_1 (\Delta t/2)^2\, \rho$
Energy density	$\sigma^* = (q/m)_1^2 (\Delta t/2)^4 (1/\Delta r)^2\, \sigma$

Note : quantities with * are rescaled ones.

The difference equations of particle motion of species 1 are written as in the following simple forms. The *'s on r, t, v, n, q, m, E, B, J, ϕ, ρ and σ are omitted hereafter.

$$v^- = v^{n-1/2} + E^n \tag{2.46}$$

$$v' = v^- + v^- \times B^n \tag{2.47}$$

$$v^+ = v^- + \frac{2}{1 + (B^n)^2}\, v' \times B^n \tag{2.48}$$

$$v^{n+1/2} = v^+ + E^n \tag{2.49}$$

$$r^{n+1/2} = r^n + v^{n+1/2} \tag{2.50}$$

$$r^{n+1} = r^{n+1/2} + v^{n+1/2} \tag{2.51}$$

For the i-th species of particles ($i \neq 1$), E and B must be multiplied by $(q/m)_i/(q/m)_1$.

The difference equations for fields are written as

$$B^n = B^{n-1/2} - \nabla^* \times E^n \tag{2.52}$$

$$B^{n+1/2} = B^{n} - \nabla^{*} \times E^{n} \tag{2.53}$$

$$E^{n+1} = E^{n} + 2c^{2} \nabla^{*} \times B^{n+1/2} + 2J^{n+1/2} \tag{2.54}$$

where the operation $\nabla^{*} \times A_{i,j}$ (A = E or B) are realized by the following simple operations.

$$(\nabla^{*} \times A_{i,j})_{x} = A_{z\ i,j+1} - A_{z\ i,j} \tag{2.55}$$

$$(\nabla^{*} \times A_{i,j})_{y} = A_{z\ i,j} - A_{z\ i+1,j} \tag{2.56}$$

$$(\nabla^{*} \times A_{i,j})_{z} = A_{y\ i+1,j} - A_{y\ i,j} - A_{x\ i,j+1} + A_{x\ i,j} \tag{2.57}$$

The rescaling is performed after all the input parameters are given to the simulation code, and all the output data are reconverted again to the values in the relative unit system. Since all input and output data are expressed in the relative unit system, users of the code do not have to be familiar with the rescaling inside the code.

2.4 Long Time Scale Code

A reduction of CPU time is attainable in particle simulations by limiting the allowed wave modes in the simulation to a monochromatic wave with the assumption of slow variations in amplitude and frequency. This code is called the Long-Time-Scale (LTS) code [Rathmann et al., 1978, Omura and Matsumoto, 1981]. Instead of solving the Maxwell equations and equations of motion of all particles as is usually done in the conventional electromagnetic codes, only the wave amplitude, frequency and wavenumber of a monochromatic wave is incremented forwards in time with a self-consistent updating of charge and current density calculated from numerical solutions to the equation of motion obtained solely for resonant particles in the monochromatic wave.

Basic equations for the monochromatic whistler mode wave and resonant electrons are described in Subsections 2.4.1 and 2.4.2, respectively [Omura and Matsumoto, 1981]. These equations are coded into difference equations in Subsections 2.4.3 and 2.4.4. The flow chart of the LTS whistler simulation is given in Subsection 2.4.5.

2.4.1 Equations of Wave Fields

We assume a purely transverse whistler mode wave which propagates along the geomagnetic field line and interacts with counter-streaming high energy resonant electrons existing in the magnetosphere. We use a right-handed coordinate system; z being a distance along the field line from the equatorial plane, and x and y axes being perpendicular to the external magnetic field. For convenience the wave fields are expressed in complex variables with dot marks on their top. The x and y components are represented by real and imaginary parts of the complex quantities, respectively.

$$\dot{B}_w = B_{wx} + iB_{wy} \quad , \qquad \dot{E}_w = E_{wx} + iE_{wy} \tag{2.58}$$

Neglecting the term for the displacement current in Maxwell's equation, and dividing a conduction current into a cold plasma current $\dot{J}_c$ and an energetic resonant electron current $\dot{J}_R$, we have Maxwell's equations in the form

$$i\frac{\partial E_w}{\partial z} = -\frac{\partial B_w}{\partial t} \quad , \qquad i\frac{\partial B_w}{\partial z} = \mu_o(\dot{J}_c + \dot{J}_R) \quad . \tag{2.59}$$

The linearized momentum equation of the cold electrons is

$$\frac{\partial \dot{J}_c}{\partial t} - i\Omega_e \dot{J}_c = \varepsilon_o \Pi_e^2 \dot{E}_w \tag{2.60}$$

where Ω_e is the electron cyclotron frequency. Eliminating $\dot{J}_c$ and $\dot{E}_w$ from (2.59) and (2.60), we have

$$\left[\frac{\partial}{\partial z}\left(\frac{\partial}{\partial t} - i\Omega_e\right)\frac{\partial}{\partial z} - \frac{\Pi_e^2}{c^2}\frac{\partial}{\partial t}\right]\dot{B}_w = -i\mu_o\left(\frac{\partial}{\partial t} - i\Omega_e\right)\frac{\partial}{\partial z}\dot{J}_R \tag{2.61}$$

where Π_e is the electron plasma frequency. We have assumed that the inhomogeneity of the medium is sufficiently small within a distance of the wave length, i.e.,

$$\left|\frac{\partial \Omega_e}{\partial z}\right| << |k(\omega - \Omega_e)| \quad , \qquad \left|\frac{\partial \Pi_e^2}{\partial z}\right| << |k\Pi_e^2| \quad . \tag{2.62}$$

The quantities $\dot{B}_w$ and $\dot{J}_R$ are expressed in terms of the amplitude B_w, J_R and phase ψ and $\psi + \psi_R$ as

$$\dot{B}_w = B_w \exp\{i\psi\} \quad , \quad \dot{J}_R = J_R \exp\{i(\psi + \Psi_R)\} \tag{2.63}$$

where Ψ_R is a relative phase angle between J_R and B_w, and is assumed to be a slowly varying function with respect to time and space.

The frequency ω and wavenumber k for the right-handed polarized wave are defined by

$$\omega = \frac{\partial \psi}{\partial t} \quad , \quad k = -\frac{\partial \psi}{\partial z} \quad . \tag{2.64}$$

We assume here that the terms involving the first-order time and space derivatives of k, J_R and Ψ_R as well as the second-order derivatives of B_w are negligible. Substitution of (2.63) into (2.61) yields

$$\left(k^2 + \frac{\Pi_e^2}{c^2} \right) \frac{\partial B_w}{\partial t} + 2k \left(\Omega_e - \omega \right) \frac{\partial B_w}{\partial z} - i \left\{ k^2 \left(\Omega_e - \omega \right) - \frac{\Pi_e^2}{c^2} \omega \right\} B_w$$

$$= \mu_o k \left(\Omega_e - \omega \right) \left(J_R \sin \Psi_R - i J_R \cos \Psi_R \right) \tag{2.65}$$

Separating imaginary and real parts in (2.65), we have

$$\left(k^2 + \frac{\Pi_e^2}{c^2}\right) \frac{\partial B_w}{\partial t} + 2k(\Omega_e - \omega) \frac{\partial B_w}{\partial z} = - \mu_o k (\Omega_e - \omega) J_E \tag{2.66}$$

$$\left\{k^2 (\Omega_e - \omega) - \frac{\Pi_e^2}{c^2} \omega\right\} B_w = \mu_o k (\Omega_e - \omega) J_B \tag{2.67}$$

where

$$J_E = J_R \sin(-\psi_R) \quad , \quad J_B = J_R \cos(-\psi_R) \quad , \tag{2.68}$$

and J_E and J_B are the components of the transverse resonant current J_R parallel to the wave electric field E_w, and to the wave magnetic field B_w, respectively (see Figure 2.11). These J_E and J_B are calculated by the following equations

$$J_E = -e \sum_i v_{\perp i} \sin(-\zeta_i) \qquad J_B = -e \sum_i v_{\perp i} \cos(-\zeta_i) \tag{2.69}$$

where $v_{\perp i}$ is a velocity component perpendicular to the external magnetic field and ζ_i is a phase angle between $v_{\perp i}$ and B_w, and Σ is taken over resonant electrons in a unit cell. Since the group velocity is expressed by

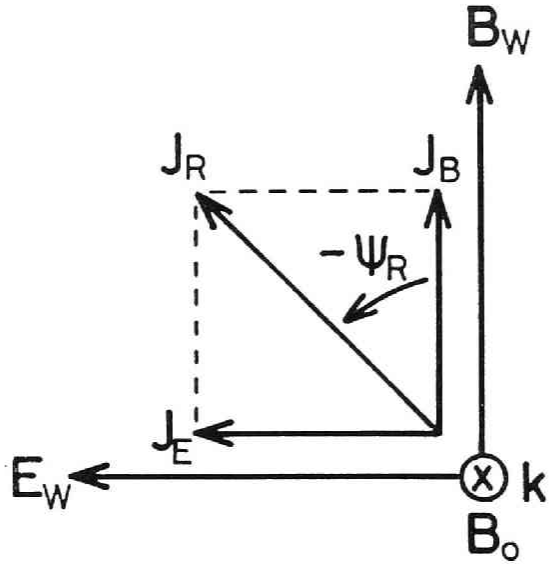

Fig. 2.11 Configuration of the wave magnetic (B_w) and electric (E_w) fields, wavenumber vector (k), external magnetic field (B_w), and resonant current (J_R) and its component J_B and J_E.

$$V_g = \frac{2k(\Omega_e - \omega)}{k^2 + (\Pi_e^2/c^2)} \tag{2.70}$$

we have from (2.66)

$$\frac{\partial B_w}{\partial t} = - V_g \left(\frac{\partial B_w}{\partial z} + \frac{1}{2} \mu_o J_E \right) \tag{2.71}$$

The second order differentiation of the wave phase ψ gives a relation of k and ω as

$$\frac{\partial k}{\partial t} = \frac{\partial \omega}{\partial z} \tag{2.72}$$

Using (2.71) and (2.72), we can follow the time evolution of B_w and k, while the frequency ω is calculable from (2.67) which is rewritten as

$$\omega = \frac{k(k - \mu_o J_B/B_w)}{k(k - \mu_o J_B/B_w) + \Pi_e^2/c^2} \Omega_e \tag{2.73}$$

As is seen in (2.71) and (2.73), J_E causes a change of the wave amplitude B_w, and J_B modifies the frequency ω.

2.4.2 Equations of Motion

We have derived the wave equations showing how the wave is modified by the presence of the resonant current J_R, which is formed as a result of cyclotron resonance between hot electrons and the wave. The equations of motion of resonant electrons are expressed in the following form. We introduce polar coordinates ($v_\parallel$, $v_\perp$, ϕ) for the velocity, where $v_\parallel$ and $v_\perp$ are the velocity components parallel and perpendicular to the external geomagnetic field respectively, and ϕ is the Larmor phase angle of $v_\perp$ in the rest frame. Equations of motion are then expressed as [e.g. Dysthe, 1971]

$$\frac{dv_\parallel}{dt} = \Omega_w v_\perp \sin(\phi - \psi) - \frac{v_\perp^2}{2\Omega_e}\frac{\partial \Omega_e}{\partial z} \tag{2.74}$$

$$\frac{dv_\perp}{dt} = \Omega_w\left(\frac{\omega}{k} - v_\parallel\right)\sin(\phi - \psi) + \frac{v_\parallel v_\perp}{2\Omega_e}\frac{\partial \Omega_e}{\partial z} \tag{2.75}$$

$$\frac{d\phi}{dt} = \frac{\Omega_w}{v_\perp}\left(\frac{\omega}{k} - v_\parallel\right)\cos(\phi - \psi) + \Omega_e \tag{2.76}$$

$$\frac{dz}{dt} = v_\parallel \tag{2.77}$$

where the wave amplitude B_w is replaced by $\Omega_w = eB_w/m$. The first terms in the right-hand sides of (2.74) ~ (2.76) correspond to the effect of the wave, while the second terms express the effect of the external geomagnetic field. The effect of the inhomogeneity of the medium is expressed by the second terms in (2.74) and (2.75), which disappear in a homogeneous case.

2.4.3 Particle Pushing Algorithm

The equations for the wave field (2.71) and (2.73) show that the resonant currents J_E and J_B control the evolution of the monochromatic whistler wave. The resonant currents are calculated by solving the equations (2.74) ~ (2.77) of motion for a large number of hot electrons. An algorithm used in the "long-time-scale (LTS)" code for a whistler simulation first proposed by Rathmann et al. [1978] is adopted for particle pushing in the present simulation. The increments of the quantities $v_\parallel$, $v_\perp$, ϕ and z over a time step δt are separated into increments due to the

wave and increments due to the cyclotron motion in the external magnetic field. The particle pushing algorithm takes the form of

$$f(t_{n+1}) = f(t_n) + \delta f_w + \delta f_c \quad , \tag{2.78}$$

where $t_{n+1} = t_n + \delta t$, and f is a quantity such as $v_\parallel$, $v_\perp$, ϕ and z. δf_w and δf_c are increments due to the wave and due to the cyclotron motion, respectively, and they are obtained by integrating (2.74) ~ (2.77) over the time interval from t_n to t_{n+1} under the conditions that $|\delta v_\parallel| << |v_\parallel|$, $|\delta v_\perp| << v_\perp$, $|\delta k| << k$, $|\delta \Omega_e| << |\Omega_e|$, $|\delta\omega| << \omega$, and $|\delta \Omega_w| << \Omega_w$. The increments due to the wave are expressed in terms of the quantities at $t = t_n$ as

$$\delta v_{\parallel w} = \frac{\Omega_w v_\perp}{\zeta'} \delta\cos\zeta \tag{2.79}$$

$$\delta v_{\perp w} = -\frac{\Omega_w}{\zeta'} \left(\frac{\omega}{k} - v_\parallel \right) \delta\cos\zeta \tag{2.80}$$

$$\delta \phi_w = \frac{\Omega_w}{v_\perp \zeta'} \left(\frac{\omega}{k} - v_\parallel \right) \delta\sin\zeta \tag{2.81}$$

$$\delta z_w = \frac{\Omega_w v_\perp}{\zeta'^2} \left(\zeta' \delta t \cos\zeta - \delta\sin\zeta \right) \tag{2.82}$$

where

$$\delta\cos\zeta = \cos(\zeta + \zeta'\delta t) - \cos\zeta \ , \quad \delta\sin\zeta = \sin(\zeta + \zeta'\delta t) - \sin\zeta \tag{2.83}$$

and ζ is a relative phase angle between $v_\perp$ and B_w, i.e., $\phi - \psi$. ζ' denotes a time derivative of ζ obtained from (2.76), i.e.,

$$\zeta' \quad \frac{\Omega_w}{v_\perp} \left(\frac{\omega}{k} - v_\parallel \right) \cos\zeta + \Omega_e - \omega + k v_\parallel \tag{2.84}$$

When $\zeta' \cong 0$, (2.79) ~ (2.82) are not appropriate because the right hand sides of these equations show overflows in the calculation process. In this case the first terms of (2.81), (2.82) and (2.83) are directly integrated assuming ζ is almost constant, and we have

$$\delta v_{\parallel w} = \delta t \ \Omega_w \sin\zeta \tag{2.85}$$

$$\delta v_{\perp W} = \delta t\, \Omega_W \left(\frac{\omega}{k} - v_{\parallel} \right) \sin\zeta \tag{2.86}$$

$$\delta \phi_W = \frac{\delta t\, \Omega_W}{v_{\perp}} \left(\frac{\omega}{k} - v_{\parallel} \right) \cos\zeta \tag{2.87}$$

$$\delta z_W = -\frac{1}{2}\, \delta v_{\parallel W} \delta t \tag{2.88}$$

The increments due to the cyclotron motion are expressed as

$$\delta v_{\parallel C} = -\frac{v_{\perp}^2}{2v_{\parallel}} \frac{\Omega_e(z + v_{\parallel}\delta t) - \Omega_e(z)}{\Omega_e(z)} \tag{2.89}$$

$$\delta v_{\perp C} = \frac{v_{\perp}}{2} \frac{\Omega_e(z + v_{\parallel}\delta t) - \Omega_e(z)}{\Omega_e(z)} \tag{2.90}$$

$$\delta \phi_C = \frac{\delta t}{2} \{ \Omega_e(z) + \Omega_e(z + v_{\parallel}\delta t) \} \tag{2.91}$$

$$\delta z_C = \delta t \left\{ v_{\parallel} + \frac{\delta v_{\parallel C}}{2} \right\} \tag{2.92}$$

In the simulation, Ω_W, ω, k and ϕ are calculated at the spatial grid points, and to obtain these quantities at particle position z, we interpolated from values on the neighboring grid points Z_m and Z_{m+1} in the manner as

$$F(z) = F(Z_m) + \frac{F(Z_{m+1}) - F(Z_m)}{\Delta Z} (z - Z_m) \tag{2.93}$$

where F corresponds to quantities such as, Ω_W, ω or k, and ΔZ is the grid spacing defined by $\Delta Z = Z_{m+1} - Z_m$. Integration of $k(z)$ expressed by (2.93) gives the phase of the wave,

$$\Psi(z) = \Psi(Z_m) - k(Z_m)(z - Z_m) - \frac{k(Z_{m+1}) - k(Z_m)}{2\Delta Z} (z - Z_m)^2 \tag{2.94}$$

In the simulations presented in Section 3.3, we take into account the inhomogeneity of the geomagnetic field which is approximated by a dipole magnetic field given by the following equations.

$$B_O = B_{OS}(\frac{R_E}{R})^3 \sqrt{1 + 3\sin^2\Phi} \tag{2.95}$$

$$R = R_E L \cos^2\Phi \tag{2.96}$$

$$\frac{z}{R} = \frac{1}{2\sqrt{3}} (x + \sinh x \cosh x) \tag{2.97}$$

$$x = \sqrt{3} \sin\Phi \tag{2.98}$$

where Φ and R are a geomagnetic latitude and a distance to the point of interest from earth's center. The quantities B_O and B_{OS} are magnetic fields at (R, Φ) and at the earth's surface, respectively. R_E and L are the radius of the earth (6370km) and geocentric distance at the equatorial plane normalized to R_E. The quantity z is a distance measured along the geomagnetic field line from the equatorial plane to the point of interest. Let B_{OEQ} denote the magnetic field at $R = LR_E$ in the equatorial plane, then we have from (2.95)

$$B_{OEQ} = L^{-3} B_{OS} \tag{2.99}$$

Substituting (2.96), (2.97) and (2.98) into (2.95), we express B_O in terms of B_{OEQ} and z as,

$$B_O = B_{OEQ} \frac{\sqrt{1 + x^2}}{(1 - x^2/3)^3} \tag{2.100}$$

where x is given as a solution to the following equation.

$$F(x, z) = x + \sinh x \cosh x - \frac{2\sqrt{3}\, z}{LR_E} = 0 \tag{2.101}$$

From (2.100) and (2.101) we can calculate the external magnetic field at each grid point.

2.4.4 Field Updating Algorithm

In the previous section the algorithm for updating physical quantities associated with each particle was discussed. This section presents the method to update the quantities which are assigned to the spatial grid points. These quantities are the wave amplitude B_w and its time derivative

$\partial B_w/\partial t$, the wavenumber k and its time derivative $\partial k/\partial t$, the wave frequency ω and the wave phase ψ in the rest frame, and the resonant current J_E and J_B.

The wave amplitude and the wavenumber are advanced over the time step δt using their time derivatives at $t = t_n$, i.e.,

$$B_{wm}(t_{n+1}) = B_{wm}(t_n) + \left(\frac{\partial B_w}{\partial t}\right)_m(t_n)\ \delta t \tag{2.102}$$

$$k_m(t_{n+1}) = k(t_n) + \left(\frac{\partial k}{\partial t}\right)_m(t_n)\ \delta t \tag{2.103}$$

where the subscript m denotes a value at a grid point Z_m. The wave phase is first advanced at the boundary grid Z_1 and extended successively to the next grid by integrating k over the grid spacing as

$$\Psi_1(t_{n+1}) = \Psi_1(t_n) + \omega(t_n)\ \delta t \tag{2.104}$$

$$\Psi_{m+1}(t_{n+1}) = \Psi_m(t_{n+1}) - \frac{1}{2}\left(k_m(t_{n+1}) + k_{m+1}(t_{n+1})\right)\Delta Z \tag{2.105}$$

After the quantities z_i, $v_{\perp i}$, $v_{\parallel i}$ and ϕ_i of each resonant particle and the wave phase ψ are updated, the resonant current J_E and J_B can be calculated. An electron in the particle simulation is not a "real electron", but it is a superparticle which represents a number of electrons in the real plasma. Therefore, we assign a density n_s to each superparticle (we may regard it a super-electron with a charge $-n_s e$), and each super-particle forms resonant currents j_{Ei} and j_{Bi}

$$j_{Ei} = -n_s e \sin(-\zeta_i)\ ,\quad j_{Bi} = -n_s e \cos(-\zeta_i) \tag{2.106}$$

where i denotes a quantity of each particle; and $\zeta_i = \phi_i - \psi(z_i)$ and $\psi(z_i)$ is calculated by (2.94). These j_{Ei} and j_{Bi} are assigned to the neighboring grid points Z_m and Z_{m+1} $(Z_m < z_i < Z_{m+1})$ with the first order particle weighting, or particle-in-cell (PIC) model [e.g. Birdsall and Langdon, 1984]. Resonant currents assigned to grid Z_m and Z_{m+1} are thus obtained by

$$J_{Em,i} = j_{Ei}\frac{Z_{m+1} - z_i}{\Delta Z}\ ,\quad J_{E(m+1),i} = j_{Ei}\frac{z_i - Z_m}{\Delta Z} \tag{2.107}$$

and $J_{Bm,i}$ and $J_{B(m+1),i}$ are given in the same manner as above. Summing the currents J_{Emi} and J_{Bmi} over all particles between Z_{m-1} and Z_{m+1} gives the resonant currents J_{Em} and J_{Bm} at a grid point Z_m.

When the resonant currents are obtained, the wave frequency ω and the time derivatives $\partial B_w/\partial t$ and $\partial k/\partial t$ are calculated through (2.71), (2.72) and (2.73) as follows.

$$\omega_m = \frac{k_m (k_m - \mu_o J_{Bm}/B_{wm})}{k_m (k_m - \mu_o J_{Bm}/B_{wm}) + \Pi_{em}^2/c^2} \tag{2.108}$$

$$\left(\frac{\partial B_w}{\partial t} \right)_m = - \frac{2k_m (\Omega_{em} - \omega_m)}{k^2 + \Pi_{em}^2/c^2} \left(\frac{B_{wm} - B_{w(m-1)}}{\Delta Z} + \frac{1}{2} \mu_o J_{Em} \right) \tag{2.109}$$

$$\left(\frac{\partial k}{\partial t} \right)_m = - \frac{\omega_{m+1} - \omega_{m-1}}{2\Delta Z} \tag{2.110}$$

As (2.109) and (2.110) contain the terms of spatial finite differentiation, the boundary conditions must be chosen carefully. In the present simulation we assume the wave propagating from the left boundary Z_1 to the right boundary Z_M. The wave field at Z_M is reasonably extrapolated from the field at Z_{M-1} and Z_{M-2} as

$$B_{wM} = 2B_{w(M-1)} - B_{w(M-2)} \tag{2.111}$$

and ω_M and k_M are also extrapolated in the same manner. At the left boundary Z_1, however, extrapolation from Z_2 and Z_3 is not applicable, because the wave propagates from Z_1 to Z_2 and Z_3. In the simulation where the wave is externally injected from the boundary, the wave field at Z_1 is given arbitrarily. In the simulation where a self-evolution of a uniform and periodic wave-particle interaction is followed, the field at Z_1 is set equal to the field at Z_2.

J_{Bm}/B_{wm} in (2.108) causes a non-physical fluctuation of ω, when the wave amplitude B_w becomes very small, because the resonant current J_{Bm} calculated from a limited number of particles necessarily contains some numerical fluctuations. This difficulty is relieved by assuming a thermal magnetic noise level B_{th} in the magnetospheric plasma, and setting the term J_{Bm}/B_{wm} equal to J_{Bm}/B_{th} when $B_{wm} < B_{th}$. In the simulation presented in Section 6.3 we follow evolution of a wave whose amplitude is $B_w = 10^{-5} \sim 10^{-6} B_o$, and B_{th} is chosen as $10^{-6} B_o$.

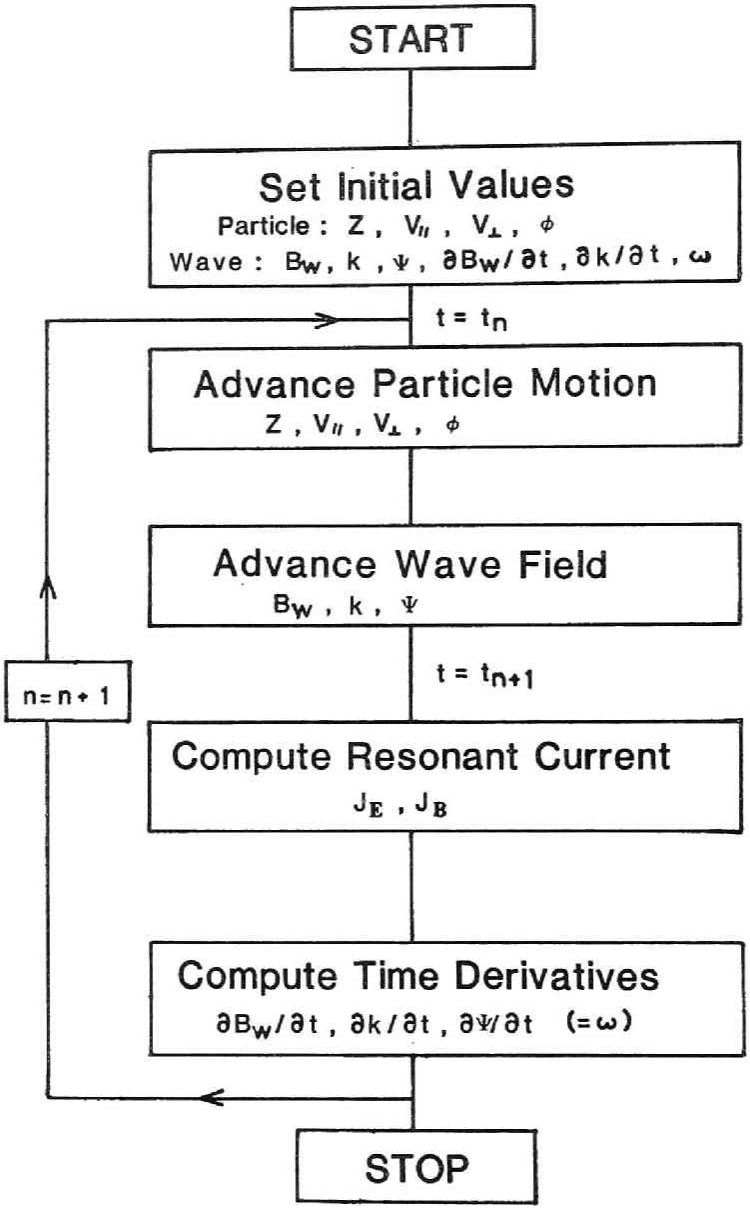

Fig. 2.12 Flow chart of LTS whistler simulation.

2.4.5 Flow Chart of Long Time Scale Whistler Simulation

Recurrent use of the particle pushing and field updating algorithms enables us to follow a self-consistent evolution of the whistler wave-particle interaction. Motion of cold plasma particles which support the wave propagation is not solved, because its effect is implicitly included

in the wave equation (2.71) and (2.73). Computing time is greatly saved by not solving equations of motion for cold electrons. It is noted that there is no necessity to choose the time step as $\delta t \cdot \mathrm{Max}(\Omega_e, \Pi_e) \ll 1$ which is usually a necessary condition in the usual particle simulation of plasmas. One requirement of the time step is $\delta t \cdot \omega_t \ll 1$, where ω_t is the trapping frequency given by $\omega_t = (kv_\perp \Omega_w)^{1/2}$. The relative phase angles ζ's of the resonant particles trapped in the wave potential change with a time scale of ω_t^{-1} and thus the resonant currents controlling the wave evolution vary with ω_t^{-1}. Another requirement is that $V_{max}\delta t \leqslant \Delta Z$, where V_{max} is the maximum velocity both in the wave group velocity and in the velocities of particles in the system. This is the loosest condition that must be satisfied in the difference scheme used in the algorithm.

The present simulation method is basically the long-time-scale (LTS) algorithm first formulated by Rathmann et al. [1978]. In their algorithm, however, they follow the time evolution of the wave frequency ω using the equation

$$\frac{\partial \omega}{\partial t} + V_g \frac{\partial \omega}{\partial z} = - \frac{\mu_0}{2k} V_g \frac{\partial}{\partial t} \left(\frac{kJ_B}{B_w} \right) \tag{2.112}$$

which is obtained by differentiating (2.67) with time t under the assumption that the cold plasma dispersion relation without the contribution of hot resonant electrons is valid. We found this equation vulnerable to a numerical instability because of the time differentiation of kJ_B/B_w which picks up numerical fluctuations of J_B, where J_B is calculated from a limited number of particles and correspondingly involves statistical errors. Actually, (2.112) is not necessary in the algorithm if the phase relation (2.72) is made use of to follow the time evolution of the wavenumber k. In our method the frequency ω is determined by (2.73) as a function of k and J_B/B_w after advancing k in time by (2.72). In the method of Rathmann et al., however, the wavenumber k is determined by (2.67) or (2.73) as a function of ω and J_B/B_w after advancing in time by (2.112). The flow chart of the LTS simulation is shown in Figure 2.12.

2.5 Hybrid Electromagnetic Code

2.5.1 Hybrid Model and Basic Equations

We have developed a one dimensional electromagnetic hybrid simulation code [Sgro and Nielson, 1976; Byers et al., 1978] where electrons are treated as a massless fluid and ions are treated as particles moving in the four dimensional phase space (x, v_x, v_y, v_z). Since we are studying low frequency phenomena, we neglect the transverse displacement current in Maxwell's equations (the Darwin approximation) as

$$\frac{\partial \vec{B}}{\partial t} = - \text{ rot } \vec{E} \tag{2.113}$$

$$\mu_o \vec{J} = \text{rot } \vec{B} \quad . \tag{2.114}$$

We also the neglect electron inertia effects for low frequency waves, and we have from the electron momentum equation

$$-en_e(\vec{E} + \vec{u}_e \times \vec{B}) - \text{grad } p_e = 0 \tag{2.115}$$

where $-e$, n_e, $\vec{u}_e$ and p_e are electron charge, number density, flow velocity and pressure, respectively. Furthermore, we assume the quasi-neutrality condition

$$-en_e + q_s n_s = 0 \tag{2.116}$$

where q_s and n_s are the charge and number density of an "s" ion species, respectively. The electron pressure is integrated in time by using the electron energy equation

$$(\frac{\partial}{\partial t} + \vec{u}_e \cdot \text{grad}) \, p_e = - \frac{5}{3} p_e \, \text{div } \vec{u}_e \quad . \tag{2.117}$$

The electron flow u_e is obtained from the current equation as

$$\vec{u}_e = (\Sigma q_s n_s \vec{u}_s - \vec{J})/n_e q_e \tag{2.118}$$

where u_s is the drift velocity of a "s"-th ion species. The ion density n_s and drift velocity $\vec{u}_s$ are calculated from the motion of ion particles whose positions and velocities are determined by integrating the equations of motion

$$\frac{d\vec{v}}{dt} = \frac{q_s}{m_s} (\vec{E} + \vec{v} \times \vec{B}), \qquad \frac{d\vec{x}}{dt} = \vec{v} \quad . \tag{2.119}$$

The magnetic field $\vec{B}$ and the electron pressure p_e are integrated in time using (2.113) and (2.117), while the electric field is determined by a

predictor-corrector method using (2.114), (2.115), (2.116) and (2.118).

For simplicity, spatial variations are restricted to one dimension, i.e., the x direction, and periodic boundary conditions are assumed.

Basic equations presented above are written in the forms which are identical to those in MKS unit system. However, it is noted that ε_0 and μ_0 can be chosen arbitrarily except that $\varepsilon_0\mu_0 \quad 1/c^2$.

2.5.2 Unit System for One-dimensional Hybrid Code

We choose four independent basic parameters in order to define the units of physical quantities in the simulation system. The basic parameters are the followings.

1. Angular frequency : (plasma, cyclotron or wave frequency)
2. System length : L
3. Charge-to-mass ratio : $(q/m)_s$
4. Number of particles in the system : N_s

For simplicity, we define $\mu_0 = 1$ and $\varepsilon_0 = 1/c^2$ in the basic equations. Making use of the following relations obtained from the basic equations,

$$\omega_{ps} = \left(\frac{n_s q_s^2}{m_s \varepsilon_0} \right)^{1/2} , \qquad \omega_{cs} = \frac{q_s}{m_s} B_0 , \tag{2.120}$$

we obtain other physical quantities as follows.

- Particle density

$$n_s = \frac{N_s}{L} \tag{2.121}$$

- Charge of a particle

$$q_s = \frac{\varepsilon_0 L \, \omega_{ps}^2}{N_s (q/m)_s} \tag{2.122}$$

- Mass of a particle

$$m_s = \frac{\varepsilon_0 L \, \omega_{ps}^2}{N_s (q/m)_s^2} \tag{2.123}$$

- Static magnetic field

$$B_o = \frac{\omega_{c1}}{(q/m)_1} \tag{2.124}$$

- Wave number of mode i

$$k_i = 2\pi i/L \tag{2.125}$$

2.5.3 Rescaling of Physical Quantities

In order to attain a high computational efficiency, we rescale physical quantities solved in a simulation by the following three quantities [Matsumoto and Omura, 1984]

grid spacing	: Δx
half time step	: $\Delta t/2$
charge-to-mass ratio of the ion species 1	: $(q/m)_1$

Other physical quantities are rescaled as follows.

distance	$x^* = (1/\Delta x)\, x$
time	$t^* = (2/\Delta t)\, t$
velocity	$v^* = (\Delta t/2)\,(1/\Delta x)\, v$
number density	$n^* = \Delta x\, n$
charge	$q^* = (q/m)_1\,(\Delta t/2)\, q$
mass	$m^* = (q/m)_1^2 \Delta\, x\, m$
electric field	$E^* = (q/m)_1\,(\Delta t/2)^2\,(1/\Delta x)\, E$
magnetic field	$B^* = (q/m)_1\,(\Delta t/2)\, B$
current density	$J^* = (q/m)_1\,(\Delta t/2)\,\Delta x\, J$
pressure	$p^* = (q/m)_1^2\,(\Delta t/2)^2\, p$

2.5.4 Grid Assignment and Difference Equations

We define a full grid point (j) and a half grid point (j+1/2) in order to solve the basic equations as difference equations. Assignment of physical quantities to these grid points are the following.

- Full grid point (j)

electric field	: E
ion flow velocity	: u_i
charge density	: ρ

electron flow velocity : u_e
current density : J

- Half grid point (j+1/2)
magnetic field : B

The magnetic field B at a half grid points is relocated to full grid points in order to calculate particle pushing fields by the Particle-in-Cell method.

$$B'_j = \frac{1}{2}\left(B_{j-1/2} + B_{j+1/2} \right) \tag{2.126}$$

The quantities with ' correspond to those relocated by (2.126) hereafter. In the calculation of E, B is relocated again in the same manner, as will be shown in the following.

Based on the grid assignment, we write the basic equations in a difference form. First, the magnetic field are advanced by $\Delta t/2$

$$B^{i+1/2}_{y,j+1/2} = B^{i}_{y,j+1/2} + \frac{\Delta t}{2\Delta x}\left(E^{i+1/2}_{z,j+1} - E^{i+1/2}_{z,j} \right) \tag{2.127}$$

$$B^{i+1/2}_{z,j+1/2} = B^{i}_{z,j+1/2} + \frac{\Delta t}{2\Delta x}\left(E^{i+1/2}_{y,j+1} - E^{i+1/2}_{y,j} \right) \tag{2.128}$$

Then, relocating the magnetic field to full grid points by (2.126), velocities of particles are advanced from t = i to i+1 by the Buneman-Boris method [Matsumoto and Omura, 1984] using electric and magnetic fields linearly interpolated from the full grid points. The magnetic field is advanced again by $\Delta t/2$

$$B^{i+1}_{y,j+1/2} = B^{i+1/2}_{y,j+1/2} + \frac{\Delta t}{2\Delta x}\left(E^{i+1/2}_{z,j+1} - E^{i+1/2}_{z,j} \right) \tag{2.129}$$

$$B^{i+1}_{z,j+1/2} = B^{i+1/2}_{z,j+1/2} + \frac{\Delta t}{2\Delta x}\left(E^{i+1/2}_{y,j+1} - E^{i+1/2}_{y,j} \right) \tag{2.130}$$

We obtain the electric field E from the magnetic field B and the electron flow velocity u_e using the electron momentum equation (2.115).

$$E_{x,j} = u_{ez,j}B'_{y,j} - u_{ey,j}B'_{z,j} - (1/2)(1/\rho)(1/\Delta x)\left(p_{e,j+1} - p_{e,j-1} \right) \tag{2.131}$$

$$E_{y,j} = u_{ex,j}B'_{z,j} - u_{ez,j}B_{xo} \tag{2.132}$$

$$E_{z,j} = u_{ey,j}B_{xo} - u_{ex,j}B_{y,j} \tag{2.133}$$

where B_{xo} is the static magnetic field along the x-axis.

The electron pressure is obtained by integrating (2.117) in time using the Lax-Wendroff scheme which is accurate to the second order.

$$\begin{aligned} p_{e,j}^{i+1} = p_{e,j}^{i} &- \frac{\Delta t}{2\Delta x} u_{ex,j}^{i}(p_{e,j+1}^{i} - p_{e,j-1}^{i}) \\ &+ 2 (\frac{\Delta t}{2\Delta x})^2 u_{ex,j}^{i\,2} (p_{e,j+1}^{i} - 2p_{e,j}^{i} + p_{e,j-1}^{i}) \\ &- \gamma p_{e,j}^{i} \frac{\Delta t}{2\Delta x} (u_{ex,j+1} - u_{e,j-1}) \end{aligned} \tag{2.134}$$

It is noted that $\Delta t/2$ and Δx are set to equal 1 after the rescaling described in the previous section, and that the number of operations in these difference equations are reduced.

CHAPTER 3
WHISTLER MODE WAVE-PARTICLE INTERACTIONS AND VLF EMISSIONS

3.1 Introduction

A lightning discharge radiates electromagnetic waves over a wide range of frequency extending beyond that of visible light. Such radiation in the frequency range, 0.3 ~ 30 kHz, is the source of "whistlers" that propagate through the ionosphere and magnetosphere in the whistler mode [Helliwell, 1965; Park, 1980]. This propagation mode is possible only in a magnetized plasma and at frequency below both the plasma frequency and the electron cyclotron frequency. In addition to whistlers, there are other types of whistler mode wave called VLF emissions which exhibit more diversified tones in the VLF range. Examples of VLF emissions are shown in Figure 3.1.

Of particular interest are artificially triggered VLF emissions because of their potential use in the study of coherent nonlinear whistler mode wave-particle interactions in the magnetosphere, because these VLF emissions are believed to originate from the region close to the equatorial plane of the magnetosphere owing to a cyclotron resonance with counter-streaming high energy electrons. The nonlinear whistler mode wave-particle interaction is one of the most fundamental and interesting phenomena in the magnetosphere, and plays an important role in the magnetospheric dynamics.

Many numerical simulation studies as well as theoretical ones are reported so far (See a review by Matsumoto [1979]). None of the theories nor simulations however, has ever given an adequate and complihensive explanation of VLF emissions. In the following sections, we will present several theoretical and computational studies we have done in an attempt of clarifying the mechanism of coherent VLF triggered emissions. In Section 3.2, we study nonlinear orbits of resonant electrons in a monochromatic whistler mode wave by test particle simulations [Matsumoto and Omura, 1981]. In Section 3.3, we investigate basic processes of self-consistent whistler mode wave-particle interactions using the LTS code [Omura and Matsumoto, 1982]. We then study frequency variations of whistler emissions triggered in a uniform magnetic field [Omura and Matsumoto, 1984] in Section 3.4. In Section 3.5, effects of a whistler mode wave on a particle

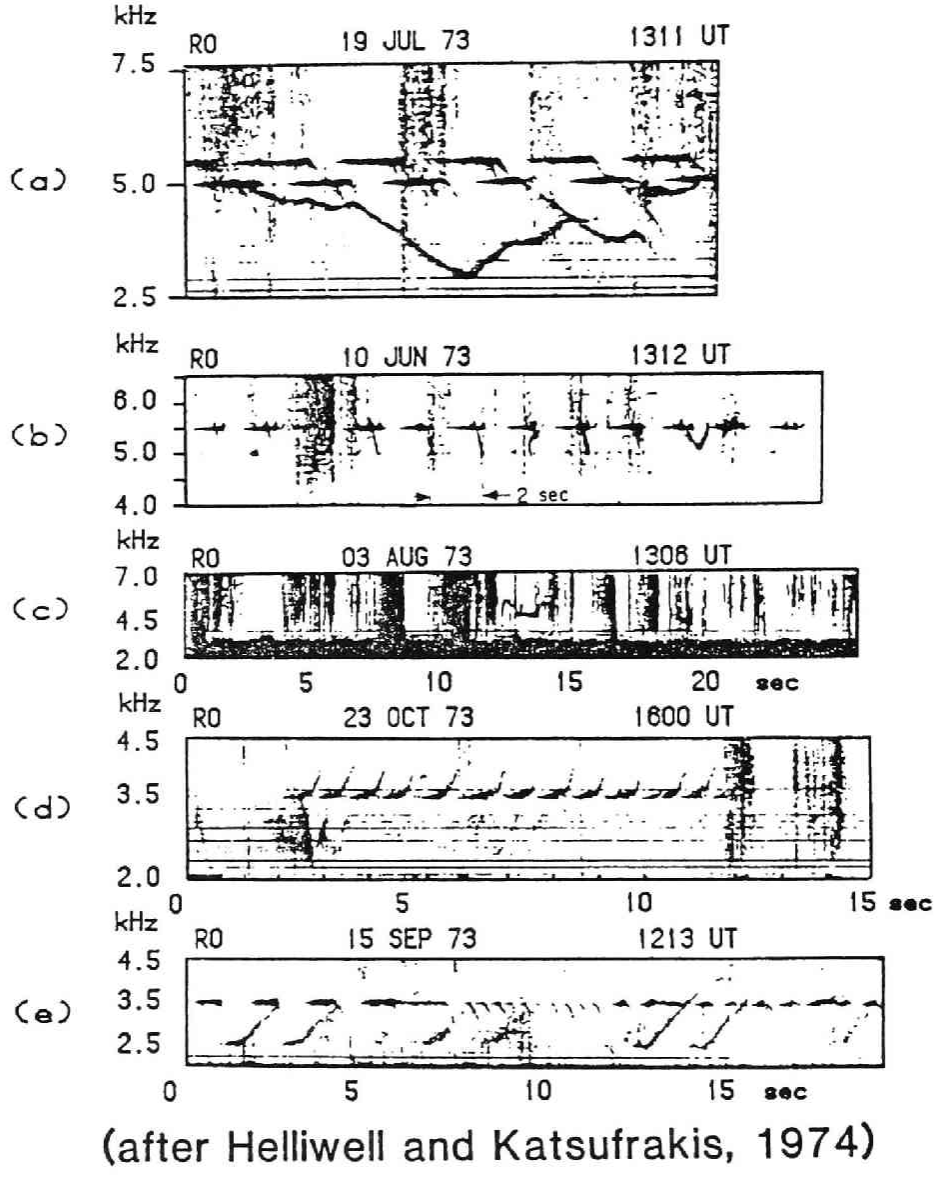

Fig. 3.1 Examples of VLF triggered emissions in the magnetosphere.

velocity distribution in a dipole geomagnetic field are studied, and a new explanation of VLF triggered emissions is given [Matsumoto and Omura, 1983]. Finally, in Section 3.6, we examine effects of co-existing electrostatic waves on whistler mode instabilities based on simulations by the FEM code [Omura and Matsumoto, 1985].

3.2 Nonlinear Orbits of Resonant Electrons

Inhomogeneity of the geomagnetic field is believed to play an important role in the nonlinear whistler interaction, because computer simulations [Matsumoto and Yasuda, 1976; Matsumoto et al., 1980; Kumagai et al., 1980] assuming a uniform external magnetic field could not give sufficient interpretations of the triggered emissions. Recently, a self-consistent computer simulation has been done under a nonuniform external magnetic field with a constant gradient [Vomvoridis and Denavit, 1980]. However, the real geomagnetic field around the equator does not have a constant gradient and should be approximated at least by a parabolic magnetic field. In this Section, behavior of resonant electrons in a finite amplitude monochromatic whistler mode wave is investigated, assuming a parabolic external magnetic field. In addition to the phase bunching pointed by Vomvoridis and Denavit [1979] we find another new type of phase bunching of resonant electrons associated with the inhomogeneity of the magnetic field. Its mechanism is interpreted by a new effect which we term the 'cluster effect'. The cluster effect makes it possible to explain a long-lasting resonant current which is quite different in nature from the resonant current produced by trapped electrons in a uniform magnetic field. A test particle simulation of whistler-particle interactions was carried out by Inan et al. [1978] and showed interesting results on pitch angle scattering. However, they did not pay attention to the phase-bunching process as discussed in the present paper.

In Subsection 3.2.1 a model of the present simulation is described. In Subsection 3.2.2 trajectories of electrons under the effects of whistler monochromatic waves propagating along the geomagnetic field line are calculated by a test particle simulation. Processes of trapping and detrapping of electrons by the waves are then discussed. In Subsection 3.2.3 two types of phase bunching in a nonuniform magnetic field observed in the simulation are explained, and their mechanisms are considered. In Subsection 3.2.4 we shall discuss formation of resonant currents due to the

phase bunching as well as their effects on the wave fields. Section 6 gives a summary and discussion.

3.2.1 Simulation Model

We consider a finite amplitude monochromatic whistler mode wave propagating along the nonuniform geomagnetic field B_o. The wave is described by wave magnetic field B_{wn} and its phase ψ_n defined at a position z in the rest frame, where the suffix n denotes the n-th wave in case several waves coexist in the plasma. In the cold background plasma the wave propagates with constant amplitude B_{wn}, frequency ω_n, and wavenumber k_n, which are determined by a cold plasma dispersion relation given by

$$k_n = \frac{1}{c}\left(\omega_n^2 + \frac{\omega_n \Pi_e^2}{\Omega_e - \omega_n} \right)^{1/2} \tag{3.1}$$

where Π_e is the plasma frequency. We introduce polar coordinates ($v_\parallel$, $v_\perp$, ϕ), where $v_\parallel$ and $v_\perp$ are the velocities parallel and perpendicular to the external geomagnetic field, respectively, and ψ is the Larmor phase of $v_\perp$ in the rest frame. Equations of motion are then expressed as [e.g., Dysthe, 1971]

$$\frac{dv_\parallel}{dt} = \sum_n \Omega_{wn} v_\perp \sin(\phi - \Psi_n) - \frac{v_\perp^2}{2\Omega_e} \frac{\partial \Omega_e}{\partial z} \tag{3.2}$$

$$\frac{dv_\perp}{dt} = \sum_n \Omega_{wn} \left(\frac{\omega_n}{k_n} - v_\parallel \right) \sin(\phi - \Psi_n) + \frac{v_\parallel v_\perp}{2\Omega_e} \frac{\partial \Omega_e}{\partial z} \tag{3.3}$$

$$\frac{d\phi}{dt} = \sum_n \left(\frac{\Omega_{wn}}{v_\perp} - v_\parallel \right) \cos(\phi - \Psi_n) + \Omega_e \tag{3.4}$$

where B_o and B_{wn} are replaced by $\Omega_e(z) = eB_o/m$ and $\Omega_w = eB_{wn}/m$, respectively. The phase Ψ changes according to a relation

$$\frac{d\Psi_n}{dt} = \omega_n - k_n v_\parallel \tag{3.5}$$

The first term on the right-hand side of (3.2)-(3.4) corresponds to the

effect of th wave, while the second term expresses the effect of the external geomagnetic field. The effect of the inhomogeneity of the geomagnetic field is expressed by the second terms of (3.2) and (3.3), which disappear in the homogeneous case, and by k_n and Ω_e in (3.2)-(3.4).

The geomagnetic field approximated by a dipole magnetic field is further approximated by the following parabolic equation around the equator as

$$B_0 = B_{0E} [1 + (4.5z_a^2 / L^2R_e^2)] \tag{3.6}$$

where B_{0E}, L, R_e, and z_a are the magnetic field at the equator, the L value of the magnetic field line, the earth's radius, and the distance from the equator along the field line, respectively. The corresponding angular electron cyclotron frequency Ω_e at position z is given by

$$\Omega_e(z) = \Omega_{eo}(1 + \beta z_a^2) = \Omega_{eo}(1 + \alpha z^2) \tag{3.7}$$

where Ω_{eo} is the angular cyclotron frequency at the equatorial plane, coefficient β is given by $4.5/(L^2R_e^2)$, and α and z are normalized dimensionless parameters defined by $\alpha = (c\Omega_{eo}^{-1})^2\beta = 4.5c^2/(\Omega_{eo}LR_e)^2$ and $z = z_a/(c\Omega_{eo}^{-1})$, respectively. The electron density N_e is assumed to be constant along the geomagnetic field line

Physical parameters in the present simulation have been chosen to be comparable to those in magnetospheric experiments. The waves are assumed to propagate along a geomagnetic field line of L = 4. Ratios of the wave frequency (in the case of a single wave) and plasma frequency to the cyclotron frequency at the equatorial plane are ω/Ω_{eo} - 0.5 and Π_e/Ω_{eo} = 10, respectively. Ratios of electron velocities to the light velocity c are chosen as follows: $v_\parallel/c$ = -0.05 and $v_\perp/c$ = 0.05. However, certain modifications are necessary to the amplitude of the wave magnetic field. The ratio Ω_w/Ω_{eo} is of the order of 10^{-5} in the magnetosphere for a typical whistler wave intensity of 5mγ where $\Omega_{eo}/2\pi$ = 14kHz is assumed. However, the value of $\Omega_w/\Omega_{eo} = 10^{-5}$ or an even smaller value causes the accumulated numerical errors in numerical solutions to equations of motion because of a shortage of effective digits in the computer. Therefore we have to scale up Ω_w/Ω_{eo} to 10^{-4}. However, we need to change the coefficient α for the inhomogeneity of B_0 correspondingly in order o keep the essential nonlinear feature of wave-particle interactions unchanged. For this purpose we imposed a requirement that the number of trapped oscillations should be the

same within a trapping zone in which trapping by the wave is possible in resistance against the inhomogeneity of B_o. This requirement gives the relation (see Appendix C)

$$\alpha \propto \Omega_w^{3/2} \tag{3.8}$$

Therefore the coefficient α, which is equal to 8.06×10^{-8} for the magnetospheric parameters L = 4 and $\Omega_{eo} = 2\pi \times 14 \times 10^3$, is scale up to $\alpha = (10^{-4}/10^{-5})^{3/2} \times 8.06 \times 10^{-8}$ 2.55×10^{-6} for the value of $\Omega_w/\Omega_{eo} = 10^{-4}$. We have thus used the values $\Omega_w/\Omega_{eo} = 10^{-4}$ and $\alpha = 2.55 \times 10^{-6}$ in the present simulations.

Under the parabolic magnetic field with $\alpha = 8.06 \times 10^{-8}$ the length of the trapping zone is approximately 710 in units of $c\Omega_{eo}^{-1}$, as is shown in the appendix. Therefore a transit time, which is the time necessary for an electron with $v_{\parallel} \sim$ | 0.05[c] | to move across the trapping zone, is $710/0.05 = 1.4 \times 10^4$ $[\Omega_e o^{-1}]$, while the trapping period $T_t = 2\pi/(kv_{\perp}\Omega_w)^{1/2}$ is 2.8×10^3 $[\Omega_{eo}^{-1}]$ for a typical value of $v_{\perp} = 0.05$ [c], $k = 10$ $[c^{-1}\Omega_{eo}]$, and $\Omega = 10^{-5}[\Omega_{eo}]$. Thus the transit time normalized to the trapping period is approximated 5.0 in the magnetosphere. On the other hand, in the simulation the length of the trapping zone for $\alpha = 2.55 \times 10^{-6}$ is approximately 224 $[c\Omega_{eo}^{-1}]$ (see Appendix C), giving a transit time of 4.5×10^3 $[\Omega_{eo}^{-1}]$. For $\Omega_w = 10^{-4}$ $[\Omega_{eo}]$ we have $T_t = 890$ $[\Omega_e^{-1}]$, giving the ratio of the transit time to T_t of 5.0, which is the same as that in the magnetosphere.

In the simulation we let quasi-monochromatic waves propagate at the group velocity V_{gn}, which is also a function of position z as

$$V_{gn} = \frac{\partial \omega_n}{\partial k_n} = \frac{2c^2 k_n(z)}{2\omega_n + [\Pi_e^2 \Omega_e(z)/(\Omega_e - \omega)^2]} \tag{3.9}$$

The variations of the cyclotron frequency, wave number, resonance velocity V_R (which is defined by $V_R = \omega - \Omega_e)/k$), and group velocity are shown in Figure 3.2 as a function of distance from the equatorial plane. Note that the resonance velocity increases as the distance from the equator increases, while the parallel velocity of the electron, which shows an adiabatic motion without the effect of the whistler wave, decreases as it moves away from the equator owing to the mirror force. The model of the simulation is schematically illustrated in Figure 3.3.

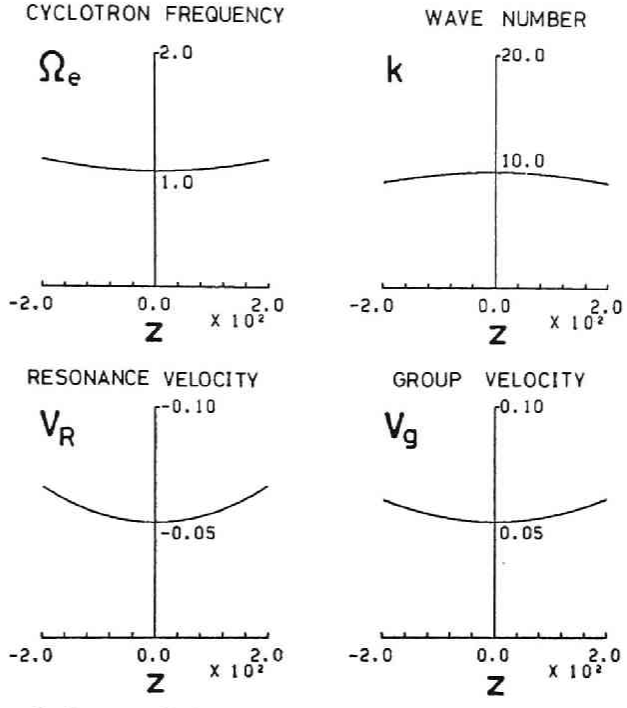

Fig. 3.2 Variation of the cyclotron frequency, wave number, resonance velocity, and group velocity in a parabolic external magnetic field. Velocity and distance z are normalized to light speed c and c/Ω_{eo}, respectively, where Ω_{eo} is a cyclotron frequency at the equator. These normalizations are the same in the following figures.

3.2.2 Trajectories of Electrons along Geomagnetic Field Lines in the Presence of Finite Amplitude Monochromatic Whistler Mode Waves

We introduce new coordinates(θ, $V_\perp$, ζ) illustrated in Figure 3.4 by defining

$$\theta = k (v_\parallel - v_R) \tag{3.10}$$

$$\zeta = \phi - \Psi \tag{3.11}$$

Note that the resonance velocity is a function of position z and changes as an electron moves along the geomagnetic field line. the equations of motion, that is (3.2)-(3.4), are converted into (θ, $v_\perp$, ζ) coordinates as [Vomvoridis and Denavit, 1979]

$$\frac{d\theta}{dt} = kv_\perp \Omega_w \sin\zeta - \frac{1}{2}\left(-3v_\parallel + \frac{kv_\perp^2}{\Omega_e} \right) \frac{\partial \Omega_e}{\partial z} \tag{3.12}$$

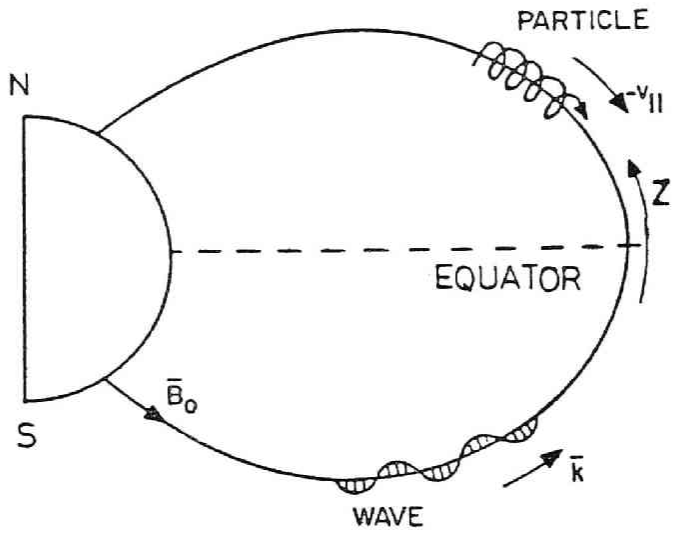

Fig. 3.3 Model of the present test particle simulation.

$$\frac{dv_\perp}{dt} = \frac{\Omega_w}{k}\left(\Omega_e - \theta\right)\sin\zeta + \frac{1}{2}\left(V_R + \frac{\theta}{k}\right)\frac{v_\perp}{\Omega_e}\frac{\partial\Omega_e}{\partial z} \tag{3.13}$$

$$\frac{d\zeta}{dt} = \frac{\Omega_w}{k}\left(\Omega_e - \theta\right)\cos\zeta + \theta \tag{3.14}$$

where it is assumed that the wave frequency ω and the plasma frequency Π_e are constant.

In the magnetosphere the conditions

$$\Omega_e \sim kv_\perp \sim \omega\left(\Omega_e - \omega\right) >> \omega_t >> \Omega_w \tag{3.15}$$

are generally satisfied where ω_t is a trapping frequency defined by $\omega_t = (kv_\perp\Omega_w)^{1/2}$. The variations $\delta\theta$ and $\delta(kv_\parallel)$ of the resonant electron over the period ω_t^{-1} are both of the order of ω_t. In contrast to the fact that $\delta\theta/\theta \sim 1$, $\delta v_\perp/v_\perp$ is much less than unity, as is understood from (3.13), since $\Omega_w << kv_\perp$ and $\delta\Omega_e/\Omega_e << 1$. Therefore the equation for $v_\perp$ is not essential to the resonant interaction [Helliwell, 1967]. In view of the condition

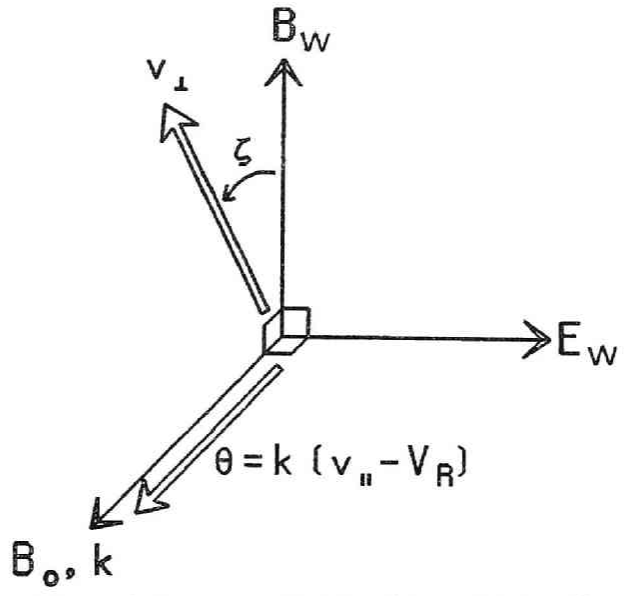

Fig. 3.4 Configuration of the wave fields (E_w and B_w), the static magnetic field and the wavenumber vector k in the coordinates (θ, $v_\perp$, ζ).

(3.15) the equations of motion are approximated by

$$\frac{d\zeta}{dt} = \theta \tag{3.16}$$

$$\frac{d\theta}{dt} - \omega_t^2 (R + \sin \zeta) \tag{3.17}$$

where

$$R = - \frac{1}{d\omega_t^2} \left(- 3 V_R + \frac{k v_\perp^2}{\Omega_e} \right) \frac{\partial \Omega_e}{\partial z} \tag{3.18}$$

and $v_\parallel \simeq V_R$ is assumed.

It is easily understood that the value of R is an essential quantity for the resonant interaction in the inhomogeneous field; it is called an inhomogeneity ratio [Nunn, 1971; Vomvoridis and Denavit, 1979]. when $|R| > 1$, (3.16) and (3.17) give no equilibrium state. Electrons which satisfy the condition $|R| < 1$ can be trapped by the wave when their parallel velocity $v_\parallel$ satisfies a condition $|v_\parallel - V_R| < V_t$ which corresponds to $\theta < 2\omega_t$. Hence we call this range where $|R| < 1$ is satisfied a 'trapping zone'. Note that the trapping zone is specified for each electron because the perpendicular velocities $v_\perp$ are different for different electrons. A

typical example of the variation of the inhomogeneity ratio R with distance from the equatorial plane is shown in Figure 3.5, assuming that $v_{\parallel}$ and Ω_w are constant.

In order to demonstrate a difference of behavior between trapped and untrapped electrons under the effect of a single monochromatic whistler wave in the inhomogeneous magnetic field, trajectories of two electrons are shown in Figure 3.6. The parameters of the two electrons are the same except for their initial ζ. As they travel along the geomagnetic field toward the equator, $|v_{\parallel}|$ increases owing to the mirror force $-\mu\nabla B_0$ and finally becomes equal to the resonance velocity $|V_R|$, which becomes smaller with distance. The point where $v_{\parallel} = V_R$ is satisfied is called a 'resonant point'. After passing this first resonance point the trajectories of trapped and untrapped electrons are separated, as is seen in the figure [Roux and Pellat, 1978]. The untrapped electrons continues to be accelerated by the mirror force after a small jump in $v_{\parallel}$ at the first resonant point. After crossing the equatorial plane it is decelerated by the mirror force and comes to the second resonance point, where its $|v_{\parallel}|$ decreases.

On the other hand the trapped electron is captured by the wave at the first resonance point and afterward moves at an average velocity equal to the resonance velocity. As the electron moves away from the equator, its inhomogeneity ratio R increases so that the potential trough of the wave becomes shallow enough to make the electron detrapped. Note that trapping and detrapping of electrons takes place only within the trapping zone where $|R| < 1$.

In Figure 3.7, trajectories of 64 electrons whose initial values differ only in their phase ζ are shown. There are two cases, each with the same parameters except for the initial parallel velocity: $v_{\parallel}(t = 0) = -0.487c$ for case 1, and $v_{\parallel}(t = 0) = -0.486c$ for case 2. The number of trapped electrons is obviously different between case 1 and 2, though the difference in initial parallel velocities is very small. The reason will be discussed later.

In the case shown in Figure 3.8 the resonance points are situated outside the trapping zone, and therefore we do not see any occurrence of trapping.

The effects of the whistler wave on an electron depend on the deviation of the parallel velocity $v_{\parallel}$ from the resonance velocity V_R, that is on θ. If the deviation is large, the effect of the wave is small, because the phase ζ changes so rapidly that the average value of the second

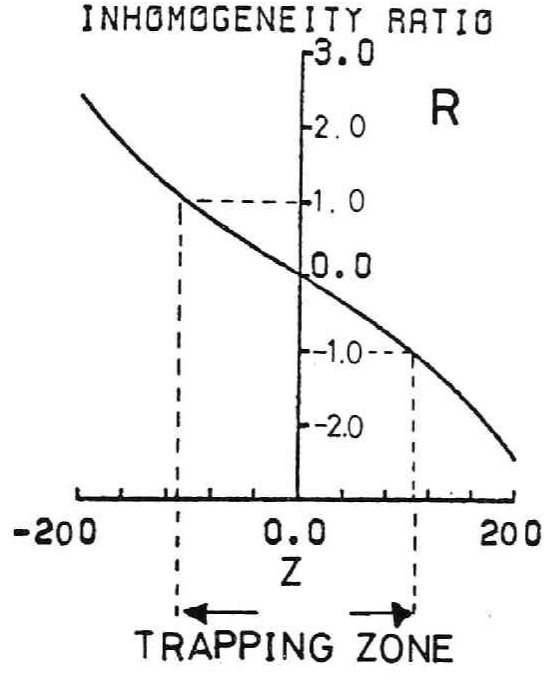

Fig. 3.5 Variation of inhomogeneity ratio R in a parabolic magnetic field: $v_\perp = 0.05$; $\alpha = 2.55 \times 10^{-6}$.

erm, sin ζ in (3.17), becomes nearly equal to zero. However, if electron ieet two monochromatic whistler waves, the effects of the waves are ifferent from a simple superposition of the effect of each wave. To see he two-wave effect, we consider a situation where electrons which are rapped by the first wave encounter the second wave with a frequency lightly different from that of the first wave but with the same mplitude. Effective disturbance by the second wave occurs when $v_\parallel$ of the rapped electrons falls inside the resonance range of the second wave. herefore it is required for the effective disturbance that the difference f the resonance velocities between the two waves is smaller than the econd-wave-trapping speed V_{t2} defined by $2\omega_{t2}/k_2$, that is

$$\delta V_R < V_{t2} \tag{3.19}$$

nder the approximation that $k \simeq k_1 \simeq k_2$ and Ω_e are constant, we obtain

$$\delta\omega \simeq k\delta V_R \tag{3.20}$$

here $\delta\omega$ is the frequency difference of the two waves. Since $V_t = 2\omega_t/k$, he necessary condition for the effective disturbance becomes

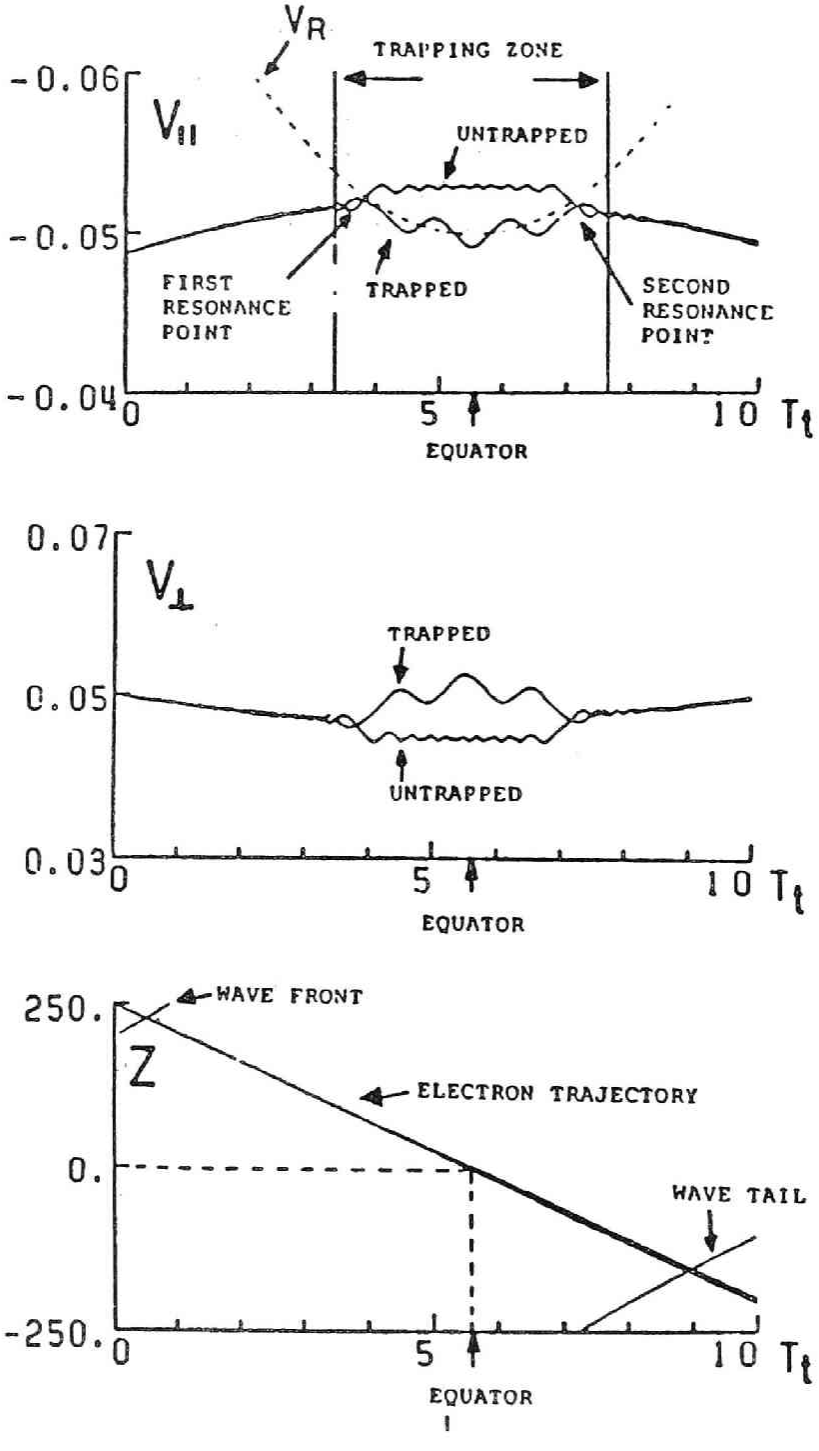

Fig. 3.6 Trajectories of trapped and untrapped electrons.

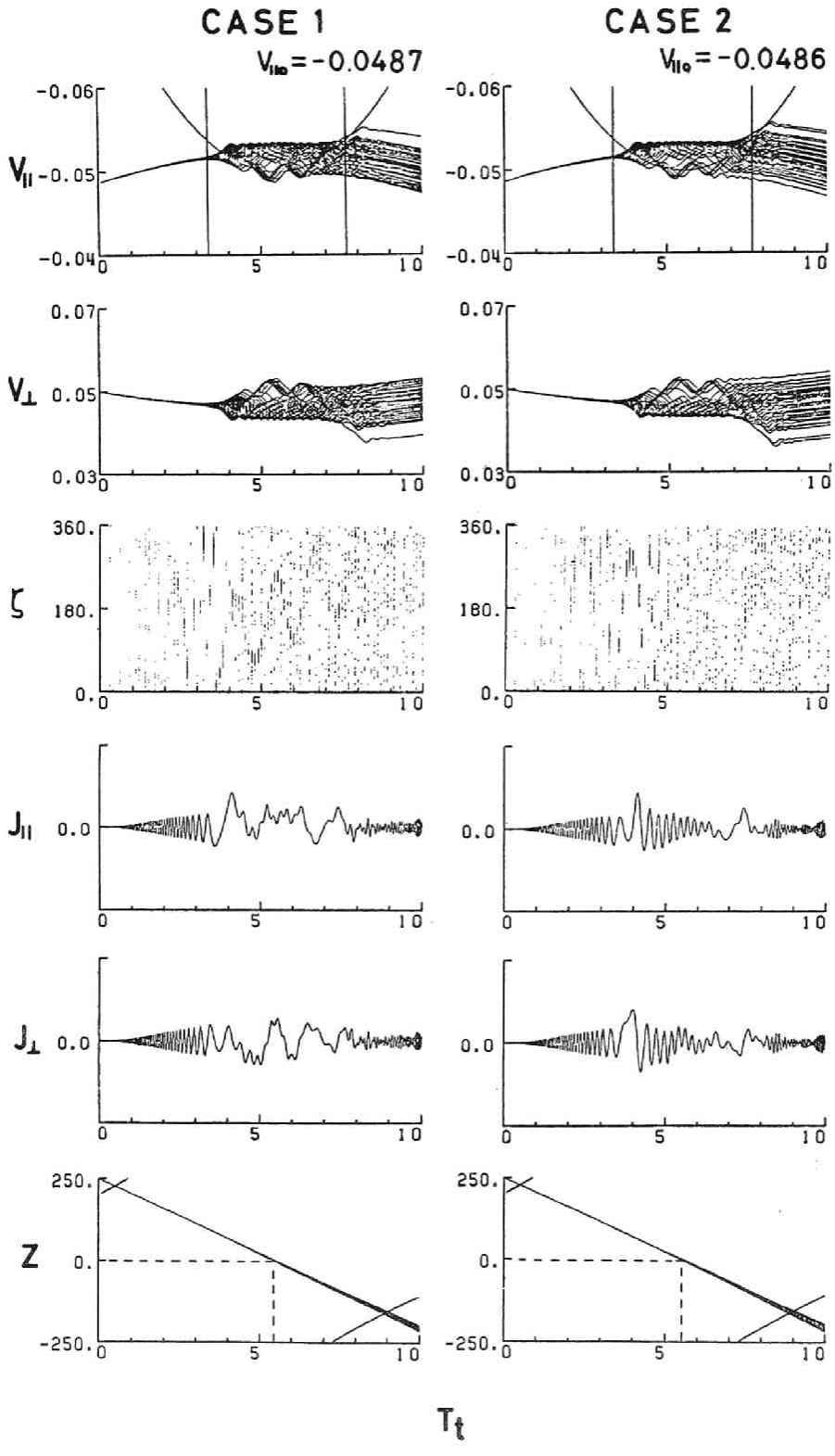

Fig. 3.7 Trajectories of 64 electrons. Their initial values are different only in their phase ζ.

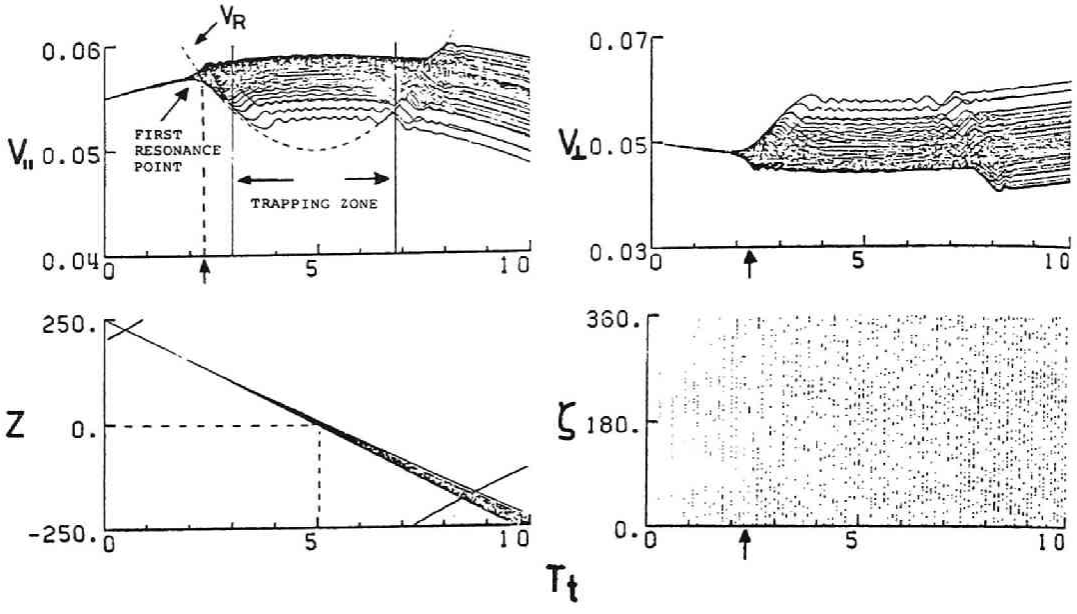

Fig. 3.8 Trajectories of 64 electrons. Note that the first resonance point is situated outside the trapping zone in this case.

$$\delta\omega \simeq 2\omega_t \tag{3.21}$$

In Figure 3.9 the results for several cases with different second-wave frequencies are presented. The trapping frequency is about 0.007, and ω_1 and ω_2 denote the first-and second-wave frequencies, respectively. In the case where $\omega_1 = 0.5$ and $\omega_2 = 0.48$, the condition (3.21) is not satisfied, and the disturbance by the second wave is relatively small. However, in the case of $\omega_1 = 0.5$ and $\omega = 0.495$ the trapped electrons are detrapped drastically owing to the second-wave effect. It should be noted that the possibility of detrapping decreases when the difference $\delta\omega$ becomes too small. The sum of the two waves is

$$A_0 = 2B_w \cos\left(\frac{\delta\omega}{2}t - \frac{k_1 - k_2}{2}z + \frac{\Psi_1 - \Psi_2}{2}\right)$$

$$\times \sin\left(\frac{\omega_1 + \omega_2}{2}t - \frac{k_1 + k_2}{2}z + \frac{\Psi_1 + \Psi_2}{2}\right) \tag{3.22}$$

where Ψ_1 and Ψ_2 are the initial wave phase. From the definition of a group velocity we have $k_1 - k_2 \simeq V_R^{-1}\delta\omega$. Then assuming $v_\parallel$ is constant, we have

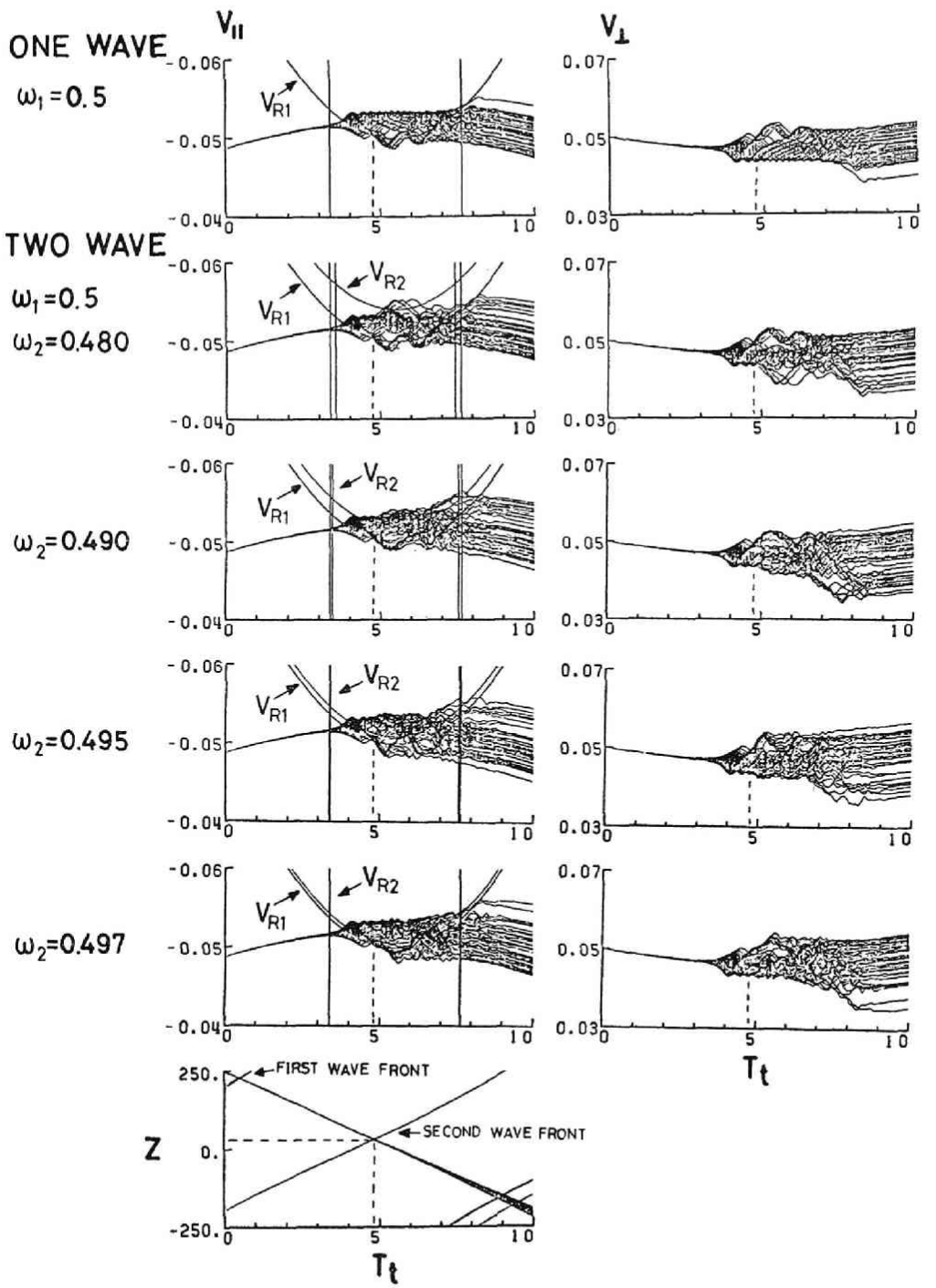

Fig. 3.9 Effects of the second wave on electrons trapped by the first wave. Note that a different frequency of the second wave gives a different effects. Wave frequencies are normalized to a cyclotron frequency at the equator, Ω_{eo}.

$$A_o = 2B_w \cos \{ (1 - \frac{v_\parallel}{V_g}) \frac{\delta\omega}{2} t + \frac{\Psi_1 - \Psi_2}{2} \}$$

$$\times \sin (\frac{\omega_1 + \omega_2}{2} t - \frac{k_1 + k_2}{2} z + \frac{\Psi_1 + \Psi_2}{2}) \qquad (3.23)$$

As a condition $v_\parallel \simeq -V_g$ is generally assumed, (3.23) can be written

$$A_o = 2B_w \cos (\delta\omega t + \frac{\Psi_1 - \Psi_2}{2})$$

$$\times \sin (\frac{\omega_1 + \omega_2}{2} t - \frac{k_1 + k_2}{2} z + \frac{\Psi_1 + \Psi_2}{2}) \qquad (3.24)$$

The maximum value of the amplitude A_o of the total wave field seen by the electrons varies slowly with the frequency $\delta\omega$ and becomes zero with the period of $\pi/\delta\omega$. Therefore for very small $\delta\omega$ the chance for electrons to encounter a small wave amplitude and hence undergo detrapping becomes small.

3.2.3 Phase Bunching in a Nonuniform Magnetic field

In a nonuniform external magnetic field, electrons in resonance with a monochromatic whistler mode wave are phase-bunched in ways that are different from those in a uniform magnetic field. Two striking effects are observed in the process of phase bunching. One is called the 'channel effect', and the other is called the 'cluster effect'. Phase bunching due to the channel effect was pointed out by Vomvoridis and Denavit[1979] and is analyzed first in the present paper. Then the cluster effect, newly found in the present simulation, is discussed in detail.

We first consider the trajectories of electrons in the ζ-θ phase space under a constant R. In Figure 3.10, configurations of trajectories are shown for various R values. They are calculated by the simplified equations of motion ((3.16) and (3.17)) under given values of the constant R. The initial phase was given uniformly over the interval 4π in order to demonstrate periodic behavior in ζ with a period of 2π. In the case of R = 0, which corresponds to a uniform ambient magnetic field, every particle at the resonance velocity is trapped, forming closed contours, and untrapped electrons can never cross the resonance velocity line where $\theta = 0$. In the case of $0 < |R| < 1$, however, untrapped particles can cross the resonance

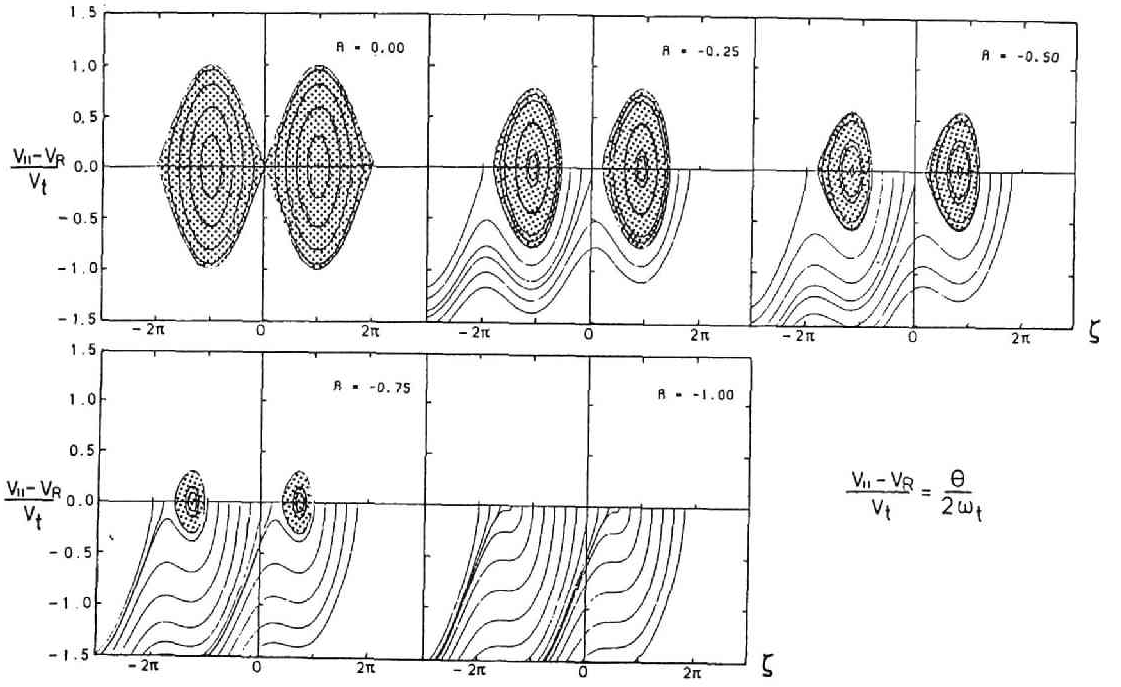

Fig. 3.10 Electron trajectories in the ζ - $v_{\parallel}$ plane for various values of the constant R. The shaded area shows the trapping region. Note that the size of the trapping region becomes smaller as R decreases.

velocity only in a limited phase range lying between adjacent closed contours. Note that the closed region occupied by trapped electrons becomes smaller as the absolute value of R increases. Even in the case $|R| > 1$ the phase range in which the trajectories cross the resonance velocity is limited, as is shown in Figure 3.11.

The reason for this phase limitation can be explained as follows. When the electrons approach the resonance velocity in the ζ-θ plane, the acceleration in the direction along θ takes place because of the sum of the mirror effect $\omega_t^2 R$ and the wave effect $\omega_t^2 \sin\zeta$. Those electrons which lie between $(2n-1)\pi$ and $2n\pi$ (n is an integer) are more accelerated in θ than those lying between $2n\pi$ and $(2n+1)\pi$ because of the sign of R and $\sin\zeta$ in the case $R < 0$. Less accelerated electrons have a higher probability of falling in the phase range between $(2n-1)\pi$ and $2n\pi$ before crossing $\theta = 0$. Thus the probability of crossing at $\theta = 0$ with ζ between $(2n-1)\pi$ and $2n\pi$ is higher than it is with ζ between $2n\pi$ and $(2n+1)\pi$. Consequently, particles whose initial phases are uniform outside the resonance range become phase-bunched when they traverse $v_{\parallel} = V_R$. in the ζ-$v_{\parallel}$ plane even if $|R| > 1$. We call this phase bunching channel effect bunching because the passage in the ζ-$v_{\parallel}$ plane at $v_{\parallel} = V_R$ looks like a channel, especially in

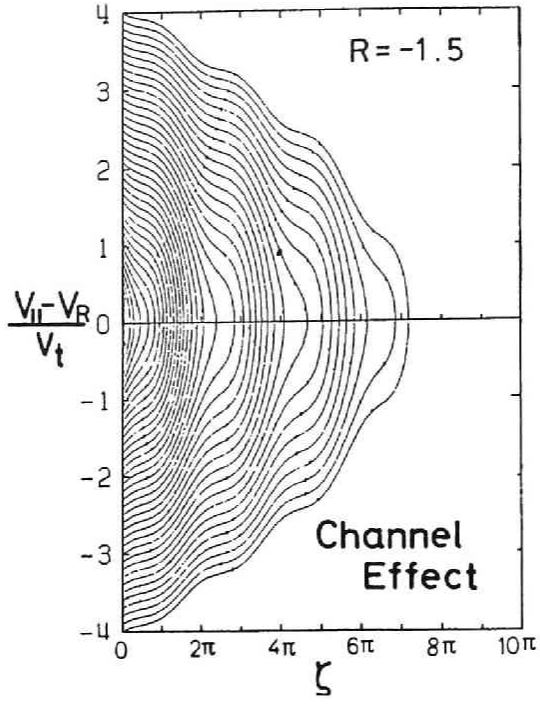

Fig. 3.11 Trajectories of electrons in the ζ - $v_{\parallel}$ plane. The trajectory density is high at a phase range between $(2n-1)\pi$ and $2n\pi$ and low between $2n\pi$ and $(2n+1)\pi$. This effect is called a channel effect.

the case $|R| < 1$. However, we use the term channel effect even for cases where $|R| > 1$, because in these cases the passage is also restricted.

As is shown in Figure 3.7, the number of trapped electrons differs greatly depending upon the initial parallel velocity at the moment of resonance with the wave. In order to clarify the reason for this, trajectories were examined for a number of electrons having a delta function distribution with respect to $v_{\parallel}$ and a uniform phase distribution at the moment of the encounter. They are calculated from (3.16) and (3.17), using a constant inhomogeneity ratio R, and shown in Figure 3.12. The initial phase was given as being uniform over the interval 2π. A number of electrons exhibit very closely spaced trajectories, indicated by the dark regions in Figure 3.12. This is because the gradient of these trajectories with respect to ζ was small at the moment when the group of electrons was injected into the wave. The gradient of the trajectory of an electron in the ζ-θ plane is obtained by eliminating a time parameter from (3.16) and (3.17) and is given by

$$d\theta/d\zeta = \omega_t^2 (R + \sin \zeta)/\theta \qquad (3.25)$$

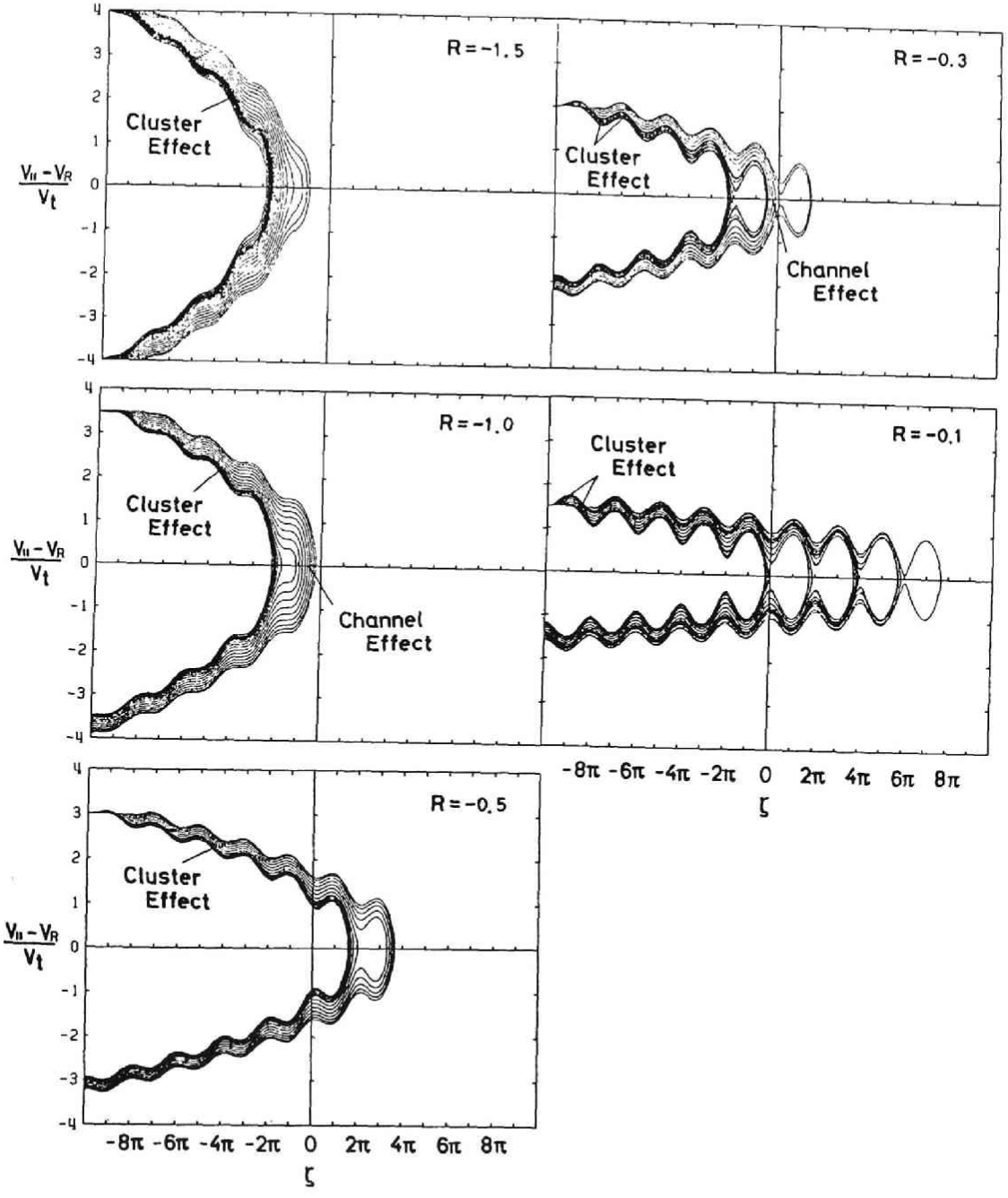

Fig. 3.12 Trajectories of electrons in the ζ - $v_{\parallel}$ plane. An initial delta-functional $v_{\parallel}$ distribution and a uniform phase distribution are assumed. A clear cluster effect is seen (see text). Note that the cluster effect is most clearly seen in the case R = -1.0.

at a fixed value of θ. The absolute value of the gradient $d\theta/dt$ differs according to the phase ζ, and thus nonuniformity is caused in the distribution of trajectories in the ζ-θ. Let ζ_c denote the phase which gives the minimum absolute value of the gradient $d\theta/d\zeta$. The electrons whose initial phases are near ζ_c move close together along a trajectory specified by (ζ_c, θ_o), where θ_o represents the initial parallel velocity. In the case $R < -1$, $\zeta_c = \pi/2 + 2n\pi$. The electrons then show clustered trajectories around one curve passing through (ζ_c, θ_o) in the ζ-θ plane. In the case $-1 < R < 0$, however, the gradient $d\theta/d\zeta$ becomes zero at two different phases, satisfying the equation

$$\sin \zeta_c + R = 0 \tag{3.26}$$

Therefore there exist two kinds of curves around which electrons cluster. We call this a cluster effect and illustrate it for various values of R in Figure 3.12. Note that there is one main trajectory around which other trajectories gather in the cases $R < -1$ and that there are two in the cases $-1 < R < 0$.

In the above discussion a delta function distribution of the parallel velocities was assumed as initial condition, but it is not a necessary condition for the cluster effect. In the following discussion we derive a criterion for the effective cluster effect with respect to the $v_\parallel$ spread in the initial distribution. The equation of the trajectories in the ζ-θ plane is obtained by integrating (3.25) as

$$C = \theta^2 + 2\omega_t^2(\cos \zeta - R\zeta) \tag{3.27}$$

where C is a constant which specifies the trajectory. We first estimate an initial parallel velocity range $D(\theta)$ for a given fixed initial ζ which corresponds to a phase spread over 2π in ζ at $\theta = 0$. From (3.27), giving $\theta = 0$, the two values of C, C_1 and C_2 for $\zeta = \zeta_A$ and $\zeta = \zeta_A + 2\pi$ (ζ_A is arbitrary), are calculated to give a difference $\delta C = C_1 - C_2 = 4R\omega_t^2$. The difference $D(\theta)$ which gives the same difference δC is easily obtained from (3.27) for a fixed ζ as

$$D(\theta) = 4\pi R\omega_t^2 / [2\theta - D(\theta)] \simeq 2\pi R\omega_t^2/\theta \tag{3.28}$$

where the second approximation is allowed if $D(\theta) \ll \theta$. It is clear that the cluster effect appears effectively when the initial θ distribution has a spread over a small range of $\delta\theta$, satisfying the condition $\delta\theta \ll D(\theta)$.

The trajectories cross the resonance velocity almost vertically in the ζ-θ plane. Therefore the clustered electrons moving along the clustered trajectories show a strong phase bunching near the resonance velocity, the phase tends to be around $\zeta = (3/2)\pi + 2n\pi$ because of the channel effect.

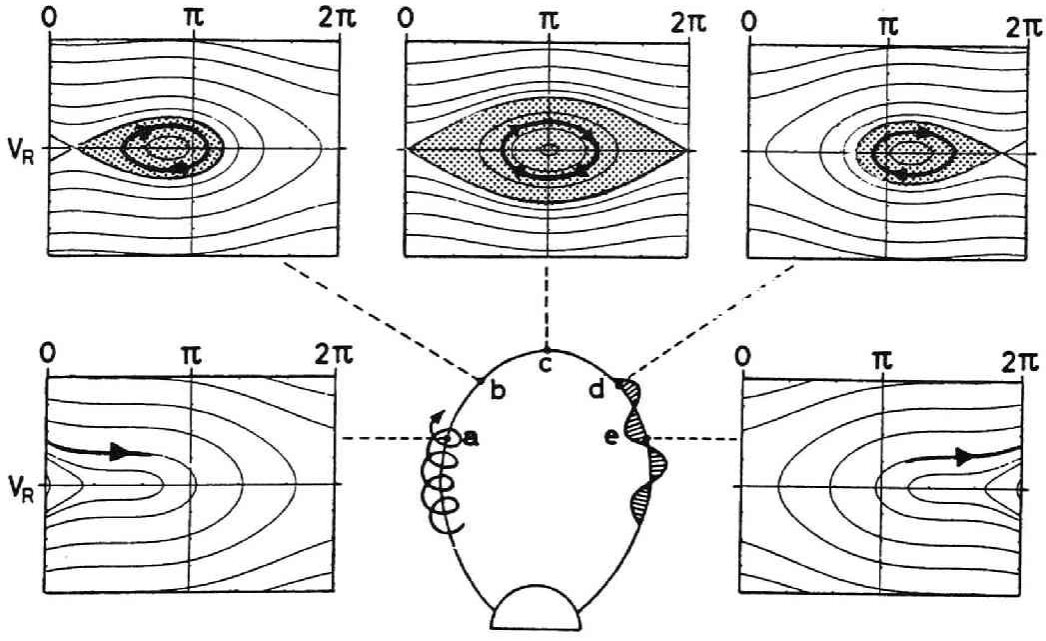

Fig. 3.13 Schematic illustration of trapping and detrapping due to a change of size of the trapping region in the inhomogeneous geomagnetic field.

In the preceding discussion we have assumed that the inhomogeneity ratio R is constant. In reality, however, the absolute value of R decreases as the electrons approach the first resonance point, and there exists a trajectory along which the electrons are trapped in the wave potential trough, as is shown schematically in Figure 3.13. As |R| decreases with distance, the size of the trapping region in the ζ-$v_{\parallel}$ plane (shaded area) changes accordingly. Therefore some of the initially untrapped electrons have a chance to enter into the trapping region and be trapped. After passing over the equator those electrons suffer the inverse process and are finally detrapped. Results of the computer simulation on trajectories of electrons in the parabolic model magnetic field under which R changes with distance are shown in Figure 3.14. Two cases with a small difference in initial parallel velocity are presented in the figure. Clustered electrons are seen in both cases. They happen to be trapped in case 1 but not in case 2. These two cases correspond to those presented in

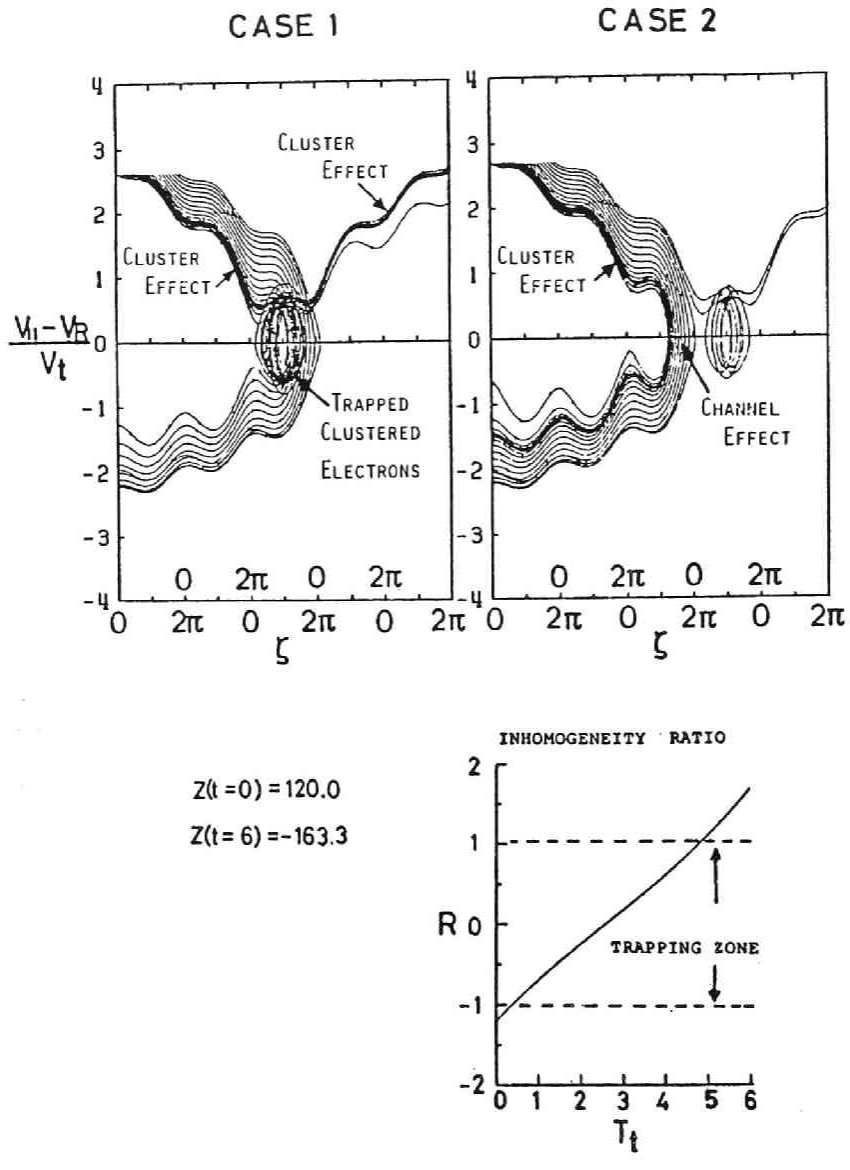

Fig. 3.14 Trajectories of electrons in the parabolic magnetic field under which R changes with position. Case 1: $(v_{\parallel} - V_R)/V_t = 2.62$ at $t = 0$. Case 2: $(v_{\parallel} - V_R)/V_t = 2.70$ at $t = 0$.

Figure 3.7. Thus the difference in the number of trapped electrons is explained well by a subtle dependence of the cluster effect on the initial parallel velocity.

3.2.4 Resonant Current due to Phase Bunching

Trapped resonant electrons can give rise to transverse resonant currents with a frequency very close to the frequency of the trapping wave, because the phase of their $v_{\perp}$ are correlated with respect to the wave

magnetic field. This type of resonant current in a uniform magnetic field has been well investigated. One example of phase bunching, in this case

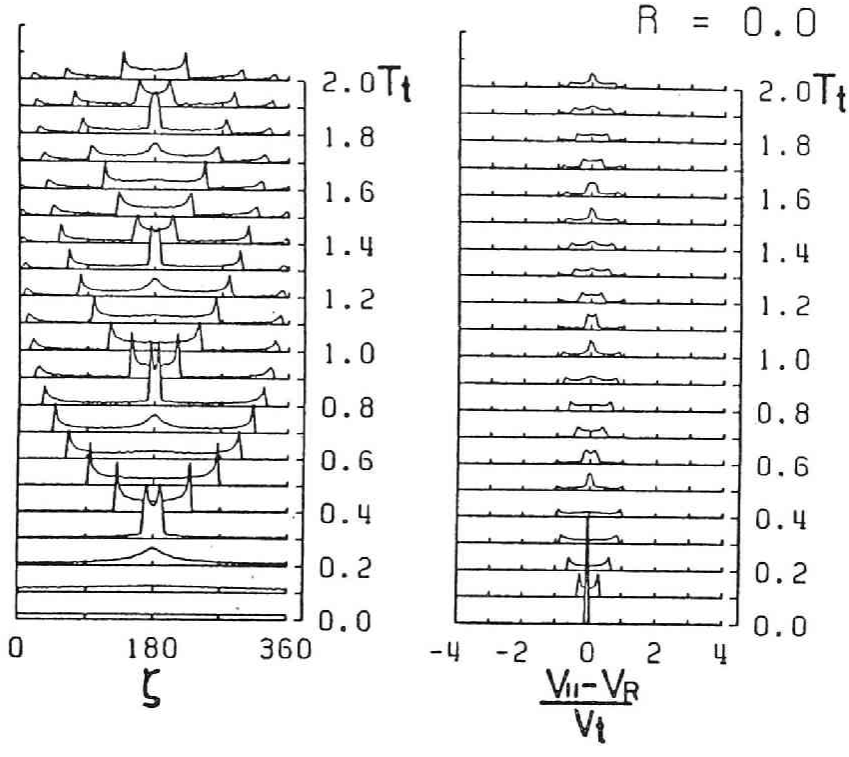

Fig. 3.15 Evolution of the distribution of resonant electrons in the case of a uniform magnetic field. A delta-functional $v_{\parallel}$ distribution at V_R is assumed at t = 0.

calculated from (3.16) and (3.17), is shown in Figure 3.15. A uniform phase distribution and a delta functional $v_{\parallel}$ distribution at the resonance velocity are assumed as the initial values. A strong phase bunching appears around the phase $\zeta = 180^0$ at a time of a quarter of the trapping period, and thereafter the phase bunching repeats with a period of half the trapping period. Since the phase distribution is symmetric around $\zeta = 180^0$, as is seen in Figure 3.15, the current is formed parallel to the wave magnetic field. However, if the uniform distribution in $v_{\parallel}$ has a spread greater than the resonance range as shown in Figure 3.16, very little phase bunching is observed around the phase $\zeta = 180^0$, which is the center of oscillation of trapped electrons as shown in the case of R = 0 in Figure 3.10.

The analysis of the resonant current in a uniform magnetic field is

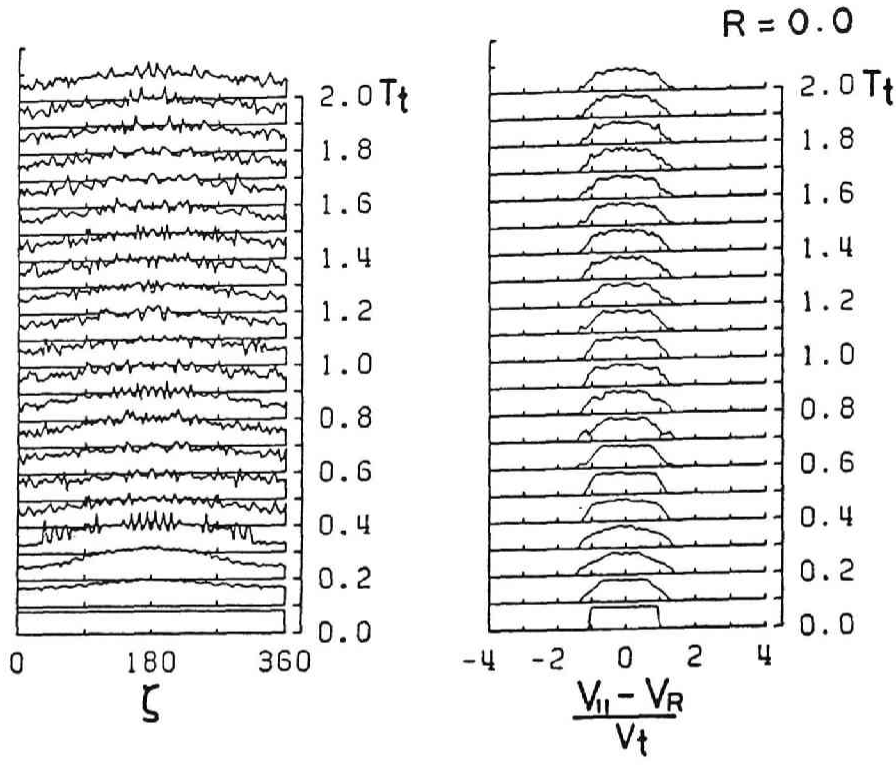

Fig. 3.16 Evolution of the distribution of resonant electrons in the case of a uniform magnetic field. A uniform $v_{\parallel}$ distribution over the resonance range is assumed at t = 0.

effective for real magnetospheric conditions only if the situation includes a group of electrons encountering the waves near the equator is shown in Figure 3.17. In the following discussion we sill consider how the resonant current, which is purely parallel to B_w in the uniform B_o case, changes its direction as the inhomogeneity of the magnetic field becomes effective. We define two current components, the parallel component $J_{\parallel}$ and the perpendicular component $J_{\perp}$, with respect to the wave magnetic field. They are computed by

$$J_{\parallel} = -e \Sigma v_{\perp} \cos \zeta_i \tag{3.29}$$

$$J_{\perp} = -e \Sigma v_{\perp} \sin \zeta_i \tag{3.30}$$

We could see in Figure 3.17 that a strong parallel component $J_{\parallel}$ appears at the equatorial encounter and then decreases with an oscillation, whereas the perpendicular component $J_{\perp}$ increases as the electrons move away from

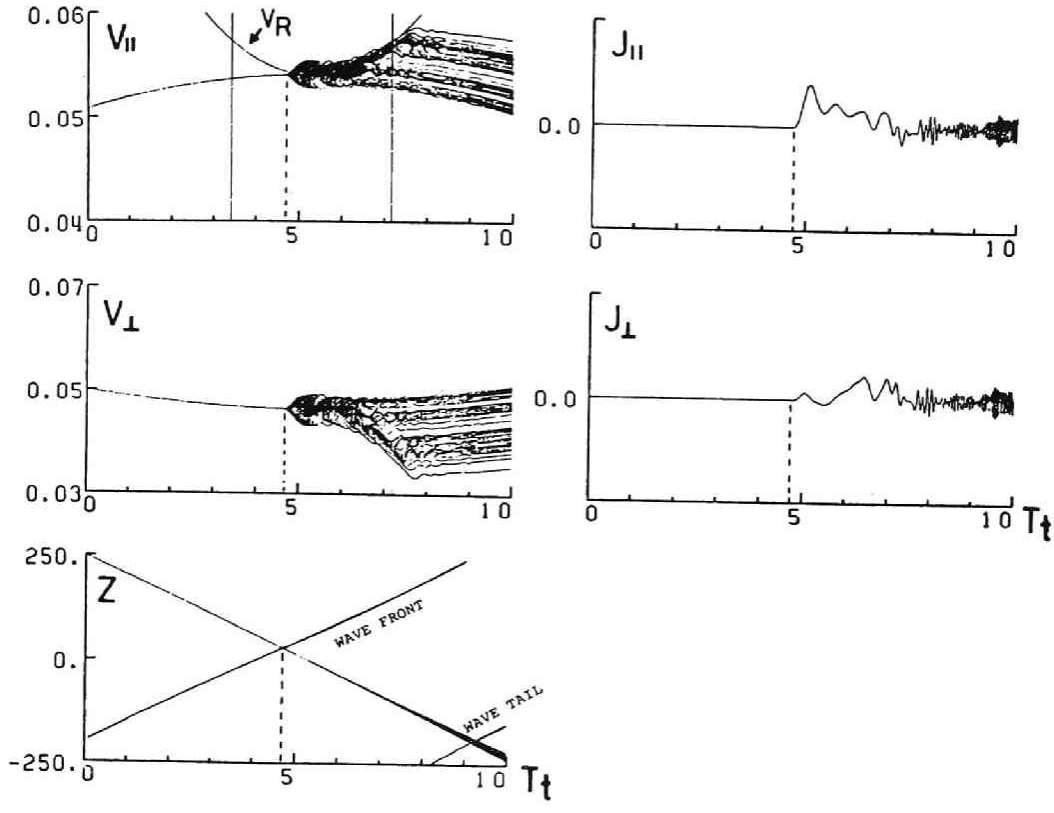

Fig. 3.17 Trajectories of 64 electrons trapped near the equator and resonant current by them.

the equatorial plane. This is due to a slow change from π to $(3/2)\pi$ of the center of the phase oscillation of trapped electrons as the inhomogeneity ratio R increases from 0.0 to 1.0. The slow change of the phase ζ_0, around which the trapped electrons oscillates, is governed by $R + \sin \zeta_0 = 0$. When R reaches 1.0, however, the electrons are detrapped, and the resonant current disappears. The disappearance is seen in Figure 3.17 at $t \simeq 7T_t$.

In a nonuniform magnetic field, resonant currents are formed even if electrons are not trapped in the wave potential trough. In Case 2 of Figure 3.14 the phase range of the untrapped electrons at the resonance velocity is limited because of the channel effect, which makes the resonance current. In addition, some number of the untrapped electrons show the cluster effect, as shown by the dense trajectories in the ζ-θ plane, yielding a strong phase bunching near the resonance velocity. The temporal variations of the phase distribution and the parallel velocity distribution of electrons are presented in Figure 3.18 for Case 2 of Figure

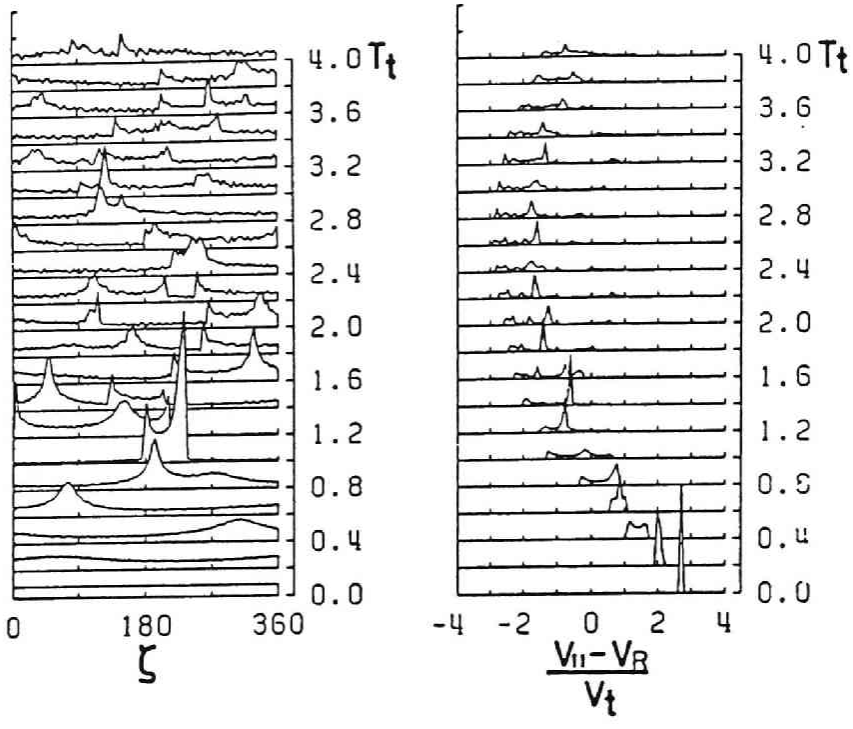

Fig. 3.18 Evolution of phase and $v_{\parallel}$ distributions of electrons with the same initial values as those in Case 2 of Figure 3.14.

3.14. When the electrons come into the resonance range $|v_{\parallel} - V_R| < V_t$, broad phase bunching by the channel effects is seen in which a very steep peak caused by the cluster effect is included. We can observe the same kind of phase bunching in Case 2 of Figure 3.7. A strong resonance current exists at the resonance point because of the superposition of the channel and cluster effects. However, it should be noted that a resonance current exists even outside the resonance range. Before reaching the first resonance point the electrons begin to form the resonance current with gradually increasing magnitude and with high frequency, as is seen in Figure 3.7. This current is due to the cluster effect, because clustering of the trajectories is possible outside the resonance range, as was mentioned previously. When the curve of clustering trajectories in the ζ-θ plane has a steeper gradient with respect to ζ, the clustered electrons are more phase-bunched. It is apparent from (3.25) that the magnitude of the gradient increases as the parallel velocity $v_{\parallel}$ becomes close to the

resonance velocity V_R, and the clustered electrons tend to populate within a very narrow phase range. Therefore, the magnitude of the resonant current increases as the electrons approach the first resonance point. However, this resonance current observed outside the resonance range disappears if the initial parallel velocity distribution is broad in $v_{\parallel}$ because of cancellation of cluster effects for each initial $v_{\parallel}$. The reduction of the current due to the cancellation is seen in Figure 3.19, in which a broader initial $v_{\parallel}$ is given than that in Figure 3.7 with otherwise the same parameters.

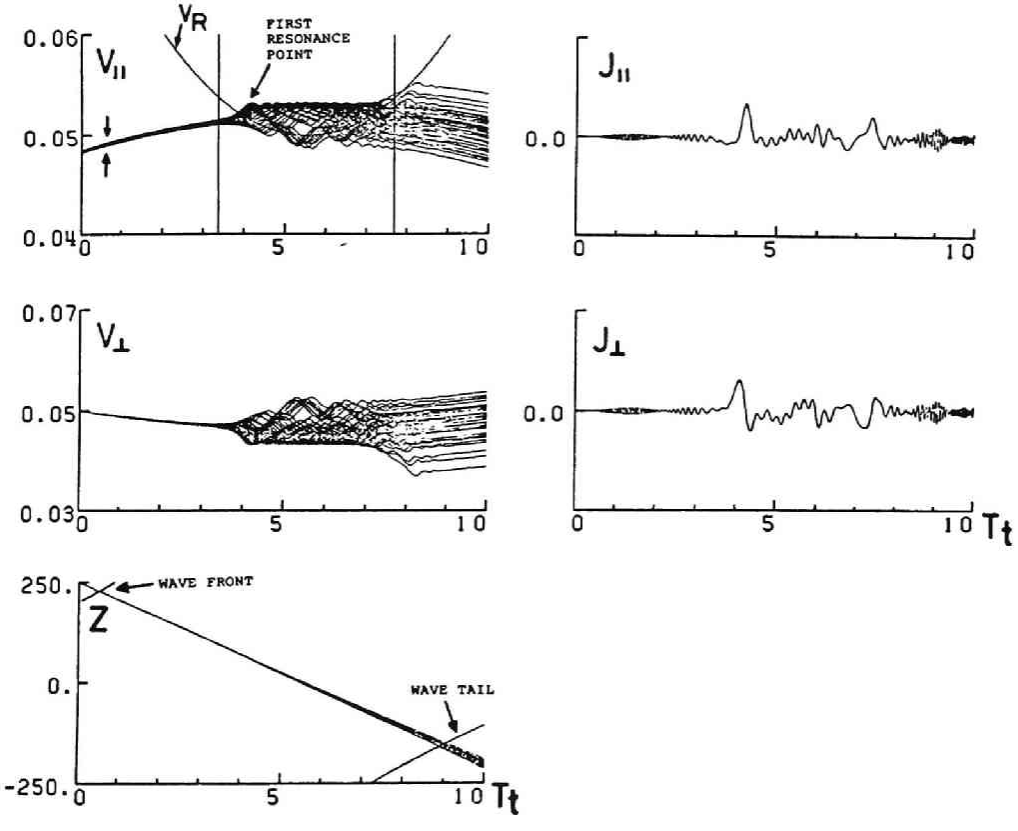

Fig. 3.19 Trajectories of 64 electrons with various initial values of $v_{\parallel}$. Compare currents at $t \leqslant 3.8T_t$ with those in Case 2 of Figure 3.7.

In the previous discussion we have shown the existence of two type of phase bunching: one due to the channel effect and the other to the cluster effect. Under a constant R the electrons which encounter the whistler wave at a point where their $v_{\parallel}$ is not within the resonance range are never trapped by the wave. Therefore the resonant current due to these untrapped electrons is formed mostly by the channel effect and for a short time,

normally shorter than one trapping period. However, when the inhomogeneity ratio R changes as the electrons move, as occurs in the actual magnetospheric plasma, initially untrapped electrons may possibly be trapped by the wave potential trough, because the size of the trapping region in the ζ-θ plane becomes large as the electrons move toward the equator. Examples of this trapping due to the change of R are illustrated in Figure 3.14, in which two cases are shown. Case 2 illustrates a situation in which untrapped nonclustered electrons are drawn into the trapping region, while Case 1 shows an interesting situation in which electrons already clustered in the untrapping region are engulfed by the

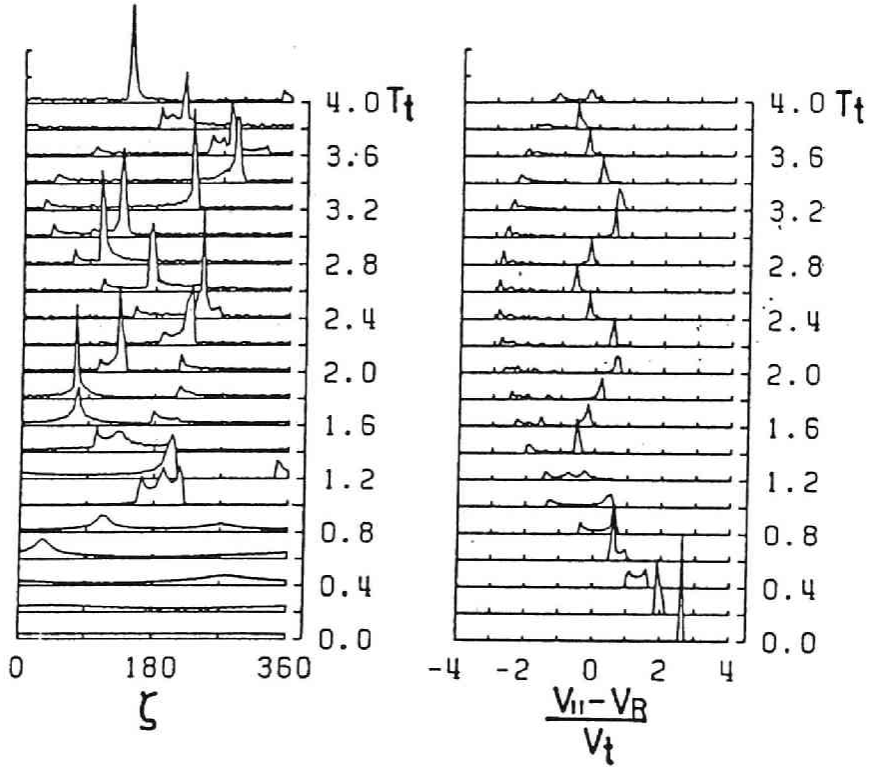

Fig. 3.20 Evolution of phase and $v_{\parallel}$ distributions of electrons with the same initial values as those in Case 1 of Figure 3.14.

enlarging trapping region. Figure 3.20 shows the time variation of the phase and $v_{\parallel}$ distributions for this case. The electrons thus trapped remain clustered and then rotate along a closed orbit in the ζ-θ plane inside the trapping boundary, giving rise to a large-amplitude current which lasts for several trapping periods until the electrons, moving away

from the equator, are detrapped as the trapping capacity of the wave shrinks. This long-lasting current due to clustered trapped electrons is a concept not previously mentioned in the literature. This new type of resonant current should be taken into account in the interpretation of generation mechanisms of triggered emissions in the magnetosphere.

It is noted that in Figures 3.14 and 3.20 a delta function is used for the initial $v_{\parallel}$ distribution in order to demonstrate the effect of clustered trapped electrons. However, even in cases of more realistic distributions of $v_{\parallel}$ with a spread the significance of the clustered trapped electrons is still observed, as is shown in Figure 3.21. A strong phase bunching at $t = 1T_t$ around $\zeta = 210^0$ is due to the channel effect. However, it is temporary and never lasts long. In contrast, trapped electrons which are kept clustered make a significant contribution to the long-lasting resonant current, because other electrons are phase-randomized.

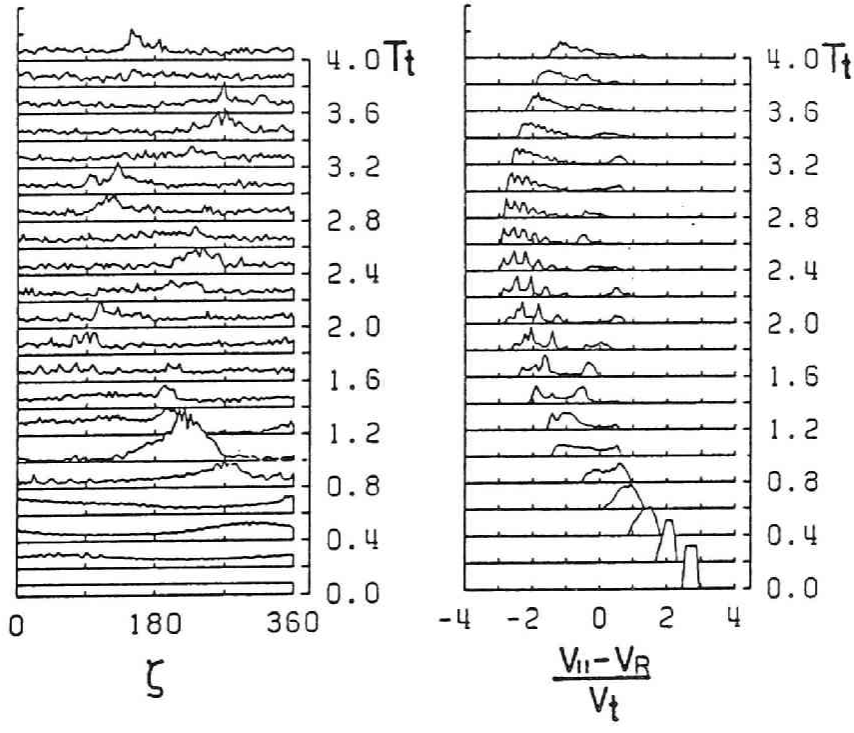

Fig. 3.21 Evolution of phase and $v_{\parallel}$ distributions of electrons with initial wide $v_{\parallel}$ distribution.

3.2.5 *Conclusion and Discussion*

Resonance characteristics of whistler wave-electron interaction in the nonuniform magnetic field have been discussed by many authors. Helliwell [1967] discovered the importance of long-lasting resonant current due to the 'self-consistent wave condition' which is expressed by $v_{\parallel} - V_R$ and $dv_{\parallel}/dt = dV_R/dt$. Nunn [1971] studied the behavior of resonant electrons in the nonuniform geomagnetic field which satisfy the same condition as Helliwell's [1967]. Nunn termed the condition 'second-order resonance condition'. In Nunn's study, trapped electrons are thought to be a main carrier of resonant currents. However, trapping of resonant electrons by whistler waves is seemingly a priori assumed.

As long as $\partial\Omega_e/\partial z$ and the wave amplitude Ω_w are assumed to be constant, the contours of the trapped electrons in the $v_{\parallel}$ -ζ phase space are closed and separated from those of untrapped electrons by a separatrix, as shown in Figure 3.10. Therefore any electrons which are originally untrapped could not be trapped as long as the inhomogeneity ratio R is constant. However, even in the case of constant $\partial\Omega_e/\partial z$, trapping of originally untrapped electrons is possible at the wave front because of a rapid change of R due to a rapid change of the wave amplitude Ω_w there. At the wave front some untrapped electrons located outside the trapping region (shaded area in Figure 3.13) are suddenly placed in the trapping region because of a rapid expansion of the trapping region. Thus the whistler wave train, propagating along the magnetic field line with constant $\partial\Omega_e/\partial z$, looks like a streamer in the velocity (or phase) versus distance space with a front-opening and nonbroken side, swallowing electrons into the trapping region only at the opening. Electrons approaching the resonance velocity toward the side of the whistler streamer, that is, those encountering the whistler waves not at the wave front but at the main portion of the wave train, could not enter into the streamer (i.e., around the separatrix in the $v_{\parallel}$-ζ plane). It is noted that the size of the opening changes as the wave front moves away from the equator and is finally reduced to zero at $|R| > 1$. Thus the feeding of the trapped electrons into the trapping region is apparently possible only during a period when the wave front (not the main portion of the wave train) passes through the trapping zone where $|R| < 1$ is satisfied. However, since $d\Omega_e/dz$ is not constant in the magnetosphere, it is possible that untrapped electrons outside the streamer enter into the inside of the streamer and are trapped by the wave, from its leaky side, as is schematically shown in Figure 3.13.

In this section, a test particle simulation is carried out to study

the trapping and associated detrapping process through a leaky side of the wave streamer in the nonuniform geomagnetic field. It was determined that the trapping of originally untrapped electrons is actually possible owing to the change of the size of the trapping region in the $v_{\parallel}$-ζ phase space, as shown in Figures 3.7, 3.9, and 3.14. Therefore, after the wave front passes away from the trapping zone, the feeding of trapped electrons into the wave potential trough is still possible. An interesting and important point in this trapping process is that the trapped electrons never fill out the trapping region in the $v_{\parallel}$-ζ plane, as do those entering from the wave front, but take clustered closed trajectories as a group. Therefore direction of the resonant current due to the clustered trapped electrons changes with a characteristic period inherent to the clustered orbits, while the resonant current due to electrons trapped at the opening, which fill the trapping region, gradually changes its direction only by a change of a center phase ζ_o of the trapping region due to the change of the inhomogeneity factor R.

Helliwell [1967] studied the nonlinear whistler interaction, taking all resonant electrons — both trapped and untrapped — into account in his pioneering work. Vomvoridis and Denavit [1979] studied the role of untrapped electrons explicitly, which contribute to the resonant current through the channel effect. They found that untrapped electrons could form a significant resonant current when they pass through the resonance velocity outside the resonance region (i.e., outside the wave streamer in our image). Thereafter Vomvoridis and Denavit [1980] performed a self-consistent simulation of the whistler interaction in a nonuniform magnetic field with constant $d\Omega_e/dz$. In addition to the growth mechanism similar to the homogeneous case they take two other effects into account. One is the contribution from untrapped electrons. The other is the inhomogeneity effect on the trapped electrons. The latter is essentially the same as the effect considered by Nunn [1981]. However, since constant $d\Omega_e/dz$ is assumed in this simulation, the contribution of clustered electrons, which are trapped and remain clustered because of the varying R effect, is not included. Electrons which enter from the leaky side of the wave packet and are trapped—some of them are clustered in the wave potential trough—would form additional trapped electrons entering from the front opening of the wave. The contribution of these newly trapped electrons at the main portion of the wave train is significant, especially after the electrons trapped at the wave front flow away from the trapping zone.

In summary, we have pointed out that a new type of phase bunching,

called cluster effect phase bunching, should be additionally considered in the nonlinear whistler interaction in a nonuniform magnetic field with a spatially varying gradient. A full simulation under a condition of varying R would be necessary to investigate a relative contribution of the cluster effect phase bunching in a self-consistent feedback model and to see the competing process of untrapped and trapped electrons, because the size of the trapping region changes with time and with space.

3.3 Self-consistent Evolution of Whistler Mode Waves

In this section basic mechanisms of the wave growth and frequency shift involved in the interaction are investigated with the aid of self-consistent computer simulations. The simulation method used in the present study is basically the long-time-scale algorithm [Vomvoridis, 1978; Rathmann et al., 1978], though an improvement is made on it. Special emphasis is laid on roles of trapped and untrapped resonant electrons in a nonuniform dipole magnetic field. A numerical study of coherent whistler mode interactions in an inhomogeneous plasma has been performed by Nunn [1974], who assumed that resonant currents due to untrapped particles are negligible in comparison with those caused by trapped particles. A theory of triggered emissions has also been presented by Roux and Pellat [1978], who focussed their attention on a change in the distribution function of particles due to trapping effects of resonant electrons in the inhomogeneous geomagnetic field. However, we will see that untrapped resonant particles as well as trapped particles play an important role in the interaction.

We present wave equations showing how the wave amplitude and frequency are changed by resonant currents in Subsection 3.3.1. In Subsection 3.3.2 equations of motion of resonant particles are presented. In Subsection 3.3.3 the simulation method is explained and interactions in a homogeneous medium are studied for two types of simulation models, namely a uniform periodic model and a nonuniform encounter model. In Subsection 3.3.4, interactions in an inhomogeneous medium is studied. Roles of trapped and untrapped particles in the evolution of the wave amplitude are investigated. A computer simulation of the whistler wave evolution in a nonuniform magnetic field of a constant gradient has been done by Vomvoridis and Denavit [1980]. They followed the evolution under the effects of both trapped and untrapped particles. However, the complexity

of their simulation model made it difficult to understand the effects of trapped and untrapped particles separately, which we clarify in this section. Subsection 3.3.5 gives a summary and discussions.

3.3.1 Equations for the Wave Fields

We assume a purely transverse whistler mode wave that propagates along the magnetospheric field line and interacts with counter-streaming high energy resonant electrons. In Section 2.4, we have derived a set of equations showing how the wave amplitude and frequency are modified by the resonant currents J_B and J_E. In this subsection, we relate these equations to the linear dispersion relation and the linear growth rate. For reference we rewrite (2.71) and (2.73).

$$\frac{\partial B_w}{\partial t} = - V_g \left(\frac{\partial B_w}{\partial z} + \frac{1}{2} \mu_o J_E \right) \tag{3.31}$$

$$\omega = \frac{k(k - \mu_o J_B/B_w)}{k(k - \mu_o J_B/B_w) + \Pi_e^2/c^2} \Omega_e \tag{3.32}$$

As is seen in (3.31) and (3.32), J_E causes a change of the wave amplitude B_w, and J_B modifies the frequency ω. It is noted that (3.32) corresponds to the real part of a dispersion relation of the whistler mode wave in the presence of hot electrons. For the linear theory of the inter-action, the following relation is deduced from the linearlized Vlasov equation and Maxwell's equation,

$$\frac{J_B}{B_w} = \mathrm{Re}\left[\frac{\pi e^2}{km} \int_{-\infty}^{\infty} dv_{\parallel} \int_{-\infty}^{\infty} v_{\perp}^2 dv_{\perp} \cdot \frac{(v_{\parallel} - \frac{\omega^*}{k}) \frac{\partial g_b}{\partial v_{\perp}} - v_{\perp} \frac{\partial g_b}{\partial v_{\parallel}}}{v_{\parallel} - V_R^*} \right] \tag{3.33}$$

where g_b is a distribution function of hot electrons, -e and m are the electron charge and mass, respectively. ω^* and V_R^* are complex quantities defined by

$$\omega^* = \omega + i\gamma \qquad V_R^* = \frac{\omega^* - \Omega_e}{k} \tag{3.34}$$

where γ is the growth rate given by

$$\gamma = \frac{1}{B_w}\frac{dB_w}{dt} \tag{3.35}$$

Assuming $|\gamma| << \omega$, we obtain the real part of the well-known linear dispersion relation from (3.32) and (3.33)

$$c^2k^2 - \frac{\omega\Omega_e^2}{\Omega_e - \omega} = \frac{\pi\Pi^2}{N_b}\int_{-\infty}^{\infty} dv_{\parallel}\int_{-\infty}^{\infty} v_{\perp}^2 dv_{\perp} \cdot \frac{(v_{\parallel} - \frac{\omega}{k})\frac{\partial g_b}{\partial v_{\perp}} - v_{\perp}\frac{\partial g_b}{\partial v_{\parallel}}}{v_{\parallel} - V_R} \tag{3.36}$$

where V_R is the resonance velocity defined by $V_R=(\omega - \Omega_e)/k$. N_b and Π_b are the beam density and the beam plasma frequency, respectively. In the linear stage of the interaction the frequency remains constant because J_B/B_w - constant. In the nonlinear stage, however, (3.36) is no longer valid and we expect a nonlinear frequency change satisfying (3.32).

On the other hand, the imaginary part of the integral in the right-hand side of (3.33) gives

$$\frac{J_E}{B_w} = -\frac{\pi^2 e^2 \Omega_e}{mk^2} \cdot \int_0^{\infty} v_{\perp}^2 \, dv_{\perp} \left(\frac{\partial g_b}{\partial v_{\perp}} + \frac{kv_{\perp}}{\Omega_e}\frac{\partial g_b}{\partial v_{\parallel}} \right)\Bigg|_{v_{\parallel} = V_R} \tag{3.37}$$

while the following relation is obtained from (3.31).

$$\gamma = -\frac{1}{2}\mu_o V_g \frac{J_E}{B_w} \tag{3.38}$$

Substitution of (3.37) into (3.38) gives the linear growth rate

$$\gamma = \frac{\pi^2(\Omega_e - \omega)^2}{kN_C}\int_0^{\infty} v_{\perp}^2 \, dv_{\perp} \left(\frac{\partial g_b}{\partial v_{\perp}} + \frac{kv_{\perp}}{\Omega_e}\frac{\partial g_b}{\partial v_{\parallel}} \right)\Bigg|_{v_{\parallel} = V_R} \tag{3.39}$$

Therefore, the equation (3.31) governing the evolution of the wave amplitude gives the growth rate described by the linear theory.

3.3.2 Equations of Motion of Resonant Electrons

We have presented the wave equations showing how the wave is modified by the resonant current J_R, which is formed as a result of cyclotron resonance between hot electrons and the wave. The equations of motion of resonant electrons are expressed in the following form. We introduce polar

coordinates $(v_\parallel, v_\perp, \phi)$ for the velocity, where $v_\parallel$ and $v_\perp$ are the parallel and perpendicular velocities to the external geomagnetic field respectively, and ϕ is the Larmor phase angle of $v_\perp$ in the rest frame. Equations of motion are then expressed as [e.g., Dysthe, 1971]

$$\frac{dv_\parallel}{dt} = \Omega_w v_\perp \sin(\phi - \psi) - \frac{v_\perp^2}{2\Omega_e}\frac{\partial \Omega_e}{\partial z} \tag{3.40}$$

$$\frac{dv_\perp}{dt} = \Omega_w\left(\frac{\omega}{k} - v_\parallel\right)\sin(\phi - \psi) + \frac{v_\parallel v_\perp}{2\Omega_e}\frac{\partial \Omega_e}{\partial z} \tag{3.41}$$

$$\frac{d\phi}{dt} = \frac{\Omega_w}{v_\perp}\left(\frac{\omega}{k} - v_\parallel\right)\cos(\phi - \psi) + \Omega_e \tag{3.42}$$

$$\frac{dz}{dt} = v_\parallel \tag{3.43}$$

where the wave amplitude B_w is replaced by $\Omega_w = eB_w/m$. The first terms in the right-hand side of (3.40)-(3.42) correspond to the effect of the wave, while the second terms express the effect of the external geomagnetic field. The effect of the inhomogeneity of the medium is expressed by the second terms in (3.40) and (3.41), which disappear in a homogeneous case, as well as by k and Ω_e in (3.40)-(3.42), which vary slowly with the distance in the present model.

These equations are used to calculate the motion of resonant electrons. However, these are not in an appropriate form for a theoretical analysis of trajectories of the electrons. We, therefore, introduce new coordinates $(\theta, v_\perp, \zeta)$ for this purpose by defining

$$\theta = k(v_\parallel - V_R) \tag{3.44}$$

$$\zeta = \phi - \psi \tag{3.45}$$

The equations of motion, i.e., (3.40) ~ (3.42) are converted into $(\theta, v_\perp, \zeta)$ coordinates as

$$\frac{d\theta}{dt} = kv_\perp\Omega_w\sin\zeta - \frac{1}{2}\left(-3V_\parallel + \frac{kv_\perp^2}{\Omega_e}\right)\frac{\partial \Omega_e}{\partial z} \tag{3.46}$$

$$\frac{dv_\perp}{dt} = \frac{\Omega_w}{k}\left(\Omega_e - \theta\right)\sin\zeta + \frac{1}{2}\left(V_R + \frac{\theta}{k}\right)\frac{v_\perp}{\Omega_e}\frac{\partial\Omega_e}{\partial z} \tag{3.47}$$

$$\frac{d\zeta}{dt} = \frac{\Omega_w}{kv_\perp}\left(\Omega_e - \theta\right)\cos\zeta + \theta \tag{3.48}$$

where the frequency ω is assumed to be constant to clarify the effect of the inhomogeneity due to the dipole geomagnetic field. In view of the magnetospheric condition as $\Omega_e \sim kv_\perp \sim \omega \sim (\Omega_e - \omega) \gg \omega_t \gg \Omega_e$, the equations shown above are well approximated by

$$\frac{d\zeta}{dt} = \theta \tag{3.49}$$

$$\frac{d\theta}{dt} = \omega_t^2\left(R + \sin\zeta\right) \tag{3.50}$$

$$R = \frac{1}{2\omega_t^2}\left(3V_R - \frac{kv_\perp^2}{\Omega_e}\right)\frac{\partial\Omega_e}{\partial z} \tag{3.51}$$

where $\omega_t = (kv_\perp\Omega_w)^{1/2}$ and the equation for $v_\perp$ is not essential to the resonant interaction because $|\delta_\perp/v_\perp| \ll 1$ while $|\delta\theta/\theta| \sim 1$, where $\delta v_\perp$ and $\delta\theta$ are the increment or decrement due to the interaction of $v_\perp$ and θ, respectively. R is called an inhomogeneity ratio of the medium [Karpman et al., 1974; Vomvoridis and Denavit, 1979]. Resonant electrons for which $|R| < 1$ can be trapped by the wave when their parallel velocities satisfy a condition $|v_\parallel - V_R| < V_t$ where V_t is the trapping velocity defined by $2(v_\perp\Omega_w/k)^{1/2}$.

Let us consider the variation of the kinetic energy $K_i = m(v_{\parallel i}^2 + v_{\perp i}^2)/2$ of the i-th electron in the wave. From (3.40) and (3.42) we have

$$\frac{dK_i}{dt} = mv_{\perp i}\omega\Omega_w k^{-1}\sin\zeta_i \tag{3.52}$$

The energy change depends on ζ_i which is the phase angle between the wave magnetic field and the perpendicular velocity of the resonant electron. Resonant electrons for which $v_\parallel \simeq V_R$ have relatively slow change in their ζ's, and play major roles in the energy exchange with the wave. This fact is consistent with the previous equation (3.31). From (3.12) and (3.52) we

obtain

$$J_E = \frac{ek}{m\omega\Omega_w} \frac{d}{dt} \sum_i K_i \tag{3.53}$$

Therefore, if the summation of kinetic energies K_i's of resonant electrons decreases, J_E becomes negative, which causes wave growth via (3.31).

3.3.3 Interactions in a Homogeneous Medium

Self-consistent simulations are carried out by solving the equations (3.40) - (3.43) of motion of a large number of resonant electrons with a time step much smaller than the trapping period and updating the wave field by using (3.31)-(3.32). Computer time is greatly saved by not solving equations of motion for cold electrons. The wave phase is determined by (3.32) instead of following the motion of cold plasma particles. This method is basically the long-time-scale (LTS) algorithm first formulated by Rathmann et al. [1978]. In their algorithm, however, they follow the time evolution of the wave frequency ω by using the equation

$$\frac{\partial\omega}{\partial t} + V_g \frac{\partial\omega}{\partial z} = -\frac{\mu_0}{2k} V_g \frac{\partial}{\partial t}\left(\frac{kJ_B}{B_w}\right) \tag{3.54}$$

which is obtained by differentiating (3.10) with time t under the assumption that the cold plasma dispersion relation without the beam contribution is valid. We found this equation liable to a numerical instability because of the time differentiation of kJ_B/B_w, which picks up numerical fluctuations of J_B, where J_B is calculated from a limited number of particles and involves statistical errors. Actually, (3.54) is not necessary in the algorithm if the phase relation (3.15) is made use of to follow the time evolution of the wave number k. In our method the frequency ω is determined by (3.32) as a function of k and J_B/B_w after advancing k in time by (3.15). In the method of Rathmann et al., however, the wavenumber k is determined by (3.10) or (3.32) as a function of ω and J_B/B_w after advancing ω in time by (3.54). The numerical stability has been improved greatly by our method. We have examined basic processes of coherent nonlinear wave-particle interaction in the whistler mode by the following two simulation.

To begin with, we adopt a very simple simulation model where the wave and particles interact with each other uniformly in space. In other words, the interaction begins simultaneously at every point in space. The medium

is assumed to be homogeneous and constant in space and time. This corresponds to the conventional theoretical treatment of whistler instabilities [e.g., Kennel and Petschek, 1966]. A periodic boundary condition is used in the present simulation. By a favor of the LTS scheme, the number of grid points in the system is only three, and the number of resonant electrons is only 320. In this model, the total energy, i.e., the sum of the wave and particle energies must be conserved, because the incoming wave/particles into the simulation region are the same as the outgoing ones. The wave energy density W_w and the particle energy density W_b are calculated as follows.

$$W_w = \frac{1}{2}\varepsilon_o E_w^2 + \frac{1}{2\mu_o} B_w^2 + \frac{1}{2} N_c m V_w^2 \cong \frac{1}{2\mu_o} B_w^2 \frac{1}{\Omega_e - \omega} \tag{3.55}$$

$$W_b = \frac{1}{2} N_b m \langle v_\parallel^2 + v_\perp^2 \rangle \tag{3.56}$$

where N_c and N_b are the cold plasma and beam densities, respectively, and V_w is a velocity of the cold plasma given by $V_w = -J_c/(eN_c)$. In Figure 3.22 the variations of W_w and W_b as well as the total energy density are shown. We see a good energy conservation, because the change in the total energy caused by numerical errors is very small in comparison with the amount of the exchanged energy between the wave and the electron beam.

Before going into the detailed discussion of the simulation result, we examine a physical meaning of the effects of resonant currents expressed in (3.31) and (3.32). For simplicity, we assume the uniform interaction in a homogeneous medium where spatial variation of the wave amplitude is neglected. From Maxwell's equations we obtain the energy conservation law,

$$\frac{\partial W_w}{\partial t} + \vec{J}_R \cdot \vec{E}_w = 0 \tag{3.57}$$

In the case where $\vec{J}_R$ is antiparallel to $\vec{E}_w$ (i.e. $J_E<0$ and $J_B=0$), we have $\partial W_w/\partial t > 0$. Therefore, the wave energy increases when $J_E < 0$, which is consistent with the wave equation (3.31). In the case where $\vec{J}_R$ is parallel to $\vec{E}_w$ (i.e. $J_E>0$ and $J_B=0$), the same discussion leads to the fact the wave energy decreases when $J_E > 0$. In this connection, examination of the configuration of the wave vectors involved in the present analysis would be fruitful. From (2.60) and (3.55) we could show that

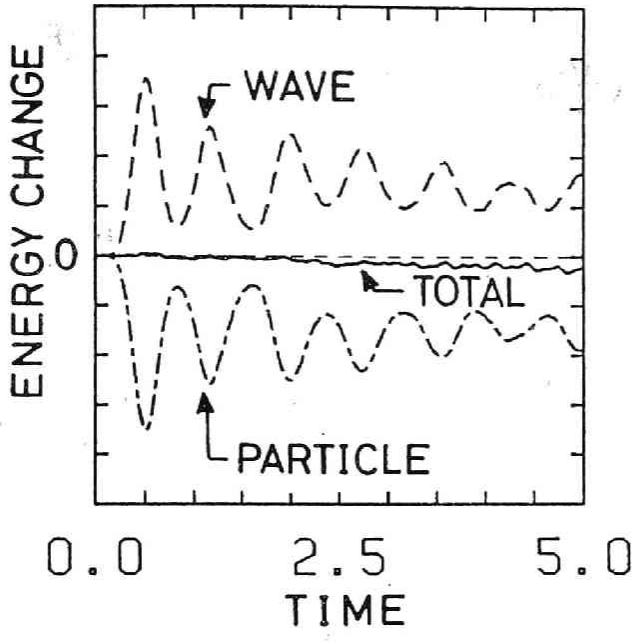

Fig. 3.22 Variation of the wave and particle energies and the total energy in the simulation of the uniform periodic interaction in a homogeneous medium. $\Pi_e/\Omega_e = 10$, $N_b/N_c = 8 \times 10^{-7}$.

$$\vec{E} \cdot \vec{J}_c = \frac{\partial}{\partial t} \left(\frac{1}{2} m N_c V_w^2 \right) = \frac{\omega}{\Omega_e} \frac{\partial W_w}{\partial t} \tag{3.58}$$

Substitution of (3.58) into (3.57) gives

$$\left(\frac{\Omega_e}{\omega} \vec{J}_c + \vec{J}_R \right) \cdot \vec{E}_w = 0 \tag{3.59}$$

while Maxwell's equations (3.2) require that the total transverse current must be parallel to the wave magnetic field B_w, i.e.

$$\left(\vec{J}_c + \vec{J}_R \right) // \vec{B}_w \tag{3.60}$$

In the case where $\vec{J}_R$ is antiparallel to $\vec{E}_w$, the wave vectors take the configuration depicted in Figure 3.23 as a requirement of (3.59) and (3.). The phase angle between $\vec{B}_w$ and $\vec{E}_w$ deviates from the right angle by $\delta\theta$.

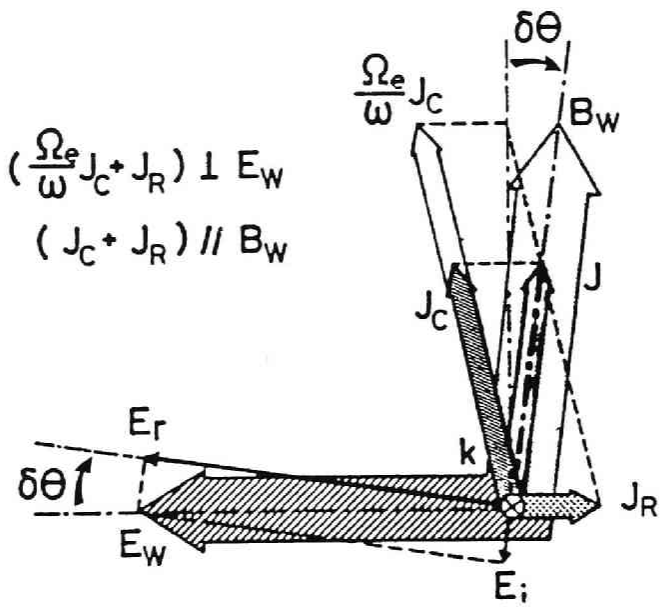

Fig. 3.23 Relation between the wave vectors and the current vectors in the case of wave growth due to the uniform periodic interaction.

which is given by

$$\delta\theta = \tan^{-1}\left(\frac{\omega - \Omega_e}{\Omega_e} \frac{J_E}{J_C} \right) \tag{3.61}$$

On the other hand, Maxwell's equations (3.2) yield

$$\dot{E}_w = -\left(i \frac{\omega}{k} + \frac{\gamma}{k} \right) \dot{B}_w \tag{3.62}$$

which indicates that the electric field $\vec{E}_w$ has a parallel component $\dot{E}_i = -(\gamma/k)\dot{B}_w$ to $\vec{B}_w$ as well as a perpendicular component $\dot{E}_r = -i(\omega/k)\dot{B}_w$ when the wave grows or attenuates. The deviation angle is also calculable from (3.62) as

$$\delta\theta = \tan^{-1}\left(\frac{\gamma}{\omega} \right) \tag{3.63}$$

Equating (3.61) with (3.63), we have

$$\frac{\gamma}{\omega} = \left(\frac{\omega}{\Omega_e} - 1 \right) \frac{J_E}{J_C} \tag{3.64}$$

Assuming $|\gamma| << \omega$, we obtain from (3.2) and (3.3)

$$J_C = \frac{\omega \varepsilon_o \Pi_e^2}{k (\Omega_e - \omega)} B_w \tag{3.65}$$

Combining (3.64) and (3.65), we have the same growth rate expression as (3.38)

$$\gamma = -\frac{1}{2} \mu_o \frac{\partial \omega}{\partial k} \frac{J_E}{B_w}$$

The above discussion shows that the wave equation (3.31) or (3.38) is also derived by analyzing the vector relation in the case where the resonant current $\vec{J}_R$ is parallel or antiparallel to $\vec{E}_w$. However, it should be noted that the deviation angle $\delta\theta$ is generally very small when $|\gamma| << \omega$, as understood from (3.63), and that the effect of $\delta\theta$ that should be involved in the calculation of the resonant current J_E and J_B is neglegible.

In the case where J_R is parallel to the wave magnetic field, we have $\vec{J}_c \cdot \vec{E}_w = 0$, and the wave energy does not change but the frequency changes as indicated by (3.32). It should be noted that ω is a function of J_B/B_w. Therefore, if the wave amplitude becomes small in the presence of J_B, a large frequency change is expected. It is noted that a derivative of ω with respect to J_B/B_w has a negative sign, i.e.,

$$\frac{\partial \omega}{\partial (J_B/B_w)} < 0 \tag{3.67}$$

The variations of the wave amplitude and frequency corresponding to the result in Figure 3.22 are shown in Figure 3.24. Initially, the wave exists all over the simulation region as well as the beam whose initial velocity distribution has the following form

$$f(v_\parallel, v_\perp) = A \exp \left\{ -\left(\frac{v_\parallel - V_{\parallel o}}{V_T} \right)^2 \right\} \delta(v_\perp - V_{\perp o}) \tag{3.68}$$

and is uniform in phase ϕ. $V_{\parallel o}$ and V_T are chosen as $V_{\parallel o} = V_R$ and $V_T = 0.5V_t$ so that most of the electrons are trapped and V_{To} as $V_{To} = -V_R$ so that pitch angles of the electrons are about 45^0. This distribution is far

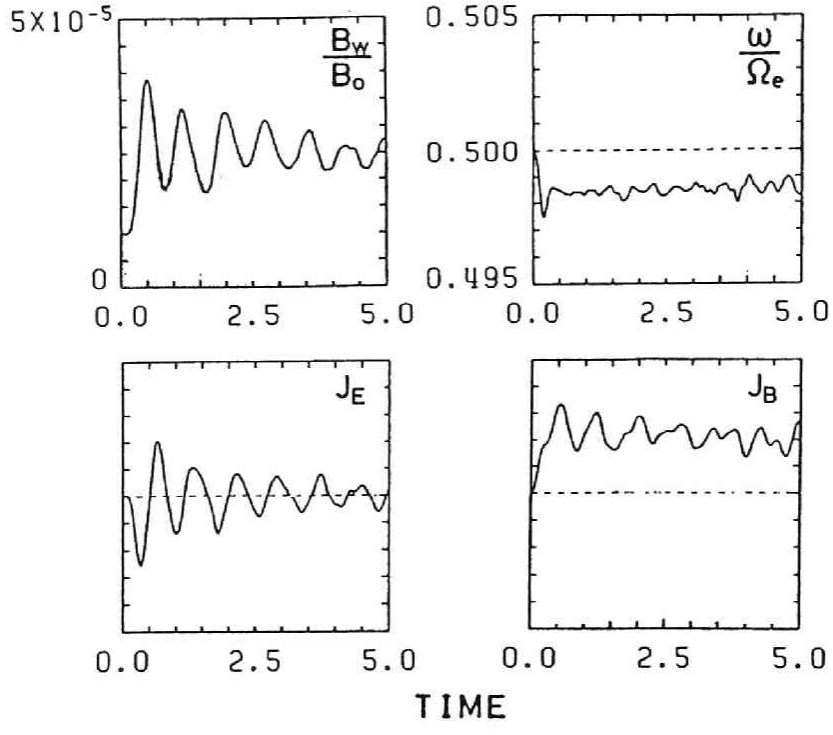

Fig. 3.24 Variation of the wave amplitude and frequency and the resonant current J_E and J_B corresponding to the simulation result shown in Figure 3.22.

from the realistic plasma condition in the magnetosphere but is very effective in showing characteristic features of trapped electrons in a coherent wave-particle interaction within a limited computer time.

The location of the resonant electrons in $v_{\parallel}$ - ζ space and its time evolution are shown in Figure 3.25. At the initial stage of the interaction the hot electrons rotate symmetrically around the point of (ζ, $v_{\parallel}$) = (180^0,V_R) in the $v_{\parallel}$ - ζ space. As understood from (3.12), the J_B increases rapidly, while the increase of J_E is relatively small because of the initial symmetry around (ζ, $v_{\parallel}$)=($180^`$,V_R). Therefore, in a quarter of the trap ping period, the amplitude B_w remains almost constant, while the frequency decreases because of the increase of J_B/B_w. The frequency change $d\omega$ leads to the shift of the resonance velocity through $dV_R = d\omega/k$ and hence the distribution of the resonant electrons in the $v_{\parallel}$ - ζ plane loses the symmetry around the point (ζ, $v_{\parallel}$) = (180^0,V_R), giving rise to J_E which causes a growth and subsequent oscillations of the wave amplitude.

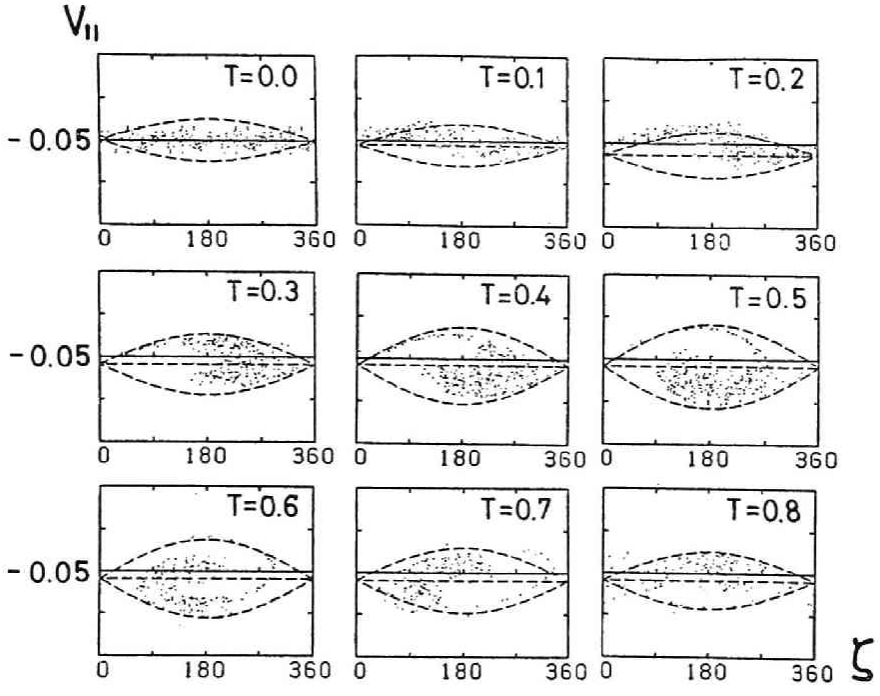

Fig. 3.25 Phase-diagrams of resonant electrons in the $v_{\parallel}$ - ζ space at different times. Eye-shaped dashed lines indicate the separatrices of trapping regions.

The same simulation with an electromagnetic (EM) code in which Maxwell's equations are solved and motion of both cold and hot electrons are solved was reported elsewhere [Matsumoto and Yasuda, 1976; Matusmoto et al., 1980]. Their simulation model and the results are essentially the same as the present ones, though their code and needed CPU time were different. In order to carry out the same simulation by the EM code, it takes about 100 times as much CPU time as the present simulation code. These facts as well as the good energy conservation stated above indicate the validity and effectiveness of the wave equations (3.31) and (3.32) used in the present simulation.

The model of the uniform interaction discussed above is appropriate to investigate the basic mechanisms of the whistler interaction. However, a more realistic model is necessary for modeling an encountering interaction where a whistler wave packet encounters electrons and hence the interaction begins gradually from the front edge of the wave packet. Therefore, the second simulation is carried out with this encounter model. The external magnetic field is again assumed to be homogeneous for simplicity. The

velocity distribution of hot resonant electrons is the same as in the previous simulation of the uniform interaction.

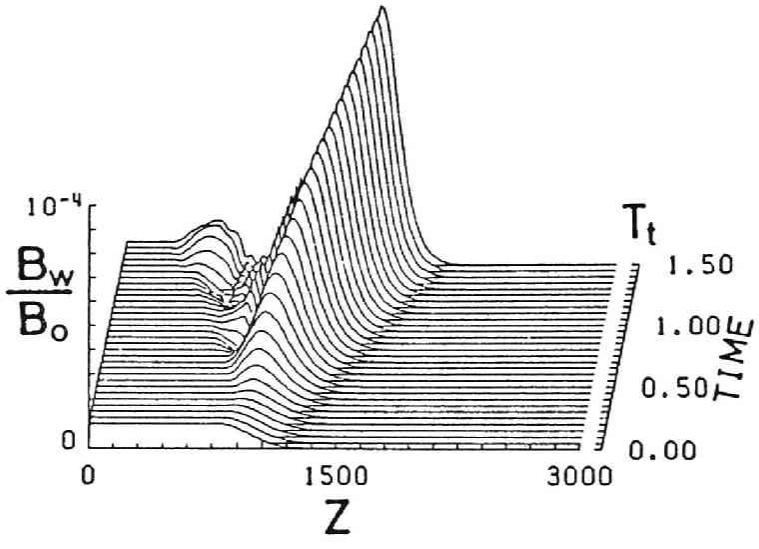

Fig. 3.26 Spatial profile of the wave packet and its time evolution in a homogeneous medium. Hot electrons are initially placed over the region z = 1000 ~ 3000.

The spatial profile of the wave packet and its evolution in time are shown in Figure 3.26. The wave front with Gaussian shape is initially placed at z = 800. It propagates to the positive z direction. The hot electrons are initially placed over the region z=1000 ~ 3000 and move to the negative z direction. Newly coming particles are subsequently injected at the right side edge of the simulation region with a velocity distribution (3.68). As is shown in Figure 3.27, J_B is formed first at the front portion of the whistler wave packet where the electrons begin to interact with the wave, and then J_E is eventually formed by the same V_R-shift mechanism as in the case of the uniform interaction, causing the wave growth at the wave front. The amplified wave front propagates to the right and encounters newly coming electrons, gaining energy from them. Therefore, the wave front continues to grow without saturation, forming a very peaky wave packet. In reality, however, the inhomogeneity of the external magnetic field gives a limitation to the wave growth.

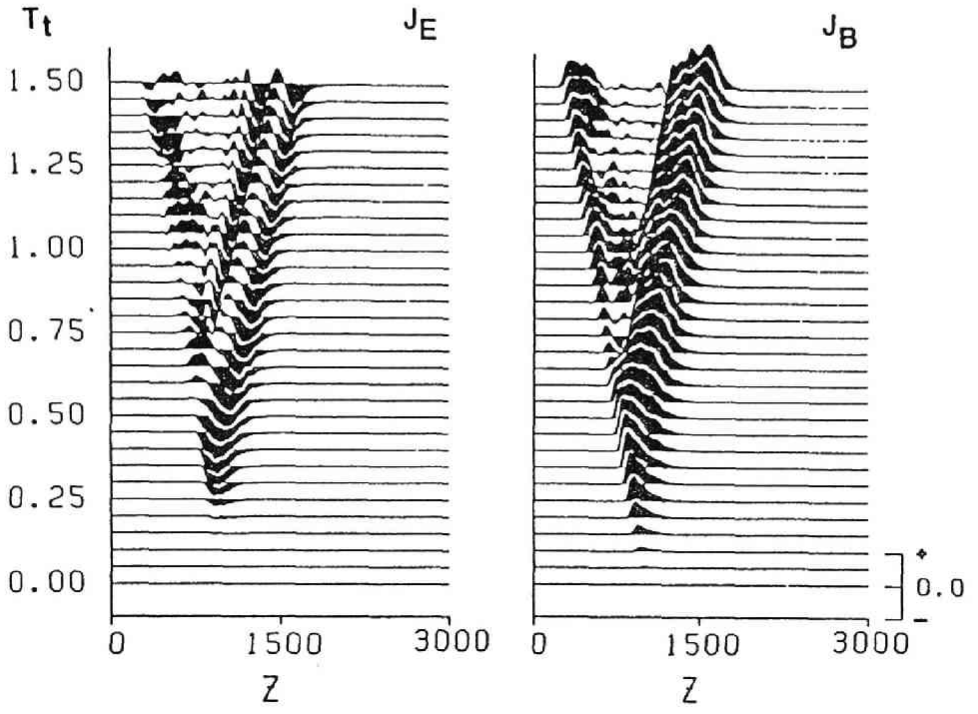

Fig. 3.27 Spatial profiles of the resonant currents J_E and J_B and their time evolution corresponding to the interaction shown in Figure 3.26.

3.3.4 Interactions in an Inhomogeneous Medium

Inhomogeneity of the geomagnetic field modifies trajectories of resonant electrons in the $v_{\parallel}$ - ζ space as shown in Figure 3.13. The shaded area in $v_{\parallel}$ - ζ plane is the trapping region which takes different shapes depending on the inhomogeneity ratio R. It should be noted here that transition from untrapped to trapped electrons never occurs in a monochromatic whistler mode wave with a constant amplitude and a fixed frequency, propagating in a medium of a constant gradient of the external magnetic field, i.e., R = const. in (3.50) What causes the transition is a change of the magnetic field gradient or a variation in the wave amplitude, frequency, or wavenumber. Especially at the wave front where the amplitude changes drastically, a large number of particles are trapped and moves with the local resonance velocity, while untrapped electrons follow the adiabatic motion. However, at any points where the wave already exists, untrapped electrons have little chance to be trapped. Thus in certain

cases, there arises a situation where either trapped or untrapped electrons dominate in the interaction.

As seen in Figure 3.13, the range of phase ζ where trapped particles can occupy at $v_{\parallel} = V_R$ is limited when $0 < |R| < 1$, while they can occupy the whole range of ζ in the equatorial region where R=0. On the other hand, untrapped electrons occupy a limited phase range at $v_{\parallel} = V_R$ and thus phase-bunched at $v_{\parallel} = V_R$. Therefore, untrapped particles can equally cause a resonant current as well as trapped electrons. In the following we discuss the results of computer simulations which show the growth or damping of whistler wave packets by trapped or untrapped electrons, separately.

We use a model of the simulation in which the wave propagating from the southern hemisphere encounters with counter-streaming hot electrons in the vicinity of the equator. This model simulates the Siple active experiment [Helliwell and Katsufrakis, 1974]. The geomagnetic field is assumed to be a dipole field, and the interaction region is assumed to be along the geomagnetic field line of L = 4. The initial amplitude and frequency of the wave are $10^{-5} \sim 10^{-4} B_{oEQ}$ and $0.5\Omega_{eEQ}$, where B_{oEQ} and Ω_{eEQ} are the geomagnetic field and the electron cyclotron frequency at the equator. The cold plasma density is assumed to be constant and taken as $\Pi_e/\Omega_{eEQ} = 10$.

To begin with, we focus our attention only on the effects of trapped electrons. The average phase of trapped electrons is readily deduced from the simplified equations of motion (3.49) - (3.51). The resonance condition for trapped electrons requires

$$\frac{d\zeta}{dt} \simeq 0 \quad , \quad \frac{d\theta}{dt} \simeq 0 \tag{3.69}$$

which give

$$v_{\parallel} \simeq V_R \quad , \quad \zeta = -\sin^{-1} R \tag{3.70}$$

In a case where electrons move away from the equator, R becomes positive. Therefore, the center phase around which trapped electrons oscillate shifts toward 2π from π and falls in the range $\pi < \zeta < 2\pi$, and hence the phase of the resonant current J_R is in the range of $0 < \Psi_R < \pi$. Consequently, we have a negative J_E which causes a growth of the wave amplitude according to (3.31).

The middle panel in Figure 3.28 shows the spatial profile of the wave amplitude and its time evolution. The wave is uniformly distributed all

over the simulation region and propagates to the right. Electrons are continuously injected from the right boundary, which corresponds to the equator, with a velocity distribution given by (3.68) where $V_{\parallel 0}/c \sim -0.05$, $V_T = 0.5V_t$, and $V_{\perp 0}/c = 0.05$ (c: light speed). $V_{\parallel 0}$ is chosen to be equal to the local resonance velocity, so that these electrons are trapped. Trajectories of selected four electrons injected at t = 0 are shown in the upper panel. All of four electrons are clearly trapped and oscillate around $v_\parallel = V_R$. The phase diagram of electrons located at z = -1100 ~ -900 at $t = 2.3T_t$ is shown in the lower panel where T_t is a trapping time computed by the initial wave amplitude. A clear separation of trapped from untrapped electrons is seen. Most of the trapped electrons fall in the phase range $\pi < \zeta < 2\pi$, giving rise to a negative J_E, which causes the wave growth.

On the other hand, if trapped electrons move toward the equator, most electrons fall in the phase range $0 < \zeta < \pi$, and hence a positive J_E is formed to cause damping of the wave. The evolution of the wave amplitude, selected trajectories of electrons and their phase diagram are shown in Figure 3.29. Electrons are injected from the right boundary so that a velocity distribution given by (3.68) are realized at the equator if they follow adiabatic motions. $V_{\parallel 0}$ and V_T are chosen so that most of electrons are trapped at the right boundary.

The effects of untrapped electrons are examined by the following two simulations. Each untrapped electron does not remain in resonance for a long period, and the interaction is localized at the resonance point where a parallel velocity of the electron satisfies $v_\parallel \simeq V_R$. However, as understood from (3.49), the rate of phase change is relatively slow at $v_\parallel \simeq V_R$ and the untrapped electrons should pass a limited range of ζ outside the trapping region. Thus untrapped electrons also show phase-bunching. This effect was called channel effect phase bunching [Matsumoto and Omura, 1981].

In the case where electrons are approaching the equator, most untrapped electrons fall in a phase range of $\pi < \zeta < 2\pi$ at the resonance velocity, because of the presence of the forbidden region (trapping region) over the phase between 0 and π. The lower panel in Figure 3.30 shows the phase bunching of untrapped resonant electrons, and a negative J_E is formed at the resonance point where a wave growth is observed. Electrons are injected in the same manner as in the previous two simulations. However, $V_{\parallel 0}$ chosen so that electrons resonate with the wave not at the right boundary but at the middle of the simulation region where $0 < |R| < 1$. The

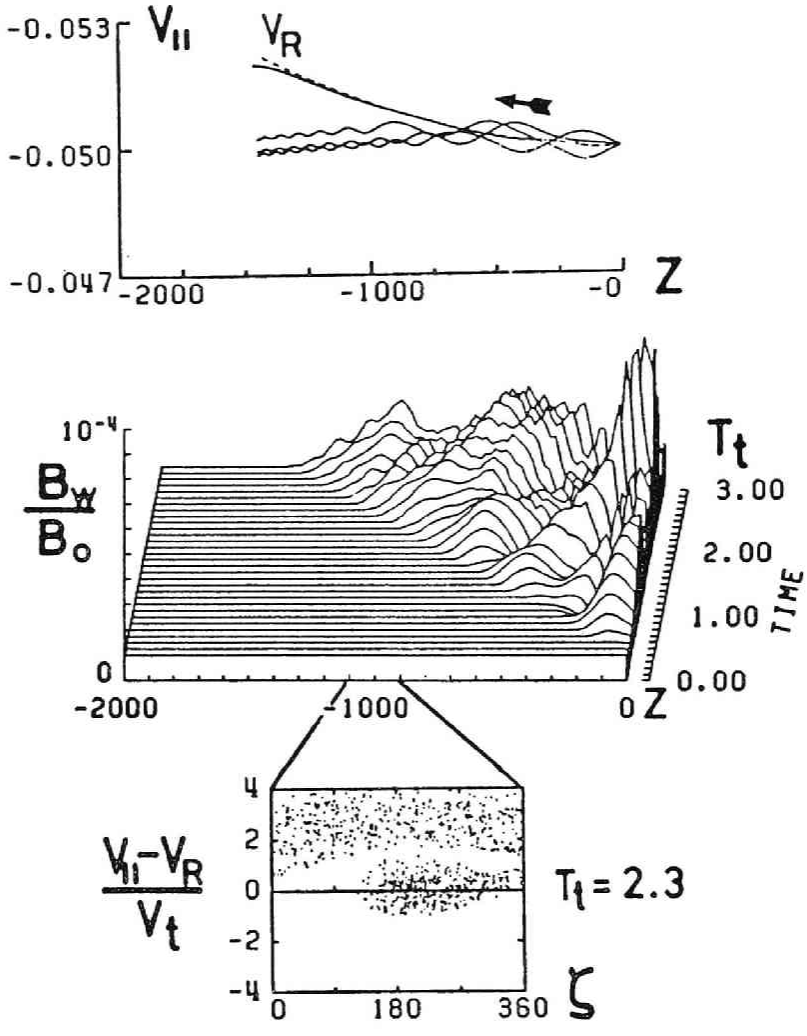

Fig. 3.28 Wave growth due to the interaction with trapped electrons moving away from the equator. (upper panel) Variation along z is represented by $v_{\parallel}$. The dotted line is a variation of resonance velocity V_R. (middle panel) Spatial profiles of wave amplitude at different times. (lower panel) A $v_{\parallel}$ - ζ phase diagram in the range shown by two straight lines. Parameters of hot electrons are $N_b/N_c = 8 \times 10^{-7}$, $V_{\parallel o} = -0.05$, $V_T = 0.5V_t$ and $V_{To} = 0.05$. Velocity is normalized to light speed c and distance is in the unit of kilometer. This is the same in the following figures.

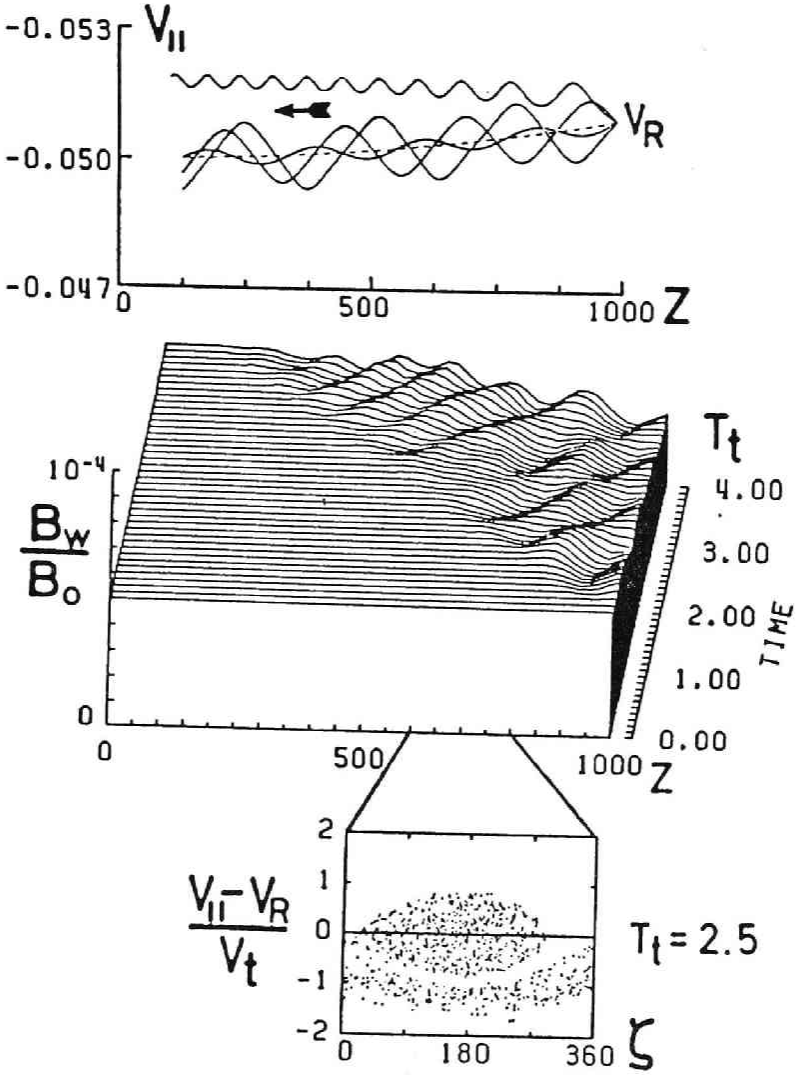

Fig. 3.29 Wave damping due to the interaction with trapped electrons moving toward the equator (the same as in Figure 3.29 except that $V_{||o} = -0.0512$.)

time evolution of the wave amplitude and trajectories of selected electrons injected at t = 0 are also shown in Figure 3.30. As can be clearly seen, the resonance point is situated at $z \simeq 1000$ where a strong wave growth occurs, and the amplified wave at the resonance point propagates to the right with an almost constant amplitude.

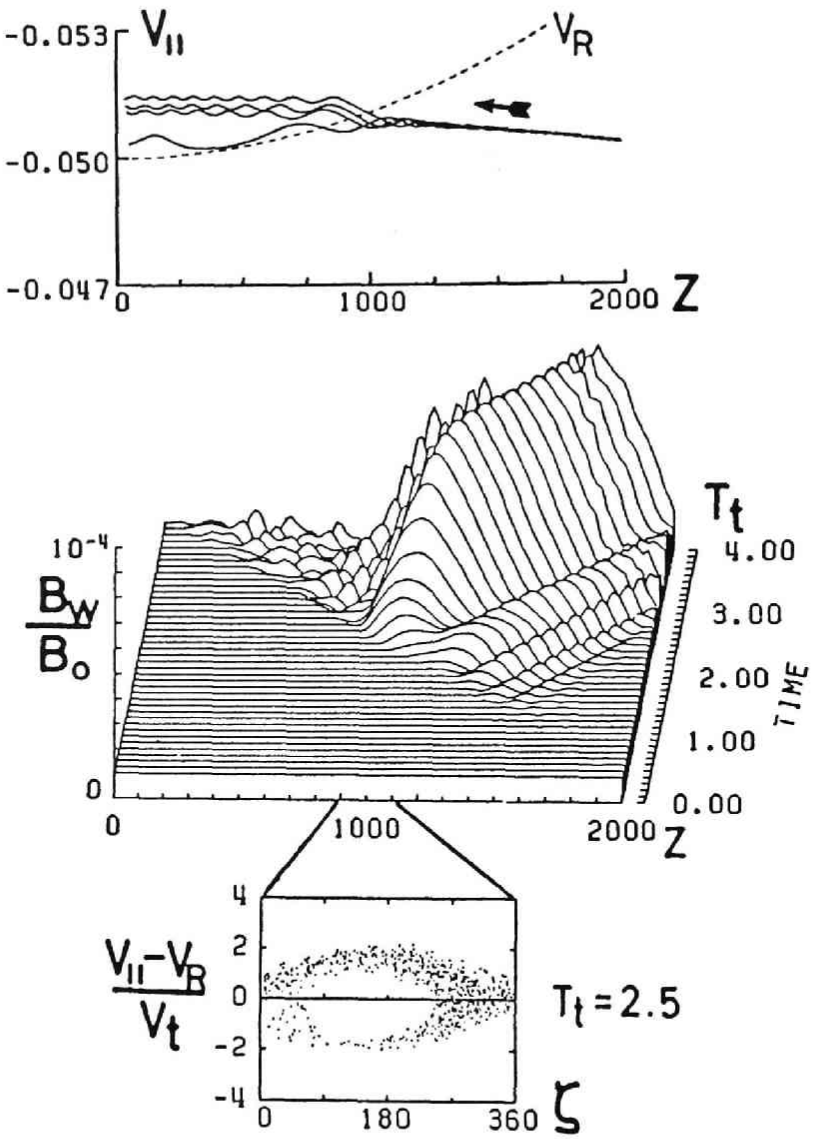

Fig. 3.30 Wave growth due to the interaction with untrapped electrons moving toward the equator (the same as in Figure 3.29 except that $V_{IIO} = -0.0510$.)

In the case where untrapped electrons move away from the equator, their phase bunching at the resonance velocity takes place around $\zeta = 0.5\pi$. The lower panel in Figure 3.31 shows the phase diagram of electrons located at $z = -1500 \simeq -1300$ at $t = 4.2Tt$. The phase bunching causes a positive J_E that causes wave damping as shown in the middle panel. As seen

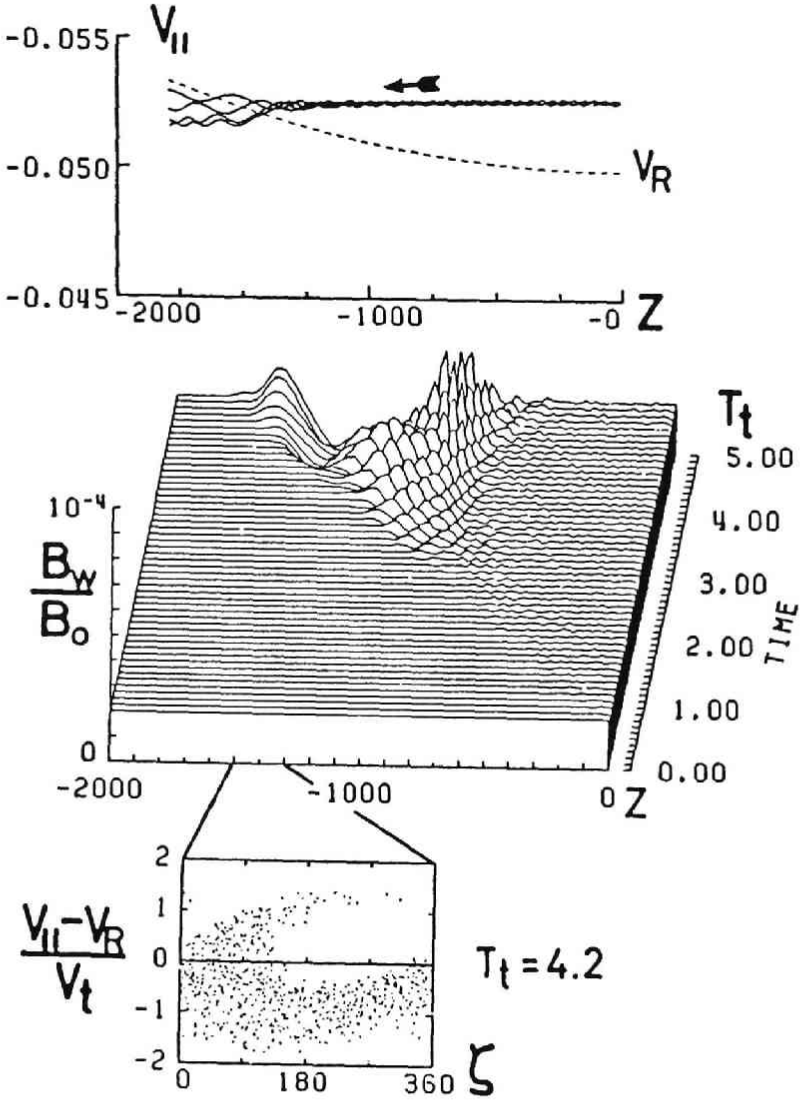

Fig. 3.31 Wave damping due to the interaction with untrapped electrons moving away from the equator (the same as in Figure 3.29 except that $V_{||O} = -0.0527$.)

in the upper panel, the resonance point is situated at $z \simeq -1400$. After the wave is damped at the resonance point, the wave begins to grow at the left side of the resonance point. This is because some of the untrapped resonant electrons are trapped owing to the sudden change in wave amplitude. These trapped electrons cause wave growth as discussed

previously. The ripples of the wave amplitude on the right side of the resonance point is caused by the untrapped electrons approaching the resonance velocity, because those electrons are phase-bunched owing to the cluster effect [Matsumoto and Omura, 1981].

3.3.5 Discussion and Conclusion

Formation of resonant current by trapped particles has been discussed by many authors (e.g., Dysthe [1971] for a homogeneous magnetic field and Nunn [1974] for a inhomogeneous field; see a review by Matsumoto [1979]). Resonant current due to untrapped particles has also been reported by Matsumoto and Omura [1981]. We have presented the wave equations that show how these resonant currents modify the wave amplitude and wave frequecncy and discussed the physical meaning of the wave equations in Subsections 3.3.1, 3.3.2 amd 3.3.3. On the basis of the wave equations, we have first done self-consistent computer simulations by which we confirm detailed nonlinear processes of the wave growth in a homogeneous case. Taking into account the inhomogeneity effect of the dipole geomagnetic field, we then clarified the effects of trapped and untrapped resonant electrons on the wave amplitude. The roles of trapped and untrapped electrons are different and exchange their roles depending on the sign of the geomagnetic gradient. In the hemisphere where the whistler wave propagates toward the equator, trapped electrons cause wave growth, while untrapped resonant electrons cause wave damping. In the opposite hemisphere, these roles are exchanged. The simulation results shown in Subsection 3.3.4 demonstrate this difference clearly. Nonlinear frequency shift is also observed in the simulation when and only when the wave amplitude is significantly reduced in the presence of strong resonant currents. It may be necessary to adopt a wider velocity distribution in $v_{\parallel}$ for resonant electrons which is more realistic and enables us to simulate the situation where both trapped and untrapped electrons exist simultaneously. In the present simulations the wave is injected continuously into the simulation region. However, it is necessary to examine the termination effects of a whistler pulse because the Siple experiments show that many of artificially triggered emissions are preferentially triggered at the termination of triggering waves. Computer simulations including these effects will be reported in our subsequent paper.

3.4 Frequency Variations of Whistler Emissions in a Homogeneous Field

In this section we present a computer simulation of coherent whistler wave-particle interaction in which a whistler wave pulse propagating along an external magnetic field interacts with counter-streaming high energy electrons. Several simulations similar to this model were performed by several authors. [Denavit and Sudan, 1975; Vomvoridis, 1978; Omura and Matsumoto, 1982; Hashimoto et al., 1984]. Among these simulation studies, only Denavit and Sudan[1975] report formation of new emissions with rapid frequency variations in their homogeneous model. However, the parameters they assumed are unrealistic and quite different from those in the magnetospheric conditions. Assuming the magnetospheric parameters, we also found a generation of a new wave packet, i.e., a triggered emission in our homogeneous model but the emission shows a relatively small frequency variations, i.e., about 5% of the triggering wave frequency. We interpret the observed emission is the indication of the initial phase of VLF triggered emissions. Vomvoridis[1978] studied the emissions in a nonuniform magnetic field, and he found only small frequency shifts could happen in his model. We show that a rising tone is caused by detrapping of phase bunched electrons and that small frequency shifts are possible even in a uniform magnetic field. Following the introduction, the simulation model is described in Subsection 3.4.1. The results of the simulations and their interpretation are presented in Subsection 3.4.2. Subsection 3.4.3 gives a summary and discussion.

3.4.1 Simulation Model

We assume a purely transverse whistler mode wave that propagates along the geomagnetic field line and that interacts with counter-streaming high energy electrons. The evolution of the wave amplitude and frequency are followed by the LTS code described in Section 2.4. The simulation parameters are chosen as follows, reflecting a magnetospheric condition at the equatorial region of L = 4.

- Electron cyclotron frequency : 14 kHz
- Electron plasma frequency : 140 kHz
- Amplitude of the whistler pulse : 5 pT
- Frequency of the whistler pulse : 7 kHz
- Length of the whistler pulse : 700 km
- Group velocity of the whistler pulse : 15000 km/sec

- Drift velocity of energetic electrons : -15000 km/sec
- Parallel temperature of energetic electrons : 57 eV
- Perpendicular temperature of energetic electrons : 7.4 keV
- Density ratio of energetic and cold electrons : 8×10^{-7}

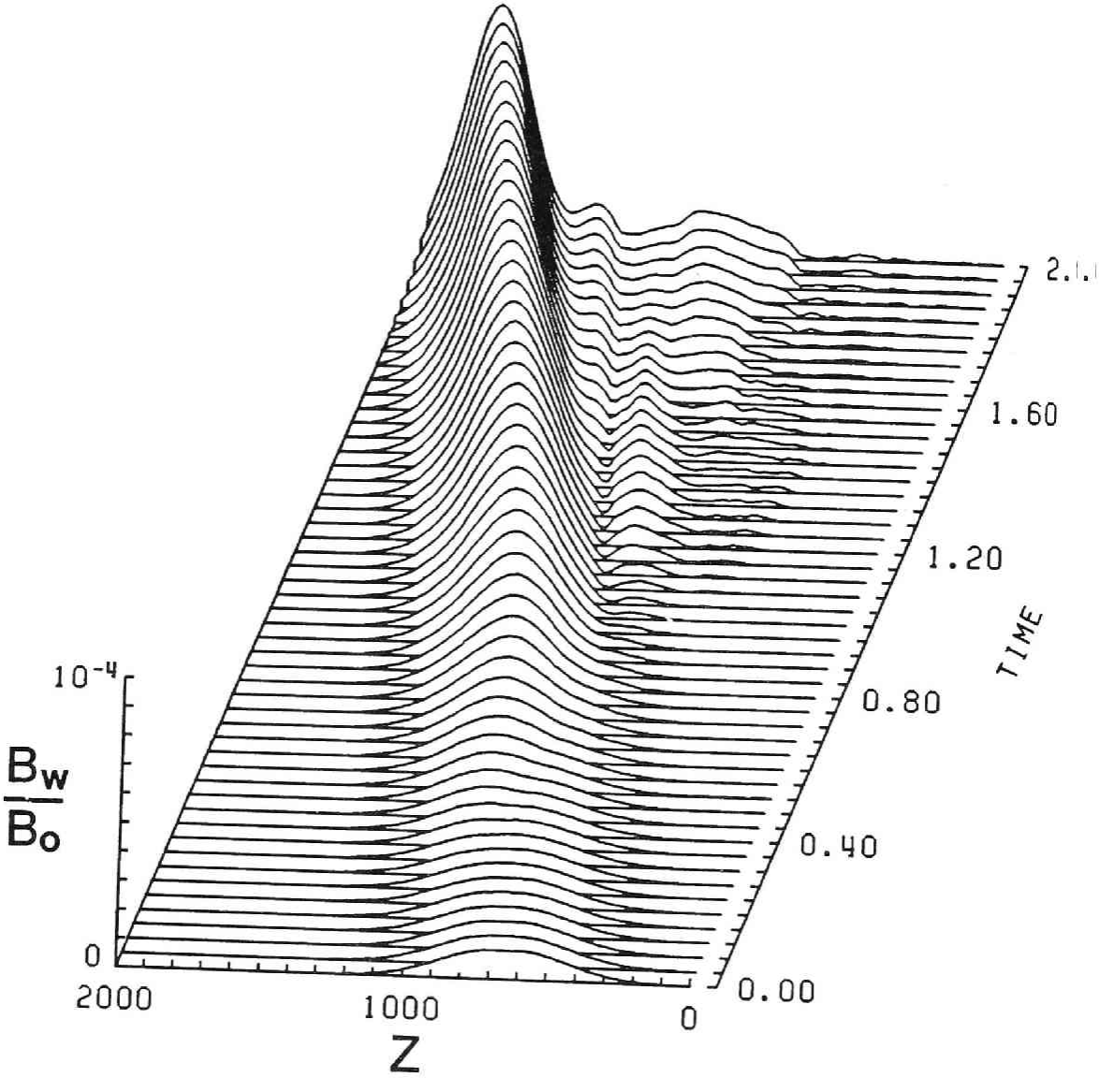

Fig. 3.32 Spatial profile of wave amplitude and its time evolution.

The cold electrons are not treated as particles but as a fluid which

gives the plasma dispersion assumed in Eqs. (3.1) and (3.3). A finite length of a whistler wave packet is initially placed in the simulation region as seen in Figure 3.32 where the spatial profile of the wave packet and its time evolution are plotted. The wave front with Gaussian shape is initially placed at Z = 1000km. It propagates toward the positive z direction. The amplitude of the wave B_w is $10^{-5}B_0$ where B_0 is the external magnetic field. The simulation region consists of 101 grid points with a spacing of 20km. The energetic electrons are initially placed in the region $z \geqslant 1000$km and move toward the negative z direction. Newly coming particles are subsequently injected at the left side boundary of the simulation region. In each cell 400 particles are placed on the average to represent a velocity distribution of energetic electrons which is a shifted Maxwellian distribution in $v_\parallel$ and a subtracted Maxwellian realizing a loss cone distribution in $v_\perp$[Kennel and Abdalla, 1978]

$$f(v_\parallel, v_\perp) = A \exp\left\{ - \left(\frac{v_\parallel - V_{\parallel 0}}{V_{\parallel T}} \right)^2 \right\} g(v_\perp) \tag{3.71}$$

$$g(v_\perp) = \frac{1}{1 - \beta} \left\{ \exp\left(- \frac{v_\perp^2}{V_{\perp T}^2} \right) - \exp\left(- \frac{v_\perp^2}{\beta V_{\perp T}^2} \right) \right\} \tag{3.72}$$

where $V_{\parallel 0}$ and V_T are chosen as $V_{\parallel 0} = V_R = 0.05c$ and V_R is the resonance velocity $(\omega - \Omega_e)/k$. $V_{\parallel T} = 0.5V_t = 2.2\times10^{-4}c$, where V_t is a trapping velocity $2(v_{\perp 0}\Omega_w/k)^{1/2}$ in which $\Omega_w = eB_w/m$, and e and m are electronic charge and mass, respectively. $V_{\perp T}$ and β are chosen as $V_{\perp T} = 0.029c$ and $\beta = 0.5$ so that the average perpendicular velocity $v_{\perp 0}$ is 0.05c, and that the average pitch angle of the electrons is 45^0.

3.4.2 Simulation Results and Their Interpretation

The spatial profiles of the wave amplitude and its time evolution are shown in Figure 3.32. The time is normalized by the trapping period $T_t = 2\pi/(kv_{\perp 0}\Omega_w)^{1/2}$ calculated from the initial parameters. Under the present parameter, T_t corresponds to 447 electron cyclotron periods (~ 32 msec). The front portion of the pulse continuously grows receiving free energy from newly coming electrons through cyclotron resonance. We find the emission at the rear end of the triggering pulse. This triggered pulse is emitted from the resonant current formed by resonant electrons which have been trapped and phase bunched by the triggering pulse.

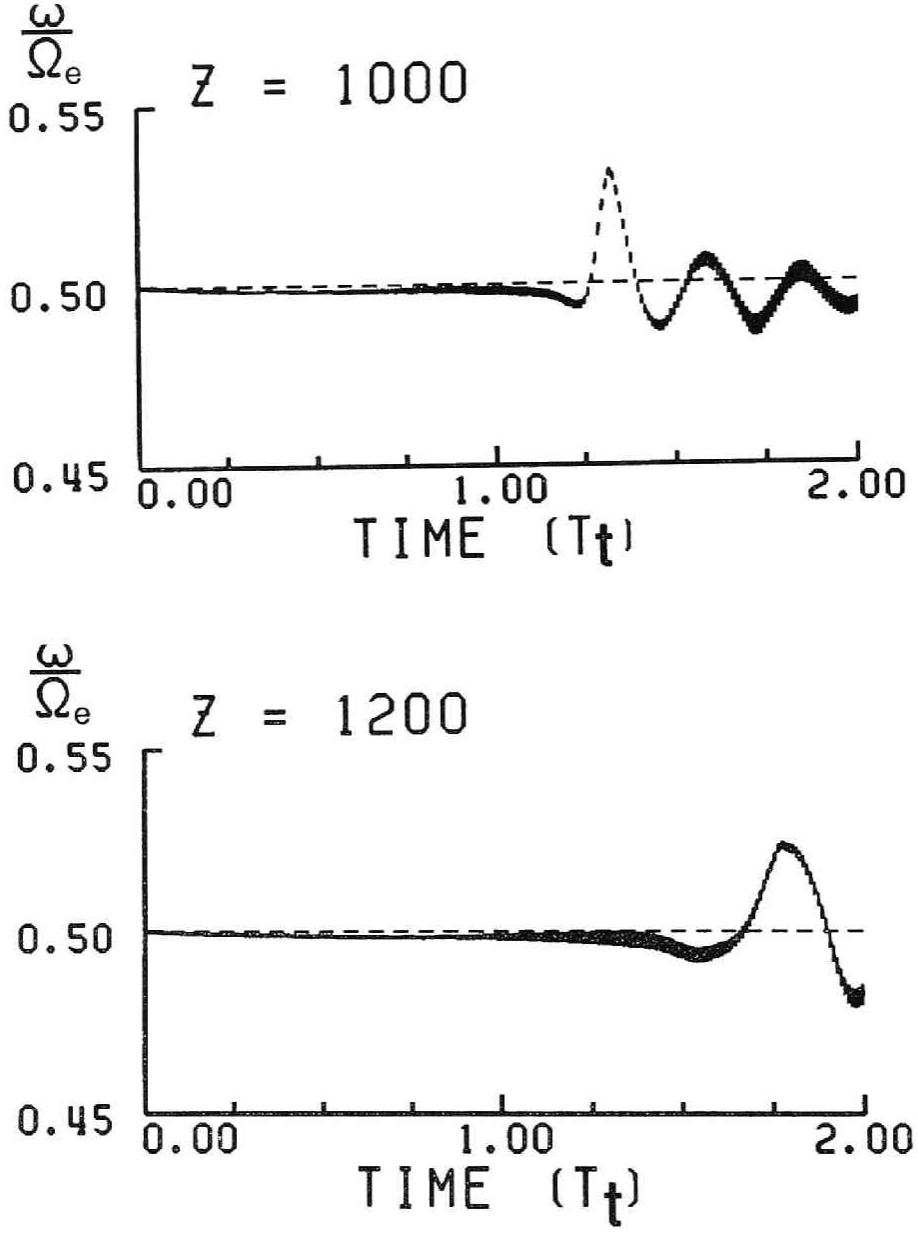

Fig. 3.33 Dynamic frequency spectra observed at z = 1000 and 1200 km.

The dynamic frequency spectra observed at z = 1000km and at z = 1200km are shown in Figure 3.33. The amplitude of the wave is indicated by the width of the frequency spectra. The frequency of the triggering pulse shows a slight decrease first. When the amplitude decreases at the end of the triggering pulse, the frequency shows a small falling tone and turns to

a rising tone followed by frequency oscillations. The portion which shows rising tone and subsequent oscillations corresponds to a triggered emission.

As expressed in Eq. (2.73), the frequency is controlled by the resonant current J_B and B_w through a factor of J_B/B_w, while the amplitude B_w is modified by J_E as expressed in Eq. (2.71). The resonant currents are formed through the process of trapping, phase bunching and detrapping of resonant electrons. In order to analyze the process in detail, we plotted the local amplitude of the wave and the phase diagram of resonant electrons in the $v_{\parallel}$-ζ phase space at different times. Figure 3.34 shows the phase diagram of resonant electrons in the range of z = 1050 ~ 1150km. The effect of the wave is indicated by the separatrix of the trapping region whose range of $v_{\parallel}$ is given as

$$V_R - V_t \leqslant v_{\parallel} \leqslant V_R + V_t \quad . \tag{3.73}$$

The vertical movement of the separatrix indicates the change of resonance velocity and correspond to the change of the frequency and wavenumber. The change of the size of the trapping region correspond to the amplitude variation.

Before encountering the wave packet, electrons are distributed uniformly in phase. At t = 0.4 ~ 0.6 the electrons are being engulfed by the front portion of the wave packet. Owing to the cyclotron resonance with the wave, the electrons trapped in the wave potential well begin a spiral motion around the center of the trapping region $(v_{\parallel}, \zeta)=(V_R, 180^0)$. Since the trapped electrons populate around the phase angle 180^0, they form the positive resonant current J_B and cause the frequency decrease, which is recognized from the downward motion of the separatrix in the phase diagram. Although the electrons are initially distributed symmetrically around the center of the trapping region, the symmetry breaks owing to the frequency decrease. This results in the phase bunching in the phase range of $\zeta = 180^0 \sim 360^0$ at T = 0.8 ~ 1.0, which forms a negative J_E causing the wave growth. The wave growth is recognized from the enlargement of the separatrix. The phase bunched electrons still continue to rotate in the potential well and fall in the phase range of $\zeta - 0^0 \sim 180^0$ at T = 1.2, forming the positive J_E. Since the positive J_E causes the wave damping, the trapping region shrinks and the phase bunched electrons are then detrapped from the potential well.

It is noted that the wave damping leads to the frequency decrease in the presence of the positive J_B. Therefore, the detrapping is induced by

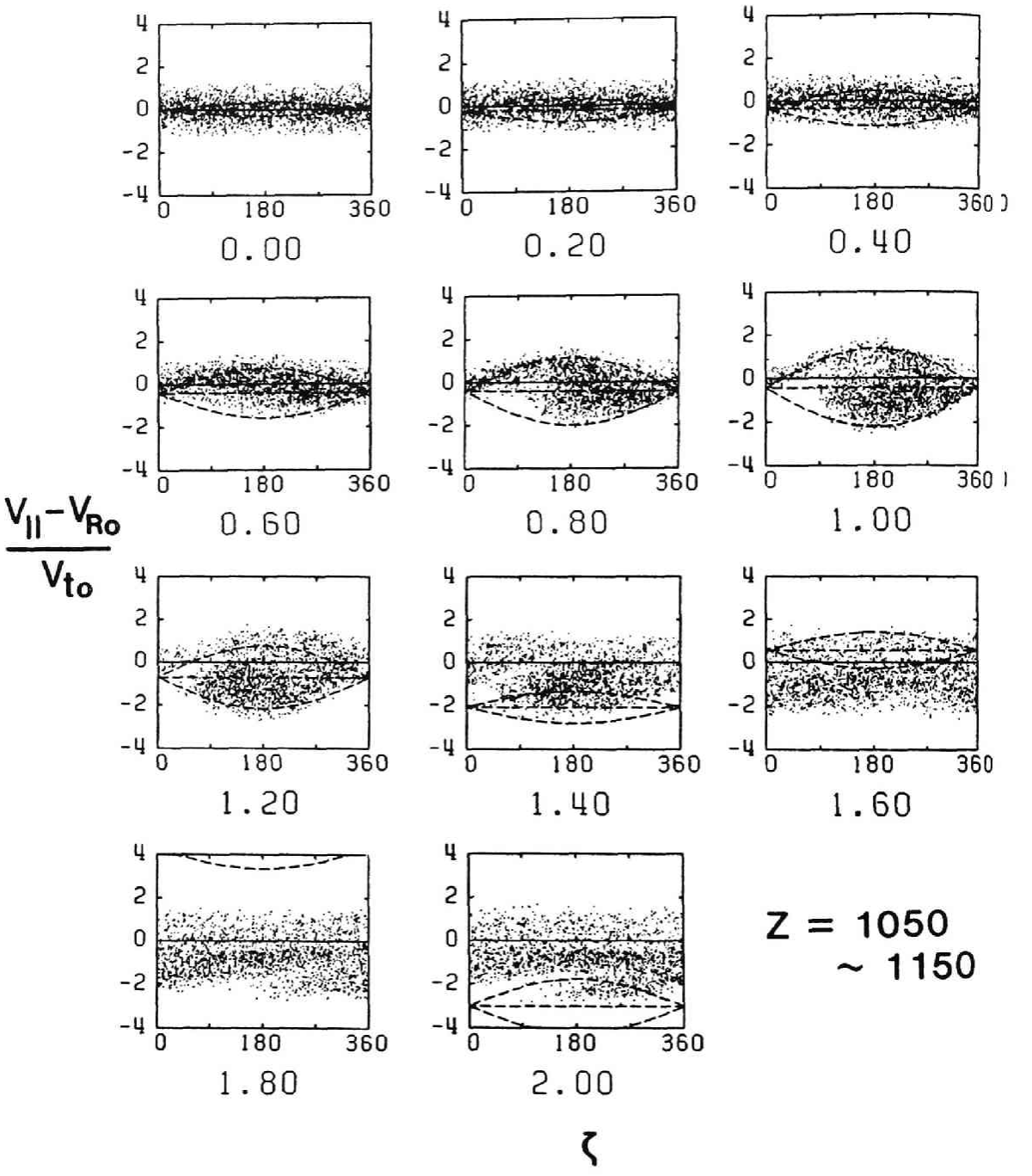

Fig. 3.34 Phase diagrams of resonant electrons in the $v_{||}$ - ζ space at z = 1050 ~ 1150km. Numbers at the vertical axis indicate difference of $v_{||}$ from the initial resonance velocity V_{Ro} normalized by the initial trapping velocity V_{to}. Numbers below the phase diagrams indicate the trapping time. Eye-shaped dashed lines indicate the separatrices of trapping regions.

the frequency decrease as well as the wave damping. At T = 1.4 we can observe the detrapping due to the both effects. Once detrapped from the potential well, the phase bunched electrons change their phase ζ with the rate as

$$\frac{d\zeta}{dt} = k(v_{\parallel} - V_R) \tag{3.74}$$

When the electrons comes to the phase range of $\zeta = -270^0$ to 90^0, they form the positive J_B causing the frequency increase, which corresponds to the rising tone in Figure 3.33. As far as the phase correlation is retained, the detrapped electrons form resonant currents J_E and J_B whose signs change rapidly in time. These resonant currents cause the subsequent oscillations of the frequency and amplitude after the rising tone.

The interpretation stated above is not complete, for we have to consider the propagation effects as well. The changes of the amplitude and frequency observed at z = 1200km are not the simple reflection of the local interaction as stated above, but they include those induced in the upstream region, as is obvious from the comparison between the spectra observed at z = 1000km and z = 1200km. Basically, however, the resonant electrons undergo the above process of trapping, phase bunching and detrapping, causing the frequency decrease, wave growth, wave damping, rising tone and subsequent frequency oscillations.

3.4.3 Summary and Discussion

The computer simulation described in the preceding section showed an evolution of a monochromatic whistler wave pulse encountering counter streaming hot electrons in a homogeneous magnetic field. Our findings in the simulation are the following.

1) The front portion of the triggering pulse grows continuously receiving energy from resonant electrons.
2) The frequency of the triggering pulse decreases slightly due to the formation of a positive resonant current J_B. The decrease further lead to a small falling tone with a diminishing amplitude at the end of the triggering pulse.
3) Following the triggering pulse, an emission is generated by hot electrons which have been phase bunched by the triggering pulse.
4) The diminishing wave amplitude with the falling tone causes a detrapping of phase bunched electrons, resulting a rising tone and

subsequent frequency oscillations.

5) The range of the frequency variation is about 5% of the initial wave frequency.

6) The time scale of the frequency variation is a fraction of the trapping period corresponding to ~ 10msec.

The range of frequency variations found in the simulation is smaller, and the time scale of the variations is shorter than a typical triggered emission observed in the magnetosphere. This suggests a limitation of the present simulation model, i.e., the assumption of the homogeneous magnetic field. Since the detrapped electrons remain at a constant parallel velocity in the homogeneous magnetic field, the resonance condition $\omega = kv_{\parallel} + \Omega_e$ remains constant. The frequency can be changed only by as resonant current J_B. Especially for a rising tone J_B must be negative, which is impossible if the resonant electrons are stably trapped in a wave potential well. Therefore, detrapping of phase-bunched electrons are necessary for a rising tone [Roux and Pellat, 1978; Matsumoto and Omura, 1983]. In the inhomogeneous geomagnetic field the rising tone could continue for a longer period, because the phase-bunched electrons, if detrapped at the equator, increase their parallel velocities $v_{\parallel}$'s($\leqslant 0$). The inhomogeneity of the magnetic field seems to be indispensable for a wider and longer frequency variation.

Another limitation of the present simulation is that only a single monochromatic whistler wave is treated in the system. The frequency oscillation after the rising tone may reflect a situation where side bands are excited. A full electromagnetic particle simulation code can only treat the situation properly. The electromagnetic simulation with an inhomogeneous magnetic field is currently undertaken in our group, and will be published elsewhere.

3.5 Deformation of Distribution Function by Trapping and Detrapping

There are three main categories in theories of VLF triggered emissions: (1) : Feedback oscillator theory which is based on the phase bunching current in a feedback oscillator system locating in the inhomogeneous geomagnetic field [e.g., Helliwell and Inan, 1982]. This theory is not based on a concept of nonlinear phase trapping of resonant electrons by the triggering wave. (2) : Nonlinear resonant current theory

based on the nonlinear phase trapping of resonant electrons in the inhomogeneous geomagnetic field [e.g., Nunn, 1974, 1983, Omura and Matsumoto, 1982]. This theory does not require the phase detrapping of resonant electrons in its mechanism. (3) : Distribution deformation theory based on both the nonlinear phase trapping and subsequent phase detrapping of resonant electrons in the inhomogeneous geomagnetic field [e.g. Roux and Pellat, 1978; Melrose et al., 1983].

In this letter, we report a simulation study corresponding to the theory of the third category. Roux and Pellat [1978] found that a strong modification of the velocity distribution function of resonant electrons is created by a combined action of nonlinear phase trapping and inhomogeneity of the geomagnetic field due to the difference of phase space orbits between trapped and untrapped electrons. As a result of this orbital difference, either a beam or a hole is formed in the distribution function in the vicinity of the resonant velocity after the triggering wave releases these electrons at the tail end. In order to evaluate the resultant deformed distribution function at a detrapping point analytically, they had to make a simple assumption that (1) all of the trapped electrons are trapped only at the wave front and all of these trapped electrons are detrapped at the wave tail end ; and (2) those electrons which suffer from orbital change due to the monochromatic whistler wave are only trapped electrons, i.e., the contribution of orbital modification of untrapped electrons due to the whistler wave to the deformation of the distribution function is neglected. The objective of the present letter is to estimate the resultant deformed distribution function numerically including the points mentioned above which had been neglected in the theory of Roux and Pellat.

3.5.1 Phase Trapping in the Midst of the Wave Train (Side Trapping)

As Matsumoto and Omura [1981] pointed out in their test particle simulation, phase-trapping takes place not only at the wave front where the wave amplitude increases suddenly, but also in the midst of the whistler wave train other than the wave front because of the the gradual change of the inhomogeneity ratio R (as for the definition of R, see e.g., Nunn, [1974] or Vomvoridis and Denavit, [1979]) as the whistler wave propagates along the geomagnetic field. In this section, we call this trapping "side trapping" in contrast to the "wave-front trapping". The problem is then, how many electrons can be trapped by the side trapping when the triggering

wave propagates through the sea of the resonant electrons. In order to demonstrate this effect, we assume the unperturbed distribution function of a form of $\delta(v_\perp - V_{\perp O})$ for perpendicular velocity, of uniform in phase and of a shape as depicted in Figure 3.35(a) for parallel velocity, where $V_{\perp O}$ = 0.087 which gives a pitch angle of 60^0 for a resonant electron at the equator. Figure 3.35 shows a difference of the $v_\parallel$ distribution function averaged over the phase angle and v_T at the equator along a field line of L = 4 between t - 0 and t = 6 T_t where T_t is the trapping time. In order to make it possible to trace back the original velocity, we divide the velocity range into nine sectors with nine different shaded tones. The wave front of the whistler wave train is assumed to be located well to the northern side of the trapping zone (as for the definition of the trapping zone, see Matsumoto and Omura, [1981]). Therefore, no wave -front trapping takes place in this model. By the time of t = 6 T_t, all electrons which have had the local resonance velocity V_R at t 0 have passed the equator toward the southern hemisphere. Therefore, at t = 6 T_t, all we see in the vicinity of the resonance velocity, $v_\parallel$ = -0.5 are either untrapped electrons or those trapped by the "side trapping". As seen in the figure, we could see humps in the vicinity of the resonance velocity indicating invasions of electrons from higher velocity region. These invading electrons from higher velocity region show the amount of the "side trapping" which take place all the way along the wave train from the northern limit point of the trapping zone to the equator.

3.5.2 Contribution of Untrapped Electrons Perturbed by the Triggering Wave to the Deformation of Distribution Function

In addition to the contribution of trapped electrons, we need to take into account the contribution of untrapped electrons to the total deformation of the velocity distribution function. The importance of untrapped resonant electrons has been recognized by Bell and Inan [1981], even though their main interest is not the deformation of the velocity distribution function but pitch angle scattering of those electrons. Figure 3.36 shows an example of how the velocity orbits are strongly modified by the triggering whistler wave even for untrapped electrons. The upper panel of Figure 3.36 shows the orbits in the $v_\parallel$ - z plane of many electrons which encounter the whistler wave in the northern hemisphere within the trapping zone. The lower panel shows the corresponding orbits in the $v_\perp$ - z plane. In this example, most of the electrons are not phase

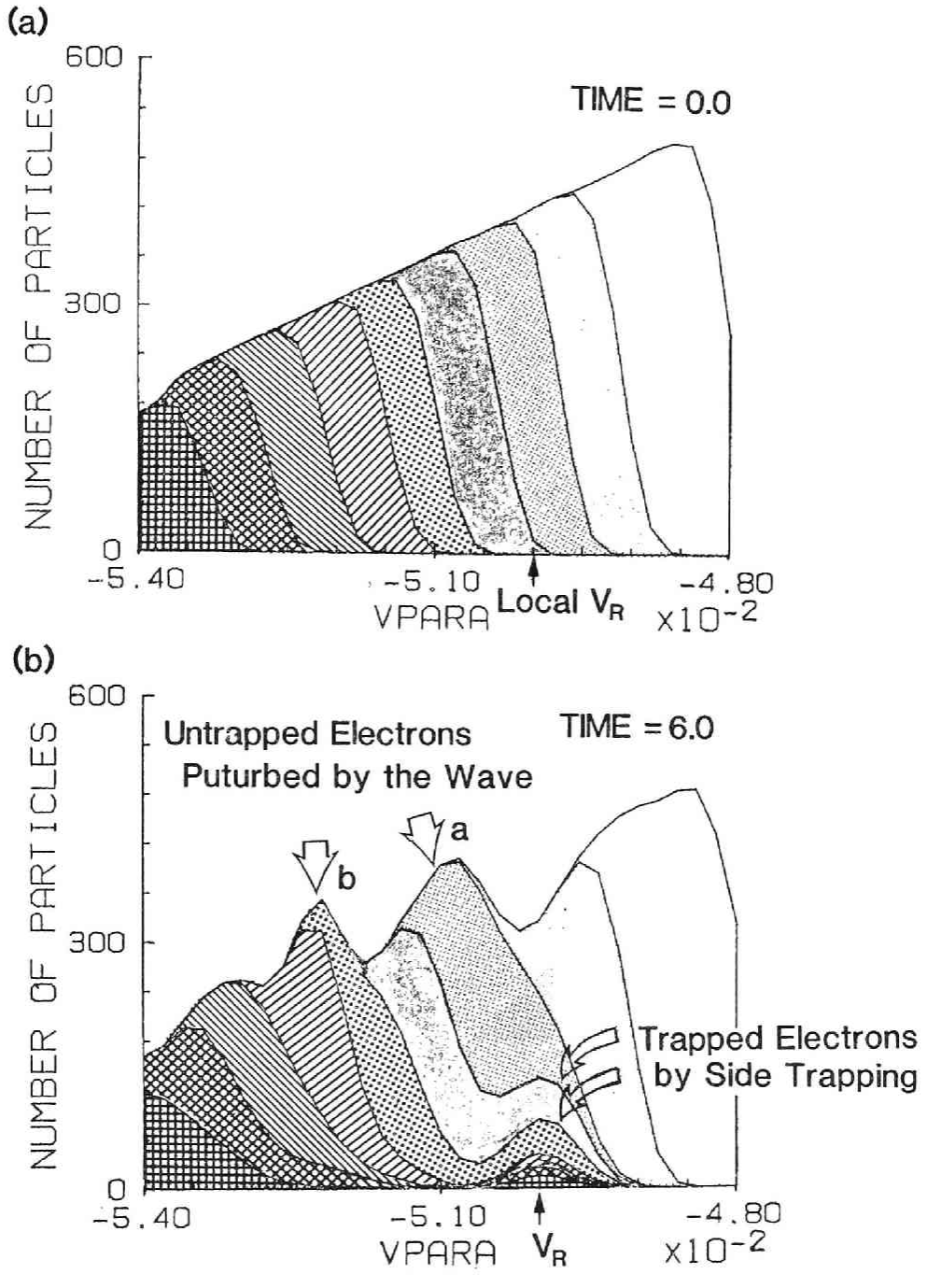

Fig. 3.35 $v_{\parallel}$ distribution function at the equator at (a) t = 0 T_t and (b) t = 6 T_t. The parallel velocity space is divided into nine regions at t=0 Tt as seen in (a). The inclined boundaries among the nine regions is caused by the counting method of particles in each region.

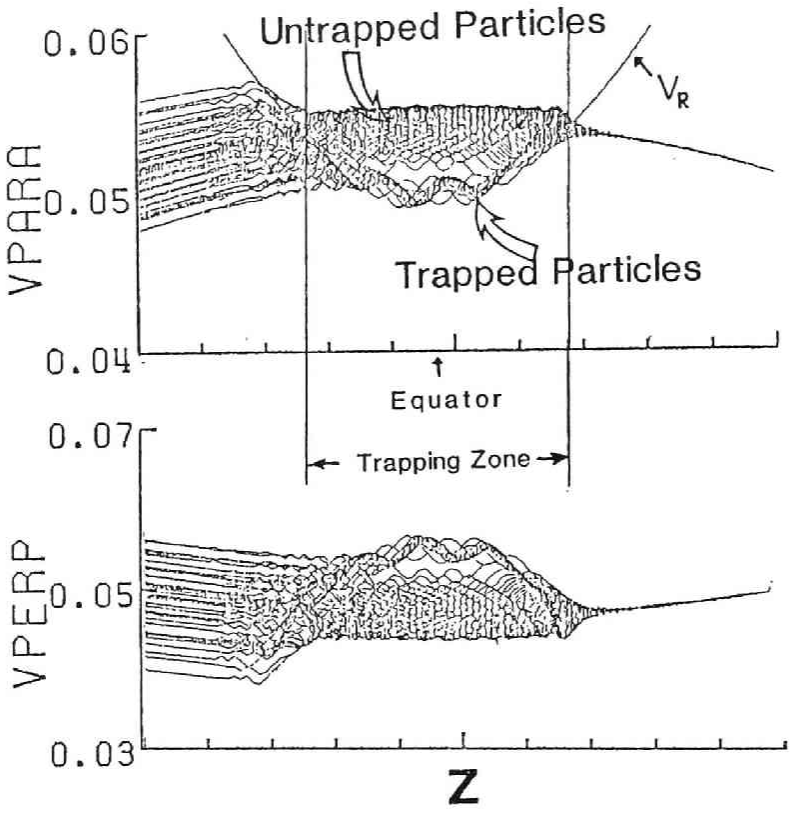

Fig. 3.36 Trajectories of 64 electrons with the same initial $v_{\parallel}$ and $v_{\perp}$, and with different phases of $v_{\perp}$.

trapped and remain untrapped but their orbits are strongly perturbed from the adiabatic orbits and pumped up into a higher parallel velocity region. Therefore, in the calculation of the resultant deformed distribution function, we could not disregard this pumping effect for the untrapped electrons. One example of the contribution of these perturbed untrapped electrons to the deformation of the distribution function is seen in Figure 3.35(b). Humps appearing in the vicinity of $v_{\parallel} \simeq -0.051c$ and $-0.052c$(indicated by "a" and "b" in the figure) are created by the pumping effect for the untrapped electrons, where c is the light speed.

3.5.3 Deformed Distribution Function caused by a Whistler Pulse Train

Figures 3.37 and 3.38 show a simulation result of the deformed distribution function at two different times $t = 3T_t$ and $6T_t$ caused by a whistler wave pulse with an amplitude of 5 mγ and a length of 1000 km (corresponding approximately to 65 msec). The traces of wave front and

wave end tail are depicted in the Figure 3.39 for reference.

Nine different shading tones in Figures 3.37 and 3.38 correspond to those in Figure 3.35(a). As seen in Figure 3.39, the triggering whistler pulse occupies a region including the equator at $t = 3T_t$. A large hump indicated by "b" and its adjacent hole indicated by "Hole" in Figure 3.37, are clearly due to the pumping effect for untrapped electrons. A small hump indicated by "a" is due to locally trapped electrons (mostly by "front-trapping"). These particles in the small hump, however, are not efficiently accelerated in the direction of $v_\perp$ because of the small geomagnetic inhomogeneity in the vicinity of the equator. Therefore the hole just below the resonant velocity does not lead to any strong whistler instability. At $t = 6\ T_t$, the whistler triggering pulse is located in the northern hemisphere. The velocity distribution function is modified as shown in Figure 3.38. The velocity corresponding to the bottom of the hole is clearly deviated toward the higher velocity side from the resonance velocity. This is due to a sum of contributions from trapped and untrap ped particles. Reduction in number in this hole is due to the pump-up effect of untrapped particles which takes place in the northern hemisphere as illustrated by a typical orbit "b" in the lower panel of Figure 3.38. However, in this hole velocity range, a fairly large amount of electrons are carried down by the wave trapping from higher velocity region as indicated by "a" in the upper panel of Figure 3.38. It is noted that these electrons are detrapped at the wave termination and follow their adiabatic orbit before reaching the equator as illustrated by a typical orbit "a" in the lower panel of Figure 3.38. A small hump which appears next to the hole on the higher velocity side is due to the pump-up effect of untrapped electrons taking place in the whistler wave train in the northern hemisphere. This hole at this time has different nature than that at $t = 3\ T_t$ because it contains a large percentage of trapped electrons which have been activated by gaining their $v_\perp$ during their trapped excursion in the whistler train.

Thus, the hole region with both a steepened gradient of the velocity distribution function with respect to parallel velocity and activated perpendicular energy resources becomes unstable for an induced whistler instability. However it is noted that this distribution function becomes unstable immediately after the detrapping takes place in the northern hemisphere. As both detrapped and untrapped electrons run along their adiabatic orbits, the center velocity of the activated hole moves towards higher velocities and may give rise to a falling tone emission. This last

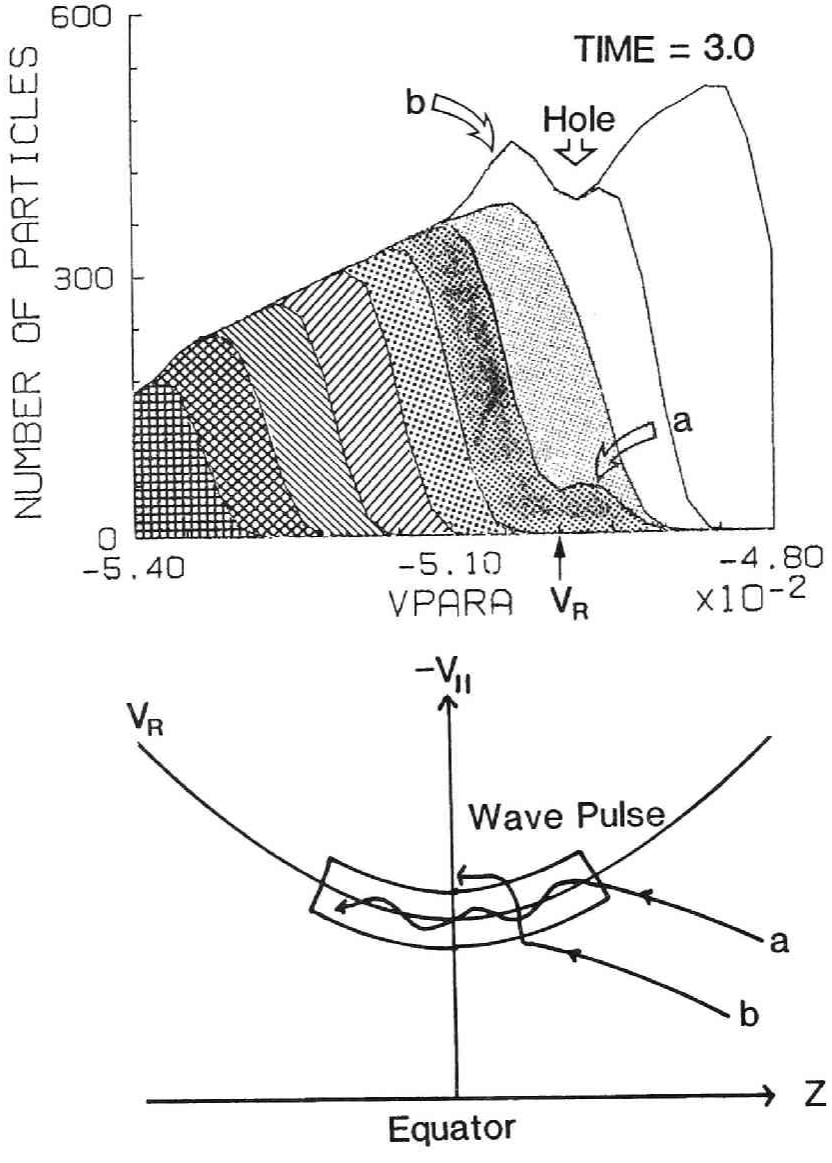

Fig. 3.37 The upper panel shows the $v_{||}$ distribution function averaged over $v_{\perp}$ and phase at the equator at $t = 3T_t$. The lower panel shows the location of the wave train and typical orbits of trapped and untrapped resonant electrons.

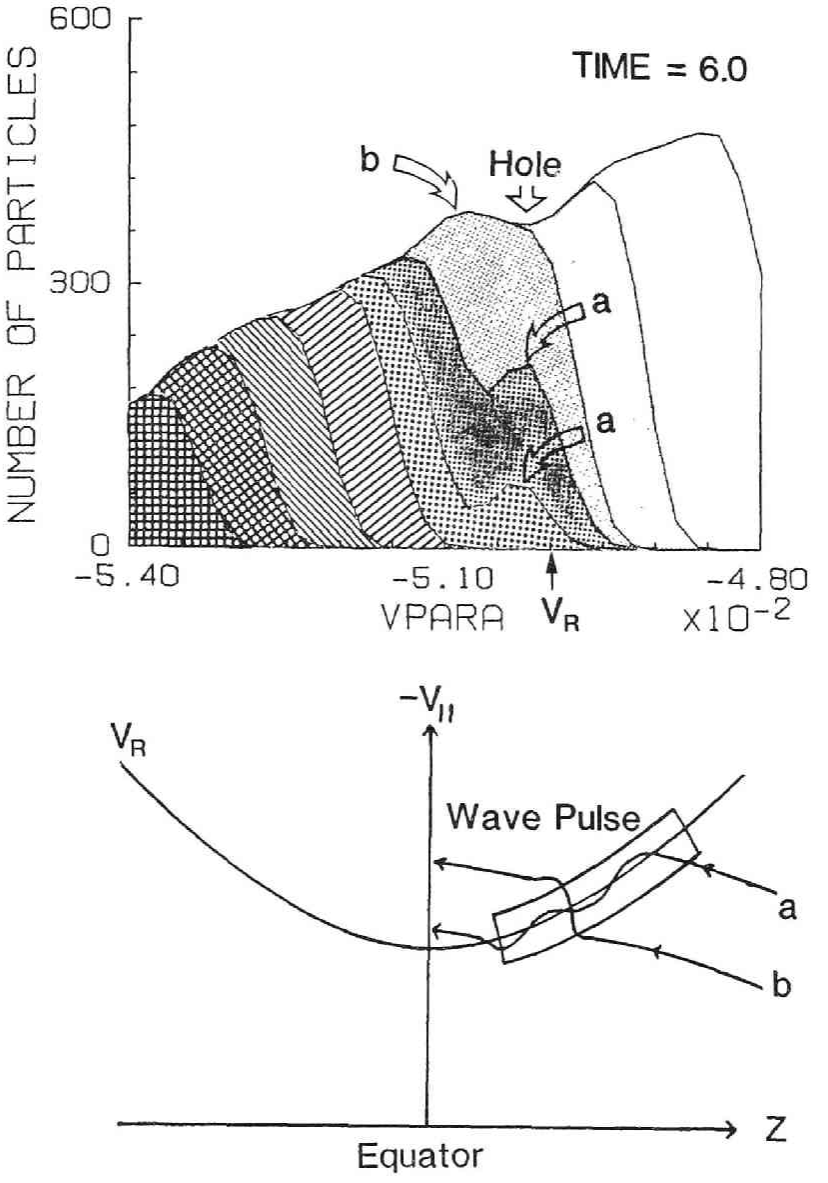

Fig. 3.38 The same figures at t = 6 Tt as those in Figure 3.38.

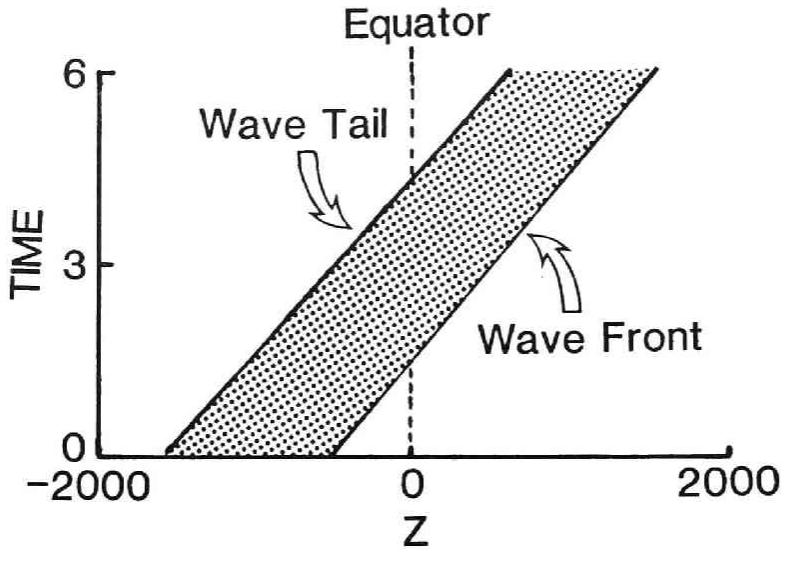

Fig. 3.39 Locations of wave front and tail as a function of time. The hatched area shows the region occupied by the monochromatic whistler wave.

statement is the same as Roux and Pellat [1978] proposed in their theory, and needs to be verified by self -consistent simulation experiments with the deformed distribution function computed by the present test particle simulation. This simulation is now being carried out and will be published in another article.

3.5.4 Interpretation of Pulse Length Dependence of Triggered Emission

Based on the features of deformation of the distribution function by the whistler triggering wave, we can interpret one of the well-known characteristics of triggered emissions. As schematically illustrated in the upper panel of Figure 3.40. the dynamic spectrum of triggered emissions changes from falling tones to risers as the length of triggering wave is changed from shorter to longer [Helliwell and Katsufrakis, 1974].

A short triggering pulse cannot trigger any emissions while it is located in the southern hemisphere because those electrons which are detrapped from the tail end of the triggering pulse are all inactivated by losing their perpendicular energy during their trapped excursion in the wave train. This situation is schematically illustrated in Figure 3.40.

However, if the pulse occupies an appropriate location within the trapping zone in the northern hemisphere where the difference of the resonance velocities at both ends of the triggering pulse is large enough to produce a strong modification of the distribution function, then activated electrons are ejected from the pulse tail end. These detrapped electrons thus generate a falling tone emissions. On the contrary, in the case of a long triggering pulse the wave tail end can be located in the southern hemisphere even when the wave front is located far away from the equator in the northern hemisphere. Then electrons trapped by both front-and side-trapping are ejected from the wave tail after a long period in the wave trapping well. Therefore these trapped electrons are well activated and are ready to generate a riser emission when they begin to run on their adiabatic orbits. A schematic illustration for this mechanism is given in Figure 3.40.

3.5.5 Conclusion

In this section, a computer simulation study is reported which corresponds to an analytic theory of triggered emissions by Roux and Pellat [1978]. Test particle simulation runs basically support their idea of deformation of distribution function created by detrapping of trapped electrons. However, it is demonstrated that contribution to the deformation comes not only from the electrons trapped at the wave front as Roux and Pellat assumed but also from those electrons trapped in the midst of the wave train (i.e., side-trapping effect) and also from untrapped electrons via strong modification of their adiabatic orbits due to the triggering wave (i.e., pump-up effect). The theoretical interpretation of dependence of dynamic spectra of triggered emission on the length of triggering pulse appears to agree with experimental data. However, it is not confirmed quantitatively that the deformed distribution function could lead to a generation of triggered emissions. It is not clear either which category of theories is the best for the interpretation of triggered emissions at the present stage of simulation studies. There are definite needs to accomplish different kinds of computer simulations for all the three theoretical models.

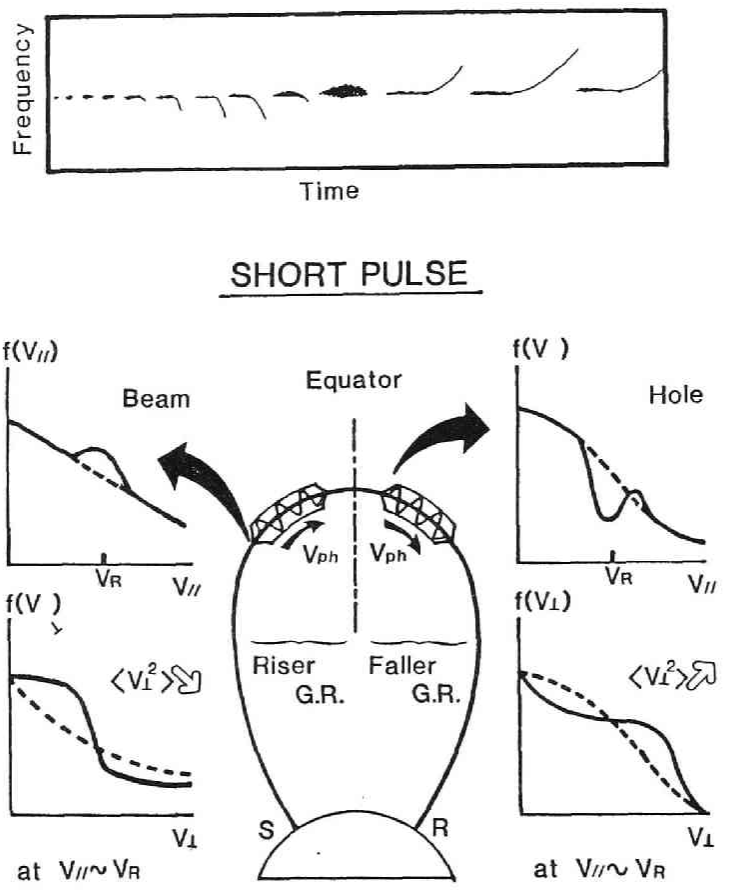

Fig. 3.40 Schematic interpretation of the pulse length dependence of triggered emissions.

3.6 Effects of Electrostatic Waves on Whistler Mode Instability

In most of simulation studies as well as theoretical studies, effects of electrostatic components are neglected for simplicity and numerical efficiency based on the assumption that the transverse whistler mode waves and the longitudinal electrostatic waves are independent each other within the limit of linear theory. Only Bell and Buneman [1964] compared the phase mixing rates of the whistler mode and longitudinal instabilities excited by an electron beam, and suggested the possibility for the whistler mode instability to take over the longitudinal instability. However, we find that the whistler beam instability is suppressed by the beam velocity spread due to the nonlinear trapping of beam electrons by the fast-growing electrostatic waves.

Assuming a coherent whistler mode wave interacting with a counter-streaming electron beam, we studied the dependence of the whistler saturation level on the initial waves amplitudes. We find that a larger initial wave can reaches a larger saturation levels. This is contrary to the simulation results by Matsumoto et al. [1980]. They neglected the electrostatic waves in the simulation, and reached a different conclusion that the saturation level is the same regardless of the initial wave amplitudes.

In Subsection 3.6.1 beam instabilities of the whistler mode waves and the electrostatic waves are theoretically studied. We compared the growth rates and the widths of parallel velocity spread by nonlinear phase trapping for the two instabilities. Based on the linear theory, we performed one-dimensional electromagnetic simulations. We performed several runs with no initial wave and with different initial waves. We also performed one simulation run where electrostatic waves are artificially eliminated. The results of these simulation runs are presented in Subsection 3.6.2. Subsection 3.6.3 gives conclusions and discussion.

3.6.1 Theoretical Study of the Electron Beam Instabilities

The electron beam with a drift velocity parallel to the static magnetic field and a perpendicular velocity can excite both the longitudinal electrostatic and transverse whistler waves in a magnetized plasma. In this section, we examine the growth rates, saturation levels and trapping velocities for the longitudinal and whistler instabilities. We assume an electron beam with a velocity distribution function given by

$$f(v_{\parallel}, v_{\perp}) = C_N \exp\left\{ -\left(\frac{v_{\parallel} - u}{V_{\parallel T}} \right)^2 \right\} g(v_{\perp}) \tag{3.75}$$

where C_N is a normalization constant and u is a drift velocity of the beam. The subscript $\parallel$ and $\perp$ attached to v denote the velocity components parallel and perpendicular to the static magnetic field B_o, respectively. The perpendicular velocity distribution $g(v_{\perp})$ is a subtracted Maxwellian realizing a loss cone distribution, which is given by [Kennel and Abdalla, 1978]

$$g(v_{\perp}) = \frac{1}{1 - \beta} \left\{ \exp\left(- \frac{v_{\perp}^2}{V_{\perp T}^2} \right) - \exp\left(- \frac{v_{\perp}^2}{\beta V_{\perp T}^2} \right) \right\} \tag{3.76}$$

The $V_{\parallel T}$ and $V_{\perp T}$ are parallel and perpendicular thermal velocity, respectively. We assume a monoenergetic beam, that is,

$$\gamma_{max} \gg k V_{\parallel T} \tag{3.77}$$

where γ_{max} is the maximum growth rate.

First, we consider the longitudinal oscillations whose dispersion relation is given by [O'Neil et al., 1971, Akhiezer et al., 1975]

$$1 - \frac{\Pi_e^2}{\omega^2} - \eta \frac{\Pi_e^2}{(\omega - ku)^2} = 0 \tag{3.78}$$

where η is a density ratio of electron beam and background cold plasma n_b/n_c. Putting $\omega = ku + \omega'$, we find the maximum growth rate and frequency are given by

$$\gamma_{max} = Im(\omega') = \frac{\sqrt{3}}{2^{4/3}} \eta^{1/3} ku \tag{3.79}$$

$$\omega = ku + Re(\eta) = \Pi_e \left\{ 1 - 2^{-4/3} \eta^{1/3} \right\} \tag{3.80}$$

where we assumed the resonance condition $\Pi_e = ku$. The longitudinal electrostatic oscillation grows with the maximum growth rate initially and eventually reaches an amplitude large enough to trap the beam electrons [O'Neil et al., 1971]. Since the trapped electrons rotate around the phase velocity ω/k, the amount of kinetic energy lost from the electron beam is

$$- \Delta W_p = n_b m u(u - \omega/k) = n_b m\, 2^{-4/3} \eta^{1/3} u^2 \qquad (3.81)$$

This energy is transfered to the wave energy which is a summation of the electric field energy and the kinetic energy of the cold plasma supporting the logitudinal wave, that is,

$$W_w = \frac{1}{2} \varepsilon_o E_w^2 + \frac{1}{2} n_c m V_w^2 \qquad (3.82)$$

where V_w is a velocity of the cold electrons which follow a sloshing motion in phase with the wave. From the equation of motion, we have

$$V_w = (eE_w)/(m\omega) \quad . \qquad (3.83)$$

Substituting (3.83) into (3.82), and assuming $w \cong \Pi_e$, we have

$$W_w = \varepsilon_o E_w^2 \quad . \qquad (3.84)$$

Equating W_w and $-W_p$, we obtain the saturation level of the electric field as [Drummond et al., 1970]

$$E_w = 2^{-2/3} \left(\frac{n_b m}{\varepsilon_o}\right)^{1/2} \eta^{1/6} u = 2^{-2/3} \frac{m}{e} \Pi_e \eta^{2/3} u \qquad (3.85)$$

where m and e are electron mass and charge, respectively.

We examine the motion of those trapped beam electrons. We assume the (x,y,z) coordinates system where both the static magnetic field B_o and the wave number vector k is along the x-axis. The equations of motion of an electron in the presence of the longitudinal electrostatic field

$$E(x,t) = E_w \sin(kx - \omega t + \phi_o) \qquad (3.86)$$

are described using variables θ and ζ

$$\theta = k \left(v - \frac{\omega}{k} \right) \quad , \quad \zeta = kx - \omega t + \phi_o \qquad (3.87)$$

as

$$\frac{d\theta}{dt} = \omega_t^2 \sin \zeta \quad , \quad \frac{d\zeta}{dt} = \theta \qquad (3.88)$$

where ϕ_o is an initial phase of the oscillation and ω_t is the trapping frequency given by

$$\omega_t = (eE_w k/m)^{1/2} \quad . \tag{3.89}$$

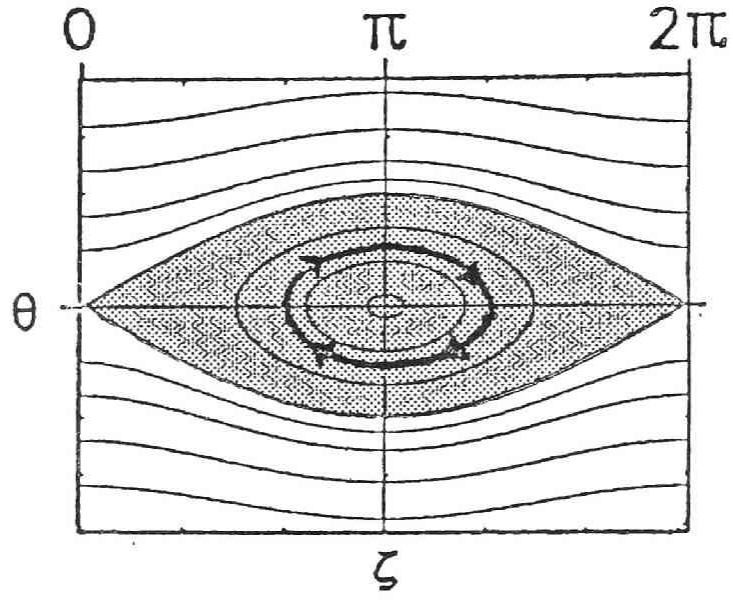

Fig. 3.41 Trajectories of resonant electrons in the θ - ζ phase space.

Trajectories of resonant electrons described by (3.88) are shown in Figure 3.41. The shaded area is the trapping region where electrons are trapped and oscillate around $(\zeta, \theta) = (180^0, 0.)$ with approximately the trapping frequency. Since the separatrix of the trapping region is given from (3.88) as

$$\theta^2 = 2\omega_t^2(1 - \cos \zeta) \quad . \tag{3.90}$$

the width of the trapping area in $v_{\parallel}$ is given by the trapping velocity

$$V_t = 2\omega_t/k \quad . \tag{3.91}$$

After the logitudinal instability reached the saturation, the beam electrons undergo trapping oscillation and are diffused over the trapping region. Therefore, the velocity spread of the beam electrons are estimated by the trapping velocity. From (3.85), (3.89) and (3.91), we obtain the trapping velocity for the longitudinal oscillation as

$$V_{tS} - 2^{2/3}\eta^{1/3}u = 1.59\ \eta^{1/3}u \quad . \tag{3.92}$$

The initially monoenergetic beam eventually spread in $v_{\parallel}$ over the range of $\omega/k - V_{tL} \leqslant v_{\parallel} \leqslant \omega/k + V_{tL}$.

Second, we examine the whistle mode instability for the electron beam with transverse velocity distribution $g(v_{\perp})$. Matsumoto et al. [1981] estimated the growth rate and the saturation level by a similar method presented above for the logitudianl instability. For comparison with the longitudinal instability we cite their results in the following. The dispersion relation is given by

$$c^2k^2 - \omega^2 + \frac{\Pi_e^2\omega}{\omega - \Omega_e} + \eta\,\frac{\Pi_e^2(\omega - ku)}{\omega - ku - \Omega_e} + \eta\,\frac{\Pi_b^2(1/2)k^2\langle v_{\perp}^2\rangle}{(\omega - ku - \Omega_e)^2} = 0 \quad . \tag{3.93}$$

where $\langle v_{\perp}^2\rangle$ is the mean square perpendicular velocity of the beam. The maximum growth rate is obtained from (3.93) as

$$\gamma_{max} = \sqrt{3}\ 2^{-4/3}\eta^{1/3}Fku \tag{3.94}$$

$$\omega = \Omega_e - ku - 2^{-4/3}\eta^{1/3}Fu \tag{3.95}$$

where F is replaced by

$$F = \left\{ \frac{k^2\langle v_{\perp}^2\rangle}{ku\Omega_e + 2(\Omega_e - ku)\,k^3u^3/\Pi_e^2} \right\}^{1/3} \simeq \left(\frac{k\langle v_{\perp}^2\rangle}{\Omega_e u} \right)^{1/3} \tag{3.96}$$

The approximation made above comes from an assumption that $0 < (\Omega_e - ku)/\Omega_e < 1$ and $\Pi_e^2 >> \Omega_e^2$ which is well satisfied in the equatorial magnetosphere. Under this approximation we obtain a saturation level for the mode with the maximum growth rate as

$$\frac{B_w}{B_o} - 2^{-1/6}\eta^{2/3}\left(\frac{k}{\Omega_e}\right)^{5/3} V_{\perp o}^{1/3}u^{4/3} \tag{3.97}$$

where $V_{\perp o} = \sqrt{\langle v_{\perp}^2\rangle} = (1 + \beta)^{1/2}V_{\perp T}$.

Equations of motion for resonant electrons with a counter-streaming whistler wave is approximated by (3.88) if we assume the following coordinates [Matsumoto and Omura, 1981].

$$\theta \quad k(v_{\parallel} - \frac{\omega \quad \Omega_e}{k}) \quad . \quad \zeta = \phi - \Psi \tag{3.98}$$

where ϕ and Ψ are phase angle of a perpendicular velocity $v_{\perp}$ and the wave magnetic field B_w in the rest frame. The trapping frequency is given by

$$\omega_t = (kV_{\perp o} eB_w/m)^{1/2} \quad . \tag{3.99}$$

Since the motion of a resonant electron in a whistler mode wave is described by the same equation as for a longitudinal oscillation. The resonant electrons undergo trapping by the whistler wave and diffused in $v_{\parallel}$ over a range of $V_R - V_{tw} \leqslant v_{\parallel} \leqslant V_R - V_{tw}$. V_R is the resonance velocity given by $(\omega - \Omega_e)/k$ and V_{tw} is the trapping velocity of the whistler wave given from (3.92) as

$$V_{tW} = 2^{11/12} \eta^{1/3} (\frac{k}{\Omega_e})^{1/3} V_{\perp o}^{2/3} u^{2/3} \quad . \tag{3.100}$$

We now compare the growth rates of electrostatic waves and whistler mode waves. From (3.79) and (3.94) we have the ratio

$$\frac{(\gamma_{max})_W}{(\gamma_{min})_S} = \frac{k_W}{k_S} F \tag{3.101}$$

where subscripts "W" and "S" denote quantities of Whistler mode waves and electrostatic waves, respectively. Since F = 1 for the magnetospheric parameter, the difference comes from the ratio of k_W/k_E. Since the frequency of the whistler mode wave is much smaller than that of the plasma oscillation, $k_W \ll k_E$. Therefore, the growth rate of a whistler wave is much smaller than that of electrostatic waves.

Bell and Buneman evaluated the competing process by defining the phase mixing rate $(\gamma)_{max}/ku$ which indicates the wave growth in a time during which the electron beam travels over one wavelength [1964]. The difference of the phase mixing rates is the factor F. Since F could be larger than unity, they conclude that the whistler mode wave eventually takes over the electrostatic waves. However, they neglected the modulations of electron beam by the electrostatic waves. The electrostatic wave grows first and reach a saturation level in the initial phase of whistler wave growth. If the trapping velocity of the electrostatic wave is small enough compared with that of whistler wave, the whistler mode wave could grow even after the saturation of the electrostatic wave. We now compare the trapping

velocities given by (3.82) and (3.99),

$$\frac{V_{tW}}{V_{tS}} = 2^{1/4}\left(\frac{k}{\Omega_e}\right)^{1/3} V_{\perp o}^{2/3}\, u^{-1/3} \tag{3.102}$$

If we assume an electron beam with a pitch angle of 45^0 resonating with a whistler mode wave of a frequency $0.5\Omega_e$, the ratio of trapping velocities is of the order of 1. Therefore, the modulation by the electrostatic wave is large enough to suppress the growth of the whistler mode wave.

3.6.2 Simulation Study of Electron Beam Instabilities

We performed a self-consistent electromagnetic simulation where electrostatic waves and electromagnetic whistler wave are solved simultaneously. We assume a one-dimensional periodic system where a whistler wave interacts with a counter streaming high energy electrons. In order to study the dependence of the whistler instability on the initial wave amplitudes of the waves, we performed several runs with different initial wave amplitude. Parameters assumed in the simulations are the followings.

Plasma frequency : $2\Omega_e$
- Thermal velocity of background electrons : 0.01c
  Parallel thermal velocity : 0.17c
- Perpendicular beam thermal velocity : 0.21c
  Parallel beam thermal velocity : 0.01c
- Density ratio of beam and background plasma η : 0.01
- Minimum wave number in the system k_{min} : $0.614c/\Omega_e$
- Wave number of initial whistler wave : $2.46c/\Omega_e$
  Number of grid points : 1024
- Number of particle : 16384
- Time step Δt : $0.005\ \Omega_e^{-1}$

The initial wave mode number is 4, that is , we have four wavelengths in the system.

First, we assume no initial wave, and we study wave excitation from thermal fluctuation noise by an electron beam (Case A). Kinetic energy history is plotted in Figure 3.42. The upper panel shows the parallel and perpendicular energy $K_{\parallel}$ and $K_{\perp}$ and drift energy K_d of background cold electrons. The lower panel shows those of beam electrons. At first the drift energy of the beam decreases. The energy lost from the beam is

transfered to the wave and background cold plasma. However, the energy transfer proceed mainly in the parallel direction, and $K_\perp$'s of the beam and cold plasma hardly change, which imply that excitation of the transverse whistler mode wave is small and its effects are negligible. Figure 3.43(a) shows a time history of the parallel and perpendicular electric field energy. Obviously the parallel electric field is strongly excited in the very early stage, while the perpendicular electric field increases slightly. The perpendicular magnetic energy density shown in Figure 3.43(b) increases slightly, indicating that excited wave is purely electrostatic.

In order to find the initial growth rates of the electrostatic wave and whistler mode wave with maximum linear growth rates, we plot time histories of the parallel electric field of mode 22, and perpendicular magnetic field of mode 4 in Figure 3.44(a) and(b), respectively. Here, mode numbers indicate a number of wavelengths in the system. The growth rate of the most dominant electrostatic wave is read from Figure 3.44(a) as ~ 0.4 and the growth rate of the whistler mode wave is read from Figure 3.44(b) as ~ 0.05. Since the theoretical growth rates given by Eqs. (3.79) and (3.94) are 0.4 for the electrostatic wave and 0.05 for the whistler mode wave, the agreement between the simulation and the linear theory is good.

Figure 3.45 is the same mode history plots as Figure 3.44, but for the whole simulation run ($t = 0 \sim 300\ \Omega_e^{-1}$). The dashed lines are theoretical saturation level given by (3.85) and (3.97). For the electrostatic wave agreement between the simulation and theory is good. For the whistler mode wave, however, the wave growth stops before reaching the theoretical saturation level. After that the wave decreases gradually.

Since the growth of the whistler mode wave stops when the electrostatic wave reaches its saturation, a possible cause of the disagreement is a modulation of the electron beam by the electrostatic wave. Figure 3.46 shows phase plots of beam electrons in the $x - v_\parallel$ ($\equiv v_x$) space at different times. Initially beam electrons are distributed uniformly in space and monoenergetic in $v_\parallel$. At $t = 20.0\Omega_e^{-1}$, when the electrostatic wave reaches the saturation, the electrons are trapped in the electrostatic potential and follow a spiral motion around the phase velocity ω/k. The number of spirals is 22 and agrees with the mode number of the most dominant electrostatic wave. The width of the velocity spread is about 0.12c, while the trapping velocity for the electrostatic wave V_{tS} is calculated from (3.92) as 0.058c. Therefore, the velocity spread is

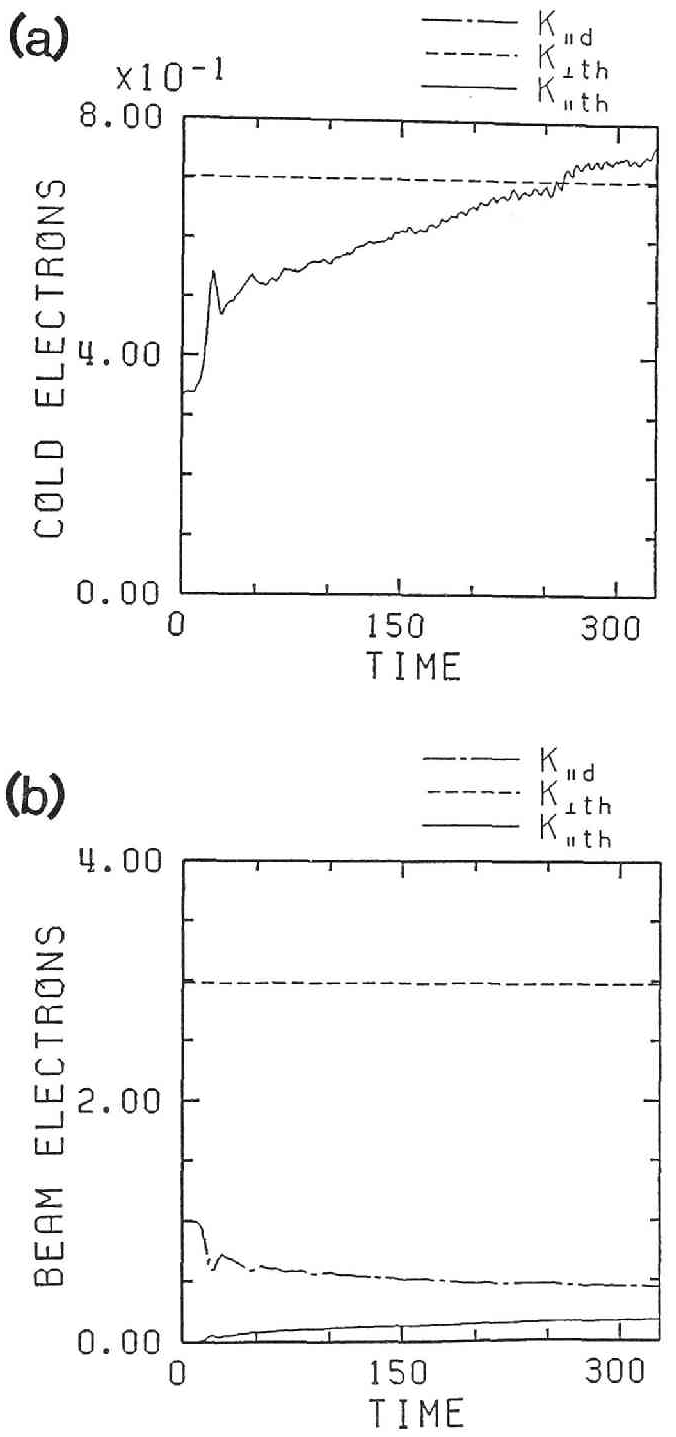

Fig. 3.42 Kinetic energy history in Case A without an initial wave : (a) cold electrons, (b) beam electrons.

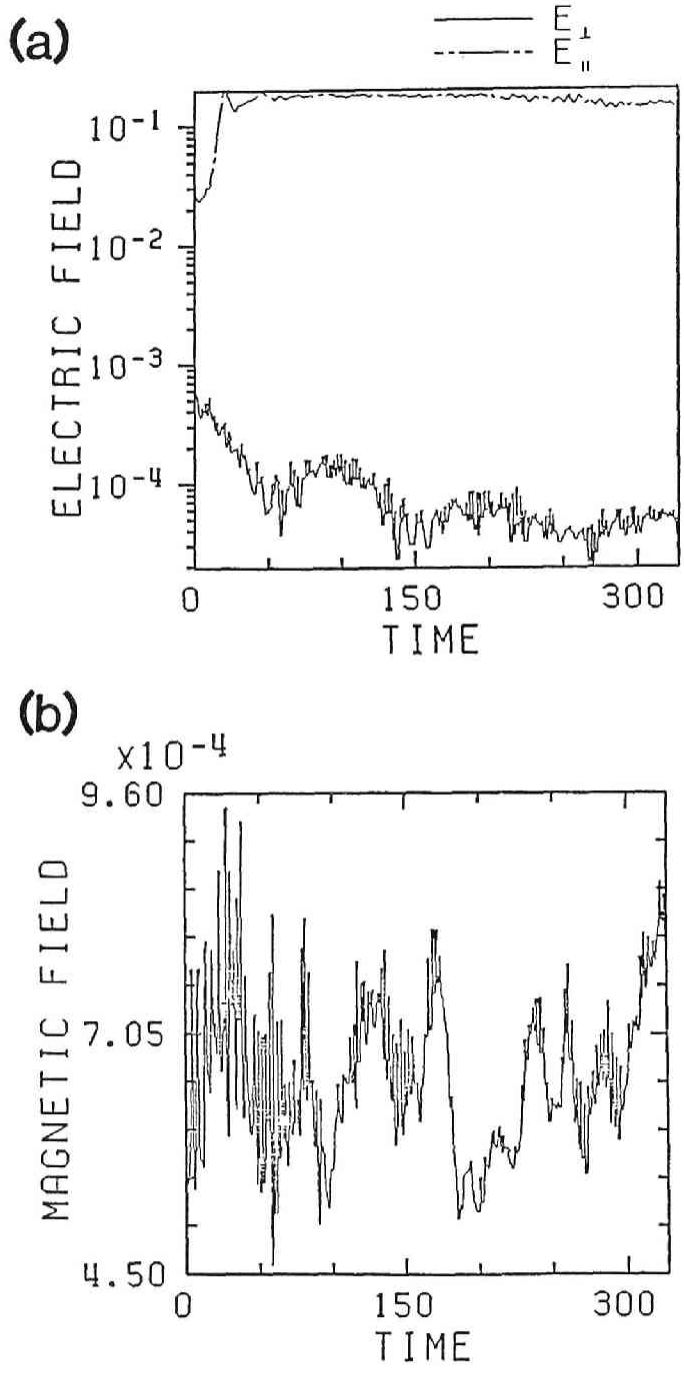

Fig. 3.43 Wave energy history in Case A: (a) parallel electric field energy (dashed line) and perpendicular electric field energy (solid line), (b) perpendicular magnetic field energy.

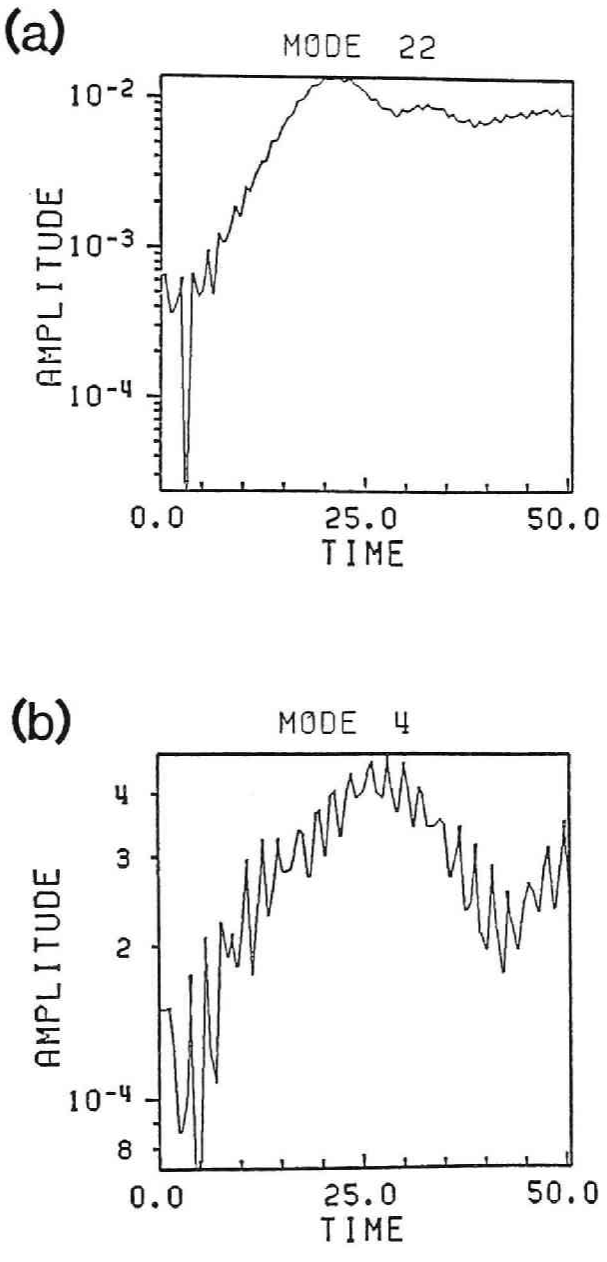

Fig. 3.44 (a) Time history of parallel electric field of mode 22. (b) time history of perpendicular magnetic field of mode 4 in Case A : the initial stage (t = 1 $50\Omega_e^{-1}$).

about $2V_tL$. At later times t - $40\Omega_e^{-1}$ and $300\Omega_e^{-1}$, the velocity spread becomes gradually larger. This is due to gradual excitation of other electrostatic modes and broadening of the spectra of the electrostatic waves.

An ω - k spectra obtained by Fourier-analyzing the wave data both in

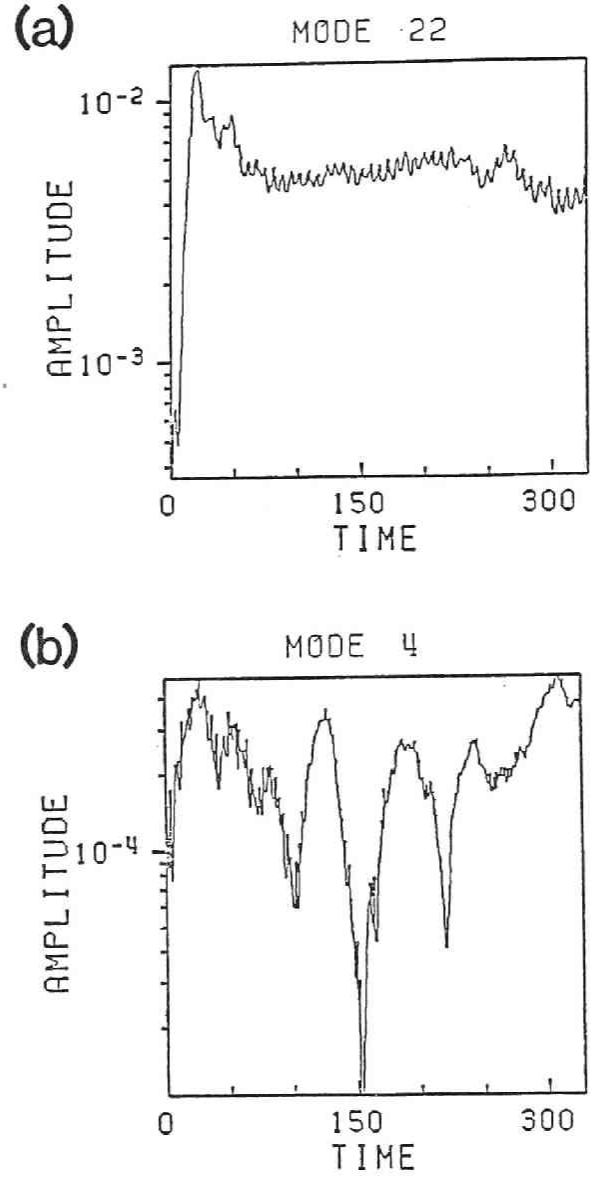

Fig. 3.45 Time history of (a) parallel electric field of mode 22 and (b) perpendicular magnetic field of mode 4 in Case A : the whole run ($t = 1 - 300\Omega_e^{-1}$). The dashed lines are theoretical saturation levels.

space and time is plotted in Figure 3.47. Panel (a) is for the longitudinal electric field E_x, and Panel (b) is for one of the transverse magnetic field B_y. We find broad spectra of the electrostatic waves near the plasma frequency $2\Omega_e$. On the other hand, a whistler mode wave of mode 4 is hardly excited and we only find spectra of thermal fluctuations of

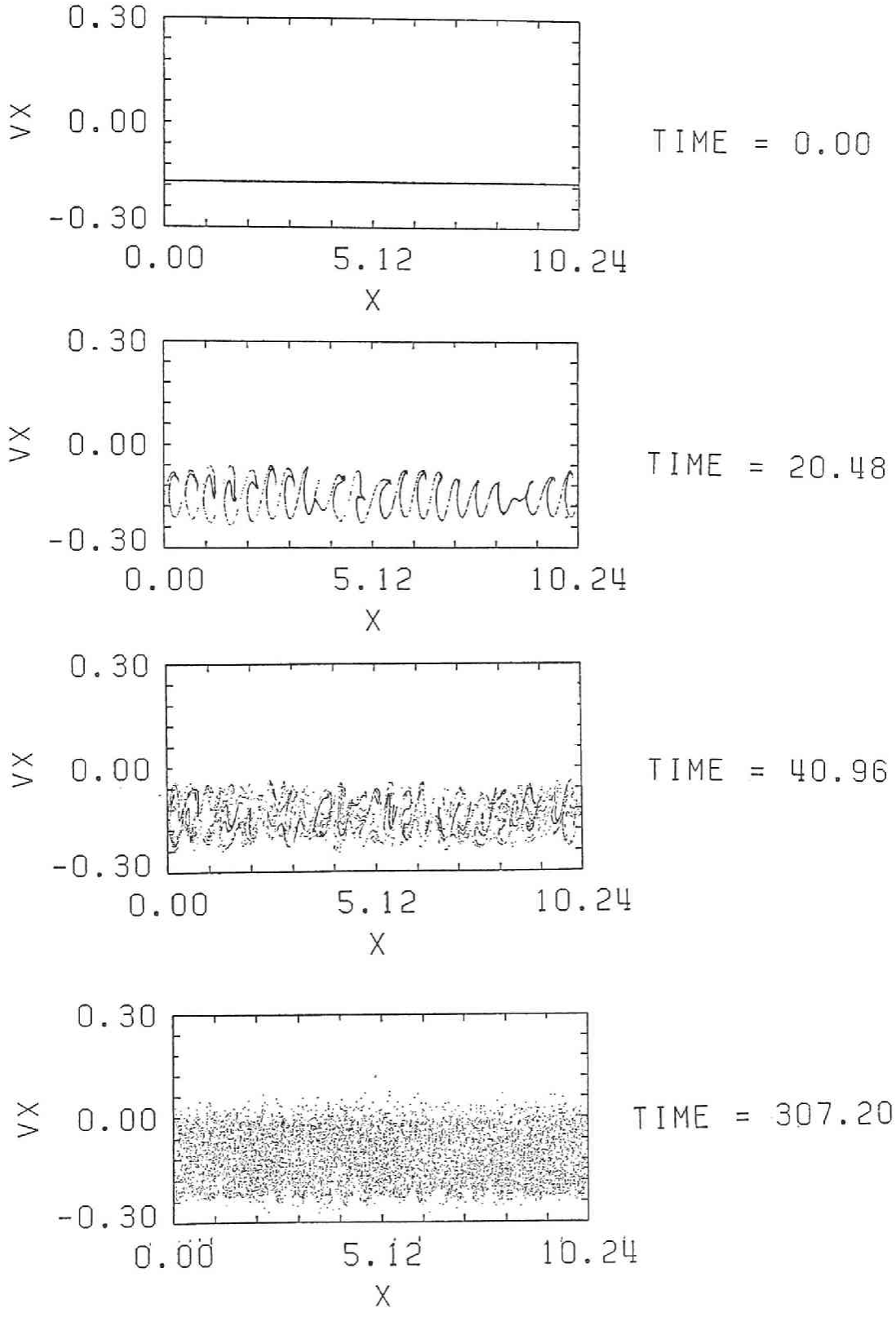

Fig. 3.46 Phase plots of beam electrons in the x - $v_{\parallel}$ space for Case A.

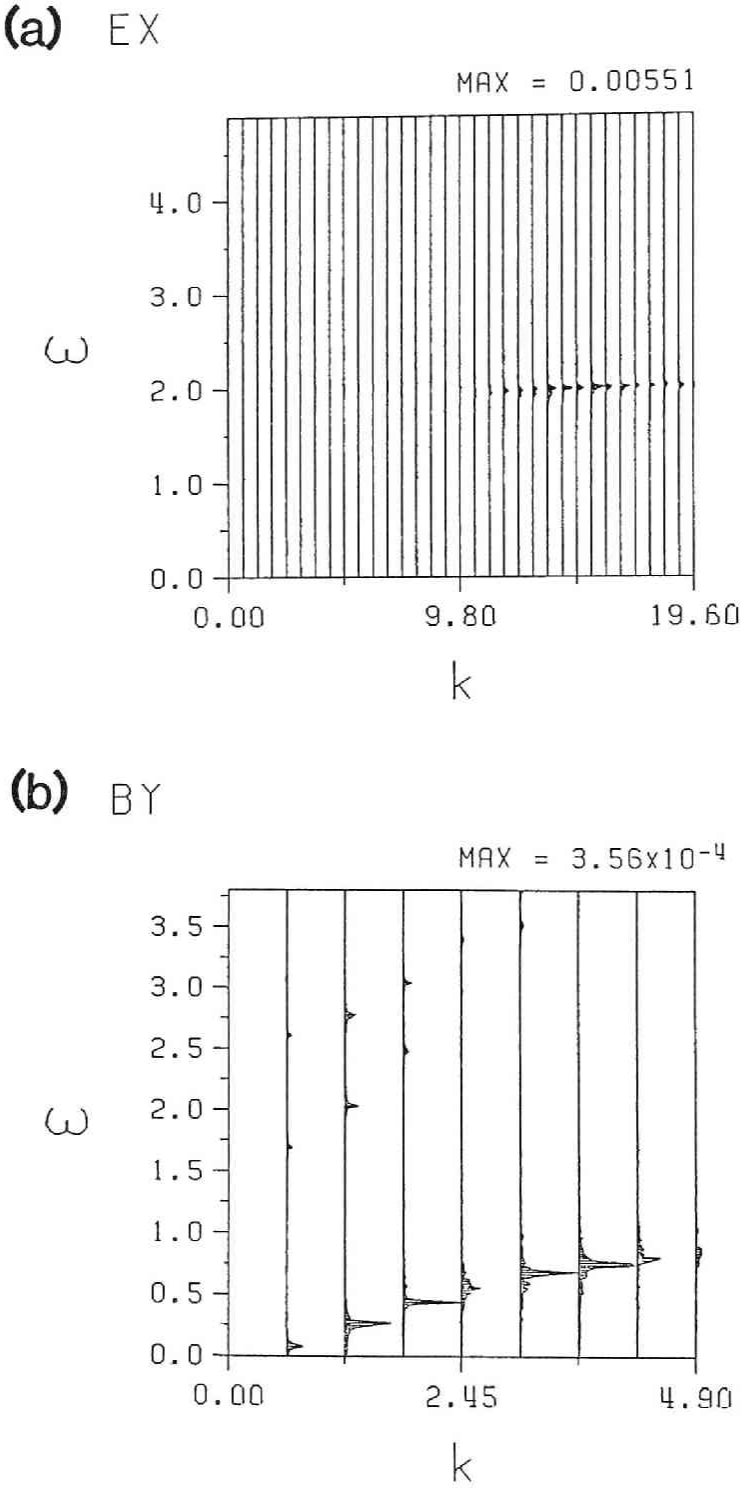

Fig. 3.47 ω - k diagram for the period t = 1 ~ 300 in Case A : (a) parallel electric field, (b) perpendicular magnetic field.

normal modes, that is, whistler mode waves, right and left handed light modes in panel (b).

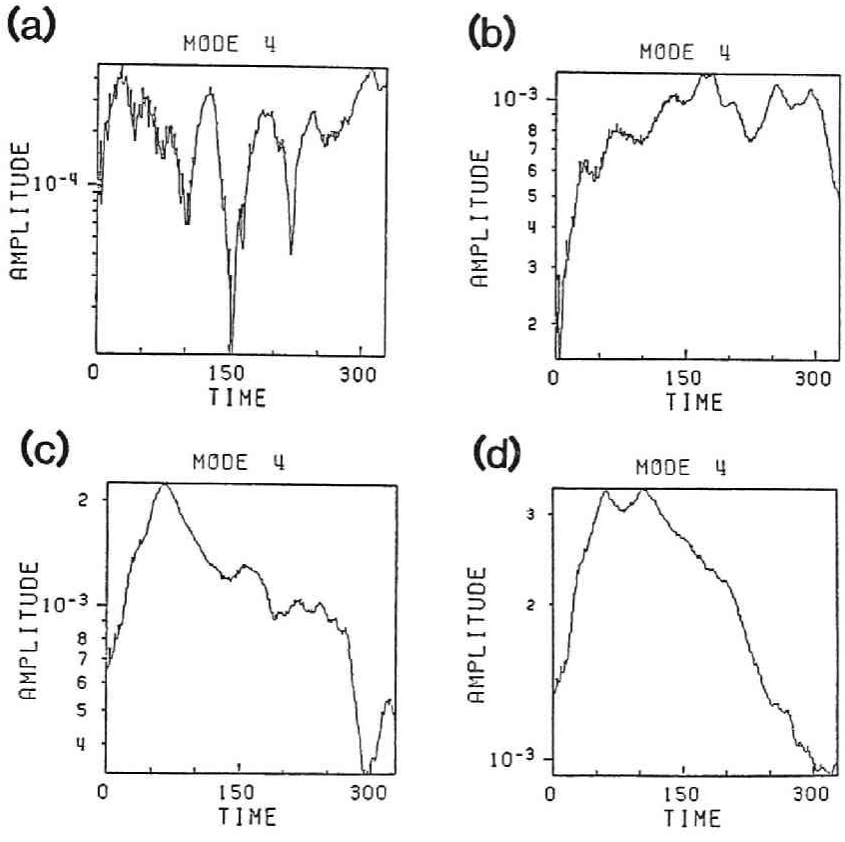

Fig. 3.48 Time histories of perpendicular magnetic field of mode 4 (a) Case A : no initial wave, (b) Case B : $B_{WO} = 1 \times 10^{-4} B_O$, (c) Case C: $B_{WO} = 5 \times 10^{-1} B_O$, (d) Case D : $B_{WO} = 1 \times 10^{-3} B_O$.

As the second step, we put the initial whistler mode wave of mode 4 which satisfy the resonance condition $\omega = \Omega_e - ku$. We performed three simulation runs with different initial amplitudes. We show the history plots of the perpendicular magnetic field of mode 4 in Figure 3.48. Panels (b), (c) and (d) show the cases with the initial wave amplitudes $B_w/B_o = 1x10^{-4}$ (Case B), $5x10^{-4}$ (Case C) and $1x10^{-3}$ (Case D), respectively. We also show the case of noise start in Panel (a). Contrary to the case of noise start, the cases with a initial wave show growth and saturation. However, the initial growth rates in Panels (b), (c) and (d) are about 0.01 and smaller than a theoretical linear growth rate 0.053 given by (3.94). The saturation levels are different depending on the initial wave amplitudes. A whistler mode wave with a larger initial amplitude reaches saturation at a larger level. Even for the case with a large initial

amplitude $B_w/B_o = 1x10^{-3}$ shown in Panel (d), the saturation level is $3x10^{-3}B_o$ and lower than the theoretical saturation level $0.01B_o$ given by (3.97). The cases with the initial amplitudes $5x10^{-3}$ and $1x10^{-3}$ also show damping after the saturation. .PP The four simulation runs presented above clearly show that the electron beam is strongly modified by the fast-growing electrostatic waves and growth of a whistler mode wave is suppressed due the the modulation. In order to confirm the pure whistler mode beam instability theoretically studied in Section 2, we performed a non-electrostatic simulation where the longitudinal electrostatic field is artificially eliminated from the system (Case E). This is achieved by assuming the current density J_x is 0 all the time and not solving Poisson's equation. The kinetic energy history is shown in Figure 3.49. Contrary, to the electrostatic case in Figure 3.42, the beam drift energy increases and perpendicular thermal energy of the beam electrons decreases, giving energy to the perpendicular component of cold electrons and the transverse electric and magnetic field, whose energy history is shown in Figure 3.50. Out of the thermal fluctuation noises, the most unstable mode grows linearly and reaches saturation and oscillates around the saturation level. Figure 3.51 shows a history plot of mode 4. The saturation level is $0.01B_o$ and agree with the theoretical value by (3.97). Phase plots of the beam electrons at different times are shown in Figure 3.52. The initial spiral motion as shown in Figure 3.46 is not found in this case. At $t = 200\Omega_e^{-1}$ the velocity spread by the whistler wave trapping is small, while by that time the electrostatic wave almost reached its saturation in the previous runs. Therefore, effects of the whistler mode wave on the electrostatic instability is very small, and the initial motion of the beam electrons are solely decided by features of the electrostatic waves. At the end of the run, the velocity spread is about 0.12c which is $2V_{tw}$, which agree with the theory of the nonlinear phase trapping presented in Section 2.

3.6.3 Discussion and Conclusion

In the present paper, we studied electron beam instabilities of the whistler mode wave and the electrostatic waves propagating parallel to the static magnetic field. Based on the linear theory, we obtained the saturation levels, and the trapping velocities for the two wave modes. For plasma parameters at the equatorial magnetosphere, the electrostatic waves grows much faster than the whistler mode wave, and it is hardly affected by

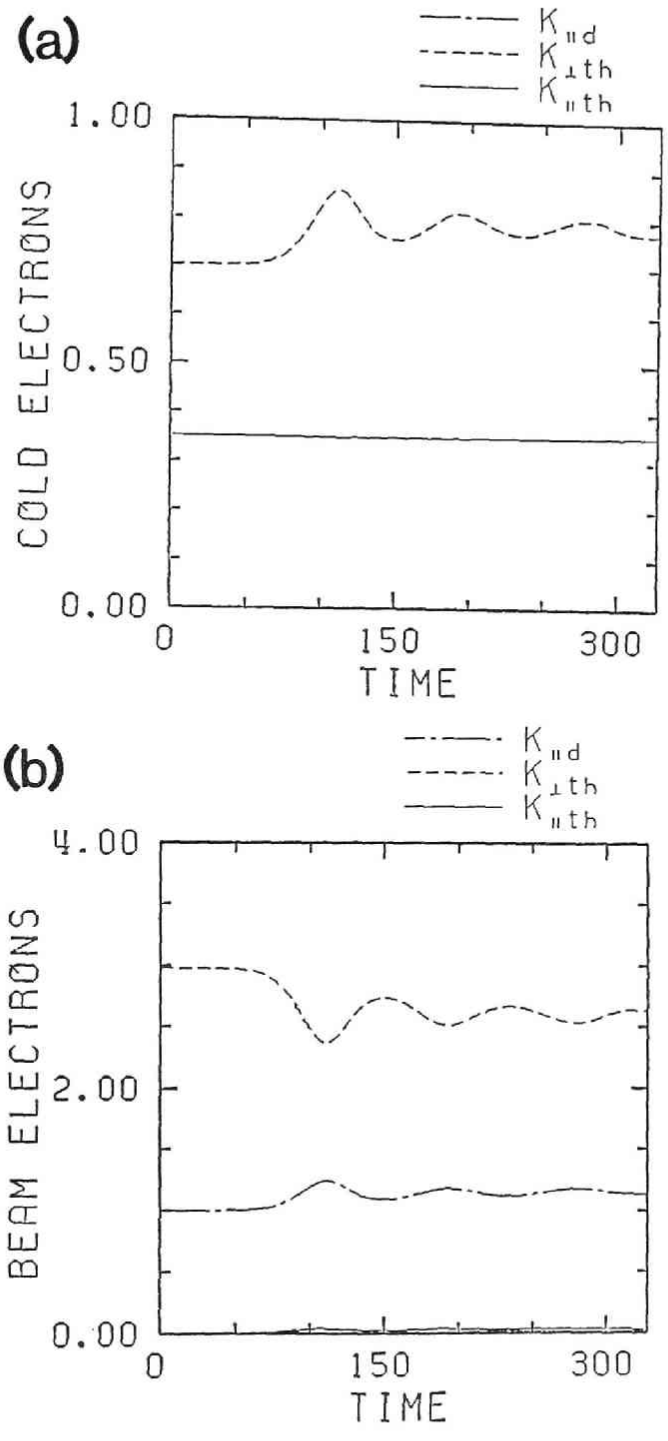

Fig. 3.49 Kinetic energy history in Case E (non-electrostatic case) : (a) cold electrons, (b) beam electrons.

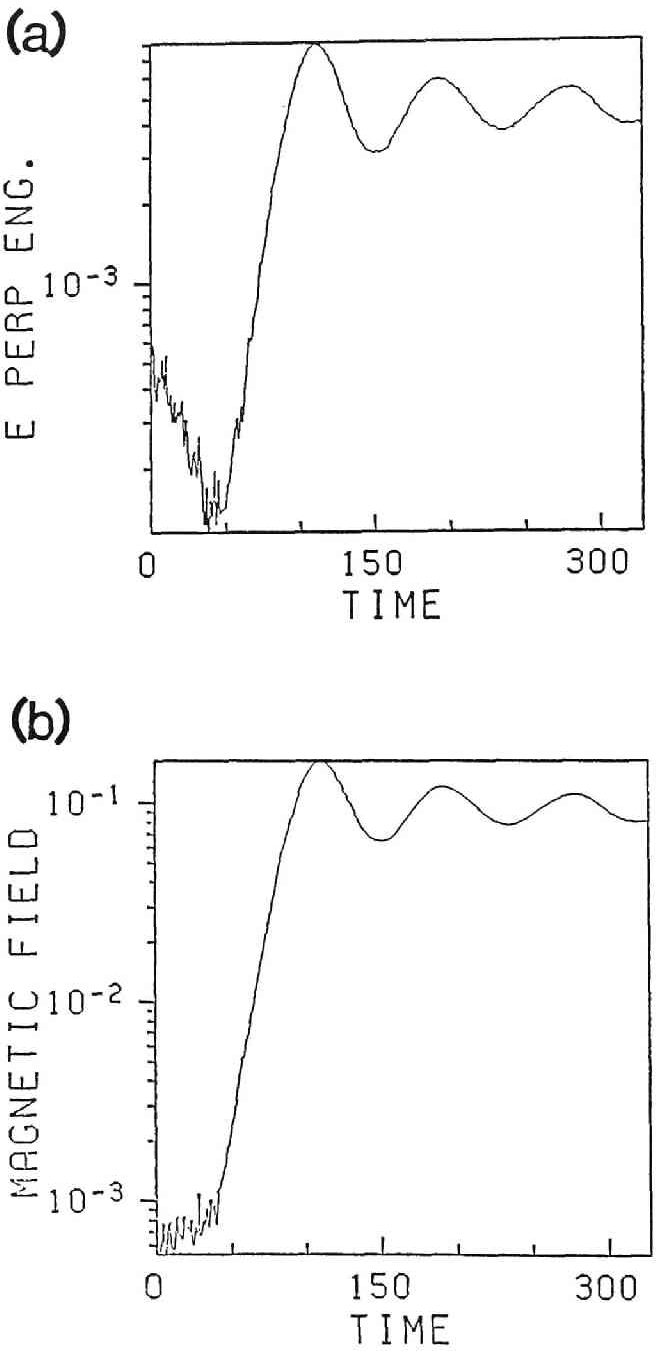

Fig. 3.50 Wave energy history in Case E : (a) perpendicular electric field, (b) perpendicular magnetic field.

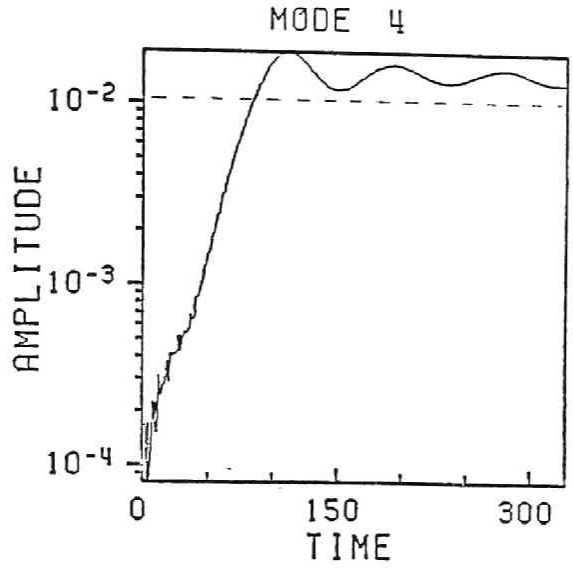

Fig. 3.51 Time history of perpendicular magnetic field of mode 4 in Case E. The dashed lines the theoretical saturation level.

the whistler mode wave. The growth rate, saturation level and trapping velocity of the electrostatic wave in the simulations are in good agreement with the linear theory. However, the whistler mode instability is strongly affected by the electrostatic waves through modulation of the electrostatic phase trapping. Without an initial coherent wave, whistler mode waves hardly excited from the thermal fluctuation noises. When we put an initial coherent wave, it grows and saturates. However, the growth rate and the saturation level are smaller than the theoretical values.

Saturation levels of the whistler instability depend on the initial wave amplitudes due to the effects of co-existing electrostatic waves. This fact is one of possible causes for the existence of power threshold for growth of coherent VLF signals in the magnetosphere [Helliwell et al., 1980]. If the initial amplitude is too small, the beam electrons are diffused by the electrostatic waves, before the growing whistler wave reaches a detectable value.

In the present study, we assumed a very sharp electron beam as a source of free energy. Since the growth rates of the electrostatic waves excited by the electron beam, is much larger than that of whistler mode wave, the electron beam soon diffuse over the width of $2V_{tS}$ before the whistler mode wave grows. Therefore, whistler wave studies with the assumption of a very sharp beam are not relevant to a realistic interpretation of observations, although the interaction itself is

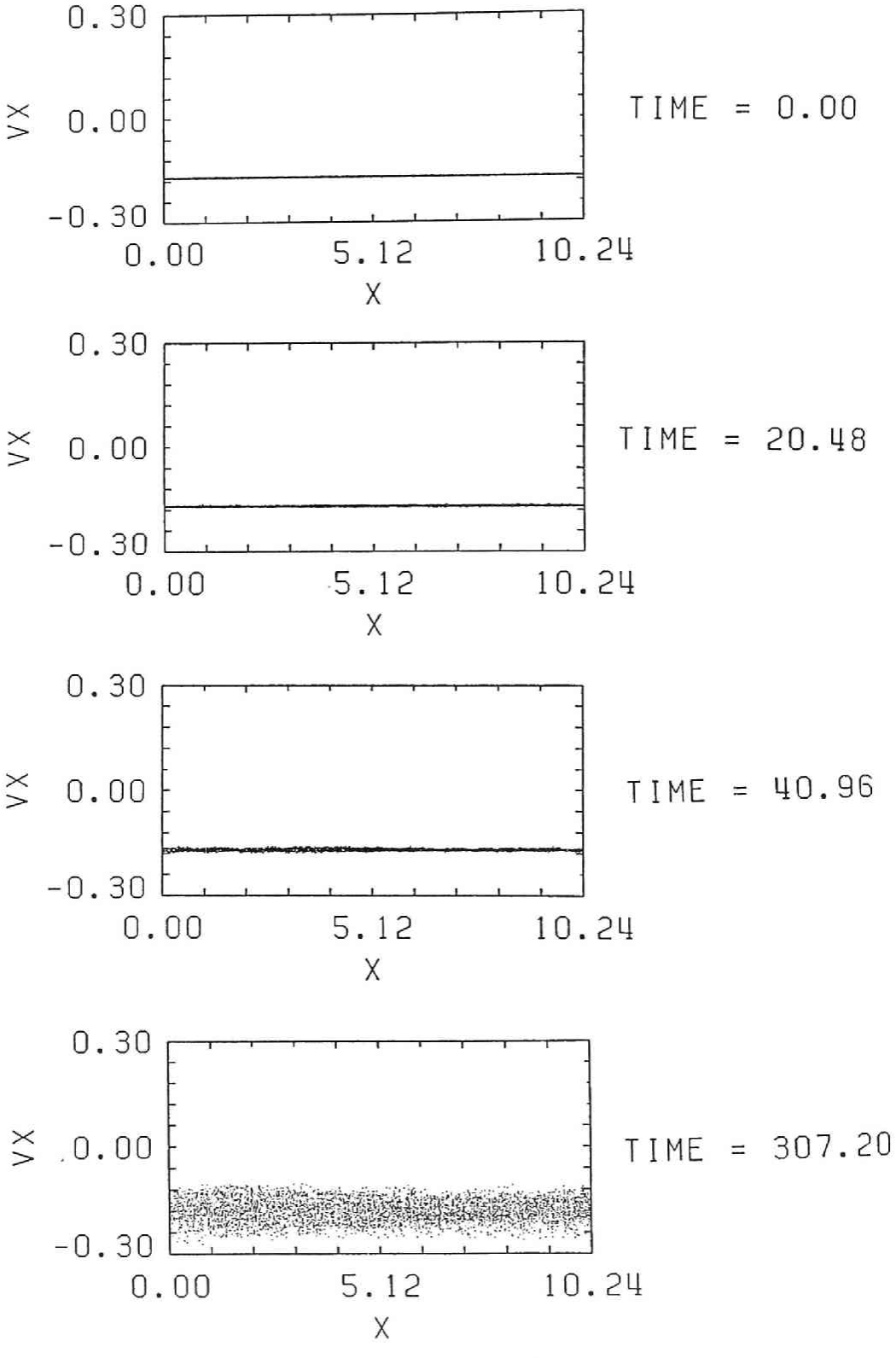

Fig. 3.52 Phase plots of beam electrons in the x - $v_{\parallel}$ space : Case E where no electrostatic wave exists.

physically interesting.

CHAPTER 4
ELECTROMAGNETIC ION CYCLOTRON MODE INTERACTIONS AND HEAVY ION HEATING

4.1 Introduction

It has recently been recognized that heavy ions are important to the dynamics and stability of different regions in the earth's magnetosphere. Shelley et al. [1976] and Ghielmetti et al. [1978] have reported observations of intense fluxes of O^+ streaming up high-latitude auroral field lines at altitudes of ~ 1 R_E. Data from the S3-3 satellite show that ion composition can vary from 10% to more than 90% oxygen [Mizera et al., 1981].

The inferences of O^+ streams deep in the magnetotail boundary layer by Frank et al. [1977] and Hardy et al. [1977] suggest that there might be measurable fluxes of energetic O^+ ions of terrestrial origin deep in the plasmasheet. Results from the energetic ion mass spectrometer on ISEE-1 show that the plasmasheet has a significant and variable ionospheric component (He^+ and O^+) which represents from more than 10% to 50% of the total number density [Petersen et al., 1981].

At the geostationary orbit, O^+ and He^+ ions of medium energy (~ 10 keV) have been found to be important constituents of magnetospheric plasma, especially during magnetic storms [Geiss et at., 1978; Young, 1979; Balsiger et al., 1980]. But the most intriguing observational results obtained by GEOS-1, -2 and ATS-6 spacecrafts are that He^+ or O^+ ions are heated up to suprathermal energies (~ 100 eV) at times when large amplitude ions cyclotron waves (ICW's) are detected [Young et al., 1981; Mauk et al., 1981; Roux et al., 1982; Fraser, 1982].

The facts that heavy ions are found in many different regions of the magnetosphere, that they are of terrestrial origin and that they can be a major constituent of the plasma have motivated the community to reexamine theoretical studies of wave particle interactions including the effects of heavy ions. When studying wave particle interactions in the presence of heavy ions, there are two problems. The first is the effect of heavy ions on the dynamics and stability of plasmas. The second and more pertinent problem is to understand the mechanism responsible for energizing such heavy ions.

In several studies, these questions have been stated for different regions of the magnetosphere. On auroral field lines, the heating of O^+

has been studied by using electrostatic waves [Lysak et al., 1980; Papadopoulos et al., 1980; Ashour-Abdalla et al., 1981; Ashour-Abdalla and Okuda, 1984]. Lysak et al. [1980] used strong turbulence theory, which considered the ion orbits in a set of fixed amplitude waves with a definite phase relation. Papadopoulos et al. [1980] argued that the heavy ions form a minority constituent of many magnetospheric multi-ion plasmas. As such, the heavy ions do not affect the collective mode structure of the plasma due to their small abundance ratios. They thus examined the acceleration of large M/Q ions in the presence of a coherent large amplitude electrostatic hydrogen cyclotron wave. It was found that when the wave amplitude exceeds a certain critical value the particle orbits become stochastic and the particles can be accelerated by the wave. The most important result was that the maximum energy achieved by an ion scales as $(M/M_H)^{5/3}$, where M_H is the mass of hydrogen and M is the mass of the ion under consideration. They concluded that heavy ions are thus preferentially accelerated. Ashour-Abdalla and Okuda [1984] studied the acceleration of ions on auroral field lines associated with the current-driven electrostatic ion cyclotron waves in a plasma consisting of hydrogen and oxygen ions by simulation techniques. To model the ionospheric source of electrons they developed a simulation model in which drifting electrons were allowed to enter at the end of the system. They found that the oxygen transverse heating generally exceeds that of hydrogen ions at the low altitude end of the field line.

There have also been studied using electromagnetic waves to explain the acceleration of heavy ions. Theoretically it is well known that the presence of heavy ions greatly modifies the propagation and amplification characteristics of magnetospheric electromagnetic waves. A detailed analysis of the wave spectra and energetic proton distribution measured on GEOS-1 have shown that the observed wave spectra can be interpreted in the framework of the linear theory of ion cyclotron instability excited by an anisotropic proton distribution in a plasma containing a small fraction ~5 -15% of He^+ ions [Roux et al., 1982]. Gomberoff and Cuperman [1982] have also performed a theoretical analysis in order to evaluate the change in the temporal growth rate of such instabilities for various plasma parameters. Gomberoff and Neira [1983] undertook the task of evaluating the corresponding change in the spatial growth rate. However, such studies have generally been done assuming the background plasma to be completely cold, $T(H^+) = T(He+) = 0$, whereas it is known from GEOS and DE experiments that both electrons and ions can reach a temperature equal to or higher

than 10 eV [Decreau et al., 1982; Chappell, 1983]. Under such conditions, cyclotron absorption by the heavy ion species will compete with the amplification induced by hot protons, and growth rates will be strongly modified, especially in the vicinity of the heavy ion gyrofrequency. Recently Gendrin et al. [1984] carried out a parameter search of ion cyclotron waves including the finite temperature effects associated with the cold species.

The heating of heavy ions by electromagnetic ion cyclotron waves has been addressed by several authors. Gendrin and Roux [1980] have studied the possibility that the observed heating of He^+ ions up to suprathermal energies could be explained by quasi-linear diffusion. Indeed quasi-linear diffusion of resonant He^+ ions having low initial parallel and perpendicular velocities can lead to a considerable increase of the perpendicular He^+ ion distribution. However, to heat the bulk of He^+ distribution, sufficient wave energy must be available at frequencies where a resonant interaction with the cold heavy ion species can take place, i.e., at frequencies which are near the heavy ion gyrofrequency. Gendrin et al. [1984] found that the maximum growth rates occur at frequencies far from the heavy ion gyrofrequency; consequently these waves cannot resonate with the bulk of heavy ion distribution. In search of another heating mechanism, Mauk [1982, 1983] studied the nonresonant interaction between an electromagnetic ion cyclotron wave and thermal He^+ ions. He showed that associated with the increase in the He^+ ion perpendicular velocity, phase bunching was observed. Unfortunately, Mauk's calculations were done by neglecting the ion parallel velocity, which led to incorrect quantitative results: an apparently infinite increase of $v_\perp$ as time elapses and a strong effect even when the wave frequency is equal to the helium cyclotron frequency. Berchem et al., [1983] and Berchem and Gendrin [1984] extended Mauk's work to include the parallel velocity of the ions. They found that phase bunching occurs, and the particle attains large perpendicular velocities. They carried out a parameter search as a function of initial parameters and were able to derive approximate analytical expressions for the maximum temperature of the heavy ions attained. These calculations were test particle calculations in which the wave amplitude was kept constant, and were therefore not self-consistent. In search of self-consistency, Tanaka and Goodrich [1984] used simulation techniques to study the heating of heavy ions at different regions of the magnetosphere with particular emphasis on the heating of Alpha particles at the bow shock. As such they considered a plasma consisting of hot highly anisotropic protons

in the presence of a minority species. Since these studies were concerned with gaining an understanding of He^{++} at the shock region, they did not include a cold hydrogen background representative of the ionospheric source.

For the sake of completeness, it is worth mentioning that a similar mechanism (resonant interaction of one ion species with waves generated by a majority ion) has been invoked to explain the excess of He^{++} ion bulk velocity in the solar wind. However, it is only until recently that the fundamental modification brought in to the dispersion relation by the presence of the heavy ions has been correctly taken into account, which means that the results previously obtained are not relevant to the problem we are studying here (see Isenberg, [1984a,b] and references therein).

In this chapter, our aim is to explain the heating of He^{+} observed by the GEOS satellite at L ~ 7. Our starting points is the observation set from the GEOS satellite. Having developed the linear theory analysis in Section 4.2 [Gendrin et al., 1984], we undertake a simulation study of electromagnetic ion cyclotron waves in a plasma consisting of hot anisotropic protons, a dominant thermal hydrogen plasma, and a minority species of helium ions which will be described in Section 4.3 [Omura et al., 1984].

4.2 Linear Analysis of Ion Cyclotron Interaction

Recent experimental data [e.g., Young et al., 1981; Mauk et al., 1981; Roux et al., 1982] obtained on board geostationary spacecraft (GEOS 1 and 2, ATS 6) have shown the importance of cold He^{+} ions in the generation of electromagnetic ULF ion cyclotron waves (ICW). A detailed analysis of the simultaneously measured wave spectra and the energetic proton distributions even has shown that the observed wave spectra can be interpreted in the framework of the linear theory of ion cyclotron instability excited by an anisotropic proton distribution in a plasma containing a small fraction (~5-15%) of He^{+} ions (see, for example, Roux et al. [1982, Figures 1 and 9].

Gomberoff and Cuperman [1982] have done a theoretical analysis of this kind of interaction in order to evaluate the change of the temporal growth rate of such instabilities for various plasma parameters. Gomberoff and Neira [1983] performed a similar analysis to evaluate the corresponding change in the spatial growth rate. Mauk [1982a] has extended these studies

by computing the integrated growth along the propagation path. The parameters of interest are the number density of cold H^+ and He^+ ions, $n(H^+)$ and $n(He^+)$ (the total cold plasma density n_c being equal to $n(H^+)+n(He^+)$, the hot proton concentration ratio n_h/n_c, the hot proton anisotropy $A_h = (T_\perp/T_\parallel)_h - 1$, and the hot temperature $T_{\parallel h}$ ($\kappa T_\parallel / 2 \sim$ 10-20kev).

However, such studies have been done assuming the background plasma to be completely cold: $T(H_c^+) = T(He^+) = 0$, whereas it is known from GEOS and DE experiments that both electrons and ions may reach a temperature equal to or higher than 10 eV [Décréau et al., 1982; Horne et al., 1981; Chappell, 1983]. Under such conditions, cyclotron absorption by the heavy ion species will compete with amplification induced by hot protons, and growth rates will be strongly modified, especially in the vicinity of the heavy ion gyrofrequency. It is therefore necessary to extend the previous computations by including the finite temperature effects associated with the cold species.

A second reasons for refining the linear stability analysis is as follows. Gendrin and Roux [1980] suggested that quasilinear diffusion of He^+ ions in the presence of ICW's could be responsible for the He^+ temperature increase which follows, within a time delay of the order of 10-20 min, the appearance of ULF waves (see, for example, Young et al.[1981, Figures 9, 11, and 1). Indeed, quasi-linear diffusion of resonant He^+ ions having low initial parallel and perpendicular velocities can lead to drastic increase of the He^+ ion energy, especially in the perpendicular direction (see, for example, Gendrin [1981]). However, in order for this process to be efficient, waves must be generated at frequencies which resonate with the bulk in the He^+ distribution, e.g., with particles whose parallel velocity is smaller than or equal to the thermal velocity. If these waves cannot be generated by linear instability, such a process would be inefficient [Gendrin, 1983]. Therefore it is necessary to know precisely the frequency range of the instability in the presence of thermal He^+ ions, especially in the vicinity of the He^+ gyrofrequency f_{He+}.

The above two reasons have motivated a parameter study of ICW generation by anisotropic distribution of energetic protons in a magnetoplasma containing a small proportion of He^+ ions $n(He^+)/n(H_c^+) = p \simeq$ 1-20%) having small but finite temperature. The linear dispersion relation has been calculated numerically by a Taylor expansion of the complex plasma dielectric function ε. The parameters which could be introduced in this calculation for each species are its number density, parallel temperature,

and perpendicular temperature (bi-Maxwellian distributions are assumed). Altogether there are four species: hot protons, cold protons, cold He^+ ions, and cold electrons The wave polarization mode could also be selected. The dc magnetic field intensity B_o is defined by $\beta_{\parallel} = 2\mu_o n_K T_{\parallel}/B_o^2$. It was chosen equal to 140 nT, a typical value in the geostationally orbit. Similarly, the number density of the cold protons was set equal to $n(H_c^+) = 10\ cm^{-3}$ [e.g., Higel and Wu Lei, 1984]. The computations were restricted to left-handed waves propagating in a direction parallel to B_o, to real values of the wavenumber k, and to hot proton parallel temperatures such that $kT_{\parallel h}/2$ - 15 keV. The results of varying this parallel energy are not included in his study, since they are well known and do not depend significantly on the plasma composition: an increase in $T_{\parallel h}$ corresponds to an increase in the maximum growth rate and to a decrease in the corresponding frequency [e.g., Gendrin et al., 1971]. With some exceptions, which will be specified in due time, the ratio $T_{\perp}/T_{\parallel}$ is set equal to 2 for hot protons and 1 for the cold population.

4.2.1 Role of He^+ Concentration

In Figures 4.1 and 4.2 the variations in the temporal and spatial growth rates (ω_i and ω_i/kV_g) are plotted as functions of the real frequency ω_r (normalized to proton angular gyrofrequency Ω_H^+) for three different He^+ concentration ratios, p = 0, 0.05, 0.2. As expected, when He^+ ions are introduced, waves are unstable in two frequency ranges: a low frequency (LF) and a high-frequency (HF) range, a phenomenon which is at least partially responsible for the frequency gap observed around F_{He+} [Mauk et al., 1981]. The LF branch is unstable between f - 0 and $f = f_1$. The value of f_1 depends on the He^+ concentration, temperature, and anisotropy, as will be discussed later. The HF branch has a low frequency cutoff f_2 and a high-frequency cutoff f_3. Low-frequency cutoff f_2 is very close to the cutoff frequency of the HF branch, defined by $f_{co} = f_{He+}[1 + 3p/(1 + p)]$ [e.g., Gendrin and Roux, 1980], whereas f_3 is the critical frequency of the instability, which depends not on the heavy species characteristics but merely on the hot proton anisotropy [Kennel and Petcheck, 1966]; $f_3 = f_{H+} A_h/(A_h + 1)$.

Figure 4.1 shows that contrary to what is sometimes claimed, introducing a small number of He^+ ions into the plasma does not lead to an increase in the maximum temporal growth rate of the instability, at least when this number does not greatly modify the total number of cold

particles. This falsely held belief is due to the fact that the very first computations of ICW growth rates in the presence of heavy ions involved heavy ions as the only cold species [Mark, 1974; Cuperman et al., 1975; Gomberoff and Cuperman, 1977]; it is well known that increasing the number of cold particles in a medium which contains a constant number of hot particles leads to a drastic increase of the growth rate, at lease until an optimum value of n_c/n_h is reached [Cuperman and Landau, 1974; Perraut and Roux, 1975; Gendrin, 1975]. However, as is shown here, when n_{ch} does not vary much, the maximum growth rate is not changed when $n(He^+)$ is increased.

The maximum spatial growth rate itself is not increased much when He^+ ions are introduced (Figure 4.2). However, at most frequencies within the frequency range of the instability, the spatial growth rate may be increased by a factor as large as 10. These frequency ranges are shifted away from the He^+ gyrofrequency toward lower frequencies (LF branch) or toward higher frequencies (HF branch). Two facts explain this behavior. When He^+ ions are introduced, at any given frequency, V_g is decreased (see, for example, Gendrin and Roux [1980, Figure 1]), so that at any given frequency for which ω_i remains approximately the same, ω_i/kV_g increases. However, this enhancement takes place only in the frequency ranges where waves can either propagate (cutoff effects in the HF branch) or be generated (heavy ion cyclotron absorption in the LF branch).

One may note in Figure 4.1 and 4.2 that the high-frequency cutoff of the LF branch, f_l, is decreasing with increasing He^+ concentration (at a constant temperature), and this characteristic will be explained later.

At this point it is worth commenting on the role which is played by He^+ ions in the generation of ICW's. Clearly, the introduction of He^+ ions does not change the growth rate of these waves. But observations show that when an increase of the thermal He^+ concentration is observed, ULF waves are excited [see Roux et al., 1982, Table 3], and an explanation of this effect must be found. An explanation has been proposed which takes into account the inhomogeneity of the medium and which is valid at least for waves generated in the HF branch [Rauch and Roux, 1982]: in this frequency range and in the presence of He^+ ions, waves bounce back and forth with no loss along the wave magnetic field line between mirror points located at low magnetic latitudes. Therefore the role of He^+ might be to enhance the length over which amplification takes place and not to increase the growth rate per unit length.

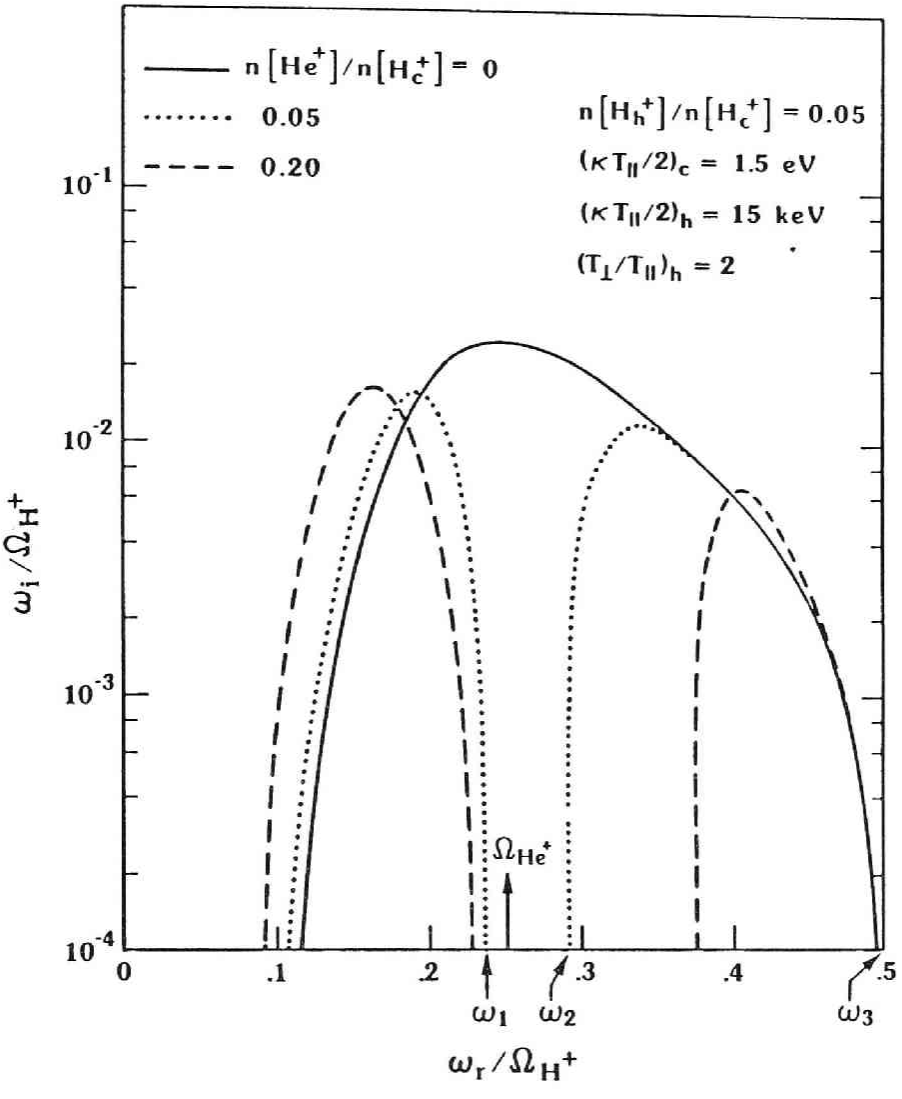

Fig. 4.1 Variation of the temporal growth rate with frequency for three He^+ concentrations. The high-frequency cutoff of the low-frequency branch, f_1, decreases when $p = n(He^+)/n(H_c^+)$ increases. The low-frequency cutoff of the high-frequency branch, f_2, increases when p increases. The high-frequency cutoff of the high-frequency branch, f_3, depends only on the hot proton anisotropy. In the two branches and for all concentrations the maximum growth rate decreases when cold He^+ ions are introduced.

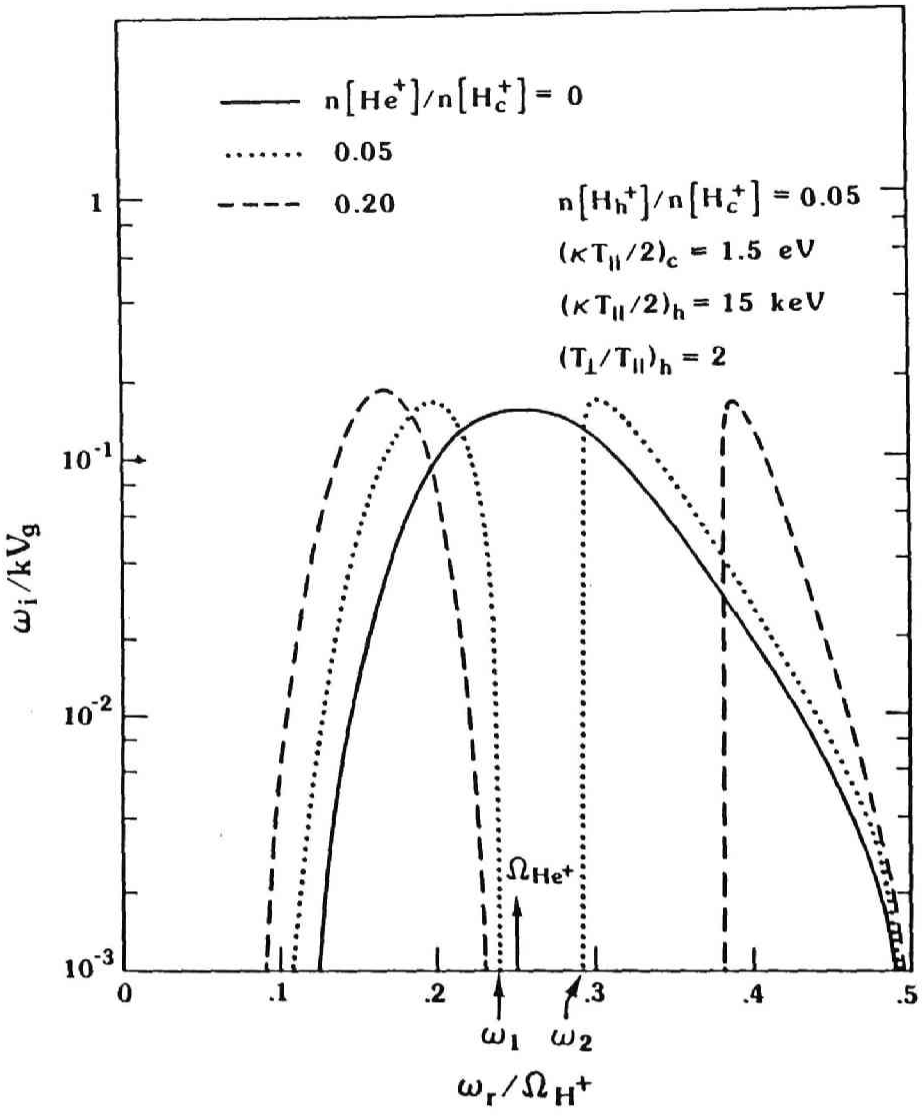

Fig. 4.2 Variation of the spatial growth rate with frequency for three cold He^+ concentrations. The maximum growth rate is only slightly increased when cold He^+ ions are introduced.

4.2.2 Role of He^+ Temperature

Figure 4.3 represents the variation of the temporal growth rate with frequency for a constant He^+ concentration (ρ - 0.2) and three different He^+ temperatures: $\kappa T_{\parallel}(He^+)/2$ = 1.5, 15, and 150eV. The thermal ions are assumed to be isotropic ($T_{\perp}(He^+)/T_{\parallel}(He^+)$ = 1). In the HF branch the three curves are identical. In the LF branch the three maximum growth rates are almost identical, and they occur at almost the same frequency. However,

the cutoff frequency f_1 is decreasing with increasing He^+ temperature.

This can be interpreted in the following manner: since He^+ ions are assumed to be initially isotropic, resonating ions gain energy, and the wave is absorbed [Gendrin, 1981]. When the He^+ temperature is increased, more ions can resonate with a wave at the frequency f slightly smaller than f_{He+}. Therefore the absorption band becomes when He^+ is increased. The frequency f_1 above which absorption by thermal He^+ ions overcomes the amplification by hot protons corresponds to the marginal stability (ω_i = 0). When the He^+ concentration ratio is reduced, a given He^+ resonant velocity corresponds to a higher frequency because of the change in the dispersion curve. Therefore f_1 is also a decreasing function of the He^+ concentration at a fixed temperature (see previous section). These effects are illustrated in Figure 4.4, where the results of the numerical analysis for different He^+ concentrations (Figure 4.1) or temperatures (Figure 4.3) are plotted on the corresponding dispersion curves. The associated He^+ parallel velocity is given by the slope of the line joining the "marginal point" to the point $\omega = \Omega_{He+}$, k = 0. The parallel energy $E_\parallel$ is of the order of $\kappa T_\parallel/2$. Except for the case ρ = 0.05 and $\kappa T_\parallel/2$ = 150 eV, $E_\parallel$ is larger than $\kappa T_\parallel/2$, the difference between $E_\parallel$ and $\kappa T_\parallel/2$ being smaller for higher He^+ temperatures and/or for smaller He^+ concentrations.

Figure 4.4 clearly shows that in general, waves cannot be generated at frequencies at which He^+ ions with parallel energies smaller than the thermal energy can resonate. Consequently, in a homogeneous medium at least, the mechanism proposed by Gendrin and Roux [1980] cannot be efficient, since quasi-linear diffusion cannot involve the bulk of the thermal He^+ distribution. Such an objection was already raised by M. Ashour-Abdalla (personal communication, 1982) and quantitatively justified [see Gendrin, 1983, appendix]. However, in the real inhomogeneous magnetosphere, one may assume that waves are generated off the equator at a frequency f smaller than the local value of f_1. When the wave propagates toward the equator, f/F_{He+} increases, and the local value of f/f_1 may become larger than 1. He^+ ions will be heated there, and the wave will be absorbed. Such a process has been suggested by Mauk [1982a, 1983] for explaining the "frequency gap" below the equatorial He^+ gyrofrequency.

4.2.3 Role of He^+ Anisotropy

The previous arguments are valid only for an isotropic He^+ distribution. When the He^+ distribution has a positive anisotropy ($T_\perp >$

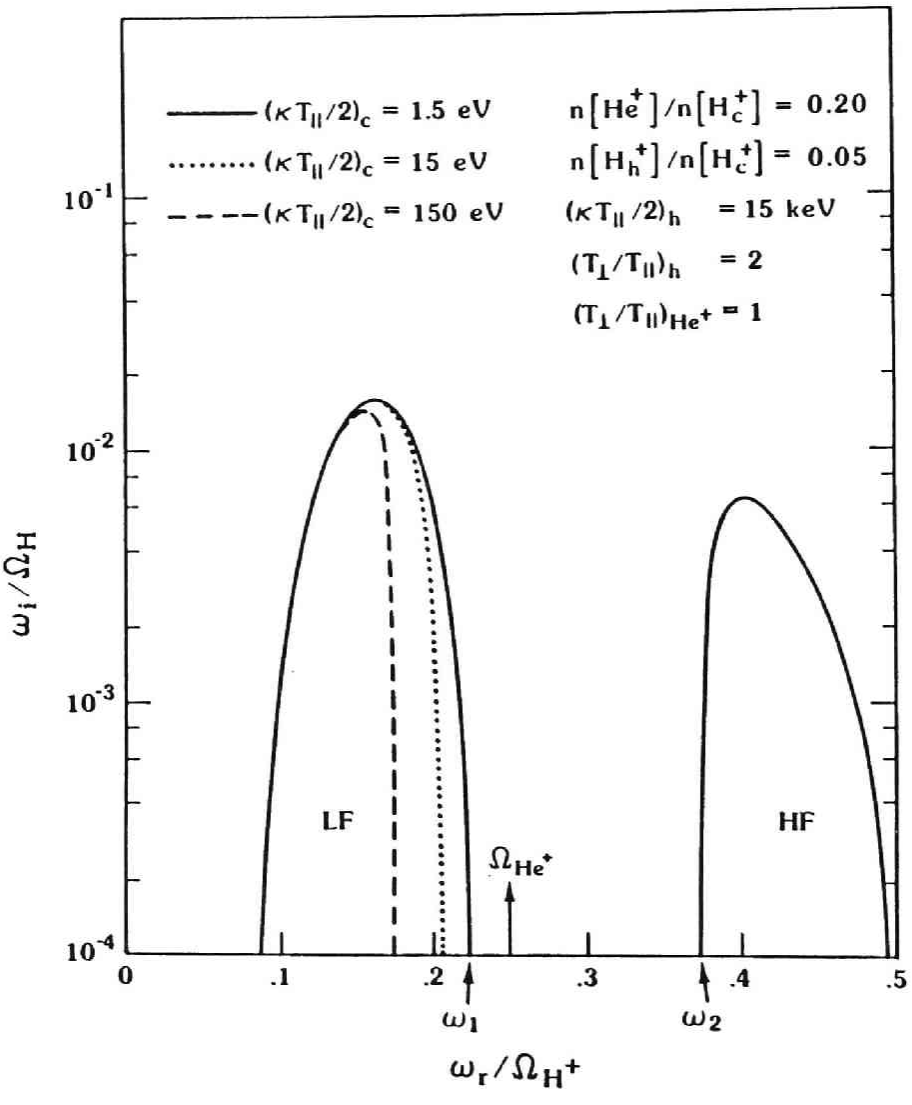

Fig. 4.3 Variation of the temporal growth rate with frequency for three values of the cold population temperature. The cold particle anisotropy is equal to zero. In the HF region the three curves are almost identical. In the LF region the high-frequency cutoff f_1 is a decreasing function of the He^+ temperature.

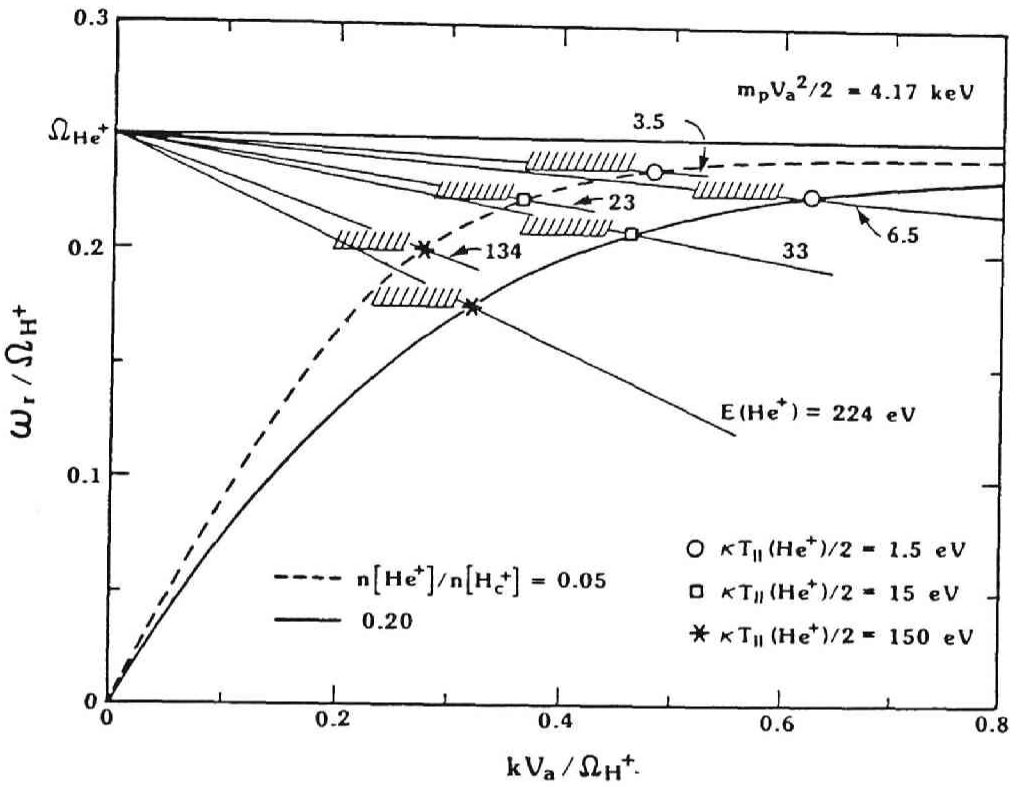

Fig. 4.4 Variation of the marginal frequency f_1 and of the marginal parallel velocity of He^+ ions for three He^+ temperatures and two waves. The hatched areas correspond to absorbed waves. The marginal parallel velocity is higher than the parallel thermal velocity, so that waves which are naturally unstable cannot resonate with the bulk of the He^+ distribution function. The normalizing parameter V_a is the Alfvén velocity associated with the cold protons only.

$T_{\parallel}$) the situation is different since, as has already been suggested by Brice and Lucas [1975], He^+ ions themselves may induce a positive growth rate. Evidence for this is shown in Figure 4.5, which was obtained for $\kappa T_{\parallel}(He^+)/2$ = 15 eV and $T_{\perp}(He^+)/T_{\parallel}(He^+)$ = 20. In such a case the marginal frequency f_1 is greatly displaced toward higher frequencies.

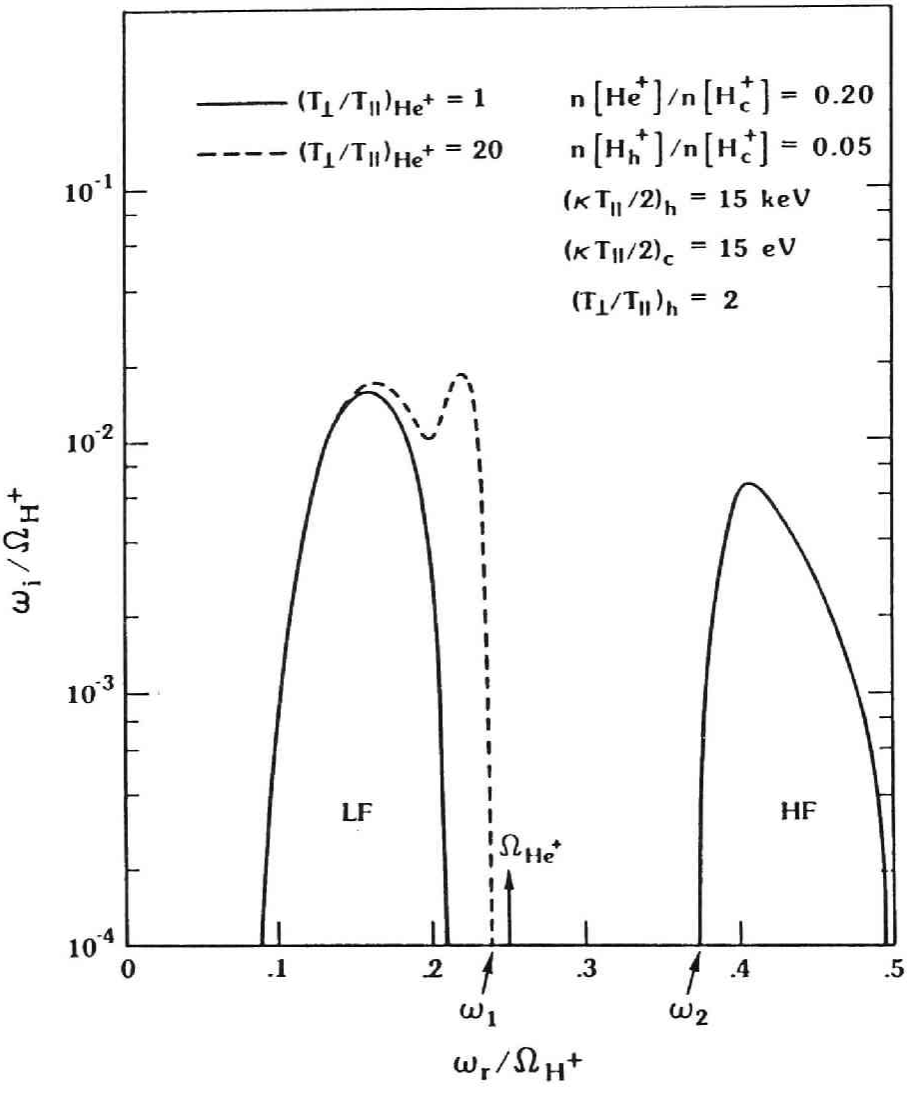

Fig. 4.5 Variation of temporal growth rate with frequency for two different anisotropies of the He^+ ion distributions. In the HF branch the two curves are almost identical. In the LF branch the marginal frequency f_1 increases when A_{He} increases.

4.2.4 Role of Hot Proton Concentration

In a plasma containing only one ion with two different temperatures the growth rate can be expressed as

$$\omega_i = \frac{k_1 n_h}{n_c^{3/2}} \exp\left(-\frac{k_2}{n_c}\right) \qquad (4.1)$$

where k_1 and k_2 depend on the magnetic field intensity and on the anisotropy and temperature of the hot protons [e.g., Gendrin, 1975]. Consequently, when n_c is kept constant, ω_i should be proportional to n_h. This is what is observed up to a certain value (~ 5%) of the ratio n_h/n_c (Figure 4.6). Above this value the temporal growth rate increases less rapidly than does n_h, especially in the LF branch. However, the spatial growth rate in the same branch increases more rapidly than does n_h. Unfortunately, our results cannot be compared with those of Gomberoff and Cuperman [1982], since these authors have made their computations for a constant β. Consequently, the hot proton energy which thus varies as n_h^{-1} is far from being a constant when n_h is varied.

For large β values the nature of the instability (absolute or convective) must also be discussed. Extending the computation of Wandzura and Coroniti [1975] to multicomponent plasmas, Roux et al. [1982] have shown that for the parameters A and ρ which we are using ($A = 1$, $0 < \rho < 0.2$), the instability becomes absolute when $\beta_\perp$ becomes larger than ~1 (their Figure 12). With the numerical values adopted here for B_o (140nT) and for $E_\perp$ (30keV), $\beta_\perp$ is larger than unity for $n_h > 1.6 cm^{-3}$. In other words, the curves which are drawn in Figure 4.6 represent truly convective instabilities up to an abscissa equal to 0.16, since $n(H_c^+) = 10\ cm^{-3}$, i.e., up to the point where the linear spatial growth rate strongly departs from proportionality with n_h.

4.2.5 Instabilities in k Space

A numerical simulation program for studying electromagnetic wave-particle interactions in a multicomponent plasma has been started at the University of California at Los Angeles [Omura et al., 1983]. In the simulation codes the grid spacing a and the system size L are important parameters to which the wavenumbers of the growing modes must be compared, that is, it is necessary that $L^{-1} \ll k/2\pi \ll a^{-1}$. Additionally, it is recommended that the parameters of the simulation experiment be selected so that the fewest modes are simultaneously excited. Figures 4.7a and 4.7b illustrate the effects of change in the simulation parameters. The temporal growth rate (in a periodic system the waves are standing, and the spatial growth rate is meaningless) is plotted as a function of k for $\rho = 0.2$, $n_h/n_c = 0.042$, and $\kappa T_{\parallel h}/2 = 15$ keV.

In Figure 4.7a, obtained for the two extreme values of $\kappa T_\parallel(He^+)/2$ (1.5 and 150eV), the anisotropy if so large ($A_h = 1$) that the two branches are

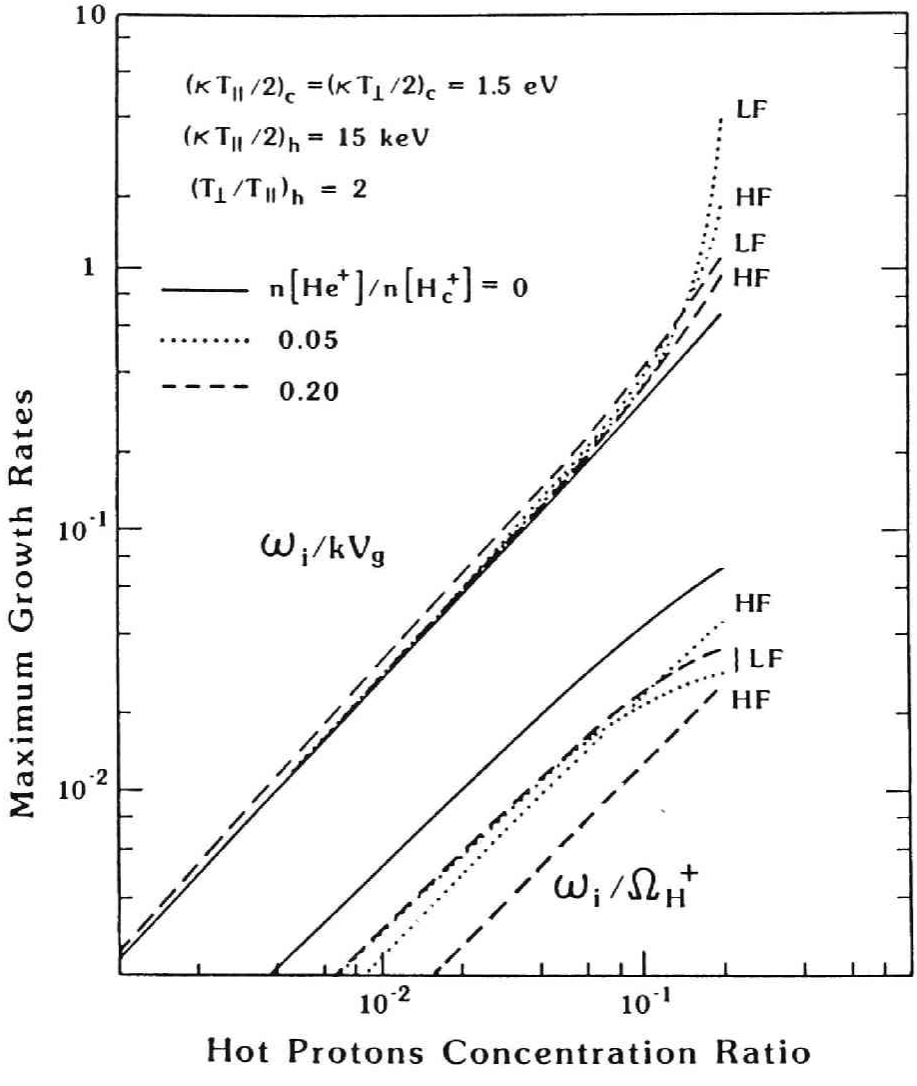

Fig. 4.6 Variation of the temporal and spatial growth rates with the hot proton concentration n_h/n_c. The cold particles' anisotropy is equal to zero. The curves are labeled according to the He^+ concentration ratio $\rho = n(He^+)/n(H_c^+)$. These curves are valid for B_o = 140 nT and $n(H_c^+)$ = 10 cm^{-3}.

simultaneously excited, which may pose a problem for the interpretation of the results. Additionally, the spectrum in k is rather large for each branch. This phenomenon has two branches consequences: (1) the grid spacing must be small so that it can accommodate large wavenumbers and (2) the run has to be long so that the wavenumber which corresponds to the maximum growth rate can emerge from the other wavenumbers. Increasing the He^+ temperature leads to a decrease in the spectral width, but only in the

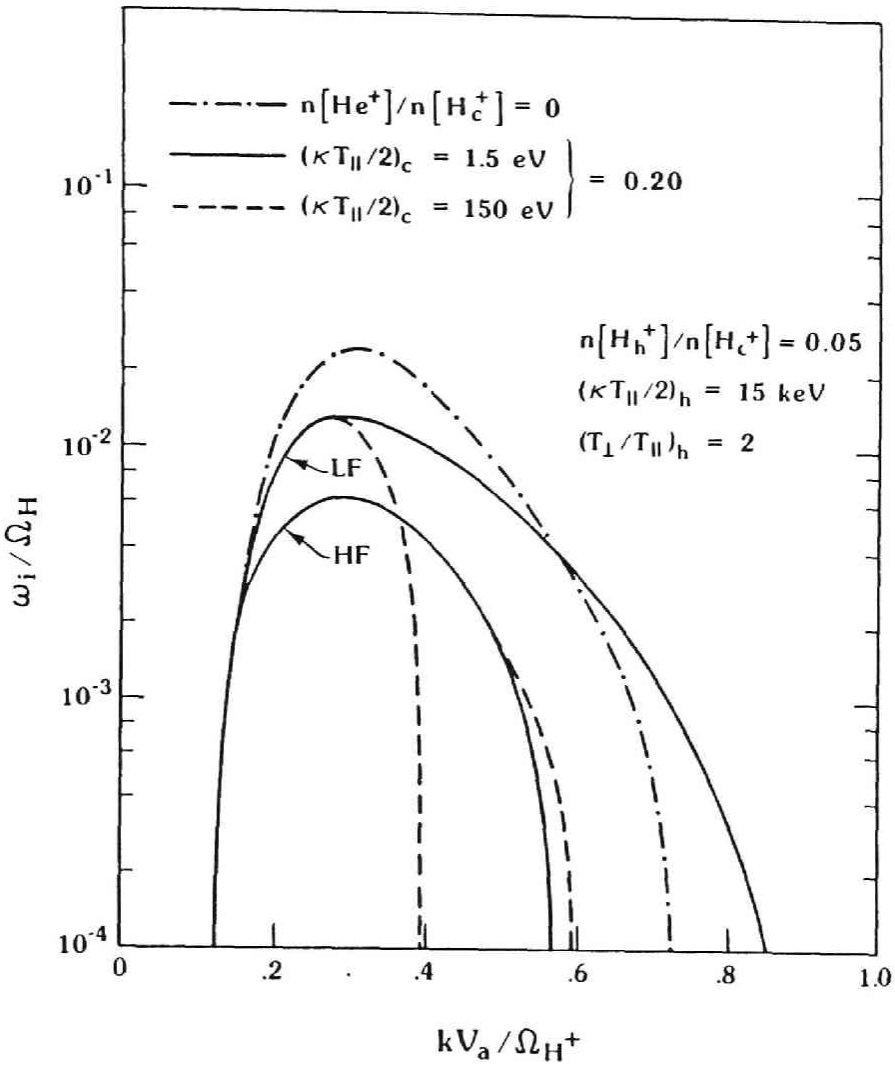

Fig. 4.7a Variation of the temporal growth rate with wave number for two He^+ concentration and two He^+ temperatures. The cold particles' anisotropy is equal to zero. Note the wide range of k values over which waves are unstable.

LF branch.

Figure 4.7b shows the results obtained for two He^+ temperatures when the hot proton anisotropy is reduced (from 1 to 0.5). When A_h = 0.5, the

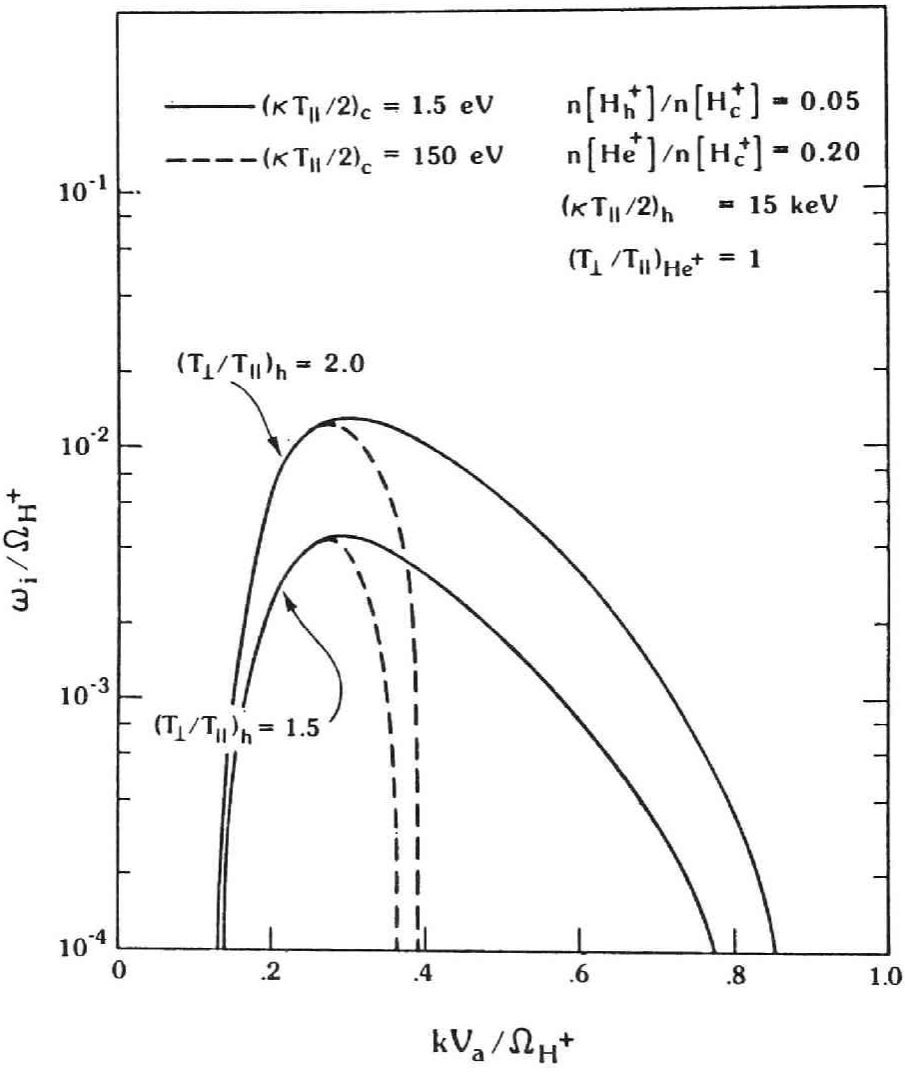

Fig. 4.7b Variation of the temporal growth rate with wave number for two He^+ temperatures and two hot proton anisotropies, $A_h = (T_\perp/T_{\parallel})_h - 1$. The cold particles' anisotropy is equal to zero. For these values of the parameters the HF branch is not unstable when A_h = 0.5. The HF branch, which is unstable when A_h = 1, is not represented here. Note the narrowing of the unstable spectrum when A_h is reduced and $T(He^+)$ is increased simultaneously.

HF branch is no longer excited, as expected from Kennel and Petschek's [1966] theory [$f_3 = A_h/(A_h+1) < f_{co}$], an effect which will simplify the interpretation of the results (in Figure 4.7b the HF branch which exists for A_h = 1 has not been plotted). The maximum growth rate for the LF

branch is almost the save as for the case A_h - 1, so that nothing is lost in the e folding time. By selecting those parameters (A_h = 0.5 and $\kappa T_{\parallel}(He^+)/2$ = 150 eV) one has only one excited mode (LF) with a reduced width ($0.15 < kV_a/\Omega_{H+} < 0.35$) instead of two modes over a wide range of k values ($0.15 < kV_a/\Omega_{H+} < 0.85$) Another advantage of such a parameter choice is that the temperature difference between the hot and the "cold" populations is reduced, thereby minimizing the conflicts in the choice of the scaling parameters. The disadvantage is that one must choose a larger number of hot particles per cell if one wants to be able to reproduce reasonably well a bi-Maxwellian distribution with such a low anisotropy [Omura et al., 1983].

4.2.6 Conclusions

A parameter study of ICW generation in a multicomponent plasma has been made. The results can be summarized as follows.

1. The introduction of a small fraction of cold heavy ions in a plasma already containing a noticeable number of cold protons does not drastically change the maximum growth rates (both temporal and spatial) of unstable electromagnetic ion cyclotron waves, a conclusion already reached by Mauk [1982a].

2. Depending on the anisotropy of the hot proton distribution, waves can be excited in two frequency ranges: a low-frequency range and a high-frequency range. As is expected from linear theory, the low-and high-frequency cutoffs of the unstable waves belonging to the HF branch are determined by the cold He^+ concentration and by the hot proton anisotropy, respectively. As is shown in this study, the high-frequency cutoff of the unstable waves belonging to the LF branch is a function of the heavy ion concentration, temperature, and anisotropy.

3. Waves generated by hot proton free energy cannot resonate with the bulk of the thermal heavy ion velocity distribution. Consequently, quasi-linear effects in a homogeneous medium, at least, cannot account for the heating of the heavy ions. Inhomogeneity effects [Mauk, 1982b, 1983; Berchem et al., 1983, also unpublished manuscript, 1984] must be invoked to explain this phenomenon.

4. During the linear phase a wide range of wavenumbers are generally excited. Only for specific combinations of the plasma parameters is this range noticeably reduced. Such a result is important for deciding which parameters should be used in numerical simulations.

4.3 Simulation Study of Heavy Ion Heating

One of the challenging magnetospheric plasma physics problems is the heating of heavy ions observed in the equatorial magnetosphere in conjunction with ion cyclotron waves (ICW) generated by anisotropic hot protons (i.e. GEOS-1 and 2 and ATS 6 results). The complexity of the mechanisms involved in this phenomenon is such that a numerical simulation is the only way to disentangle the problem. In this section we present the results of such a simulation. In Subsection 4.3.1. the computational model used in the present study is described. Simulation results of the three ion component plasma are presented in Subsection 4.3.2. We conclude in Subsection 4.3.3 by summarizing and discussing the pertinent heating mechanisms.

4.3.1 Simulation Model

We have developed a one dimensional electromagnetic hybrid simulation code [Sgro and Nielson, 1976; Byers et al., 1978] where electrons are treated as a massless fluid and ions are treated as particles moving in the four dimensional phase space (x, v_x, v_y, v_z). Since we are studying low frequency phenomena, we neglect the transverse displacement current in Maxwell's equations (Darwin approximation) as

$$\frac{\partial \vec{B}}{\partial t} = - \text{curl } \vec{E} \tag{4.2}$$

$$\mu_o \vec{J} = \text{curl } \vec{B} \quad . \tag{4.3}$$

We also neglect electron inertia effects for low frequency waves, and we have from the electron momentum equation

$$-en_e(\vec{E} + \vec{u}_e \times \vec{B}) - \text{grad } p_e - 0 \tag{4.4}$$

where $-e$, n_e, $\vec{u}_e$ and p_e are electron charge, number density, flow velocity and pressure, respectively. Furthermore, we assume the quasi-neutrality condition

$$-en_e + q_s n_s = 0 \tag{4.5}$$

where q_s and n_s are the charge and number density of an "s" ion species, respectively. The electron pressure is integrated in time by using the

electron energy equation

$$\left(\frac{\partial}{\partial t} + \vec{u}_e \cdot \text{grad}\right) p_e = -\frac{5}{3} p_e \, \text{div}\, \vec{u}_e \quad . \tag{4.6}$$

The electron flow $\vec{u}_e$ is obtained from the current equation as

$$\vec{u}_e = (\Sigma q_s n_s \vec{u}_s - \vec{J})/n_e q_e \tag{4.7}$$

where $\vec{u}_s$ is the drift velocity of an "s" ion species. The ion density n_s and drift velocity $\vec{u}_s$ are calculated from the motion of ion particles whose positions and velocities are determined by integrating the equations of motion

$$\frac{d\vec{v}}{dt} = \frac{q_s}{m_s}\left(\vec{E} + \vec{v} \times \vec{B}\right), \qquad \frac{d\vec{x}}{dt} = \vec{v} \quad . \tag{4.8}$$

The magnetic field $\vec{B}$ and the electron pressure p_e are integrated in time using (4.2) and (4.6), while the electric field is determined by a predictor-corrector method using (4.3), (4.4), (4.5) and (4.7).

For simplicity, spatial variations are restricted to one dimension, i.e., the x direction, and periodic boundary conditions are assumed. We focus our attention on waves propagating parallel to the external magnetic field. Therefore, both the wave vector k and the static magnetic field B_o are in the x direction, although the code would allow for any angle between k and B_o. We consider three species of ions, i.e., cold H^+, cold He^+ and hot H^+ with bi-Maxwellian velocity distribution. Initially both cold components are isotropic and hot protons have a temperature anisotropy of $T_\perp/T_\parallel = 2$. These particles are distributed uniformly over the simulation space consisting of 64 grid points. No wave field is assumed initially except for noises introduced by particle thermal fluctuations.

The parameters of the simulation have been chosen to represent typical conditions prevailing during the day hours at the geostationary orbit where most of events involving ICW's and energized He^+ ions have been observed:

- magnetic field intensity : 140 nT,
- cold H^+ ion density : 10 cm^{-3},
- cold He^+ ion density : 2 cm^{-3},
- thermal energy of both cold species : 1.7eV,
- anisotropy of both cold species : $T_\perp/T_\parallel = 1$,
- hot proton density : 1.1 cm^{-3},
- thermal parallel energy of hot protons : 17 keV,
- anisotropy of hot protons : $T_\perp/T_\parallel = 2$.

Note that with these parameter the ratio of the proton plasma frequency ω_H to the proton gyrofrequency Ω_H is equal to 300. and that the Alfven energy $mV_A^2/2 \sim 5$ keV. so that the parallel β of the plasma is $\sim$ 0.3.

In the simulation we do not use the physical parameters as expressed in CGS or MKS units, but instead we use conventional normalizations. It is simpler to use a system in which the Alfven velocity V_A. the proton cyclotron frequency Ω_H. the proton charge-to-mass ratio $(q/m)_H$ and the magnetic permeability μ_o are equal to 1. Other parameters are normalized to the quantities stated above. Since the static magnetic field is given by $B_o = \Omega_H/(q/m)_H$. $B_o = 1$ and the static magnetic energy density $B_o^2/2\mu_o = 0.5$. The light speed c is equal to $V_A(\omega_H/\Omega_H) = 300$. from which the electric permittivity $\varepsilon_o = 1/c^2$ is deduced. The thermal velocity of the cold protons and helium are 0.018 and 0.009 respectively. The thermal velocity of the hot protons is 1.8 and 2.55 for the parallel and perpendicular direction respectively.

The grid spacing is $\Delta x = 1$ and the time step Δt is set equal to 0.05. The number of grid points is 64 and the system length is $L_x = 64$. The number of superparticles in the system is 4096 for each of the cold species. As for hot protons, which are a free energy source in the system, a relatively large number of superparticles (32768) is necessary in order to make the initial thermal fluctuation noise low.

4.3.2 Simulation Results

The GEOS data suggest that the anisotropic proton distribution excites ion cyclotron waves, which are responsible for heating the thermal helium ions. In order to test this hypothesis, we have run the simulation code up to $\Omega_H t = 1200$. We will first consider the initial phase of the process.

In Figure 4.8, we see the time history of the magnetic and electric field energy densities for an early stage of the simulation run. Both the magnetic field and electric field energy densities increase throughout the time presented in this plot. The perpendicular component of the electric field is much larger than the parallel one, indicating that charge neutrality is conserved by the predictor-corrector code and that the wave is purely electromagnetic. It should be noted that the magnetic field amplitude attains a very large amplitude: $B_{wave}/B_o = 0.055$ at $\Omega_H t = 200$. Figure 4.9a, shows the hot proton energy density in a direction perpendicular and parallel to the ambient magnetic field. Initially at

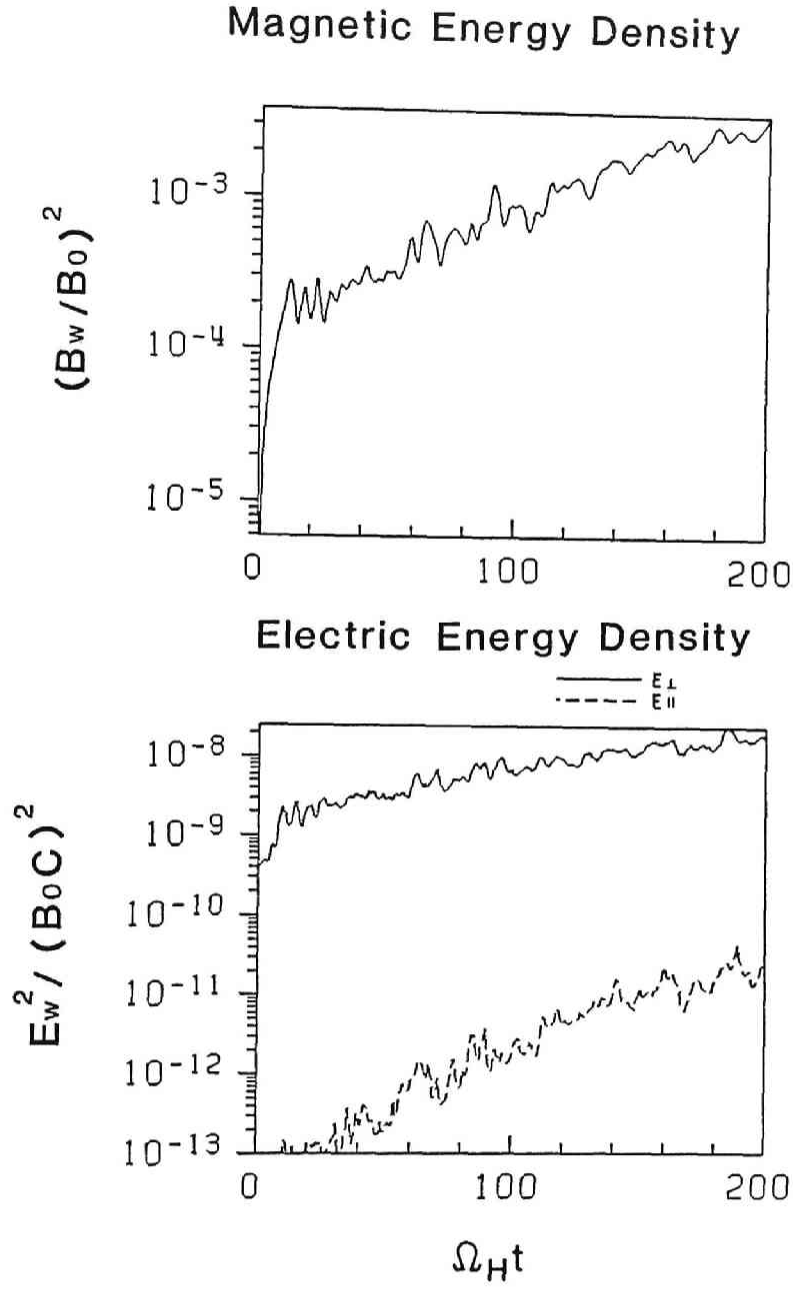

Fig. 4.8 Time history of the magnetic and electric energy densities during the early stages of the simulation. We note that both the magnetic field and electric fields are still growing at time $\Omega_H t = 200$. The dashed line on the lower panel reflects the variation of E_x, the smallness of which demonstrates the efficiency of the code and the electromagnetic nature of the wave.

time $\Omega_H t = 100$, the temperature anisotropy decreases only slightly to $(T_\perp/T_\parallel)_h = 1.9$. Later on, as we will see in (4.13b), the temperature anisotropy decreases more dramatically, as the waves attain large amplitudes, so that at $\Omega_H t = 200$, $(T_\perp/T_\parallel)_h = 1.6$, thus, the hot anisotropic proton distribution is responsible for the growth of these waves. The lower panels (b) and (c) show the energy density of thermal helium and protons respectively. Both thermal ion species are accelerated mainly in a direction perpendicular to the ambient magnetic field, with helium ions being preferentially accelerated. We will discuss this acceleration phenomenon later and we will show that it is in fact a two-step process.

To identify the wave mode during the early stages of the simulation run, we plot the dispersion characteristics of the wave. This is done by Fourier transforming individual k modes in time. Figure 4.10 is a plot of frequency ω versus wavenumber k for the B_y component of the magnetic field during the time interval $\Omega_H t = 1 - 204$. The amplitude of the wave is denoted by the height of the peak. It is well known from linear theory analysis (e.g. Gendrin and Roux, 1980; Gendrin, 1981) that the addition of thermal helium breaks the dispersion relation into two branches, one below the helium gyrofrequency known as the low frequency branch (LF) and one above the helium gyrofrequency referred to as the high frequency branch (HF). In fact the LF branch and HF branch are clearly depicted here. The fastest growing frequency occurs in the LF branch with $\omega/\Omega_H = 0.16$, $kV_A/\Omega_H = 0.29$ and $B_w/B_o = 0.023$. The dashed line is the real part of the dispersion relation calculated from the linear theory for the parameters at $\Omega_H t = 100$. By comparing the dashed line and the plot of the simulation results, the agreement between the real part of the linear dispersion relation and the simulation results are obvious.

To understand the time evolution of the wave properties during the linear stage we plot the time history of four dominant modes in Figure 4.11a.

The value of k, the wavenumber is related to the mode number m. In fact $k = (2\pi/L_x)m$ where L_x is the system length. Thus for m = 1., $kV_A/\Omega_H = 0.1$ whereas for m=2, $kV_A/\Omega_H = 0.2$, since $L_x = 64$, $V_A = 1$ and $\Omega_H = 1.0$.

In Figure 4.11b we plot the linear growth rate versus k for both the LF and HF branch. From the upper panel we see that the mode 4, $kV_A/\Omega_H = 0.4$ attains a large amplitude at an early time. The growth rates of these modes are found by calculating the slope of the straight dashed line shown in Figure 4.11. It is found that both of the growth rates of mode 3 and 4 are $\gamma/\Omega_H = 0.02$. Linear theory (Figure 4.11b) predicts the peak growth

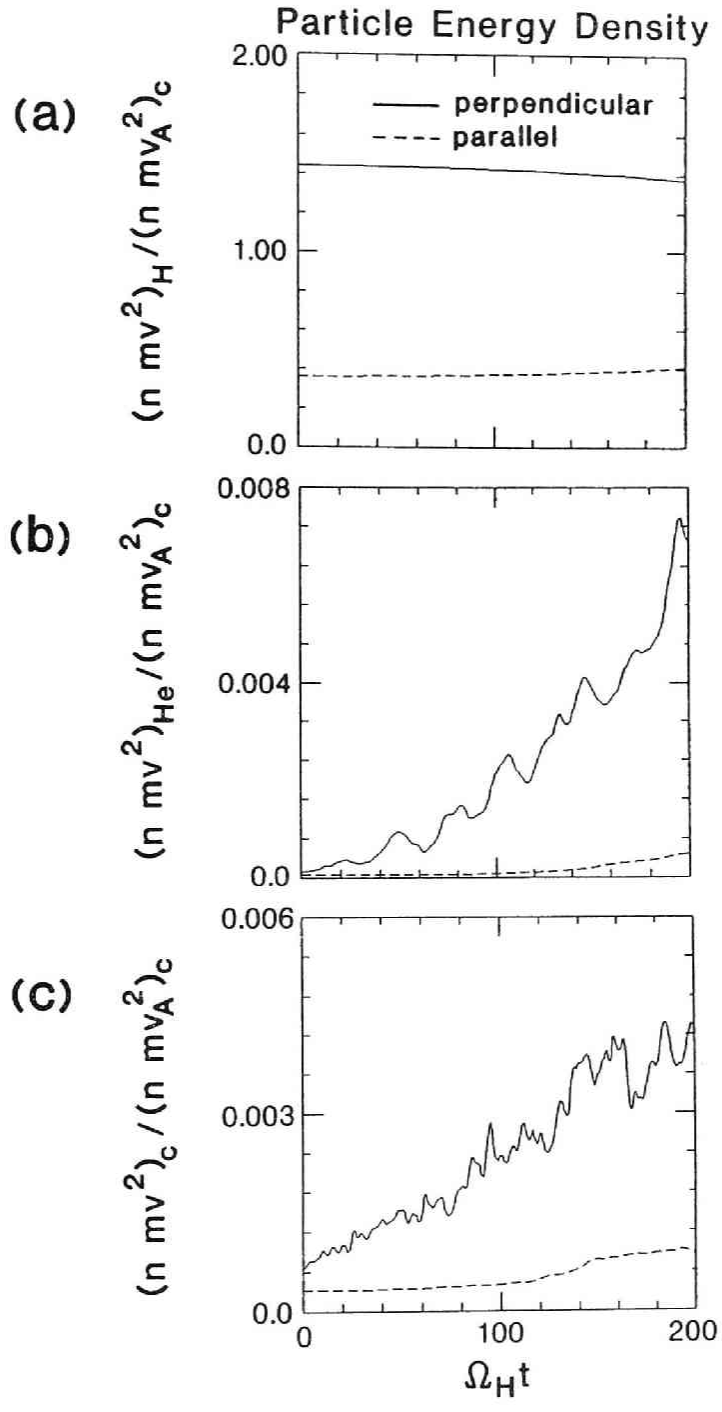

Fig. 4.9 The time history of the energy densities of the hot protons (panel (a)), helium ions (panel (b)) and thermal hydrogen (panel (c)). Note that the hot proton temperature anisotropy hardly changes until time $\Omega_H t = 100$ and then the decrease is more rapid. Both thermal species show an increase in energy density, preferentially in the perpendicular direction.

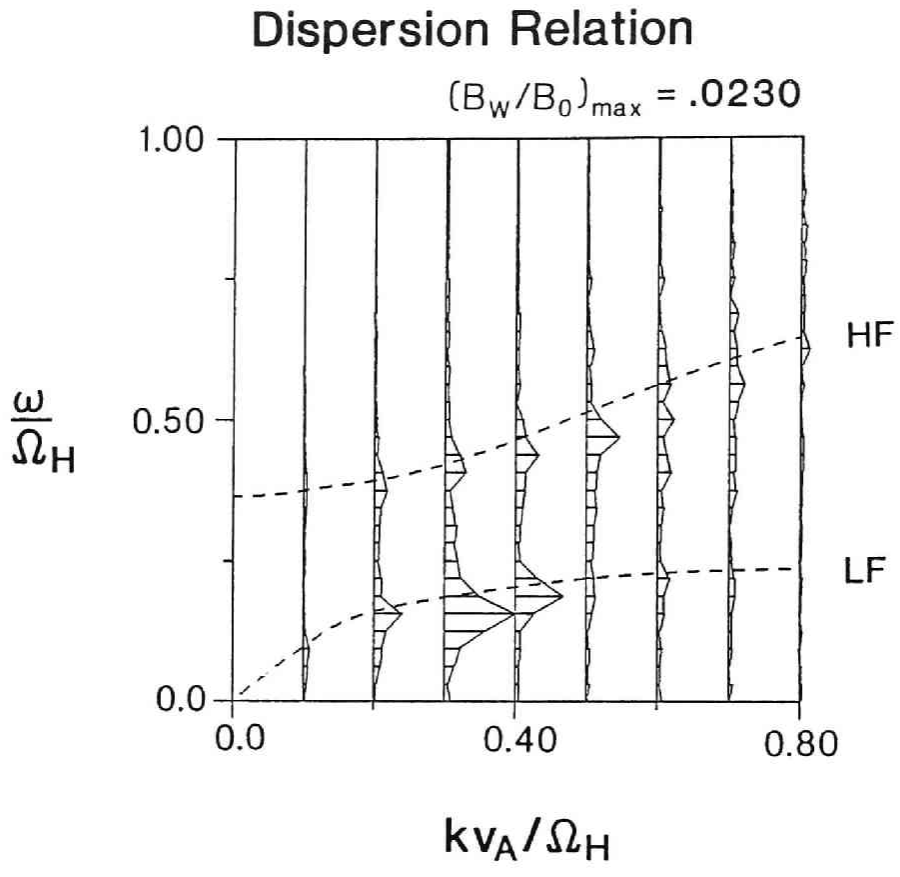

Fig. 4.10 We plot the dispersion relation of the B_y component during the early phase of the simulation $1 < \Omega_H t < 204$. We also plot the theoretical linear dispersion relation by dashed lines using the plasma parameters at $\Omega_H t = 100$. We observe that both the simulation results and the linear theory show the dispersion relation separated into two branches; the high frequency branch (HF) above the helium cyclotron frequency and the low frequency branch (LF) below the helium cyclotron frequency. The fastest growing frequency occurs in the LF branch at $\omega/\Omega_H = 0.16$ and $kV_A/\Omega_H = 0.29$.

rate to be $\gamma/\Omega_H = 0.022$ and to occur at $kV_A/\Omega_H \simeq 0.3$ in agreement with the simulation.

Having ensured that we can reproduce and understand the linear theory from our simulation study we now examine the non-linear physics of the interaction.

In Figure 4.12 we plot the time history of the magnetic and electric energy densities throughout the run. As noted previously, the magnetic

field increases until about $\Omega_H t = 250$, reaching a peak value $B_w/B_o = 0.06$ and then remains at a constant amplitude. The electric field behavior is similar, but the peak amplitude in this case is much smaller, $E_w/(B_o c) = 1.4 \times 10^{-4}$. In a one dimensional system, the peak amplitude is representative of saturation, since the wave energy cannot be lost by coupling to obliquely propagating waves and therefore remains constant. Throughout the simulation run less than 0.2% of the total energy is lost demonstrating that computing errors are negligible and that the energy of the system is conserved.

The time history of the different particle species (Figure 4.13) is a most enlightening and interesting plot. Panels (a) and (b) show the behavior of the hot anisotropic ions as a function of time. In panel (a) we see that the hot protons are losing energy in a direction perpendicular to the ambient magnetic field. This results in wave growth which in turn causes an increase in the hot proton parallel energy. This expected tendency towards an isotropic hot proton distribution is best seen in Panel (b) where we plot $(T_\perp/T_\parallel)_h$ as a function of time. It is interesting to note that the temperature anisotropy decreases rapidly until $\Omega_H t = 360$, reaching an anisotropy of $(T_\perp/T_\parallel)_h = 1.3$. At later times, the anisotropy does not change significantly, but reaches a value of 1.2 at the end of the run. Panels (c) and (d) show the large heating suffered by the helium ions. In fact, we see that the thermal helium has been heated about 100 times its initial value. We also note that most of the heating is in the perpendicular direction. Thermal protons are also heated but to a much lesser degree.

The snapshots of phase space plots v_x- x, v_y- x at different times for helium ions (Figure 4.14) and thermal protons (Figure 4.15 show complex nonlinear structure. Initially, at time $\Omega_H t = 0$, the helium ions are uniformly distributed in phase space. At later times, $\Omega_H t = 100$, we see a perturbation in v_y. This perturbation occurs from a simple $\vec{E}_w \times \vec{B}_o$ force, and results in a transverse motion of the plasma. Later on, $\Omega_H t = 300$ we see that the v_y is about the same except that the amplitude of the oscillations is larger, and tends towards smaller wavenumbers. At that time, we note oscillations in the parallel velocity v_x. In fact the oscillations appear to be folding on themselves. This is because, as the perturbation in the transverse velocity occurs, the particles experience a force $\delta v_{y,z} \times \delta B_{z,y}$ in the parallel direction. At $\Omega_H t = 400$, the motion is extremely nonlinear, with large striations and large oscillations. The motion is so nonlinear that a mixing of plasma, which was originally in

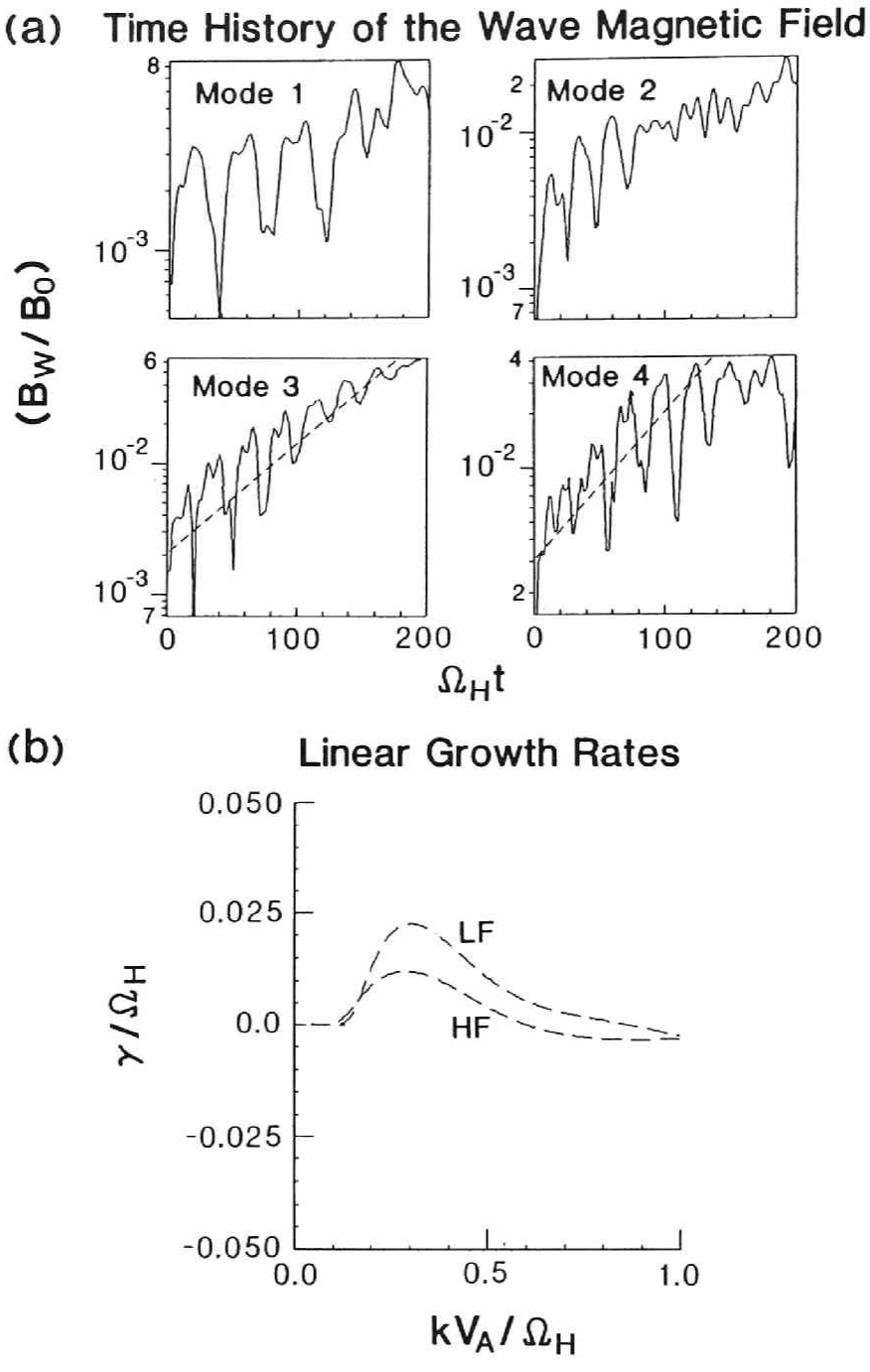

Fig. 4.11 In the upper panel we plot the time evolution of the four dominant modes during the linear phase of the simulation. The lower panel shows the theoretical linear growth rate as a function of wavenumber. From the upper panel we find that the growth rates for mode 3 and 4, corresponding to $kV_A/\Omega_H = 0.3$ and $kV_A/\Omega_H = 0.4$ respectively, are both equal to $\gamma/\Omega_H = 0.02$. The lower panel predicts the peak growth rate to be $\gamma/\Omega_H = 0.022$ at $kV_A/\Omega_H = 0.3$.

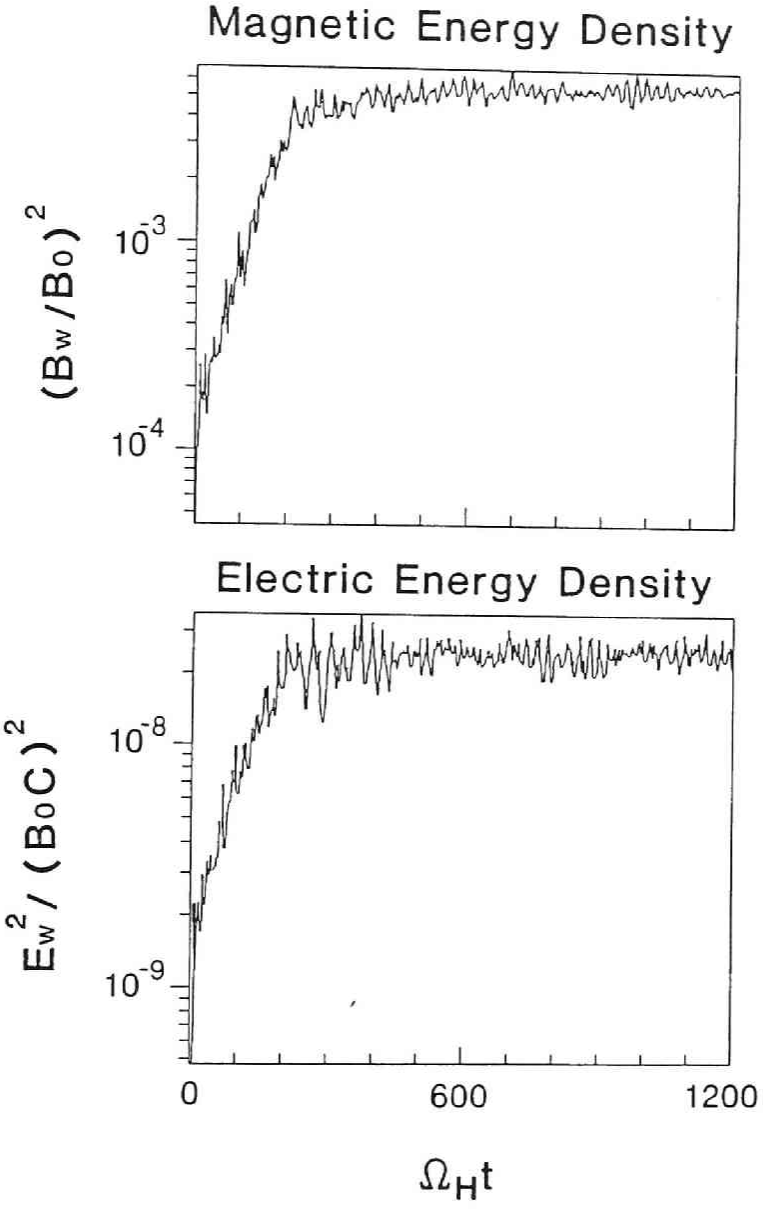

Fig. 4.12 Time history of the electric and magnetic energy densities until the end of the run. The magnetic energy density increases until about $\Omega_H t$ = 300, reaching a peak amplitude B_w/B_o =0.06. Saturation occurs about $\Omega_H t$ = 300.

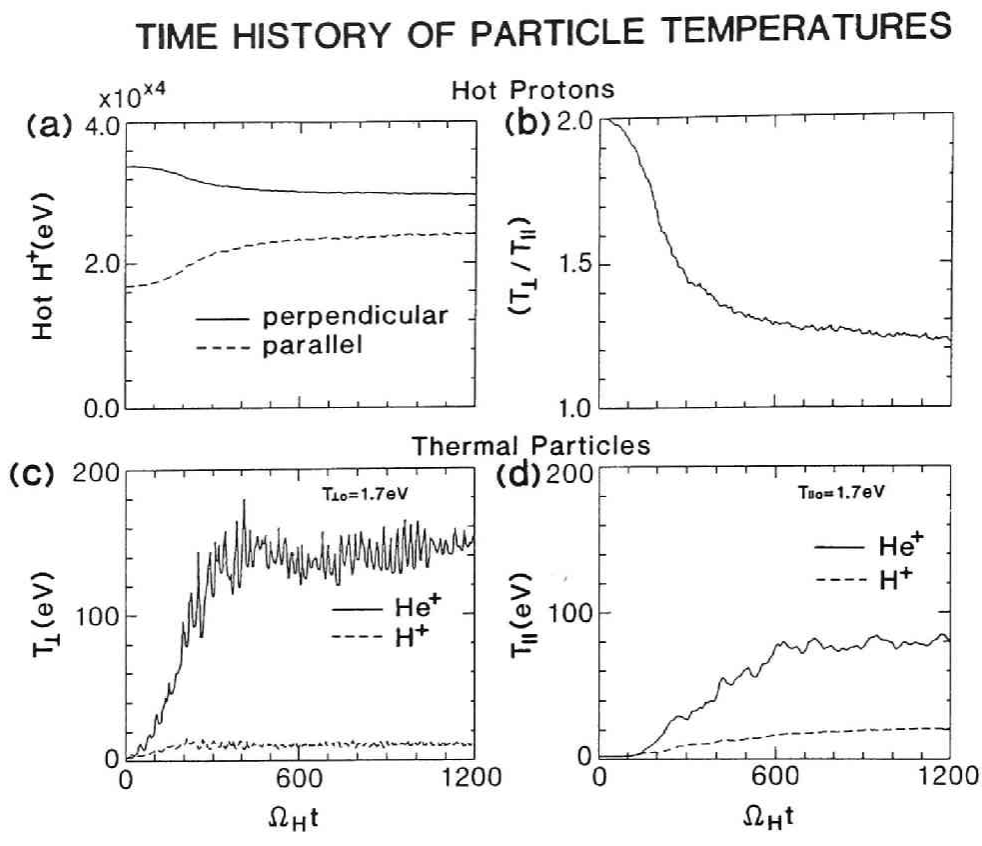

Fig. 4.13 A time history of the different particle species, the hot protons (panels (a) and (b)), the perpendicular temperature of helium and thermal protons (panel (c)) and the parallel temperature of helium and thermal protons (panel (d)). We note in panels (a) and (b) that the anisotropy decreases rapidly until about $\Omega_H t = 360$, reaching a value of $T_\perp / T_\parallel = 1.3$. At later times the He^+ ions have been heated about 100 times the initial value in the perpendicular direction. Most of the heating occurs prior to $\Omega_H t = 500$. The He^+ ions are also heated in the parallel but to a lesser degree. Thermal protons are only slightly heated.

different locations, is occurring, resulting in a hotter distribution. Similar nonlinear motions are present in the hydrogen phase space plots (Figure 4.15) but they are not as prevalent as for helium ions (Figure 4.14). The reason for that can be seen from the linearized momentum equation of motion for each species.

$$m_j \frac{\partial \vec{v}_j}{\partial t} = q_j(\vec{E}_w + \vec{v}_j \times \vec{B}_o) \qquad (4.9)$$

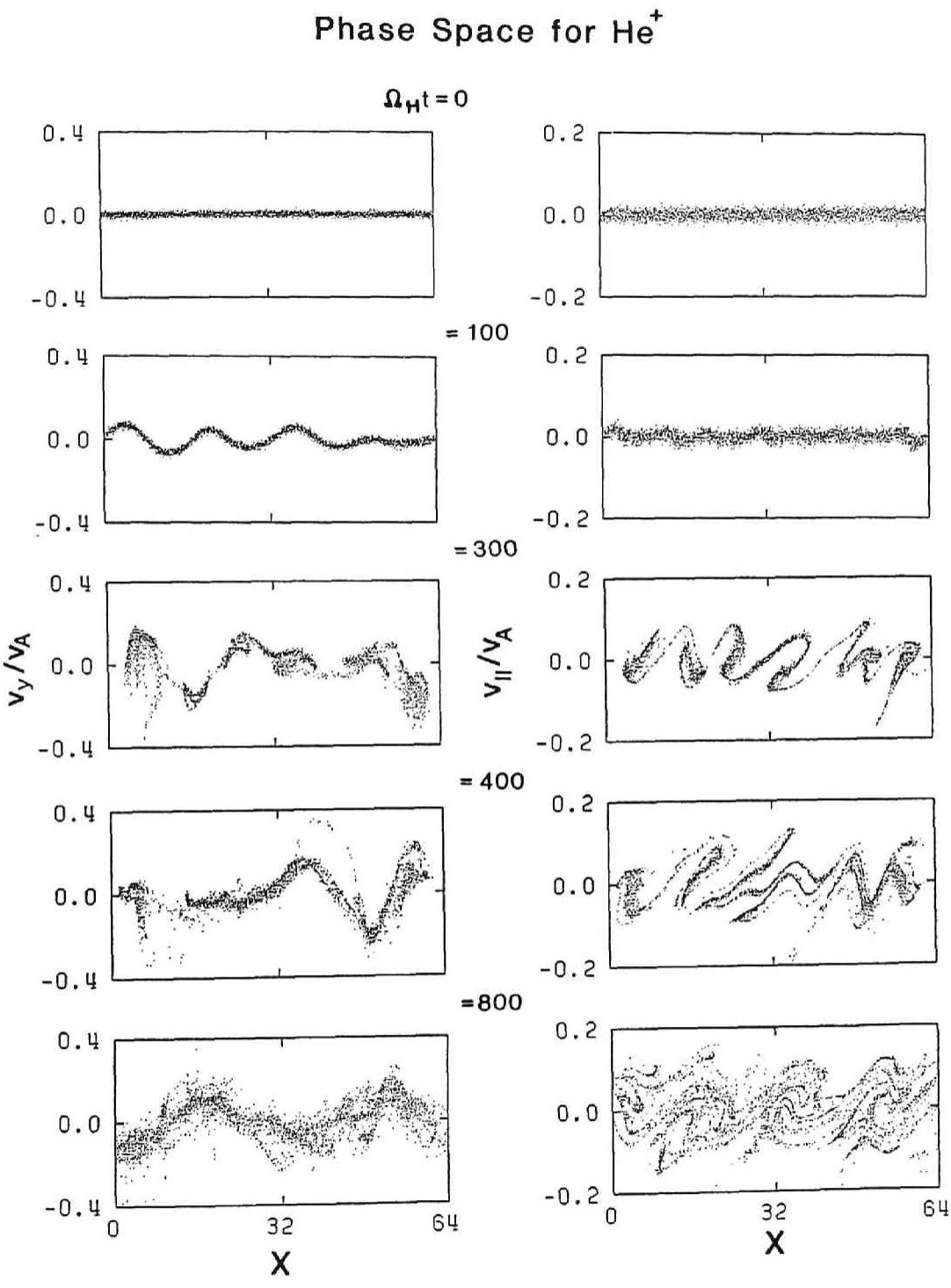

Fig. 4.14 Phase space plot for He^+ at different times. The left column is in v_y-x space, while the right column is in v_x-x space.

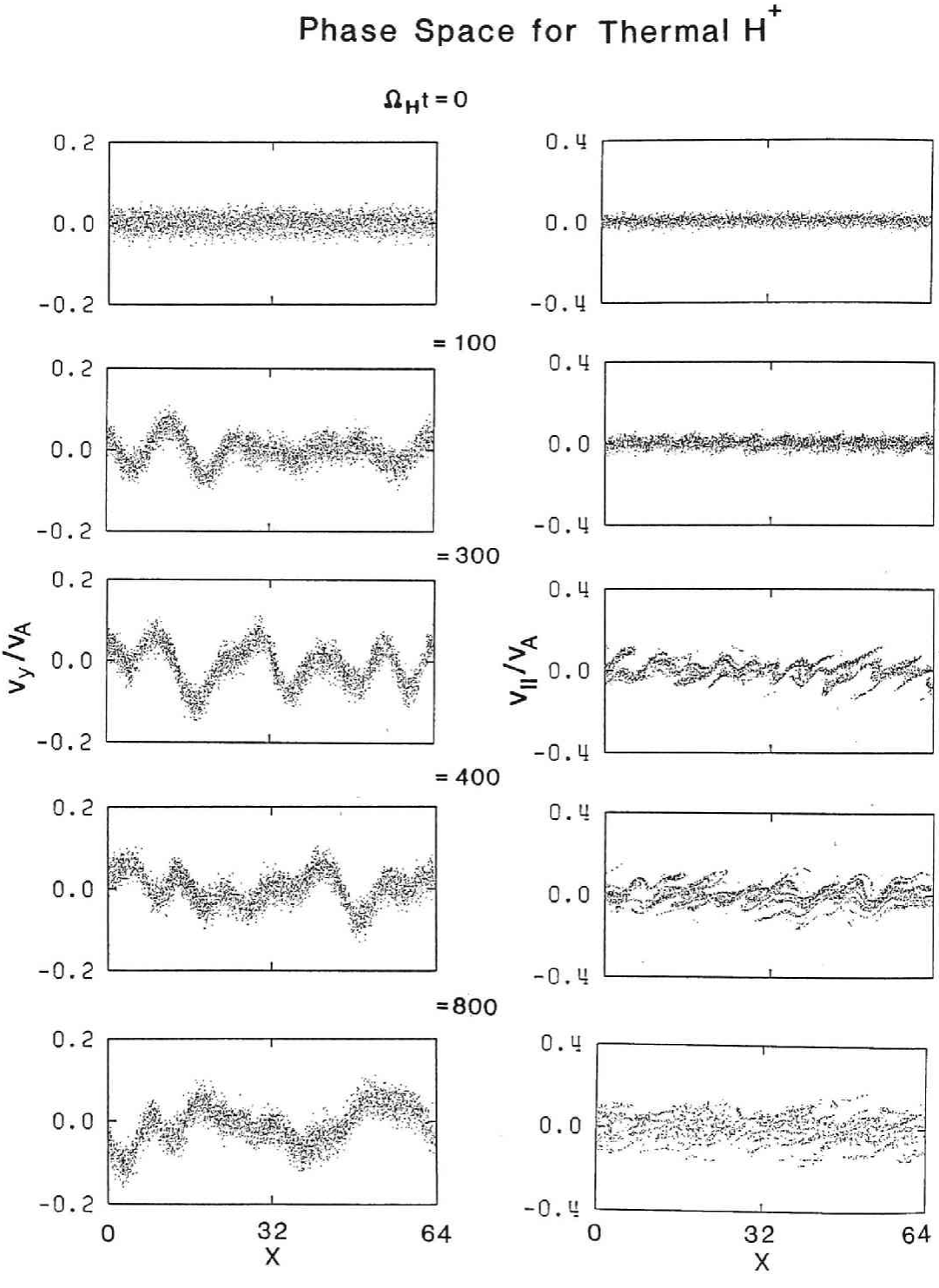

Fig. 4.15 A phase space plot for thermal hydrogen at different times. The left column is in v_y-x space while the right column is in v_x-x space.

and Maxwell equation

$$\nabla \times \vec{E}_w = - \frac{\partial \vec{B}_w}{\partial t} \tag{4.10}$$

Solving for $\vec{v}_j$, we get

$$\vec{v}_j = - \frac{\omega}{k} \frac{\vec{B}_w}{B_o} \frac{1}{(1 \quad \omega/\Omega_j)} \tag{4.11}$$

where $\Omega_j = (q/m)_j B_o$.

Thus, the species response is proportional to B_w and depends on the mass through the resonant denominator. This is why the effect is less dominant for the case of a hydrogen plasma. As the plasma evolves, $v_j \times B_w$ forces become substantial, resulting in a nonlinear motion along the field lines. This accounts for the late time behavior when 'spirals' develop in the phase space and to a lesser extent in hydrogen.

This 'weaker' spiraling for thermal protons is caused by the fact that the fastest growing wave is in the LF branch, so that the resonant velocity is far from the thermal velocity of protons. In Figure 4.16 we show the Fourier analysis of the wave properties, during the nonlinear stage of the simulation $\Omega_H t = 800 \quad 1200$. We have decomposed the wave into the forward and backward traveling components. It is found that both the forward and backward traveling waves have equal amplitudes, and only the LF branch has a considerable amplitude. The maximum growth rate $\gamma/\Omega_H = 0.016$ has shifted to lower wavenumbers. The dominant wavenumbers are best seen in Figure 4.17, where in the upper panel we plot a three-dimensional plot of the amplitude of the wave magnetic field versus k, as a function of time. Looking at Panel (a) it is easy to see that as time proceeds the wave with the largest amplitude occurs at longer wavelength. This tendency towards longer wavelengths can also be seen in the lower panel where we plot the time history of the amplitudes of the four dominant modes. Initially, mode 3 and 4 seem to be mostly responsible for the large amplitude wave observed; however, at later times the amplitude of mode 2 is larger. From linear theory analysis the shifting of the fastest growing modes to lower wavenumbers could be due to either the heating of the helium ions or to the decrease in temperature anisotropy of hot protons [Gendrin et al., 1984, Figure 7a, Figure 7b].

However, as can be seen on the referenced figures, the reduction in the bandwidth of the unstable waves is more drastic in the first case than

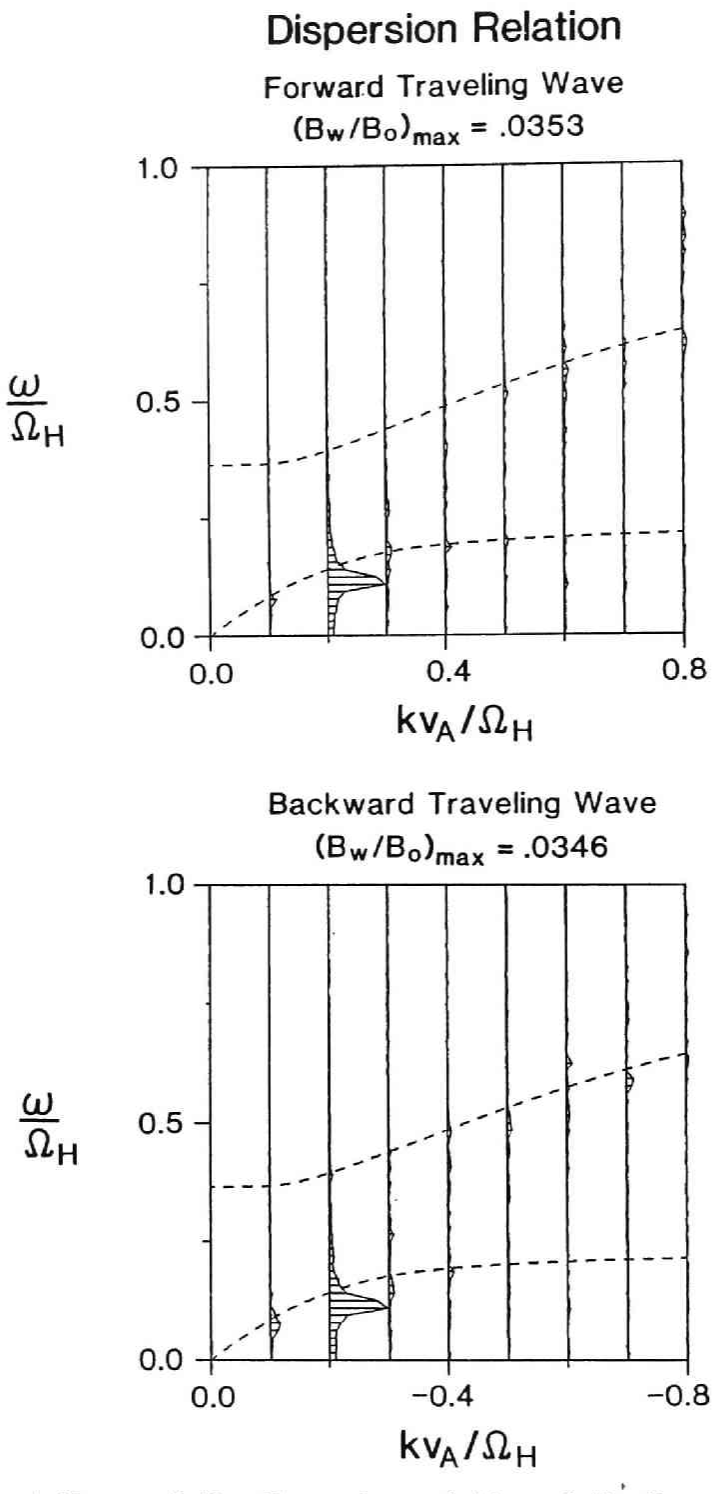

Fig. 4.16 A figure of the dispersion relation of the B_y component during the nonlinear stage of the simulation $\Omega_H t$ = 800-1200. The upper panel is for the forward traveling wave, while the lower panel is for the backward traveling wave. At this stage of the simulation only the LF branch has a considerable stimulation. The dashed line represents the linear dispersion relation calculated from the parameters at $\Omega_H t$ =1000.

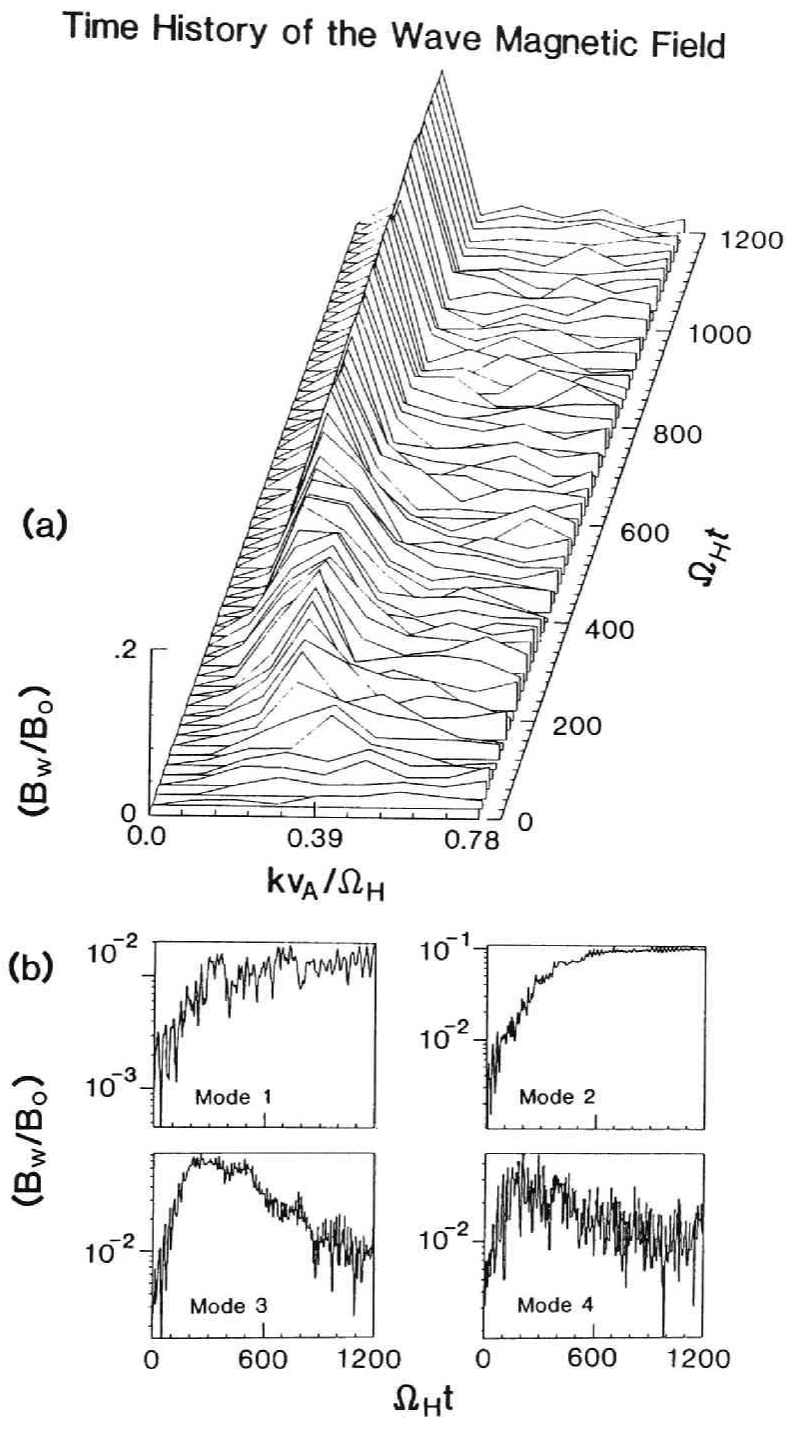

Fig. 4.17 Panel (a) shows the time evolution of the k-spectra of the wave magnetic field, while panel (b) shows the amplitude versus time of the dominant modes in the system. Note how the fastest growing modes shift to lower wavenumbers with time.

in the second. Besides, since the most amplified waves belong to the LF branch of the dispersion curve, a decrease of the hot proton anisotropy has almost no consequence on the frequency of the maximum growth as long as the anisotropy remains above the critical value [Kennel and Petschek, 1966] which corresponds to it. The critical anisotropy is defined by:

$$\omega/\Omega_H = A_c/(A_c + 1) \qquad (4.12)$$

where $A_c = T_\perp/T_\parallel - 1$.

For $\omega/\Omega_H = 0.1$, $A_c \sim 0.2$. Consequently the frequency of the fastest growing wave is not much affected by a decrease in the hot proton anisotropy as long as $(T_\perp/T_\parallel)_h \geq 1.2$. On the other hand, an increase of the hot proton parallel energy, as evidenced by the simulation (see Figure 4.13), may be at the origin of the decrease of the most amplified wave frequency (see e.g. [Gendrin et al., 1971, Figure 6]).

To test which of these factors is responsible, we ran the simulation by starting with hotter thermal proton and helium distributions, $T_\perp = T_\parallel =$ 17 eV, while keeping all the other parameters constant. In this later simulation, the helium ions were only heated by a factor of 2, while the hot proton anisotropy decreased from 2 to 1.25 (still larger than 1.2) and while their parallel energy was increased by a factor of 1.4. The shift to lower wavenumber was still observed. These results suggest that neither the heating of the helium ions nor the decrease in temperature anisotropy of the hot protons is responsible for the lowering of the most amplified wavenumber. We therefore conclude that the shift to lower wavenumber is due to the increase of the hot proton parallel energy.

4.3.3 Discussion and Conclusion

In this paper using simulation, we have studied the bulk heating of helium ions starting from an initial anisotropic proton distribution. We have shown that the thermal ions are heated to one hundred times their initial temperature, due to the growth of large amplitude ion cyclotron waves. Before discussing the heating mechanism of the helium ions and the saturation of the ion cyclotron waves, let us briefly summarize our findings.

Wave properties:

1) Large amplitude ion cyclotron waves with peak amplitude $B_w/B_o = 0.06$ are observed to grow, due to the temperature anisotropy of the hot proton distribution.

2) Analysis of dispersion properties, frequency and wavenumbers, shows that the presence of helium breaks the dispersion relation into two branches, one below the helium gyrofrequency (LF branch) and one above the helium gyrofrequency (HF branch). This is in agreement with previous work on the linear theory dispersion (see, for example, Gendrin and Roux [1980]).

3) At the early stage of the simulation, agreement with linear theory is very good. The fastest growing mode occurs on the LF branch with ω/Ω_H = 0.16, kV_A/Ω_H = 0.3 and γ/Ω_H = 0.02, whereas linear theory predicts ω/Ω_H = 0.17, kV_A/Ω_H = 0.31 and γ/Ω_H =0.022.

4) The magnetic field reaches a peak amplitude at time $\Omega_H t$ = 250 and oscillates about a constant value thereafter.

5) At later times, the fastest growing mode shifts towards longer wavelengths but remains in the low frequency branch. Spectral analysis for the time period between $\Omega_H t$ = 800 and $\Omega_H t$ = 1200 shows that the fastest growing mode is at ω/Ω_H = 0.11 and kV_A/Ω_H = 0.2. As discussed in Subsection 4.3.2 we believe this shift to a lower k mode is due to an increase of the hot proton parallel energy.

Particle properties:

1) The hot anisotropic distribution tends towards isotropy with time. The temperature anisotropy changes from $T_\perp/T_\parallel$ = 2 at $\Omega_H t$ = 0 to $T_\perp/T_\parallel$ = 1.3 at $\Omega_H t$ = 360 and then changes only slightly until the end of the run.

2) The thermal protons are only slightly heated during the run. It is because of the fact that the fastest growing wave is in LF branch, causing the resonance velocity to be far from the thermal velocity of the protons.

3) The cold helium ions are greatly heated, mostly in the perpendicular direction. The perpendicular helium temperature is about 150 eV whereas the parallel temperature is about 70 eV. Most of the perpendicular heating occurs before $\Omega_H t$ = 360, whereas the parallel heating continues until $\Omega_H t \simeq 600$.

4) Phase space plots for helium ions, and to a lesser extent hydrogen ions, show an interesting structure. At the early stages we see oscillation in the v_y component, which is simply due to an $\vec{E}_w \times \vec{B}_o$ force. As time evolves these oscillations grow causing a significant $\delta v_{y,z} \times \delta B_{z,y}$ force in the $v_\parallel$ direction. This results in spiraling and complex nonlinear motion in the $v_\parallel$ - x phase space plots. At later times, we observe thermalization of the helium ion distributions.

With these observations in mind we can now discuss the saturation mechanism and the heating of helium ions. First let us discuss saturation of the wave. If we calculate the linear growth rate using plasma parameters at the time of peak amplitude $\Omega_H t = 250$, we find a positive growth rate. In fact, for hot proton temperature $T_{\parallel} = 20$ keV, $T_\perp/T_{\parallel} = 1.5$, cold proton temperature $T_{\parallel} = 6$ eV, $T_\perp/T_{\parallel} = 2$, and helium temperature $T_{\parallel} = 30$ eV, $T_\perp/T_{\parallel} = 3.3$, we find from linear theory calculation $\gamma/\Omega_H = 0.012$.

The growth due to positive anisotropy must be balanced by a damping mechanism. One obvious candidate for this damping is trapping of heliums by electromagnetic waves. Evidence for particle trapping can be seen in the phase space plot v_x- x in Figure 4.14. In fact we calculate the trapping frequency for the mode 4 wave

$$\omega_{trap} = (kB_w \frac{q}{m} v_\perp)^{1/2} \tag{4.13}$$

substituting for $k = 0.4$, $B_w = 0.02$, $q/m = 0.25$ and $v_\perp = 0.1$, at $\Omega_H t = 250$, we find $\omega_{trap} = 0.014$. Equating $\omega_{trap} \sim \gamma_{damp}$, we find that the damping rate is of the same order of magnitude as the growth rate.

Now we turn to the problem of heating the helium ions. First, before discussing this, we would like to find out whether the heating is bulk heating or simply high energy tail formation. To do that we plot in Figure 4.18 the distribution functions of helium ions in the parallel direction as well as the distribution of helium ions in v_y, one of the perpendicular components, at various times. The dashed lines are the initial distribution function. Looking at the left column, we note that at time $\Omega_H t = 200$ there is some heating. However, at later times the distribution is much hotter. Moreover, this plot shows that indeed we do have bulk heating, as opposed to high energy tail formation.

Now looking at the time history plot (Figure 4.13) we see that the heating of helium seems to start from the very beginning. Yet the thermal velocity of helium is such that it is difficult to understand how heating takes place. To understand the exchange of energy between the helium ions and the waves, we plot $\vec{E}_\perp \cdot \vec{v}_\perp$ in Figure 4.19a. In the regions where $\vec{E}_\perp \cdot \vec{v}_\perp$ is positive, the helium ions are gaining energy from the waves and vice versa. We note that in general during the initial phase, $\vec{E}_\perp \cdot \vec{v}_\perp$ is positive whereas it is oscillating between small positive and negative values later. What we believe is happening is that during the initial phase, while particles are accelerated by the wave there is no heating since the

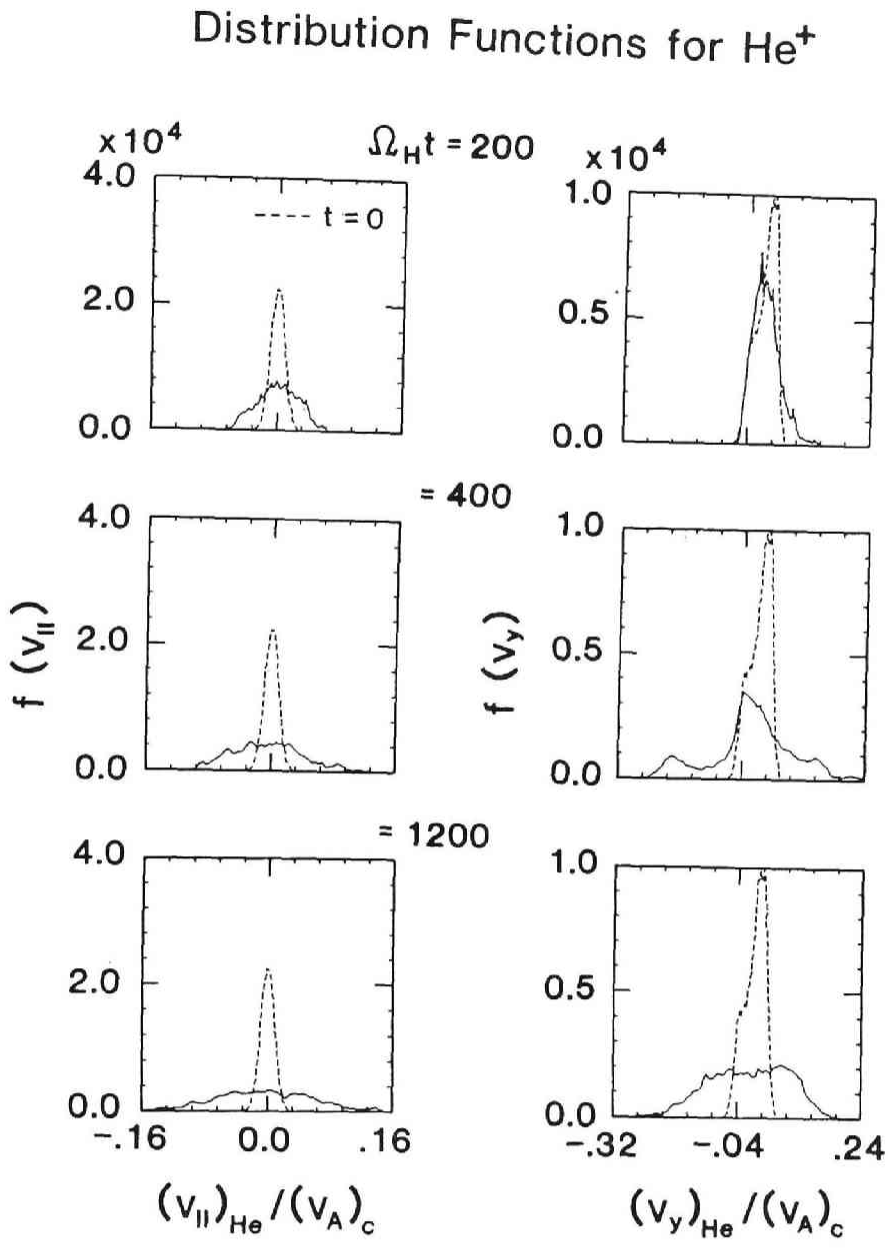

Fig. 4.18 A plot of the distribution function of thermal helium at three different times. The left column is the parallel distribution function, whereas the right column is the distribution function in one of the transverse directions. The dashed line is the initial distribution function at time $\Omega_H t = 0$. Note the broadening of the distribution function $f(v_\parallel)$ at time $\Omega_H t = 400$. Looking at the lower left panel we see that the helium continues to heat until the end of the run, but at a slower rate.

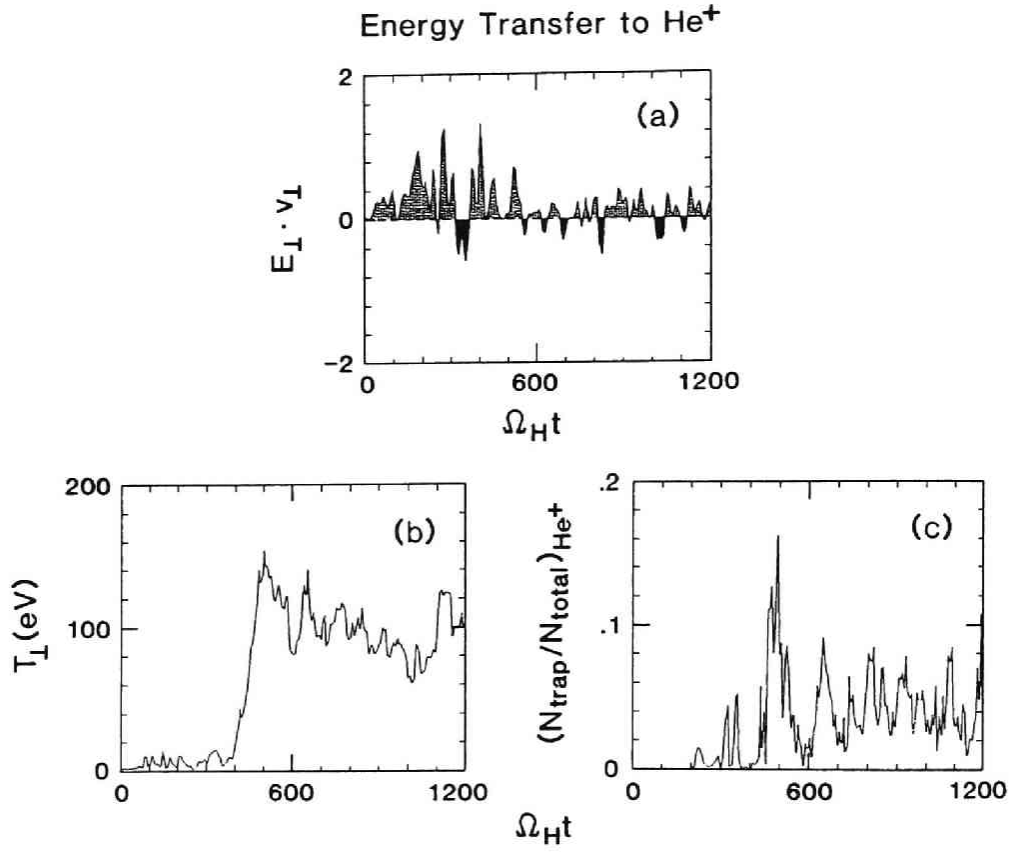

Fig. 4.19 Here we plot certain diagnostics needed to understand the heating mechanism of thermal helium. At panel (a), we plot $\vec{E}_\perp \cdot \vec{v}_\perp$. For $\vec{E}_\perp \cdot \vec{v}_\perp \geqslant 0$, the energy is transferred from the waves to the helium ions and vice versa. We note that most of the energy transfer from the waves to the helium ions occurs prior to time $\Omega_H t = 400$. In panel (b) we plot the effective temperature of the helium, by measuring the temperature in a region of space a quarter of the wavelength of mode 4 in each direction. In panel (c) we plot the number of helium ions whose velocity lies within the resonance region. We note that number of trapped particles and the effective temperature seem to increase simultaneously, at time around $\Omega_H t = 500$.

helium ions have velocities far away from the resonance velocity. We therefore advance the following scenario. Initially, the helium ions are set into oscillation (no temperature increase) in both the perpendicular and parallel directions by fields of the growing wave. When $v_{\parallel}$ reaches a value near the resonance velocity such that heating can occur, we should see a sudden increase in the perpendicular temperature. We define a resonance region in the velocity phase space as

$$V_R - V_{trap} < v_{\parallel} < V_R + V_{trap} \quad , \tag{4.14}$$

where V_R is the resonance velocity given by $(\omega - \Omega_{He})/k$, and V_{trap} is the trapping velocity given by $2\omega_{trap}/k$. In the resonance region nonlinear trapping of heliums is possible, leading to the heating. The above scenario is consistent with the lower panel of Figure 4.13, where the cold helium temperature increases from the beginning of the run. The temperature plotted there is actually the space-averaged temperature, and the oscillatory effects of the waves have been averaged over many wavelengths giving an apparent velocity spread and temperature. To bring out the effects of the waves and minimize spatial averaging, we measure the temperature in a region of space a quarter of the wavelength of mode 4 in each direction. In Figure 4.19b,c we show such a local perpendicular temperature diagnostic and also the number of helium ions whose velocity lies within the resonance region for the mode 4 wave ($V_R = -0.16$, $V_{trap} \simeq 0.07$). At first there are no particles and there is no increase in temperature. Later the number of particles has increased and we have a sudden surge in temperature. These diagnostics clearly indicate that the energy gained by the heliums during the linear phase is transfered to thermal motion due to the nonlinear trapping.

The results which have been presented show the efficiency of the simulation code to interpret complex wave particle interactions in a multicomponent plasma. Some interesting results have been obtained which concern the heating of heavy ions in the equatorial magnetosphere by ICW's. However, more experimental runs have to be performed and some improvements are still needed to answer specific questions related either with the physics of the phenomenon or to the efficiency of the simulation code.

As far as physics is concerned, there remain some discrepancies between the simulation results and experimental data. A drastic lowering in the frequency of the most amplified wave found in the simulation is generally not observed in experimental data. The delay which is observed

between the establishment of a rather large wave field and the heating of He^+ ion is much shorter in the simulation run than it seems to be in the case of experimental data [Young et al., 1981; Roux et al., 1982]. The bunching of He^+ ions, which is a striking feature of ATS-6 observations [Mauk et al., 1981] is not as clearly reproduced in the results of the simulation.

Some of these discrepancies can be explained by the fact that the numerical runs reproduce a stationary case, and not a progressive one, because a periodic boundary condition is assumed in the present simulation. Waves cannot escape, and new hot particles are not injected, thus preventing the simulation system to represent an equilibrium where input and output energy flows are balanced. The size of the system should be increased ($L_x \geqslant 128$) in order to be able to follow in more detail the evolution of the most amplified wavenumber. Finally, a parametric study (number of particles per cell, more efficient predictor-corrector schemes, ...) should be undertaken in order to optimize the cost/efficiency of the operational code which has been so successfully used throughout this study.

CHAPTER 5
RADIATION OF ELECTROMAGNETIC AND ELECTROSTATIC WAVES FROM ELECTRON BEAM

5.1 Introduction

In this chapter we investigate beam-plasma physics concerning radiation of electromagnetic and electrostatic waves from electron beams. Since the electron beam traveling through the ambient magnetoactive plasma exhibits highly nonlinear feature. we perform computer simulations using the Full Electromagnetic (FEM) code. Beam instabilities of whistler mode waves and longitudinal electrostatic waves are already studied in Chapter 3. In this chapter we study two different beam-plasma systems which are driven or modulated by external forces. One is a model with an electron beam actively injected from the electron gun on board a space vehicle. The other is a model with an electron beam modulated by a coherent whistler mode wave propagating parallel to the external magnetic field. The former model. studied in Section 5.2. is based on the SEPAC (Space Experiment With Particle Accelerators) [Obayashi. 1982] which is an active and interactive experiment in the earth's upper atmosphere and magnetosphere with a high-power electron gun on board the space shuttle. The latter model. studied in Section 5.3. is based on the observation by ISEE satellite that strong electrostatic noise bursts are often associated with a coherent chorus hook element when a high-energy electron beam with an energy of the order of several hundred electron volts is present [Reinleitner et al., 1982].

5.2 Electromagnetic Radiation from an Actively Injected Electron Beam

Computer simulations are performed to investigate beam plasma physics which takes place in the SEPAC (Space Experiment with Particle Accelerators) [Obayashi. 1982]. The SEPAC is scheduled to carry out active and interactive experiments in the Earth's upper atmosphere and magnetosphere using a high power electron gun on board the Space Shuttle. Previous active experiments of beam injection into the magnetospheric plasma such as ARAKS experiments (Gendrin. 1974; Cambou et al.. 1980: Pellat and Sagdeev. 1980 and references therein) have revealed many interesting phenomena. Beam Plasma Discharge (BPD) is one of them. and has

been studied extensively (Bernstein et al., 1979; Mishin and Ruzhin, 1980; Szucszewicz et al., 1982;). In this section, however, we focus our attention to the beam-plasma interaction and its resultant wave excitation process within the initial time period before the BPD takes place. Using two-dimensional electromagnetic particle simulation code (FEM) [e.g., Langdon and Lasinski, 1976; Matsumoto and Omura, 1983] in which Maxwell's equations and equations of motion of a large number of particles are solved simultaneously, we study the following two problems. One is divergence and propagation of the electron beam through the ambient magneto-active plasma, and the other is plasma wave excitation by the electron beam.

In Subsection 5.2.1 the FEM code is applied to a one-dimensional problem for simplicity and computational efficiency. Excitation mechanisms of the waves and their propagation characteristics are mainly studied with this model. In Subsection 5.2.2 behaviors of the electron beam as well as the background plasma are studied with a more realistic two dimensional electromagnetic model. Subsection 5.2.3 gives a summary and discussion.

5.2.1 One-Dimensional Electromagnetic Model

The simulation space formed by 2048 spatial grids is taken in a transverse plane to the static magnetic field and uniformly filled with isotropic plasma particles. The waves are assumed to propagate in x-direction and the magnetic field is taken along the z-direction. As schematically illustrated in Figure 5.1-(a), an electron beam is locally injected at x - 1024 in the simulation space with a drift velocity parallel to the static magnetic field. In the 1D model the electron beam is a slab beam which is spatially uniform in the y-and z-directions. The periodic boundary condition is applied to the simulation region along the x-axis which is taken sufficiently long so that the localized electron beam as seen in Figure 5.1-(a) may not be affected by the periodic boundary condition. As the background cold plasma 16384 cold electrons are distributed uniformly in the simulation space. The contributions of ions are neglected, although the neutrality condition is satisfied by assuming the presence of ion charges fixed at the grid points. As the electron beam 1024 electrons are locally injected at x - 1024 with a spatial spread over about 20 grid points and with a drift velocity 0.2c in the z direction, where c is the light speed. The cold plasma frequency is $2.0\Omega_e$ and the beam plasma frequency is about $2.8\Omega_e$, where Ω_e is the electron cyclotron frequency. The numerical parameters used in the 1D and 2D simulations are

as follows:

Grid size; $\Delta x = \Delta y = 1$.	Cyclotron Frequency; Ω_e 1.
Cold Plasma Frequency; $\Pi_e = 2$.	Light Speed; $c = 50$.
Time Step; $\Delta t = 0.01$.	Thermal Speed of Cold Plasma = 1.
Thermal Speed of the Beam = 1.	Drift Velocity of the Beam = 10.

which gives the Debye length $\lambda = 0.5$, Larmor radius $r_L = 1$ and the skin depth of 50.

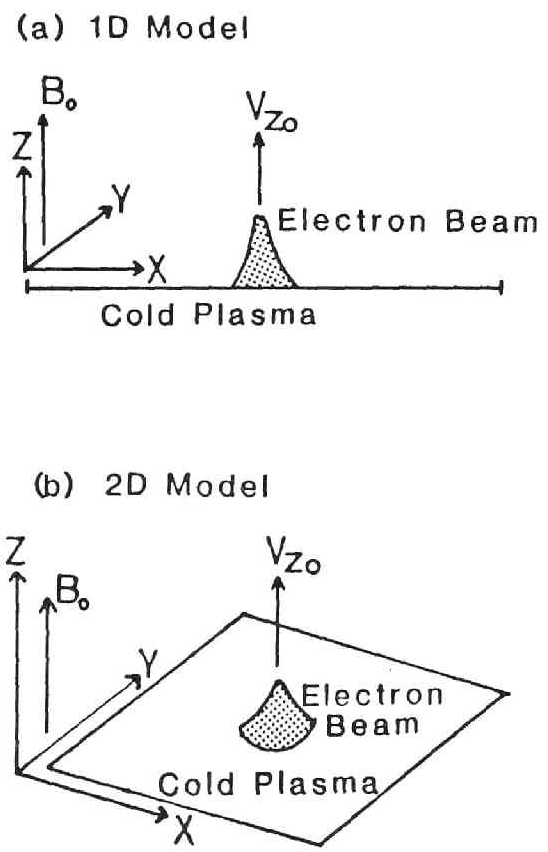

Fig. 5.1 Schematic illustrations of the simulations models; (a) 1D electromagnetic model and (b) 2D electromagnetic models.

In Figure 5.2-(a) time evolution of the parallel electrtic field E_x is shown. Owing to the local excess of the electron charge caused by the beam injection, an electrostatic field is formed and oscillates subsequently.

Applying the discrete Fourier transformation to the data of E_x, both

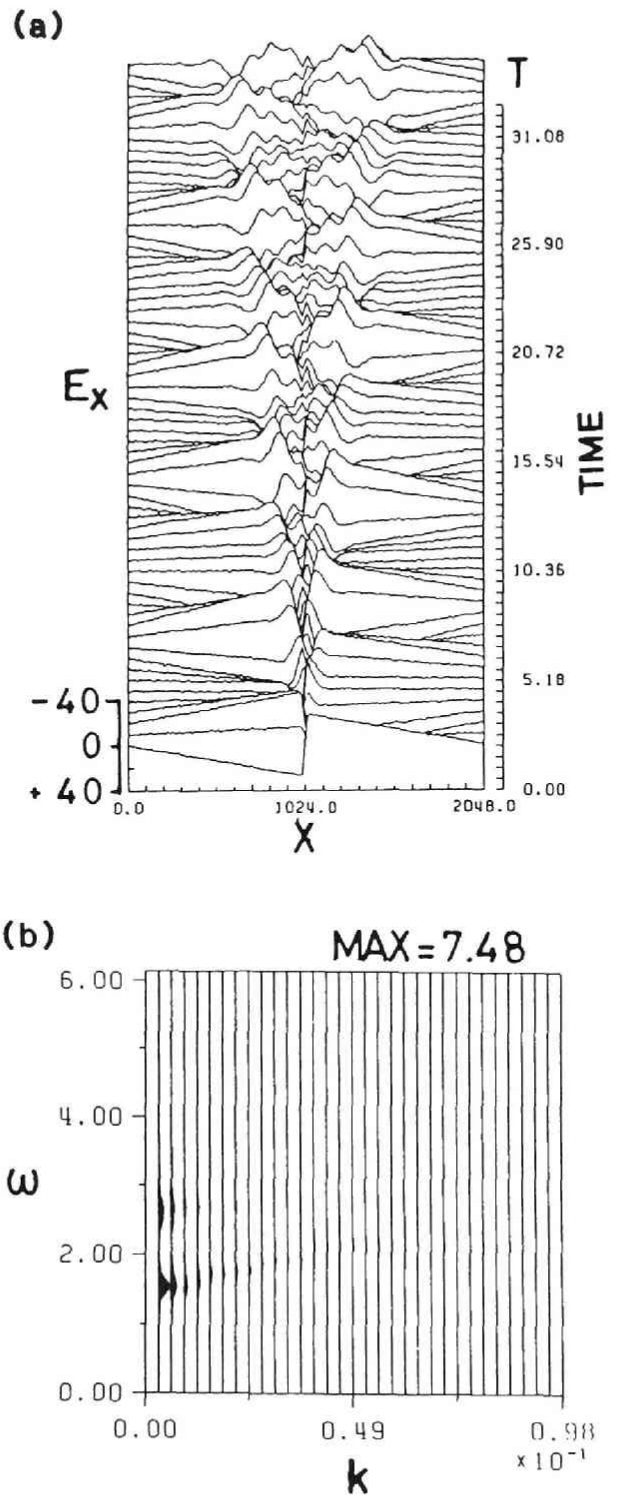

Fig. 5.2 (a) Spatial profiles of the E_x field and its time evolutions. (b) The ω - k diagram of the E_x field.

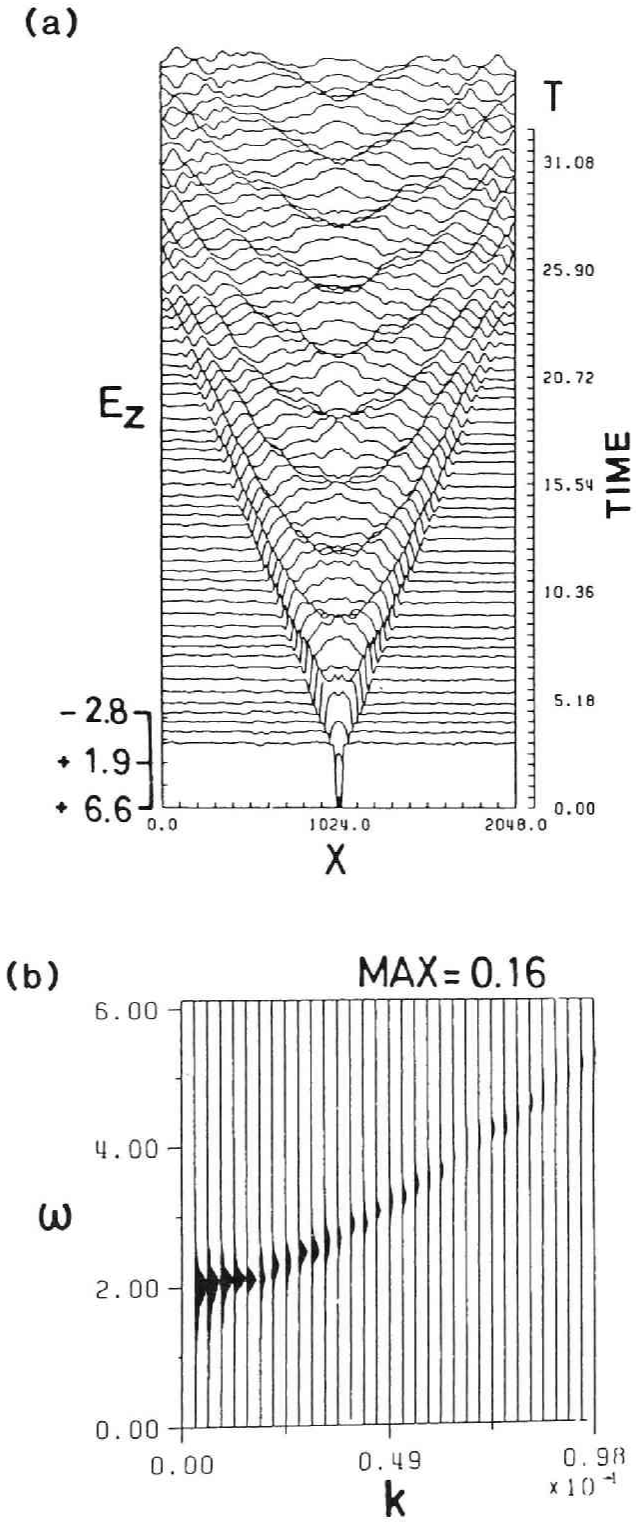

Fig. 5.3 (a) Spatial profiles of the E_z field and its time evolutions.
(b) The ω - k diagrams of E_z field.

in space and time, we obtain an ω - k diagram as shown in Figure 5.2-(b). The slow extraordinary wave (SE mode) is clearly excited as well as the fast extraordinary wave (FE mode) [Akhiezer et al., 1975]. The wave most strongly excited is the mode at the cutoff frequency of the SE mode.

The time evolution of the transverse electric field E_z is shown in Figure 5.3-(a). As the magnetic field is in the z-direction, the excited wave is the ordinary wave, which is excited by the beam current Jz. The ω -k diagram of the E_z field is shown in Figure 5.3-(b) The "MAX" in Figures in 5.2-(b) and 5.3-(b) indicates the maximum amplitude of the excited wave. The SE mode is obviously the most strongly excited mode.

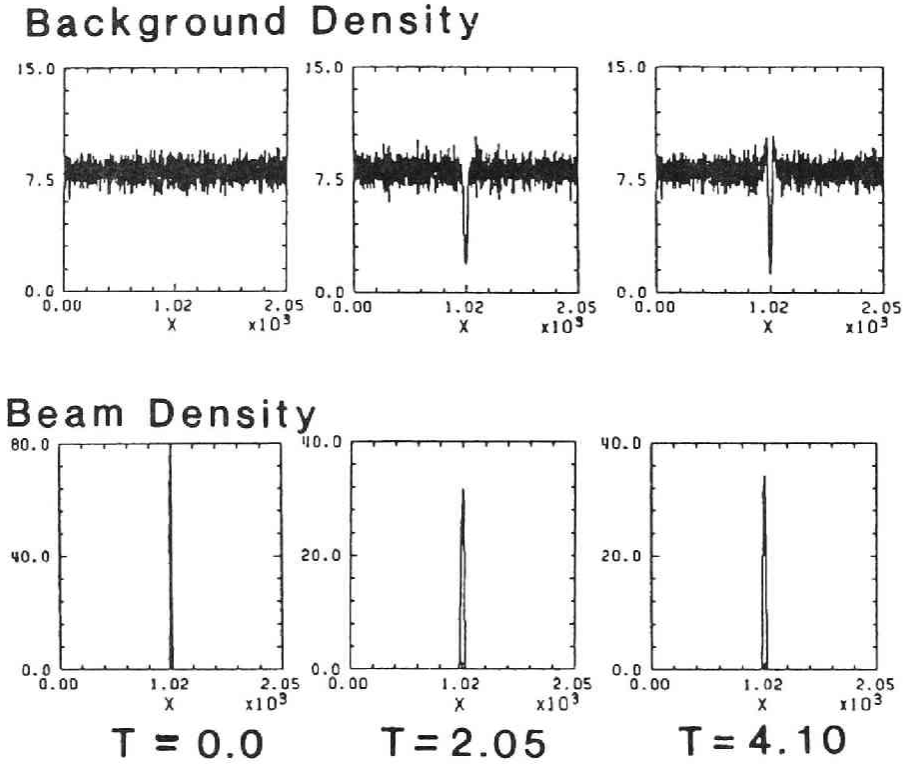

Fig. 5.4 Spatial distributions along the x-axis of the beam electrons and background plasma at different times.

The electric field E_x due to the excess charge of the beam electrons accelerates the surrounding background plasma electrons and causes a formation of a hole as seen in Figure 5.4. The electron beam itself also expands in size due to the electric field and subsequently oscillates with the period T_{SE} of the most strong SE mode wave. Therefore, the initial

expansion time of the beam is $1/2T_{SE}$. It is noted that the expansion time is decided by the background plasma condition rather than the electron beam property, because the dispersion characteristics of the SE mode waves are determined by the cold plasma.

5.2.2 Two-Dimensional Electromagnetic Model

The FEM code is applied to a more realistic two-dimensional electromagnetic model. A two-dimensional simulation space (x-y plane) formed by the spatial grid points of 128x128 are taken in a transverse plane to the static magnetic field which is taken parallel to the z-axis as seen in Figure 5.1-(b). 49152 cold electron is uniformly distributed in the simulation space. Dynamics of ions is not followed, although their presence is assumed to establish the charge neutrality. 1024 beam electrons are injected in the central area with about 4x4 grid points. In the FEM code, we assume a spatial uniformity in the z-direction, i.e., $\partial/\partial z = 0$. The x-y simulation plane is fixed at a certain $z = z_0$ point but both the background plasma and the beam are assumed to be uniform in the z-direction for all time including the injection time $t = 0$. In this model the electron beam has a cylindrical shape which is uniform in the z - direction. The initial drift velocity of the electron beam is 0.2c. and the thermal velocity is 0.02c. The thermal velocity of the background plasma is 0.02c and the plasma frequency is 2.0 Ω_e. The beam plasma frequency is about 6.4 Ω_e. Owing to the beam charge, an electric field is produced radially. The background plasma and electron beam are accelerated outward initially and oscillate subsequently. In Figure 5.5 contour maps of the distributions of the background electrons and the beam electrons are presented. As in the one-dimensional model, an initial expansion of the beam and a formation of a hole in the back ground plasma are found to take place followed by subsequent oscillations. The Fourier analysis of the electric field E_x and E_z both in time and in space gives ω k diagrams as shown in Figure 5.6. The ω - k diagrams of the cold plasma condition before the electron beam injection are also shown in Figure 5.6 for comparison. The "MAX" in the diagrams is the maximum amplitude of the wave modes shown in each diagram. Possible wave modes in the present configuration, i.e., in the transverse propagation modes, are fast and slow extraordinary waves for E_x and E_y components, and an ordinary wave for E_z component. From the ω k diagrams it is noted that the SE mode is a dominant wave to be excited.

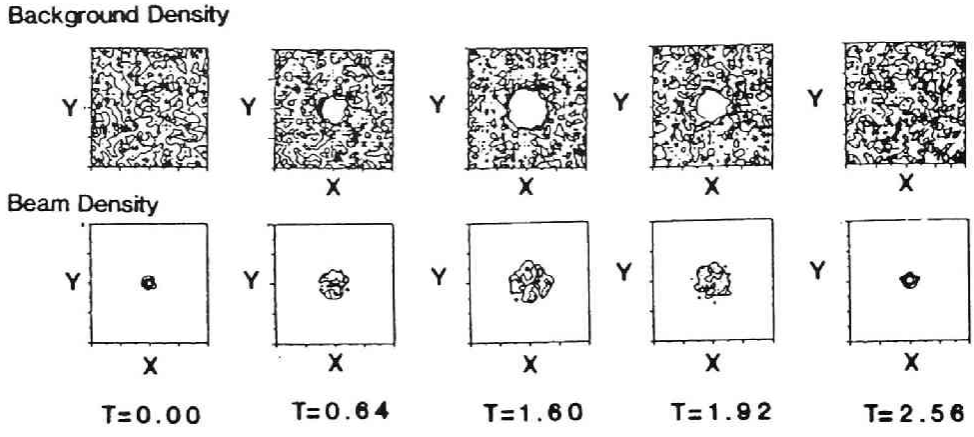

Fig. 5.5 Contour maps showing distribution in the x-y plane of the background plasma and beam electrons at different times.

Although the SE mode wave is most strongly excited around the beam, it is not likely to be observed at distance because of the group velocity of the wave is very small. On the other hand, the O mode wave propagates with a velocity nearly equal to the light speed. The O mode wave is an impulse-like wave which is excited by the sudden appearance of the beam current Jz at the start of the beam injection. In Figure 5.7 three-dimensional plots of the spatial profiles of the E_z field at different times is presented. It is noted that the O mode wave is an impulse response to the onset of the electron beam injection.

To see a spatial behavior of the beam in detail, vector plots of the current Jx and Jy in the vicinity of the beam are presented in Figure 5.8. The current flows inward at first and subsequently rotates owing to the variation of the electric field, and then flows outward. It is noted that the beam is twisted spatially owing to the ExB drift in addition to its radial oscillation.

5.2.3 Summary and Discussions

Simulation results of 1D and 2D electromagnetic models for the beam injection in space have been presented in the previous sections. In the simulation, ion kinetics is neglected and the plasma is assumed to be

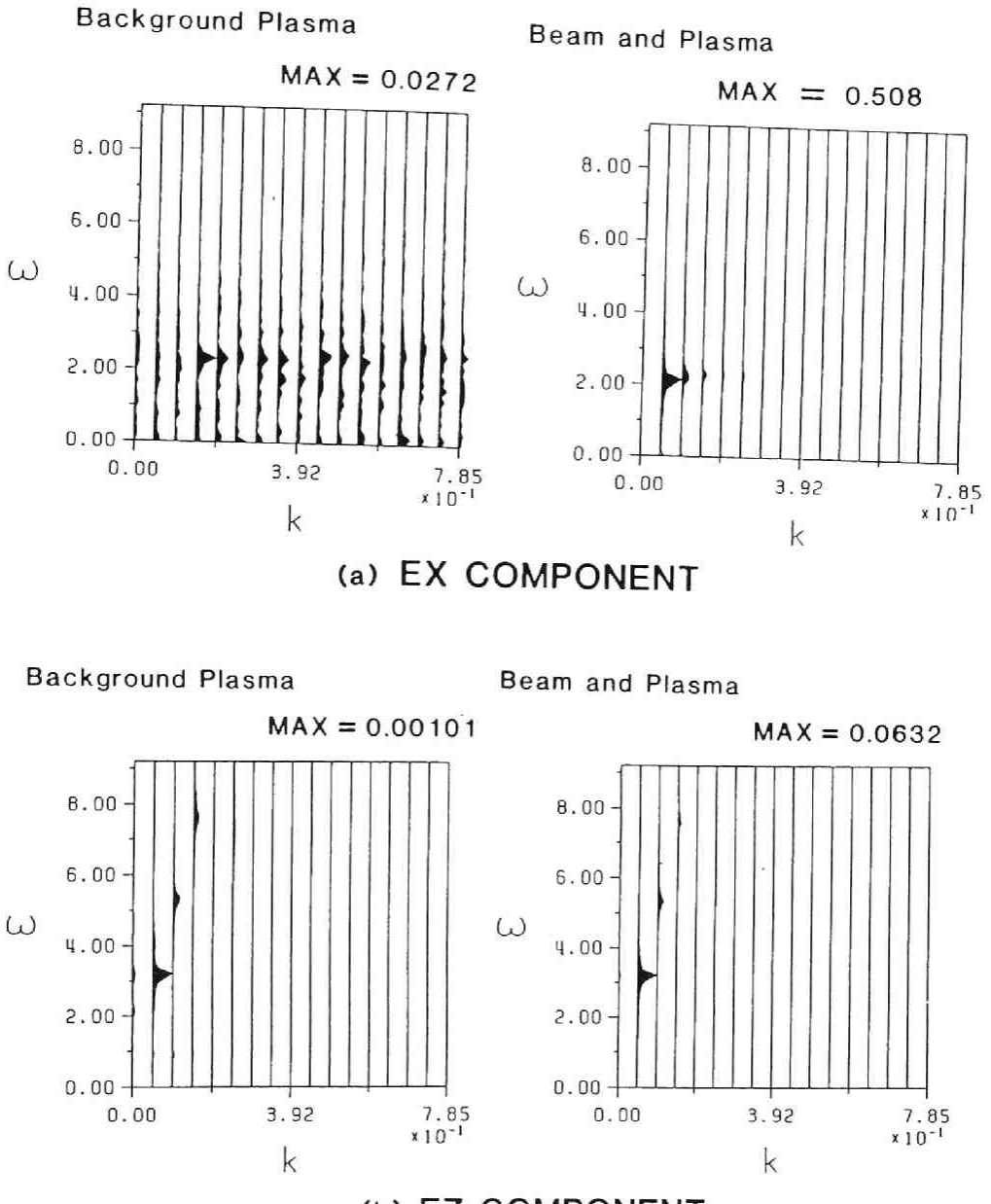

Fig. 5.6 The ω - k diagrams of (a) E_X and (b) E_Z fields of 2D models.

collisionless, which is valid at the initial stage of the beam-plasma interaction. Beam Plasma Discharge (BPD) takes place at several hundred plasma periods after the onset of the beam injection (Bernstein et al.,1979; Mishin and Ruzhin, 1980; Papadopoulos, 1981; Szucszewicz et al., 1982). The present simulation therefore is effective only within several hundreds of plasma periods. Those phenomena found in the 1D model are all reproduced in the 2D model. Slow extraordinary waves with long wavelength

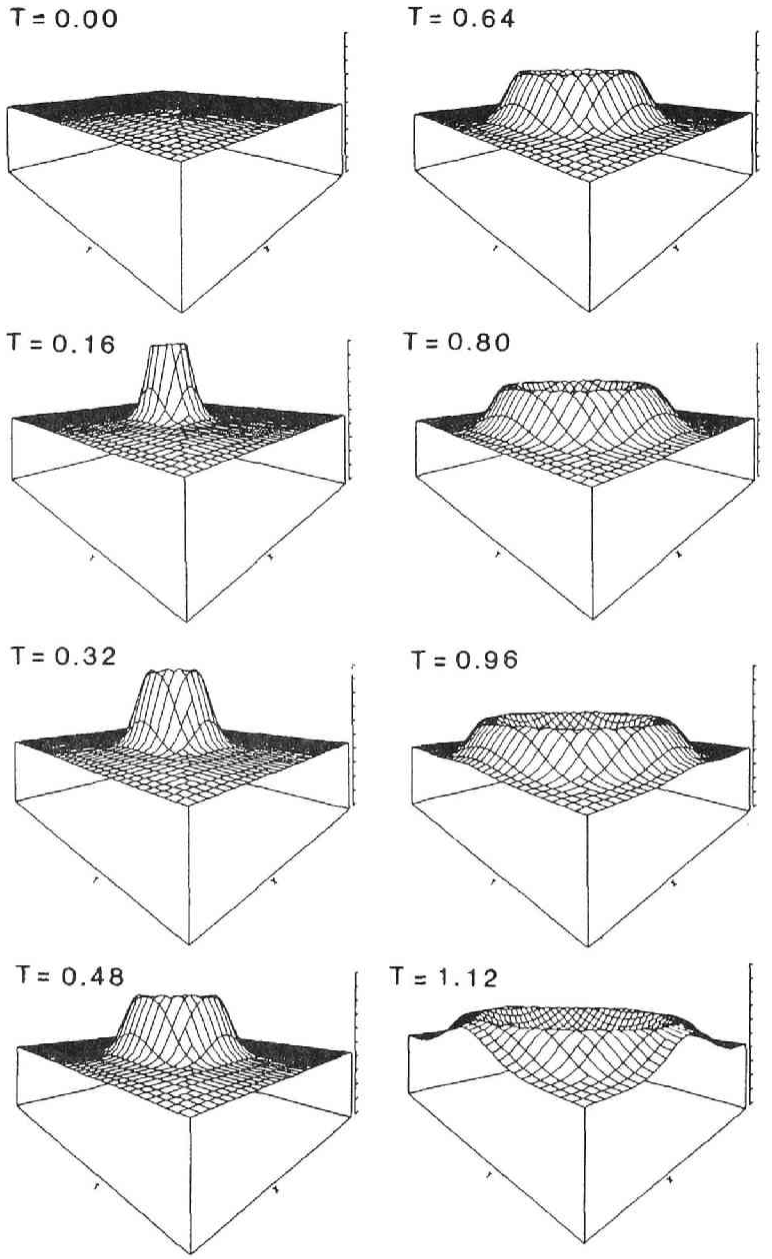

Fig. 5.7 Three dimensional plots of the spatial profiles of the E_z field at different times.

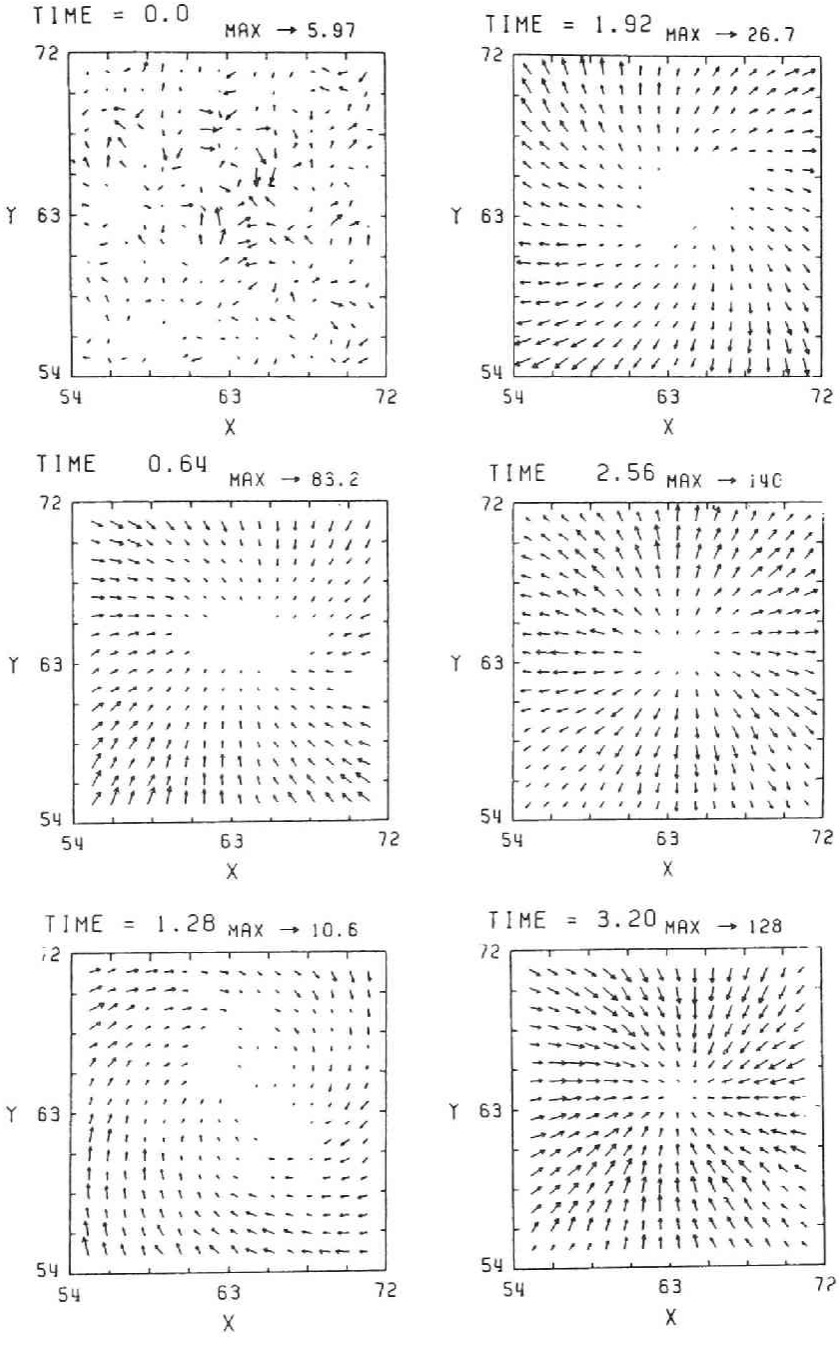

Fig. 5.8 Vector plots of the current density in the x-y plane.

are preferentially excited in the both models. Especially the mode which has a wavelength of the system length is the most dominant one among the SE mode waves. This is because of the periodic boundary condition assumed for the limited number of grid points. The wavelength of the wave that would actually excited in the space plasma is still unknown, and may depend on the magnetospheric conditions.

In the 1D model where we could obtain a better resolution, the SE mode wave at the cutoff frequency was most strongly excited. Therefore, in the real experiment the wave at the cutoff of the SE mode will be dominant and the oscillation of the beam and the background plasma will have the cutoff frequency of the SE mode. These plasma oscillations are observed only in the vicinity of the electron beam and subside as neutralization of the beam charge proceeds owing to the ion reaction. An impulse-like wave of the O mode are also found to be excited in the both 1D and 2D models, although the intensity is much lower than that of the SE mode wave. This wave having a electric field E_z is excited by the beam current J_z via

$$\partial E_z/\partial t = -J_z/\varepsilon_0 \tag{5.1}$$

This wave propagates radially as seen in Figure 5.7 and is possibly observed at distance in accordance with the onset of the beam injection. Coinciding with the excitation of the SE mode wave, the beam and background plasma start to oscillate with the frequency of the SE mode wave.

The initial expansion of the beam lasts for $1/2T_{SE}$. It is noted that the expansion time is decided by the background plasma condition rather than the beam condition itself.

In the actual SEPAC experiment on space shuttle, the injection point of the electron beam moves spatially with the space shuttle and hence the configuration and plasma conditions may be very complicated. As a first step of the simulation study of the SEPAC, we assumed a spatial uniformity for simplicity. As discussed in Subsection 5.2.3, the nonunifomity in the direction of the external magnetic field may well play an important role in the excitation of plasma waves. Therefore, as a second-step study, it is definitely necessary to do a two-dimensional electromagnetic simulation taking one of the two dimensions along the static magnetic field, e.g., in the y-direction. This is an extension of the 1D model presented in this paper. The periodic boundary condition is no longer applicable to the y-direction, as we have to simulate the electron beam injection along the y-direction from the gun. This work is currently being carried out and its results will be published elsewhere.

5.3 Electrostatic Radiation from an Electron Beam Modulated by Coherent Whistler Mode Wave

Reinleitner et al. [1982, 1983] discovered in the data from the ISEE satellite that strong electrostatic (ES) noise bursts are often associated with a coherent chorus hook element (see Figure 5.14 in their section). At the time of occurrence of these hook-induced ES bursts, a high-energy electron beam with an energy of the order of several hundred eV is always simultaneously observed. The frequency of the hook-induced ES bursts varies from just above the local plasma frequency f_{pe} down to ~ 50-60% of f_{pe}. The relative intensity of the bursts is less than the hook intensity. The measured k vector of the ES bursts is parallel to the geomagnetic field. As for the generation mechanism of this phenomenon, Reinleitner et al. [1983] and Gurnett and Reinleitner [1983] proposed the following two step mechanism: (1) First, an obliquely propagating monochromatic whistler chorus accelerates trapped Landau-resonant electrons due to an increase of its phase velocity as it propagates along the inhomogeneous geomagnetic field line and creates an electron beam which runs along the geomagnetic field keeping resonance with the obliquely propagating whistler chorus. (2) Then, the electron beam itself becomes unstable against a resistive instability giving rise to a strong ES wave.

In the present paper, we focus our attention only on the second step, assuming the co-existence of an obliquely propagating monochromatic whistler wave and a resonant electron beam. The study reported here is to quantitatively investigate features of the instability in the whistler-plus-beam system by a particle computer simulation. Our objectives are to see if the instability of the whistler + beam system is appreciably different from the conventional instability in the beam-plasma system and, if so, to study how different it is and to reveal what kind of wave mode is preferentially excited and to reveal its mechanism. For this purpose, we carried out two computer-runs with two different initial conditions: One with the obliquely propagating monochromatic whistler wave and the other is without the wave. In both runs, an electron beam with a parallel velocity equal to the resonance velocity $V_R = \omega/k_{\parallel}$ is assumed to exist in a background warm plasma where ω and $k_{\parallel}$ are the wave angular frequency and a component of the wavenumber vector projected onto the external magnetic field. The computer code used in this study is a two-and-one-half

dimensional (2-1/2D) electromagnetic particle code (referred to as the FEM code hereafter) which treats two-dimensional structure of all physical quantities as well as three-dimensional particle motion. The reason for the use of the FEM code, instead of using the more economical EM1 code with 1 spatial dimension and 3 velocity dimensions, is that we need to seek the unstable wave modes in the two-dimensional k-vector space in order to decide the direction of k vector of the most preferentially excited wave mode by the instability concerned.

5.3.1 Simulation Model and Parameters

The basic equations solved in the FEM code are:

$$\frac{d\vec{v}_s}{dt} = \frac{e_s}{m_s} (\vec{E} + \vec{v}_s \times \vec{B}) \tag{5.2}$$

$$\frac{d\vec{r}_s}{dt} = \vec{v}_s \tag{5.3}$$

$$\nabla \times \vec{E} = - \frac{\partial \vec{B}}{\partial t} \tag{5.4}$$

$$\nabla \times \vec{B} = \mu_o \vec{J} + \frac{1}{c^2} \frac{\partial \vec{E}}{\partial t} \tag{5.5}$$

$$\nabla \cdot \vec{E} = \frac{\rho}{\varepsilon_o} \tag{5.6}$$

where v_s, r_s, q_s, and m_s are velocity, position, charge, and mass of superparticles of the s-th kind; E and B are electric and magnetic fields; ε_o, μ_o, ρ, J, and c are the permeability, permittivity, charge density, current density, and speed of light, respectively. The charge, mass, and temperature of superparticles are so decided that the charge density, mass density, and kinetic energy density are kept the same as those of real plasma particles. Thus, the plasma frequency Π_s, cyclotron frequency ω_s, thermal velocity $v_{th,s}$, and the Debye length are kept unchanged from those in the real plasma. In the present FEM code, the super-particles are given a square-shaped charge. As for the method of distribution of charge and current carried by each individual superparticle to the adjacent four

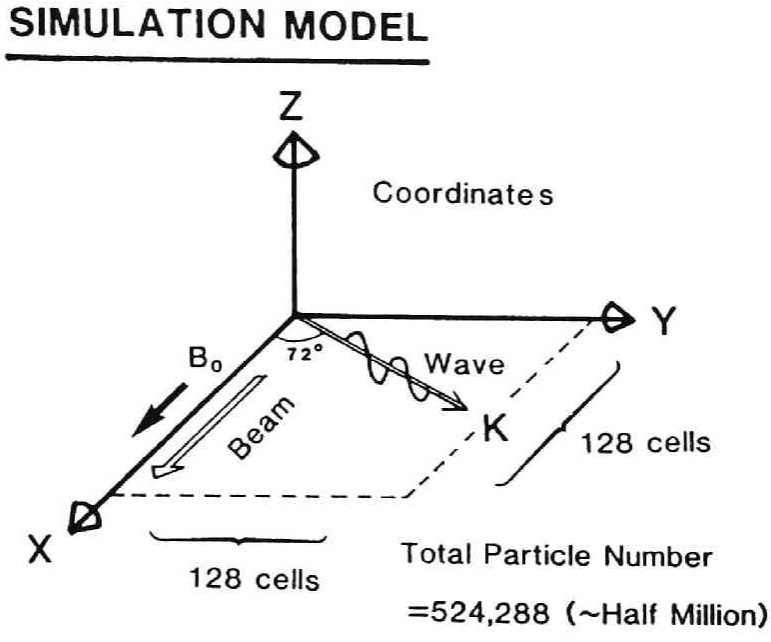

Fig. 5.9 Coordinate system for the present simulation. The simulation area is in the x-y plane with a length of 128 grids in both directions. Periodic boundary conditions are applied both to x and y boundaries. In both Cases A and B, an electron beam streaming along B_0 is set as an initial condition together with a background of warm bi-Maxwellian plasma. The drift velocity of the electron beam is identical for Cases A and B and is equal to the resonance velocity of the obliquely propagating monochromatic whistler wave. The initial conditions for E and B field are all zero except for B_0 in Case A. Only in Case B, an additional initial conditions are prepared for the electric and magnetic fields of the assumed monochromatic whistler wave along with the corresponding velocity and spatial modulation of warm plasma particles.

grids, and for that of interpolation of the fields onto the particle location from the grids, the area sharing scheme (i.e., PIC scheme) was adopted.

The conventional staggered grid system in space [e.g., Langdon and Lasinski, 1976; Hockney and Eastwood, 1983] is used along with a leap-frog scheme in time to rewrite all the basic equations in a form of centered difference equations in both space and time. A dual time-step scheme is adopted to reduce the CPU time. Particles are updated only at a

TABLE 1. List of Simulation Parameters

Quantities	Notation	Case A	Case B
Grid spacing, Δr	Δr	1.0	1.0
Debye length, λ_D	λ_D	1.0	1.0
System size	$L_x \times L_y$	128 × 128	128 × 128
Time step for waves	Δt_w	0.01	0.01
Time step for particles	Δt_p	0.08	0.08
Electron plasma frequency	Π_e	2.0	2.0
Electron beam plasma frequency	Π_b	0.2	0.2
Electron cyclotron frequency	Ω_e	1.0	1.0
Light speed	c	50.0	50.0
Number of background plasma particles per cell	N_0	16	16
Number of beam particles per cell	N_b	16	16
Density ratio of beam to background plasma	η	0.01	0.01
Total number of particles	N_t	524,288	524,288
Average velocity of the beam	V_b	5.48	5.48
Beam thermal speed	$V_{b,th}$	0.2(isotropic)	0.2(isotropic)
Thermal speed of background plasma	V_{th}	2.0(isotropic)	2.0(isotropic)
Propagation angle between k and B_0	θ	...	71.6°
Amplitude wave magnetic field	B_w	...	0.1
External magnetic field	B_0	10.0	10.0
Amplitude of wave electric field parallel to B_0	$E_{\parallel}$	...	8.4
Amplitude of wave electric field perpendicular to B_0	$E_{\perp}$	...	0.17
Wave frequency	ω (not f)	...	0.27
Number of wave cycles in L_x	L_x	...	1
Number of wave cycles in L_y	L_y	...	3
Phase velocity of the wave	V_{ph}	...	1.73
Total time steps		8,192	8,192
Total CPU time on FACOM-M200		16 hours	16 hours

Table. List of simulation parameters

large time step which is some-integer times larger than the time-step for field-updating [Matsumoto and Omura, 1984]. Before carrying the present simulation runs, we performed several test runs of our computer code. The check we made is a test of its reproducibility of the linear dispersion relations of normal mode waves in a magnetized plasma. The results are quite satisfactory. All modes including kinetic mode such as electrostatic and electromagnetic cyclotron waves are reproduced in the run and their dispersion relation agreed quite well with the linear theory. Details of the test run will be reported elsewhere [Matsumoto and Omura, 1984].

The model of the two runs for the present study is depicted in Figure 5.9. The simulation plane is in the x - y plane which are divided into 128 x 128 cells with a grid size of the Debye length. The system is assumed to be periodic in both x and y directions and hence periodic boundary conditions are used. The external magnetic field B_0 is assumed to be parallel to the x-axis. An electron beam is set to run parallel to B_0 with a velocity equal to a velocity $\omega/k_{\parallel}$ which is the resonance velocity with the obliquely propagating whistler mode wave. The velocity distribution of the beam is given by a shifted Maxwellian with center and thermal velocities as listed in Table 1. The case in which only the electron beam is set in the background of the warm plasma and where no initial wave is assumed is called Case A. While the other case is called Case B in which, in addition to the electron beam, initial conditions for particles and fields are set to make a monochromatic whistler wave propagate at an angle of 72^0 with B_0 in the x - y plane as depicted in Figure 5.9. The fields of the monochromatic wave and associated particle velocities and positions of the warm plasma particles are related with each other by the linear theory. In both Case A and Case B, ions are assumed to be immobile (i.e., $m = \infty$)

In Table 1, parameters used in Case A and Case B simulations are listed up.

5.3.2 Simulation Results

- Evolution of k-spectra and dispersion relation of excited waves

Data of electric and magnetic fields assigned to all grid points are Fourier-analyzed by an FFT-analyzer and converted to Fourier components on the $(k_{\parallel}, k_{\perp})$ plane. These Fourier components as a time series were then Fourier analyzed in time domain by a post-processor yielding an ω k

diagram of the excited waves. Figure 5.10 shows a contour-map display in the $k_{\parallel}$ - $k_{\perp}$ plane of the k spectra of electric field components, E_x, E_y and E_z integrated over from ω = 0 to ω =2.4. The "mode number" described along the $k_{\parallel}$ and $k_{\perp}$ axes gives a number of cycles of wave within the system length in the directions along and perpendicular to B_o, respectively. In the results of Case A for the study of the conventional beam instability, we do not see any strong waves are excited except for a weak excitation of a wave with $k_{\parallel}$ = 0 and $k_{\perp} \simeq 0.05$ (i.e., with a mode number = (0, 1)), which turns out to be electron cyclotron waves with $\omega \simeq 2.0$. In Case B, however, a strong electric field parallel to B_o (i.e., E_x-component) is excited with a k-vector parallel to B_o (i.e., $k_{\parallel} \simeq 0.3$ and $k_{\perp} \simeq 0$). This means the excited wave is of electrostatic nature propagating parallel to the external magnetic field. An intense spectrum peak at $k_{\parallel}$ - 0.05 and $k_{\perp}$ = 0.15 or at a modal point of (1, 3) is the obliquely propagating whistler wave. The corresponding ω - $k_{\parallel}$ diagrams for the E_x component in both Case A and Case B are shown in Figure 5.11. The frequency spectrum intensity is plotted as a function of frequency for each fixed k-value in the figure. A clear difference is seen between these two cases. In Case B, strong waves are excited with a phase velocity slightly faster than the initial beam velocity which is depicted by a dashed line for reference. The frequency range of the excited waves is approximately from $0.5\Pi_e$ ~ $0.6\Pi_e$ to $1.2\Pi_e$, where Π_e (= 2) is the plasma frequency. It is noted, however, that these spectra are the integrated ones over the whole interaction time. Therefore, the frequency or k-spectrum may be changing from time to time. To check this point, the k-spectra in the ($k_{\parallel}$, $k_{\perp}$) plane at different times are shown in Figure 5.12. In Case A, almost no strong wave is seen for all these times. In Case B, the peak at ($k_{\parallel}$ - 0.05, $k_{\perp}$ = 0.15), which represents the E_x-component of the obliquely propagating whistler wave, is reducing its height due to the Landau damping by the beam. As the whistler wave is attenuated, electrostatic waves with its center in the vicinity of ($k_{\parallel}$, $k_{\perp}$) $\simeq$ (0.25, 0) begin to grow up at t = 20.5 and become strengthened after t = 41 shifting their peaks into higher $k_{\parallel}$ from $k_{\parallel}$ = 0.25 to $k_{\parallel}$ = 0.40. This result gives if combined with the dispersion analysis in Figure 5.11 that the wave frequency of the excited electrostatic bursts varies from approximately $0.5\Pi_e$ to $1.2\Pi_e$ in a relatively short time of the order of $\tau = 80\Pi_e^{-1}$. A discussion concerning the characteristic time τ of the frequency change, will be given later. Intensities of each $k_{\parallel}$ mode in Case B are plotted as a function of time in Figure 5.13.

Appreciable growth is observed for the modes from #4 to #8 with a

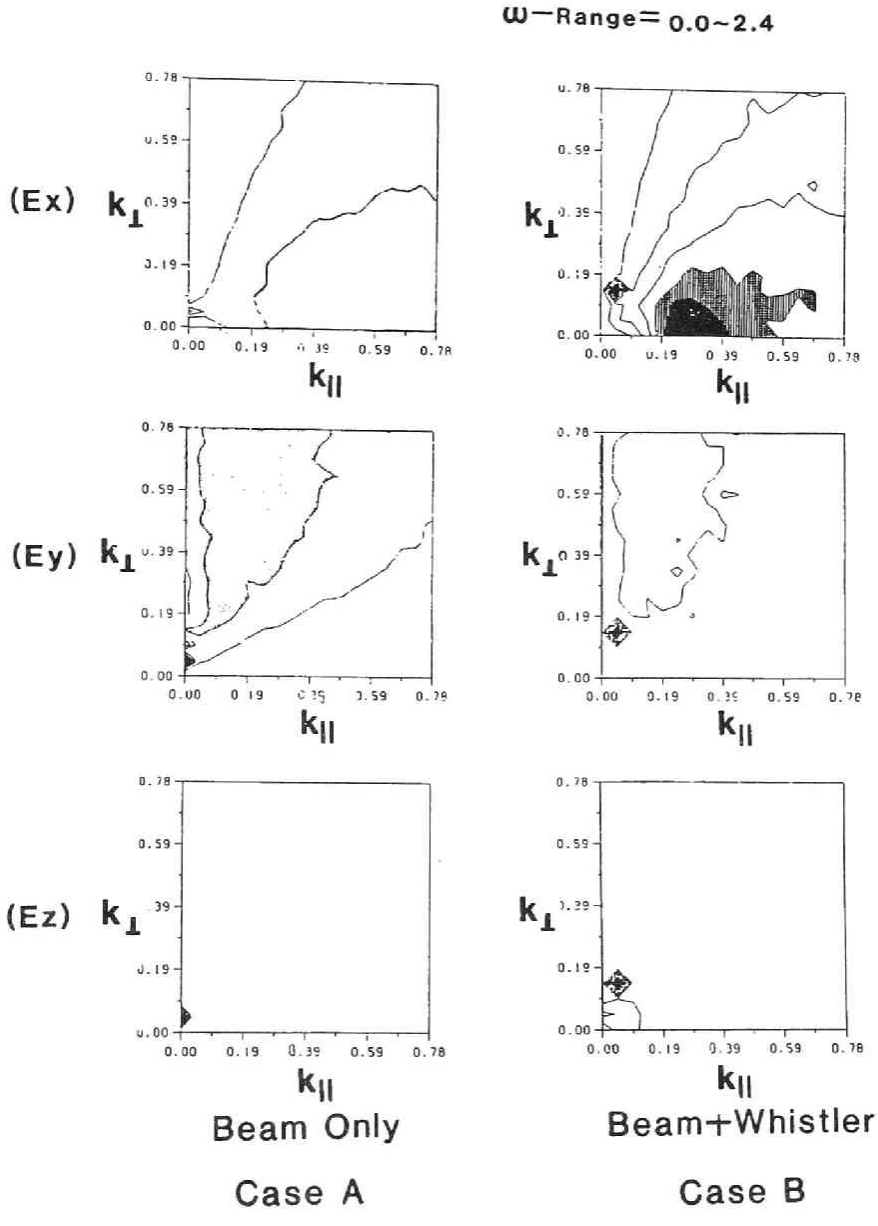

Fig. 5.10 Analyzed k-spectra of three electric field components for Case A and Case B. The k-spectra are shown by contour maps with gray code in the ($k_{\parallel}$, $k_{\perp}$) plane. These spectra are those averaged over whole simulation time and over a frequency range from $\omega = 0$ to $\omega = 2.4$ which is the maximum sampling frequency determined by the sampling rate. Though almost no wave excitations are seen in Case A, a strong E_x-component with $k \,//\, B_0$ is seen in Case B. A sharp peak with $k_{\perp} = 0.15$ and $k_{\parallel} = 0.05$ corresponds to the obliquely propagating monochromatic whistler wave.

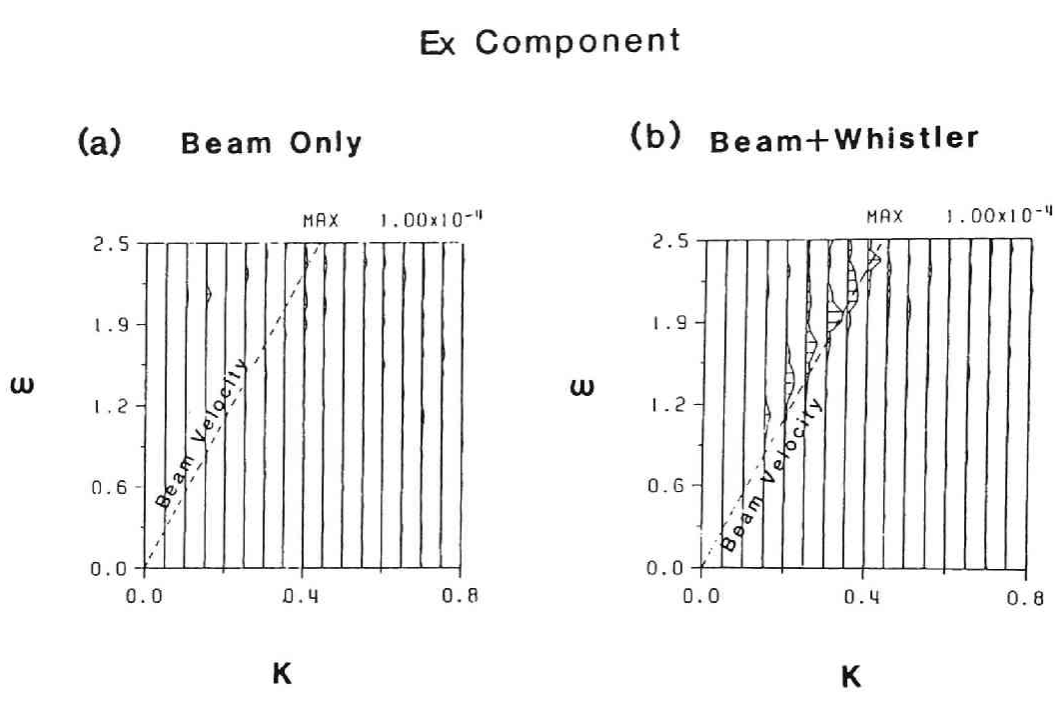

Fig. 5.11 Dispersion characteristics of the E_x component of the excited waves shown in the form of $\omega - k_{\parallel}$ diagrams. The initial beam velocity is shown by dashed lines for reference.

maximum intensity at mode #5. In the two largest modes #5 and 6, a fast growth is seen from $t \simeq 30$ to a time of the maximum peaks, following the initial slow growth phase from $t = 0$ to $t \simeq 30$. This indicates the instability nature changes at $t \simeq 30$ in the whistler + beam system.

- Evolution of Spatial and Velocity Distributions of the Beam

The electric field component $E_{\parallel}$ parallel to B_o of the obliquely propagating whistler wave spatially traps the resonant electron beam in the bottom of its potential well as schematically depicted in Figure 5.14. Accordingly, the initial velocity distribution function with a mono-peak at $V_B - V_{res} = \omega/k_{\parallel}$, depicted by a dashed line in the lower panel of Figure 5.14, is expected to be deformed into twin-peaked distribution function due to acceleration and deceleration of the beam electrons by the wave potential. Figure 5.15 shows the evolution of the spatial distribution of the electron number density for both Case A and Case B. The perturbation $\Delta N_e(x, y)$ is plotted in the x - y plane by a contour map for selected times from 0 to 71.7. In Case A, we see many patches are developed as time elapses changing their structure from more clearly lined-up structure along

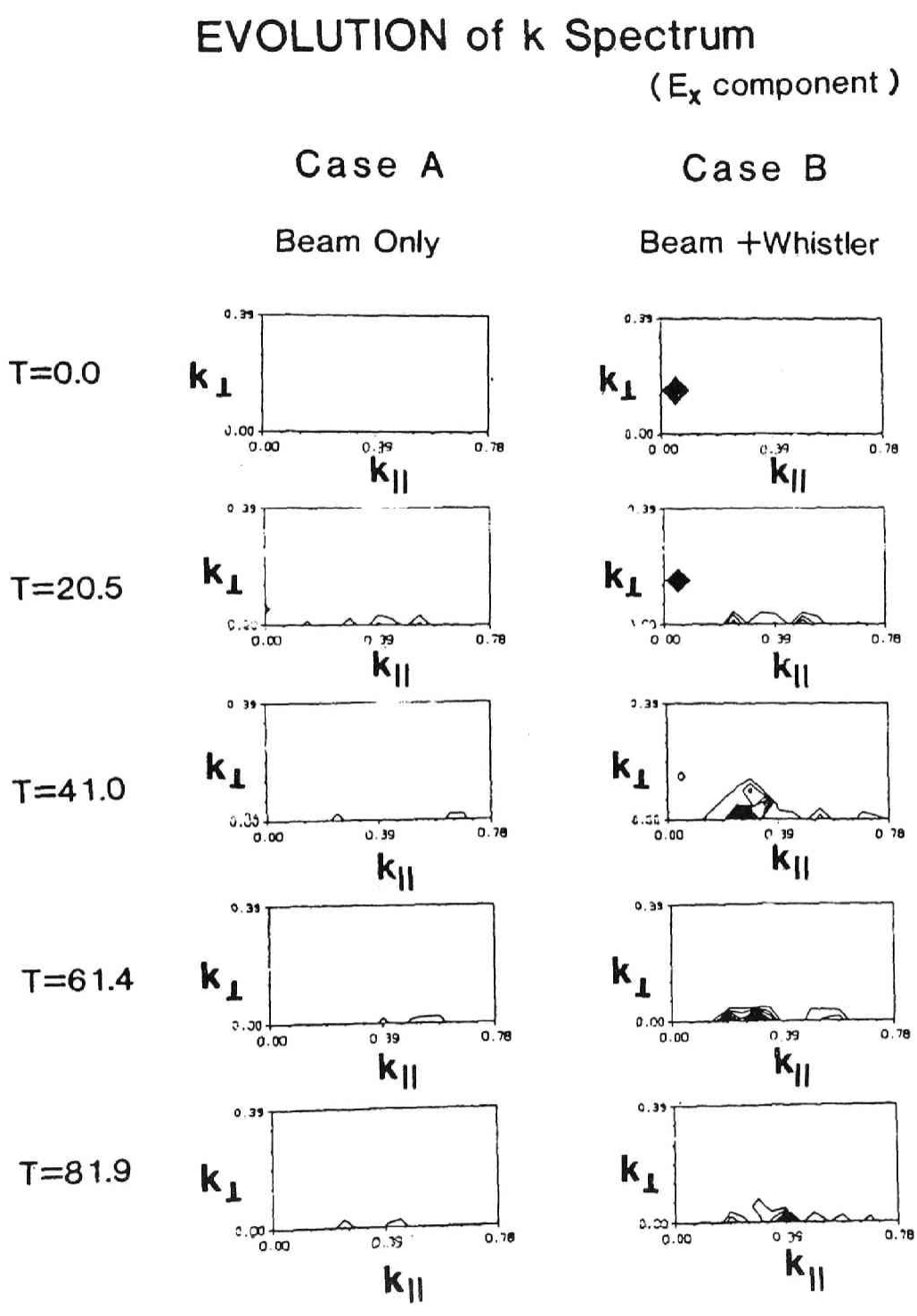

Fig. 5.12 Evolution of the k-spectra. In Case B, the spectra peak at ($k_\parallel$ = 0.05, $k_\perp$ = 0.15) representing the propagating oblique whistler wave is damped out by the Landau damping, while a strong peak appears around ($k_\parallel$ =0.25, $k_\perp$ = 0) at a time T = 41 when the E_x-component of the whistler wave is considerablly weakened.

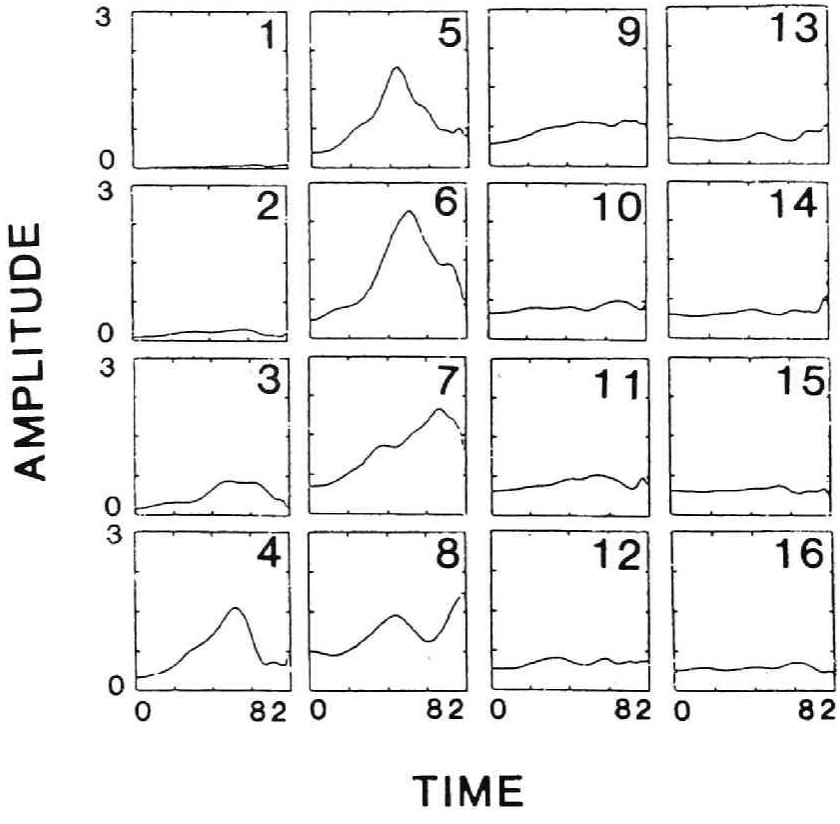

Fig. 5.13 Time evolution of each $k_{\parallel}$-mode of the excited waves in Case B. Numbers indicated in the upper right corner in each frame are mode numbers in the direction of x-axis (parallel direction).

y-axis at t = 10.2 to more scattered patches in the x y plane at later time. In Case B, however, the expected spatial trapping is seen clearly at t = 20.5, 30.7 and vaguely at t = 10.2 and 41.0. The high density regions are lined-up perpendicular to the wave normal vector of the whistler wave. The collapse of the trapping starts around t ~ 30 giving rise to a complete detrapping at t ≃ 40. Figure 5.16 shows the corresponding evolution of the parallel distribution function $f(v_{\parallel})$ as a function of time for both Case A

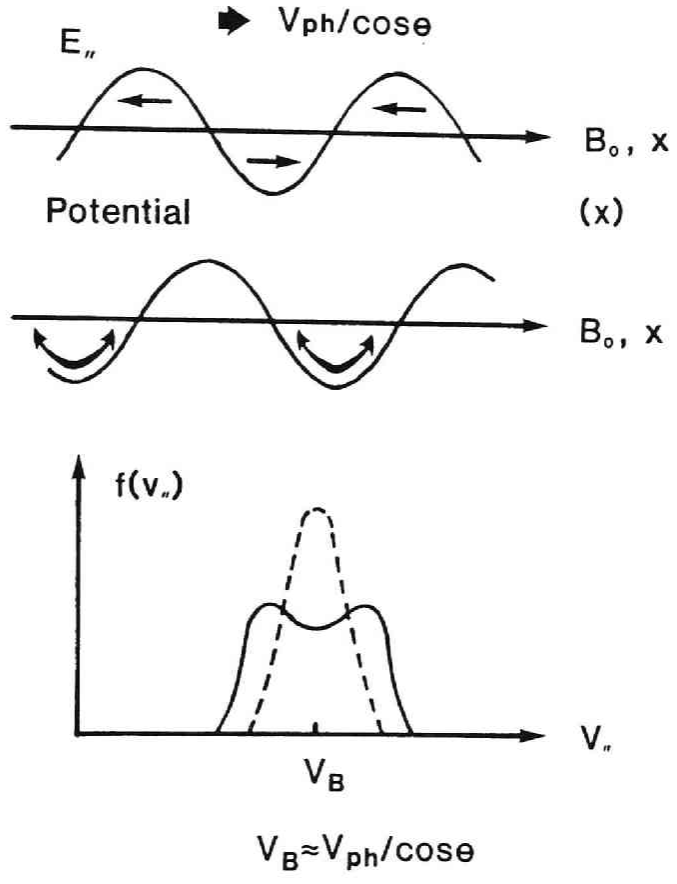

Fig. 5.14 A schematic illustration showing a spatial trapping of the resonant beam electrons in a potential well of $E_{\parallel}$ of the obliquely propagating whistler wave. The lower panel shows the expected twin-peaked $f(v_{\parallel})$ due to acceleration and deceleration of beam electrons by $E_{\parallel}$.

and Case B.

In the conventional beam instability case (Case A), the velocity distribution function of the beam shows the well known evolution, i.e., the mean velocity decreases accompanied with the spread of the distribution function. This explains the energetics of the conventional beam instability. The free energy of the instability is the drift kinetic energy of the beam which is deposited into wave energy and thermal energy of both ambient and beam electrons. In contrast to this conventional beam instability, the [whistler + beam] system shows quite different evolution of the $f(v_{\parallel})$. The initial mono-peaked distribution function is deformed into a twin-peaked distribution, separated at the resonant velocity. As time elapses, the twin-peaked nature eventually disappears because the wave

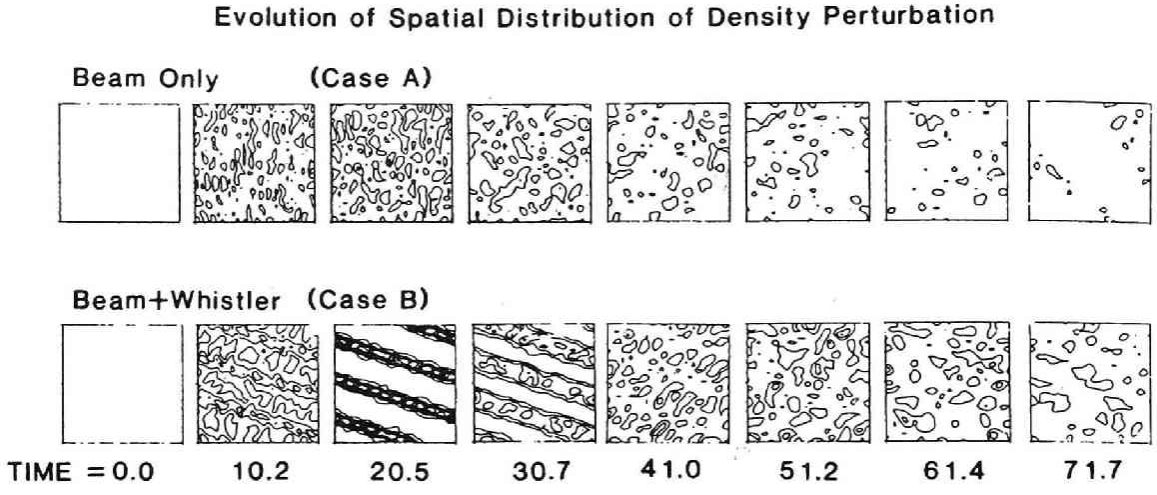

Fig. 5.15 Evolution of spatial distribution of density perturbation of the electron beam. Horizontal and vertical axes correspond to x- and y-axes, respectively. The upper and lower columns show the sequential changes of the density evolution for Case A and Case B, respectively.

loses its potentiality of trappings the beam electrons after t = 30 Th and hence no more keep the trapped electrons rotating in the trapping region in the phase space. This point will be discussed in more detail later.

- Evolution of Phase Space Plot of Resonant Beam Electrons

The difference of beam electron behavior for the two Cases A and B becomes clearer if we see the phase space plot of resonant beam electrons. Figure 5.17 gives the phase space plot in the $v_{\parallel}$- x phase space for both Case A and Case B. The result for the Case A indicates the well-known evolution of the conventional beam instability: At first the beam velocity is modified by the electric field created by the beam itself and shows the wave structure in the $v_{\parallel}$-x space as seen in the frame for t - 10.2. Then

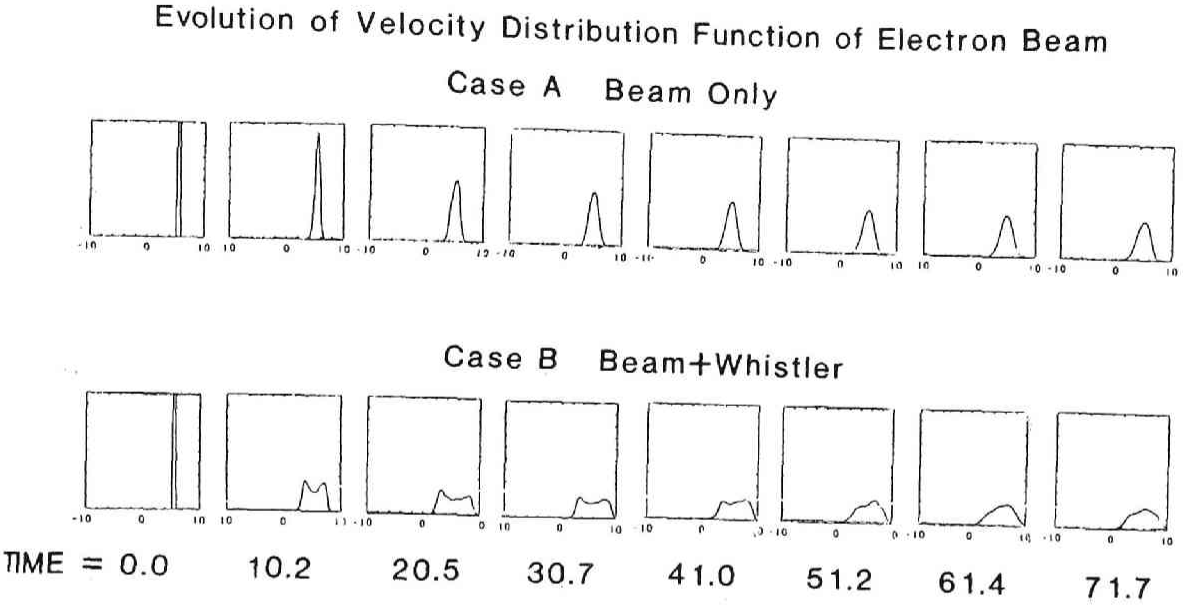

Fig. 5.16 Evolution of parallel velocity distribution function of electron beam. The upper and lower columns correspond to Case A and Case B, respectively.

the nonlinear state is set-in giving rise to the formation of eddies in the phase space as seen in the frame for t = 20.5. At later time, however, the usual thermalization process takes place yielding the spread of the beam in the $v_{\parallel}$. In Case B, the phase space behavior is much different from that in Case A. Until t = 20.5 all of the beam electrons are clearly trapped by the wave potential as schematically illustrated in Figure 5.18. Those electrons in the right half plane in the phase space plot are decelerated and those in the left half plane are accelerated as seen, e.g., in the frame for t = 10.2. Then these trapped electrons show a rotational motion in the phase space making a spiral as seen in the frame for t = 20.5. The magnitude of the velocity modulation is much larger than that in Case A under the present simulation parameters. Interesting point, however, is

seen in the frames at later times after t = 30.7. As previously mentioned, around t = 30 the intensity of the electric field component E_x parallel to the external magnetic field is reduced by the Landau damping down to a level which can no more keep these electrons being trapped in its potential well. Therefore, the electrons at higher speed than the original beam velocity, which is equal to the resonant velocity, stay in the higher velocity region in the phase diagram and those in the velocity lower than the resonant velocity stay in the lower region in the phase space after t $\simeq$ 40. This physically means that two electron beams, one with a higher speed and the other slower one than the original (initial) beam speed are created at a time of the detrapping of the beam electrons around t = 30. This two-beam jetting is a key process for the generation of a strong electrostatic wave bursts. This point will be discussed later in more detail. At later time, the two beams are merged in the velocity space via thermalization process with a slow time scale. The final velocity spread of the beam electrons is wider than that in Case A. This is an obvious result because the beam electrons are scattered additionally by the potential of the existing whistler wave in contrast to the simple beam instability in Case A.

5.3.3 Discussion and Conclusion

We have shown in the previous section that a strong electrostatic wave emission with a k vector parallel to the external magnetic field and with a frequency range from $0.5\Pi_e$ to $1.2\Pi_e$ is excited when and only when an electron beam coexists with a resonant monochromatic whistler wave propagating obliquely in the magnetized plasma. Examination of the involved microphysics of the wave-particle interactions in the simulation results leads to the following physical picture.

1. Electrons trapped by an obliquely propagating monochromatic whistler wave packet via Landau resonance are accelerated by an action of dispersive acceleration in the nonuniform geomagnetic dipole field [Gurnett and Reinleitner, 1983], thus producing an electron beam which is Landau-resonant with the whistler wave.
2. The trapped beam electrons show an oscillation in the potential well of the electrostatic electric field component of the whistler wave and absorb energy from the wave causing the Landau damping of the electrostatic component of the wave. During this process, the velocity distribution of the beam electrons changes from a mono-peaked to a

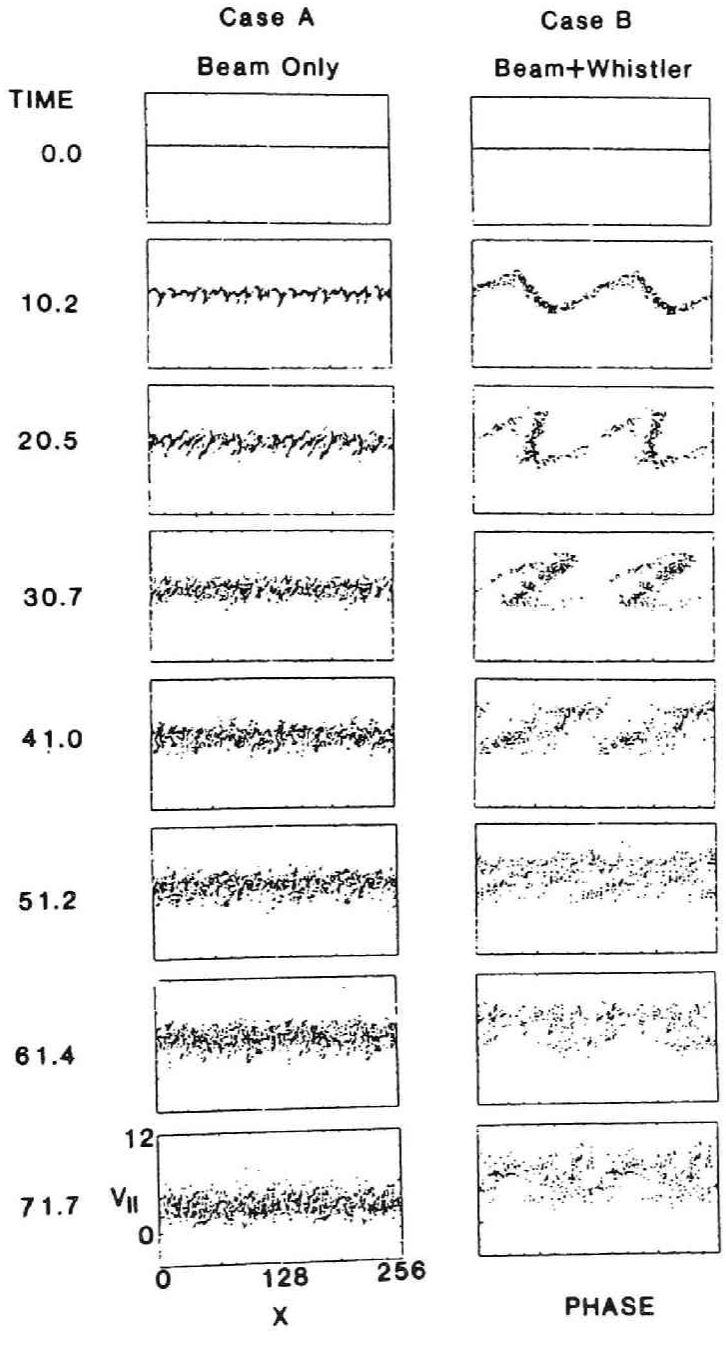

Fig. 5.17 Evolution of ($v_{||}$ - x) phase diagram of electron beam for (a) Case A and (b) Case B. A clear phase trapping of the electron beam by the monochromatic whistler wave and subsequent detrapping process is seen in Case B.

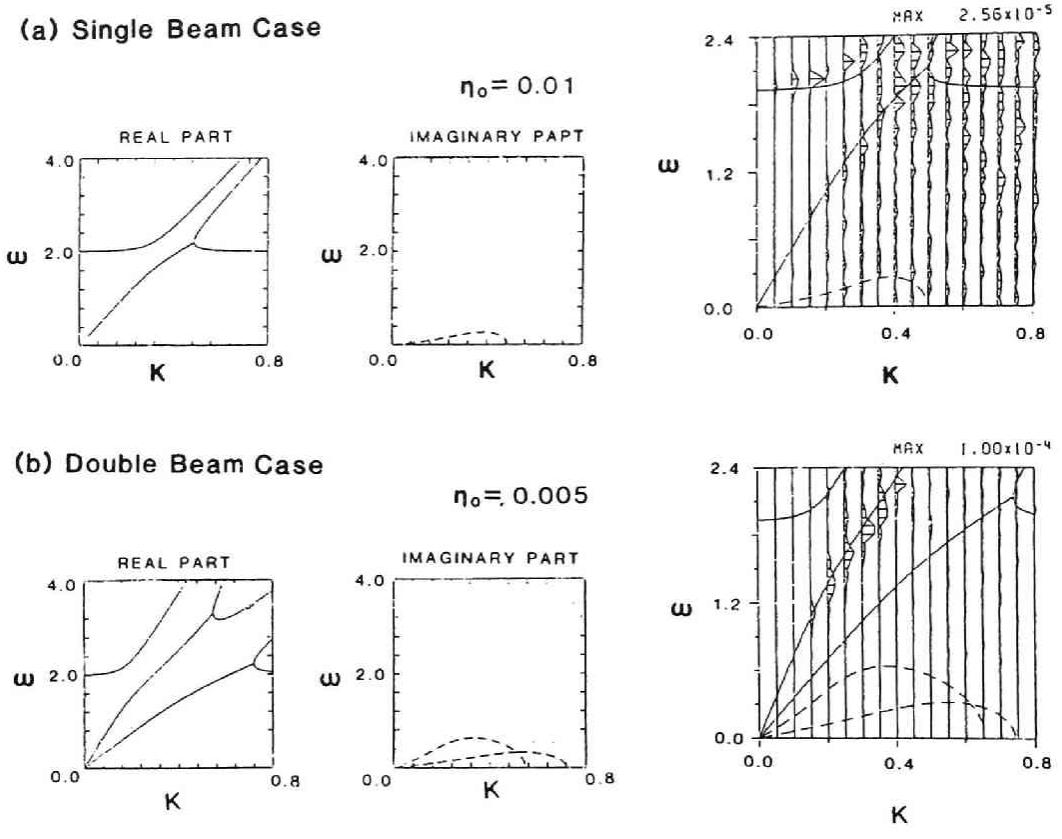

Fig. 5.18 Linear dispersion relations (ω - k diagrams) of beam instabilities. (a) Single beam case, (b) Double beam case.

double-peaked distribution with respect to the parallel velocity. This corresponds to a spiral motion of bunched electrons in the $v_{\parallel}$- x phase diagram.

3. The eventual damping of the electrostatic component of the electric field of the wave leads to a loss of a capability of trapping these electrons. Thus at a certain time of this damping process, the trapped electrons are detrapped. Approximately half of the detrapped electrons have a higher velocity than the resonant velocity and the rest half have a lower one at the moment of the detrapping. Therefore, two beams with different speeds are created by the process of trapping and subsequent detrapping.

4. The two beam jetting causes a strong electrostatic wave emission with a k vector along the external magnetic field.

To confirm the final process #4, we can examine a simplified dispersion equation of the electrostatic beam instability for both a

single-beam and dual-beam cases. The well known dispersion equation of the electrostatic beam instability for the beam-plasma system consisting of a single cold electron beam is given by

$$1 - \frac{\Pi_e^2}{\omega^2} = \eta_b \frac{\Pi_e^2}{(\omega - kV_B)^2} \tag{5.7}$$

where Π_e, η_b and V_B are the plasma frequency, relative number density of the electron beam to the background plasma density, N_b/N_o and the beam velocity, respectively. For the plasma parameters used in the Case A (Beam Only Case) simulation, the complex ω solutions against real k values are depicted in Figure 5.18(a). The real part of ω is shown by solid lines, while the imaginary part of ω is drawn by dashed lines. As is well known, the beam branch shows an unstable solution with a positive ω_i. The maximum ω_i is approximately 0.3. Our question is then to see whether or not the dispersion equation for the beam-plasma system shows larger growth rate than the single beam case when the beam density of each beam in the two beam case is half of that of the single beam case, remaining the other parameters the same. The dispersion equation for the electrostatic instability in the two-beam case is given by

$$1 - \frac{\Pi_e^2}{\omega^2} = \eta_{e1} \frac{\Pi_e^2}{(\omega - kV_{B1})^2} + \eta_{e2} \frac{\Pi_e^2}{(\omega - kV_{B2})^2} \tag{5.8}$$

where η_{e1} and η_{e2} are the relative beam density, i.e., $\eta_{e1} = N_{b1}/N_o$, $\eta_{e2} = N_{b2}/N_o$. As mentioned before, the complex ω solution for real k values are examined for $\eta_{e1} = \eta_{e2} = 0.5\eta_e$ with other plasma parameters are kept the same as before. This corresponds to the plasma parameters for Case B simulation. The numerical solutions to ω are illustrated in Figure 5.18(b). As seen by the dashed curve, the imaginary part ω_i now shows a larger value for the beam branch with higher velocity, reaching a maximum value of 0.6.

In the lower panels in both Figures 5.18(a) and (b), the ω - k spectrum of the simulation results are shown with the numerical solutions to Eq.(5.7) and (5.8), respectively. The numerical solutions agree well with the simulation results except for the slower beam branch in Case B. The simulation results show almost no wave excitation along the slower beam branch against the prediction of the linear dispersion equation. This discrepancy is probably due to the difference in temperature of the beam :

In the numerical calculation of the dispersion equation are cold beams while the two beams produced in the simulation have a significantly large temperature.

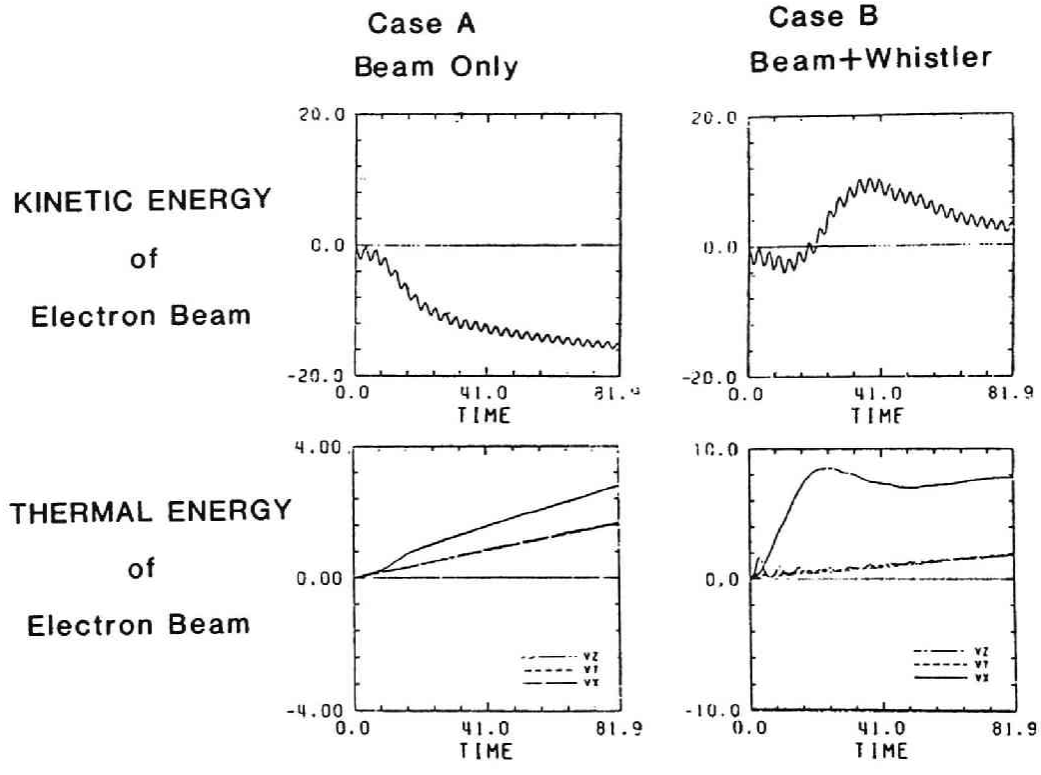

Fig. 5.19 Evolution of kinetic energies of electron beam (a) Beam only Case, (b) Beam + Whistler Case. Beam drift- and thermal-energies are plotted versus time.

Figure 5.19 shows the simulation results of the time evolution of the kinetic energies of the electron beam for both Cases A and B. The drift and thermal kinetic energies are plotted versus time. Evidently the time evolution of the drift energy of the electron beam is different between the two cases. In Case A, the drift energy shows a monotonic decrease indicating the beam drift energy is the free energy source of the beam instability and gives energy to the electrostatic wave emission. However, in Case B, the beam drift energy shows an initial decrease but soon increases for the moment and then begin to decrease after $t \simeq 35$. This means that in Case B, the electron beam is first accelerated by the electrostatic electric field component absorbing energy from the whistler wave via Landau damping of the electric field component. In terms of the

particle motion, this corresponds to the electron trapping in the potential well of the whistler wave. After a time of detrapping the enhanced kinetic energy of the electron beam is released yielding a strong electrostatic burst emissions.

The generation mechanism of the electrostatic emission burst is thus essentially a beam instability boosted-up under the action of the electrostatic component of the obliquely propagating whistler wave by a catalysis action of the beam energy reservoir which leads to the two beam jetting. Therefore the wave vector of the generated emission is parallel to the external magnetic field as observed by the satellite. It is, however, worth noting that if the wave amplitude of the whistler wave is sufficiently large, the electrostatic burst emission treated in the present paper is possible without having an electron beam at $t = 0$ because the background electrons are trapped by the potential well of the wave and thus creating an equivalent electron beam being accelerated by the potential well.

In summary, we presented results of particle simulations of nonlinear wave-wave-particle coupling among resonant particles, electromagnetic and electrostatic waves and gave an interpretation of the observed ES bursts discovered by ISEE [Reinleitner et al., 1982, 1983].

CHAPTER 6
CONCLUDING REMARKS

6.1 Summary and Conclusions

In this thesis we have made theoretical and computer-simulational studies on three types of wave-particle interactions in space plasmas. These interactions are whistler mode interactions, electromagnetic ion cyclotron interactions and interactions involved in radiations from electron beams. For the nonlinear studies of these interactions, we developed three kinds of simulation codes. These codes are the FEM, LTS and HEM codes, which have been successfully used in the present studies.

In Chapter 1, we briefly gave an overview of the present studies and discusses the increasing demands for computer simulation studies in space plasma physics. In Chapter 2, we described numerical algorithms and techniques of the three different simulation codes. The FEM code has been applied to the studies of whistler mode interactions and radiations from electrons beams. Since this code is 2-1/2 dimensional and possible to solve all kinds of plasma waves, further applications to a wide range of nonlinear wave-particle interactions are expected. The LTS code has been used to analyze the self-consistent evolution of whistler wave in various situations. The high numerical efficiency of the LTS code made it possible to assume realistic models and parameters in the magnetosphere. The HEM code has been applied to the study of electromagnetic ion cyclotron interactions. The fluid treatment of electrons made the code very efficient in solving low frequency ion mode waves.

In Chapter 3, we have investigated the whistler mode wave-particle interactions in an attempt to explain the VLF emissions in the magnetosphere. Through the analysis of nonlinear orbits of resonant electrons in a nonuniform magnetic field, we found that two types of phase-bunching, cluster and channel effects, are possible and form resonant currents. We then performed a self-consistent study. Nonlinear process of the wave growth in a uniform magnetic field is examined in detail. Difference between uniform (periodic) and nonuniform (encounter) interactions is studied. Taking into account the inhomogeneity of the dipole geomagnetic field, we found that untrapped resonant electrons as well as trapped electrons play significant roles in the wave evolution.

The role of trapped and untrapped electrons are different and exchange their roles depending on the sign of the geomagnetic gradient. In one hemisphere where the whistler wave propagates toward the equator, trapped electrons cause wave growth, while untrapped resonant electrons cause wave damping. In the opposite hemisphere, these roles are exchanged.

We found that an emission is triggered owing to detrapping of phase-bunched electrons from the pulse propagating in a homogeneous magnetic field. The emission shows a relatively small rising tone followed by subsequent frequency oscillations. Then we investigated quantitative change of the velocity distribution function of resonant electrons caused by a combined action of nonlinear phase-trapping and geomagnetic inhomogeneity. It is pointed out that the contribution by electrons which are trapped in the midst of the whistler wave train is as important as that by electrons which are trapped at the wave-front. It is further revealed that deformation of the velocity distribution function is caused not only by trapped electrons but also by untrapped electrons perturbed by a whistler triggering wave. The well-known characteristics of pulse length dependence of rising or falling tone characteristics of triggered emissions are interpreted by the simulation results. Effects of electrostatic waves of whistler mode instability have been studied in a simulation where an electron beam with a small spread of parallel velocities is assumed. It is found that the longitudinal electrostatic instability has a larger growth rate than the whistler mode instability, and strongly modifies the electron beam suppressing the whistler instability.

In Chapter 4, electromagnetic ion cyclotron wave-particle interaction has been studied first by the linear theory and then by a computer simulation. The mechanism by which hot anisotropic protons generate electromagnetic ion cyclotron waves in a plasma containing cold H^+ and He^+ ions is quantitatively studied by computing linear growth rates for different plasma parameters. It is found that for parameters typical of the geostationary altitude the maximum growth rates are not drastically changed when a small proportion (~1-20%) of cold He^+ ions are present and that because of the important cyclotron absorption by thermal He^+ ions in the vicinity of the He^+ gyrofrequency, waves which could resonate with the He^+ distribution cannot be generated. Therefore, quasi-linear effects, in a homogeneous medium at least, cannot be responsible for the heating of He^+ ions which is often observed in conjunction with ion cyclotron waves. In order to investigate nonlinear process responsible for the He^+ heating, we have performed a computer simulation. It is found that He^+ ions are heated

mainly in the perpendicular direction and they are heated more than cold H^+ ions. The heating of He^+ is a two-step process :first He^+ ions are set into oscillations by the growing wave (in both $v_\perp$ and $v_\parallel$) until some of the ions reach a parallel velocity of the order of the resonant velocity at which time strong heating occurs owing to the nonlinear trapping.

In Chapter 5, we have investigated two types of wave radiation from electron beams, electromagnetic radiation from an artificially injected electron beam and electrostatic radiation from an electron beam modulated by coherent whistler mode wave. The former radiation is in the perpendicular direction to the static magnetic field, while the latter radiation is in the parallel direction. In the former case we found a strong excitation of a slow extraordinary wave around the electron beam and a propagation of a pulse-like ordinary wave packet excited as an impulse response to the onset of the beam injection. In the latter case we found that modulation by the coherent whistler mode wave causes an interesting two-beam jetting as a result of a trapping and the subsequent detrapping process, yielding a strong electrostatic emission in the parallel direction.

In conclusion, we have studied nonlinear wave-particle interactions for several phenomena observed in space plasmas using the technique of computer simulations. We could obtain good understanding of microscopic processes in the interactions through various kind of analyses of the simulation data. We found that trapping and/or detrapping of resonant particles is one of the major cases of the nonlinearities in the wave-particle interactions. We hope that the present work contributes more or less to the establishment of the space plasma physics.

6.2 Suggestion for Further Work

We have developed three simulation codes in the present study. The FEM and HEM codes are programed so as to be applied to general problems, while the LTS code is limited to the whistler mode wave-particle interaction. Along with the development of these codes, various kinds of diagnostic tools such as graphic routines are built up as a library called Subroutine Library for Plasma Simulation (SLPS). There are plenty of nonlinear problems which could be studied with the use of these softwares.

Complexity of phenomena in space plasmas also demand improvement of these simulation codes. The FEM code which is of 2-1/2D at present is

expected to be extended to a 3D system, and it is also expected to include a relativistic effect in the particle motion. The HEM code which is of 1-2/2D at present is easily extended to a 2-1/2D system. Another improvement that must be done to the FEM and HEM code is to make these code represent an open system rather than a closed system. Under the periodic boundary condition presently assumed in these code, waves cannot escape from the system, and new energetic particle are not injected into the system. Therefore, the present simulation system is stationary rather than progressive, and it cannot represent an equilibrium where input and output energy flow are balanced. Such improvement is eagerly needed as a further work. Boundary conditions must be set up carefully to avoid numerical instabilities and to represent realistic physical models suitably.

Appendix A

Numerical Dispersion Relation of the Wave in Vacuum

We examine how the dispersion characteristic of the wave in vacuum is modified by the discretization of space and time in the numerical simulation. We assume a monochromatic plane wave in vacuum propagating in the x-y plane with the wavenumbers k_x and k_y such as

$$B_z = \bar{B}_z \exp i(\omega t - k_x x - k_y y) \tag{A1}$$

$$E_x = \bar{E}_x \exp i(\omega t - k_x x - k_y y) \tag{A2}$$

$$E_y = \bar{E}_y \exp i(\omega t - k_x x - k_y y) \tag{A3}$$

where ω is the frequency, and $\bar{B}_z$, $\bar{E}_x$ and $\bar{E}_y$ are the amplitudes of the wave. Writing Maxwell's equations (2.18) ~ (2.20) in difference forms, we have

$$\frac{B^{n+1/2}_{z,i+1/2,j+1/2} - B^{n-1/2}_{z,i+1/2,j+1/2}}{\Delta t} - - \frac{E^{n}_{y,i+1,j+1/2} - E^{n}_{y,i,j+1/2}}{\Delta x} + \frac{E^{n}_{x,i+1/2,j+1} - E^{n}_{x,i+1/2,j}}{\Delta y} \tag{A4}$$

$$\frac{E^{n+1}_{x,i+1/2,j} - E^{n}_{x,i+1/2,j}}{\Delta t} = c^2 \frac{B^{n+1/2}_{z,,i+1/2,j+1/2} + B^{n+1/2}_{z,i+1/2,j-1/2}}{\Delta y} \tag{A5}$$

$$\frac{E^{n+1}_{y,i,j+1/2} - E^{n}_{y,i+1/2,j}}{\Delta t} = - c^2 \frac{B^{n+1/2}_{z,i+1/2,j+1/2} - B^{n+1/2}_{z,i-1/2,j+1/2}}{\Delta x} \tag{A6}$$

where the subscripts and superscript indicate the grid numbers and time steps, respectively. Substituting (A1) ~ (A3) into (A4) ~ (A6), we have

$$\frac{\sin (\omega\Delta t/2)}{\Delta t/2} \bar{B}_z = \frac{\sin (k_x \Delta x/2)}{\Delta x/2} \bar{E}_y \quad \frac{\sin (k_y \Delta y/2)}{\Delta y/2} \bar{E}_x \tag{A7}$$

$$\frac{\sin (\omega\Delta t/2)}{\Delta t/2} \bar{E}_x = c^2 \frac{\sin (k_y \Delta y/2)}{\Delta y/2} \bar{B}_z \tag{A8}$$

$$\frac{\sin\left(\omega\Delta t/2\right)}{\Delta t/2}\bar{E}_y = -c^2\frac{\sin\left(k_x\Delta x/2\right)}{\Delta x/2}\bar{B}_z \tag{A9}$$

Defining

$$K_x = \frac{\sin\left(k_x\Delta x/2\right)}{\Delta x/2}, \quad K_y = \frac{\sin\left(k_y\Delta y/2\right)}{\Delta y/2}, \quad \Omega = \frac{\sin\left(\omega\Delta t/2\right)}{\Delta t/2}. \tag{A10}$$

We rewrite (A7) ~ (A9) as

$$\Omega\bar{B}_z = K_x\bar{E}_y - K_y\bar{E}_x \tag{A11}$$

$$\Omega\bar{E}_x = c^2K_yB_z \tag{A12}$$

$$\Omega\bar{E}_y = -c^2K_xB_z \tag{A13}$$

Eliminating $\bar{E}_x$ and $\bar{E}_y$ from (A11) ~ (A13), we have

$$\Omega^2\bar{B}_z = -c^2\left(K_x^2 + K_y^2\right)\bar{B}_z \tag{A14}$$

Since $\bar{B}_z \neq 0$, we obtain the nemerical dispersion relation

$$\Omega^2 = c^2\left(K_x^2 + K_y^2\right) \tag{A15}$$

It is obvious that (A15) is identical to the dispersion relation of the wave in vacuum, if K_x, K_y and Ω are replaced by k_x, k_y and ω.

Let us derive the CFL condition for the wave in vacuum. For simplicity we assume $\Delta x = \Delta y \equiv \Delta r$. Substitution of (A10) into (A15) gives

$$\sin^2\left(\frac{\omega\Delta t}{2}\right) = \left(c\frac{\Delta t}{\Delta r}\right)^2\left\{\sin^2\left(\frac{k_x\Delta r}{2}\right) + \sin^2\left(\frac{k_y\Delta r}{2}\right)\right\} \tag{A16}$$

Since the maximum wavenumbers allowed in the simulation system are given as

$$k_{x,max} = k_{y,max} = \frac{\pi}{\Delta r}, \tag{A17}$$

The dispersion relation of the wave with the maximum wavenumbers, which correspond to the highest frequency in the system, gives

$$\sin^2\left(\frac{\omega\Delta t}{2}\right) = \left(\sqrt{2}\,c\frac{\Delta t}{\Delta r}\right)^2 = \left(\frac{\sqrt{2}\,c}{V_n}\right)^2. \tag{A18}$$

where V_n is the numerical velocity defined by $V_n \equiv \Delta r/\Delta t$. If $V_n < \sqrt{2}c$, then the frequency ω becomes complex, yielding a numerical instability. Therefore, the condition for stable time-integration is

$$V_n \geqslant \sqrt{2}\, c \quad . \tag{A19}$$

This condition is for two-dimensional systems. As for one-dimensional systems, it it straight forward that the condition is modified as

$$V_n \geqslant c \quad . \tag{A20}$$

Appendix B

Derivation of (2.10)

Light mode (high frequency mode) has little contribution from the particle motion, which is expressed by the current J in Maxwell's equations.

$$\mathrm{rot}\ \vec{B} = \mu_0 \vec{J} + \frac{1}{c^2}\frac{\partial \vec{E}}{\partial t} \tag{B1}$$

Let us compare the order of magnetude of the first and the second terms in the r.h.s of (B1)

$$\frac{\mu_0 J}{(1/c)^2 \partial E/\partial t} = \frac{c^2 \mu_0 env}{\omega E} = \left(\frac{\omega_p}{\omega}\right)^2 \frac{m}{eE}\,\omega v \tag{B2}$$

From the equation of motion, we have

$$\omega v = \left|\frac{e}{m}\left(\vec{E} + \vec{v} \times \vec{B}\right)\right| \leqslant \frac{e}{m}\left(E + vB\right) \tag{B3}$$

From (B2) and (B3), we have

$$\frac{\mu_0 J}{(1/c)^2 \partial E/\partial t} \leqslant \left(\frac{\omega_p}{\omega}\right)^2 \left(1 + \frac{vB}{E}\right) \tag{B4}$$

Maxwell's equation gives

$$E = \frac{\omega}{k} B_w = V_p B_w \tag{B5}$$

where V_p is the phase velocity ω/k. Since $B = B_0 + B_w$, we have from (B5)

$$\frac{vB}{E} = \frac{vB_0}{E} + \frac{v}{V_p} = \frac{v}{V_p}\left(\frac{B_0}{B_w} + 1\right) \simeq \frac{v}{V_p}\frac{B_0}{B_w} \tag{B6}$$

where $B_w \ll B_0$ is assumed. Substituting (B6) into (B4), we obtain

$$\frac{\mu_0 J}{(1/c)^2 \partial E/\partial t} \leqslant \left(\frac{\omega_p}{\omega}\right)^2 \left(1 + \frac{v}{V_p}\frac{B_0}{B_w}\right) \tag{B7}$$

Appendix C

Derivation of Scaling Relation (3.8)

The phase trapping by whistler wave is possible as far as the absolute value of the inhomogeneity ratio R, given by (3.18) in the text, is less than unity, that is,

$$|R| = \left| \frac{1}{2\omega_t^2} \left(-3V_R + \frac{kv_\perp^2}{\Omega_e} \right) \frac{\partial \Omega_e}{\partial z} \right| \qquad (C1)$$

Since $\omega_t^2 = kv_\perp \Omega_w$ and $\partial\Omega_e/\partial z = 2\beta z_a$ for the parabolic magnetic field, (C1) becomes

$$\frac{\beta z_a}{kv_\perp \Omega_w} \left(-3V_R + \frac{kv_\perp^2}{\Omega_e} \right) \leqslant 1 \qquad (C2)$$

Thus the length L_{trap} of the trapping zone is estimated by

$$L_{trap} = \frac{2kv_\perp \Omega_w}{\beta [-3V_R + (kv_\perp^2 / \Omega_e)]} \qquad (C3)$$

where $v_\perp \simeq$ const, $k \simeq$ const, and $\Omega_e \simeq \Omega_{eo}$ are assumed. In terms of the normalized quantities, (C3) becomes

$$L_{trap} \simeq \frac{2kv_\perp \Omega_w}{\alpha(-3V_R + kv_\perp^2)} \qquad [c\Omega_{eo}^{-1}] \qquad (C4)$$

where k, Ω_w, and velocity are normalized to c^{-1}, $\Omega_{eo}\Omega_{eo}$, and c, respectively. For values of $k \simeq 20$, $v \simeq -0.05$, $L_{trap} \simeq 710$ for magnetospheric parameters of $\alpha = 8.06 \times 10^{-8}$ and $\Omega_w \simeq 10^{-5}$, while $L_{trappu} \simeq 224$ for simulational parameters of $\alpha = 2.55 \times 10^{-6}$ and $\Omega_w \simeq 10^{-4}$. The number of trapped oscillations within the trapping zone is given by $(L_{trap}/|v_\parallel|)/T_t$, that is,

$$n_{trap} = \frac{2kv_\perp \Omega_w}{\alpha |v_\parallel| (-3V_R + kv_\perp^2)} [2\pi/(kv_\perp \Omega_w)^{1/2}]^{-1}$$

$$= \frac{k^{3/2} v_\perp^{3/2}}{\pi |v_\parallel| (-3V_R + kv_\perp^2)} \frac{\Omega_w^{3/2}}{\alpha} \propto \frac{\Omega_w^{3/2}}{\alpha} \qquad (C5)$$

Thus the requirement of the same number of trapping oscillation during the passage of the trapping zone gives

$$\alpha \propto \Omega_{wi}^{3/2} \qquad (C6)$$

REFERENCES

Akhiezer, A. I., I. A. Akhiezer, R. V. Polovin, A.G. Sitenko and K. N. Stepanov, Plasma Electrodynamics, 1, Pergamon Press, 1975.

Ashour-Abdalla, M., H. Okuda and C. Z. Cheng, Acceleration of heavy ions on auroral field lines, Geophys. Res. Lett., 8, 795, 1981.

Ashour-Abdalla, M., H. Okuda, Turbulent heating of heavy ions on auroral field lines, J. Geophys. Res., 89, 2235, 1984.

Ashour-Abdalla, M., and C. F. Kennel, Nonconvective and convective cyclotron harmonic instabilities, J. Geophys. Res., 83, 1531, 1543.

Balsiger, H., P. Eberhardt, J. Geiss, and D. T. Young, Magnetic storm injection of 0.9 to 16 keV/e solar and terrestrial ions into the high-altitude magnetosphere, J. Geophys. Res., 85, 1645, 1981.

Bell, T. F. and U. S. Inan, Transient nonlinear pitch angle scattering of energetic electrons by coherent VLF wave packets in the magnetosphere, J. Geophys. Res., 86, 9047, 1981.

Bell, T. F., and O. Buneman, Plasma instability in the whistler mode caused by a gyrating electron stream, Phys. Rev., 133, 1300, 1964.

Berchem, J., R. Gendrin, and M. Ashour-Abdalla, Acceleration of heavy ions by ULF electromagnetic waves, 3. Analytical study of the nonlinear phases (abstract), EOS, 64, 815, 1983.

Berchem, J., and R. Gendrin, Non resonant interaction of heavy ions with electromagnetic ion cyclotron waves, J. Geophys. Res., submitted to, 1984.

Bernstein, W., H. Leinbach, P. J. Kellog, S. J. Monson and T. Hallinan, Further laboratory measurements of the beam-plasma discharge, J. Geophys. Res., 84, 7271, 1979.

Brice, N., and C. Lucas, Interaction between heavier ions and ring current protons, J. Geophys. Res., 80, 936, 1975.

Byers J. A., B. I. Cohen, W. C. Condit, and J. D. Hanson, Hybrid simulations of quasineutral phenomena in magnetized plasma, J. Comput. Phys., 27, 363, 1978.

Cambou, F., General description of the ARAKS experiments, Ann. Geophys., 36, 271, 1980.

Chappell, R. C., Cold plasma distribution above a few thousand kilometers at high latitude, in High Latitude Space Plasma Physics, edited by B. Hultqvist and T. Hagfors, pp. 251-269, Plenum, New York, 1983.

Cuperman, S., L. Gomberoff and A. Sternlieb, Requirements on singly ionized

lithium concentrations for magnetospheric seeding experiments, J. Geophys. Res., 80, 4643, 1975.

Cuperman, S., and R. W. Landau, On the enhancement of the whistler mode instability in the magnetosphere by cold plasma injection, J. Geophys. Res., 79, 128, 1974.

Decreau, P. M. E., C. Beghin, and M. Parrot, Global characteristics of the cold plasma in the equatorial plasmapause region as deduced from the GEOS-1 mutual impedance probe, J. Geophys. Res., 87, 695, 1982.

Decreau, P. M. E., C. Beghin and M. Parrot, Global characteristics of the cold plasma in the equatorial plasmapause region as dedeced from the GEOS 1 mutual impedance probe, J. Geophys. Res., 87, 695, 1982.

Denavit, J., and R. N. Sudan, Effect of phase-correlated electrons on whistler wave packet propagation, Phys. Fluids, 18, 1533, 1541.

Drummond, W. E., J. H. Malmberg, T. M. O'neil and J. R. Thompson, Nonlinear development of the beam-plasma instability, Phys. Fluids, 13, 2422, 1970.

Dysthe, K. B., Some studies of triggered whistler emissions, J. Geophys. Res., 76, 6915, 1971.

Frank, L. A., K. L. Ackerson, and D. M. Yeager, Observations of atomic oxygen (O^+) in the Earth's magnetotail, J. Geophys. Res., 82, 129, 1982.

Fraser, B. J., Pc 1-2 observations of heavy ion effects by synchronous satellite ATS-6, Planet. Space Sci., 30, 1229, 1982.

Geiss, J., H. Balsiger, P. Eberhardt, H. P. Walker, L. Weber, and D. T. Young, Dynamics of magnetospheric ion composition as observed by the GEOS mass spectrometer, Space Sci. Rev., 2, 537, 1978.

Gendrin R., A. Roux, Energization of helium ions by proton induced hydromagnetic waves, J. Geophys. Res., 85, 4577, 1980.

Gendrin R., Effects of heavy ions on microscopic plasma physics in the magnetosphere, in High Latitude Space Plasma Physics, edited by B. Hultqvist and T. Hagfors, pp. 415-436, Plenum, New York, 1983.

Gendrin R., M. Ashour-Abdalla, Y. Omura, and K. Quest, Linear analysis of ion cyclotron interaction in a multi-component plasma, J. Geophys. Res., 89, 9119, 1984.

Gendrin R., S. Lacourly, A. Roux, J. Solomon, F. Z. Feiguin, M. V. Gokhberg, V. A. Troitskaya, and Y. L. Yakimento, Wave-packet propagation in an amplifying medium and its application to the dispersion characteristics and to the generation mechanism of Pc 1 events, Planet. Space Sci., 19, 165, 1971.

Gendrin R., and A. Roux, Energization of helium ion by proton induced hydromagnetic waves, J. Geophys. Res., 85, 4577, 1980.

Gendrin, R., General relationships between wave amplification and particle diffusion in a magnetoplasma, Rev. Geophys. Space Phys., 19, 171, 1981.

Gendrin, R., S. Lacourly, A. Roux, J. Solomon, F. Z. Feiguin, M. V. Gokhberg, and V. A. Troitskaya, Wave packet propagation in an amplifying medium and its application to the dispersion characteristics and to the generation mechanism of Pc 1 events, Planet. Space Sci., 19, 165, 1971.

Gendrin, R., The French Soviet ARAKS experiment.

Gendrin, R., Waves and wave-particle interactions in the magnetosphere: A review,

Ghielmetti, A.., R. G. Johnson, R. D. Sharp, and E. G. Shelley, The latitudinal, diurnal and altitudinal distributions of upward flowing energetic ions of ionospheric origin, Geophys. Res. Lett., 5, 59, 1978.

Gomberoff, L., and R. Neira, Convective growth rate of ion cyclotron waves in a H^+-He^+ and H^+-He^+-O^+ plasma, J. Geophys. Res., 88, 2170, 1983.

Gomberoff, L., and S. Cuperman, Combined effect of cold H^+ and He^+ ions on the proton cyclotron electromagnetic instability, J. Geophys. Res., 87, 95, 1982.

Gomberoff, L., and S. Cuperman, Modification in the masimum convective growth rate of the electromagnetic proton cyclotron instability due to the presence of thermal ions, J. Plasma Phys., 18, 91, 1977.

Gurnett, D. A., and L. A. Reinleitner, Electron acceleration by Landau resonance with whistler mode wave packets, J. Geophys. Res., 10, 603, 1983.

Hardy D. A., J. W. Freeman, and H. K. Hills, Double-peaked ion spectra in the lobe plasma: evidence for massive ions?, J. Geophys. Res., 82, 5529, 1977.

Hashimoto K., H. Matsumoto, Y. Serizawa, and I. Kimura, Computer simulation of whistler mode wave-particle interactions using a free-boundary model, J. Geophys. Res., 88, 3072, 3078, 1983.

Helliwell R. A. and T. L. Crystal, A feedback model of cyclotron interaction between whistler-mode waves and energetic electrons in the magnetosphere, J. Geophys. Res., 78, 7357, 7371, 1973.

Helliwell R. A., and J. P. Katsufrakis, VLF wave injection into the magnetosphere from Siple station, Antarctica, J. Geophys. Res., 79, 2511, 2518.

Helliwell, R. A., A theory of discrete VLF emissions from the magnetosphere, J. Geophys. Res., 72, 4773, 1967.

Helliwell, R. A., D. L. Carpenter and T. R. Miller, Power threshold for growth of coherent VLF signals in the magnetosphere, J. Geophys. Res., 85, 3360, 1980.

Helliwell, R. A., and J. P. Katsufrakis, VLF wave injection into the magnetosphere from Siple station, Antarctica, J. Geophys. Res., 79, 2511, 1974.

Helliwell, R. A., and U. S. Inan, VLF wave growth and discrete emission triggering in the magnetosphere: A feedback model, J. Geophys. Res., 87, 3537, 1982.

Higel, B., and Wu Lei, Electron density and plasmapause characteristic at $6.6R_E$: A statistical study of the GEOS 2 relaxation sounder data, J. Geophys. Res., 89, 1583, 1984.

Hockney, R. W., and J. W. Eastwood, Computer simulations using particles, McGraw-Hill International Book Co., 1981.

Horne, R. B., P. J. Christiansen, M. P. Gough, K. G. Ronmark, J. F. E. Johnson, J. Sojka, and G. L. Wrenn, Amplitude variation of electron cyclotron harmonic waves, Nature, 294, 338, 1981.

Inan, U. S., T. F. Bell and R. A. Helliwell, Nonlinear pitch angle scattering of energetic electrons by coherent VLF waves in the magnetosphere, J. Geophys. Res., 83, 3235, 1978.

Isenberg, P. A., The ion cyclotron dispersion relation in a proton-alpha solar wind, J. Geophys. Res., 89, 2133, 1984a.

Isenberg, P. A., Resonant acceleration and heating solar wind ions : anisotropy and dispersion, J. Geophys. Res., 89, 6613, 1984b.

Karpman, V. I., Ja. N. Istomin, and D. R. Shklyar, Nonlinear theory of a quasi-monochromatic whistler mode packet in inhomogeneous plasma, Plasma Phys., 16, 685, 1974.

Kennel C. F., and H. E. Petschek, Limit on stably trapped particle fluxes, J. Geophys. Res., 71, 1, 1966.

Kumagai, H., K. Hashimoto, I. Kimura, and H. Matsumoto, Computer simulation of a Cerenkov type wave-particle interaction between obliquely propagating whistler mode waves and an electron beam, Phys. Fluids, 23, 184, 1980.

Langdon, A. B. and B. F. Lasinski, Electromagnetic and relativistic plasma simulation models, Methods Comput. Phys., 16, 327, 1976.

Lysak, R. L., M. Hudson, and M. Temerin, Ion heating by strong electrostatic ion cyclotron turbulence, J. Geophys. Res., 85, 678, 1980.

Mark, E., Growth rate of the ion cyclotron instability in the

magnetosphere, J. Geophys. Res., 79, 3218, 1974.

Matsumoto H., Y. Omura, Computer simulation studies of VLF triggered emissions: Deformation of distribution function by trapping and detrapping, Geophys. Res. Lett., 10, 607, 1983.

Matsumoto, H. and Y. Yasuda, Computer simulation of nonlinear interaction between a monochromatic whistler wave and an electron beam, Phys. Fluids, 19, 1513, 1976.

Matsumoto, H., Nonlinear whistler-mode interaction and triggered emission in the magnetosphere, in Wave Instabilities in Space Plasma, edited by P.J. Palmadesso and K. Papadopoulos, p.163, D. Reidel, Hingham, Mass., 1979.

Matsumoto, H., K. Hashimoto and I. Kimura, Dependence of coherent whistler interaction on wave amplitude, J. Geophys. Res., 85, 644, 1980.

Matsumoto, H., M. Ohashi and Y.Omura, A computer simulation study of Hook-induced electrostatic bursts observed in the magnetosphere by the ISEE satellite, J. Geophys. Res., 9, 3873, 295..

Matsumoto, H., and Y. Omura, Cluster-and channel-effect phase bunchings by whistler waves in the nonuniform geomagnetic field, J. Geophys. Res., 86, 779, 1981.

Matsumoto, H., and Y. Omura, Electromagnetic Particle Simulation and its Application to Space Plasmas, in Computer Simulations of Space Plasmas, T. Sato, D. Reidel/Terra Pub., 1984.

Mauk, B. H., C. E. McIlwain, and R. L. McPherron, Helium cyclotron resonance within the earth's magnetosphere, Geophys. Res. Lett., 8, 103, 1981.

Mauk, B. H., Helium resonance and dispersion effects on geostationary Alfven/ion cyclotron waves, J. Geophys. Res., 87, 9107, 1982a.

Mauk, B. H., Electromagnetic wave energization of heavy ion by the electric 'phase bunching' process, Geophys. Res. Lett., 9, 1163, 1982b.

Mauk, B. H., Frequency gap formation in electromagnetic cyclotron wave distribution, Geophys. Res. Lett., 10, 635, 1983.

Melrose, D. B., R. M. Winglee and I. H. Cairus, Amplification of triggered VLF emissions: Is it due to trapping or phase bunching?, paper presented at Chapman Conference on Waves in the Magnetosphere, Kona, Hawaii, 1983.

Mishin, E. V. and Yu. Ya. Ruzhin, The model of beam-plasma discharge in the rocket environment during an electron beam injection in the ionosphere, Ann. Geophys., 36, 423, 1980.

Mizera, P. F., J. F. Fennell, D. R. Croley, A. L. Vampola, F. S. Mozer, R. B. Torbt, M. Temerin, R. Lysak, M. Hudson, C. A. Cattell, R. G. Johnson, R. D. Sharp, A. G. Ghielemetti, and P. M. Kintner, The aurora inferred from S3-3 particles and fields, J. Geophys. Res., 86, 2329, 1981.

Nunn, D., A self-consistent theory of triggered VLF emissions, Planet. Space Sci., 22, 349, 1974.

Nunn, D., A theroy of triggered emissions, Planet. Space Sci., 19, 1144, 1971.

Nunn, D., The quasi-static theory of VLF emissions, Univ. of Southampton, 1983.

Omura, Y., and H. Matsumoto, Computer simulations of basic processes of coherent whistler wave-particle interactions in the magnetosphere, J. Geophys. Res., 87, 4435, 1982.

Obayashi, T., Science Problems of SEPAC/SPACELAB-1 MISSION, Sol. Terr. Environ. Res. Jpn., 6, 1982.

Omura Y., M. Ashour-Abdalla, R. Gendrin, and K. Quest, Acceleration of heavy ions by ULF electromagnetic waves, 2, Simulation results (abstract), Eos Trans AGU, 64, 815 1983.

Omura, Y., and H. Matsumoto, Simulation study of frequency variations of VLF triggered emissions in a homogeneous field, J. Geomag. Geoelectr., in press, 1985.

Papadopoulos, K., J. D. Gafey, Jr. and P. J. Palmadesso, Stochastic acceleration of large M/Q ions by hydrogen cyclotron waves in the magnetosphere, Geophys. Res. Lett., 7, 1014, 1980.

Papadopoulos, K., Theory of the beam plasma discharge, paper presented at NATO Symposium, Geilo, Norway, 1981.

Pellat, R. and R. Z. Sagdeev, Concluding remarks on the ARAKS experiments, Ann. Geophys., 36, 443, 1980.

Perraut, S., and A. Roux, Respective role of the cold and wave plasma densities on the generation mechanism of ULF waves in the magnetosphere, J. Atomos. Terr. Phys., 37, 407 1975.

Petersen, W. K., R. D. Sharp, E. G. Shelley, R. G. Johnson and H. Balsiger, Energetic ion composition of the plasma sheet, J. Geophys. Res., 86, 761, 1981.

Rauch, J. L., and A. Roux, Raytracing of ULF waves in a multicomponent magnetospheric plasma: Consequences for the generation mechanism of ion cyclotron waves, J. Geophys. Res., 87, 8191, 1982.

Reinleitner, L. A., D. A. Gurnett, and D. A. Gallagher, Chours related electrostatic bursts in the Earth's outer magnetosphere, Nature, 295, 46, 1982.

Reinleitner, L. A., D. A. Gurnett, and T. E. Eastman, Electrostatic bursts generated by electrons in Landau resonance with whistler mode chorus, J. Geophys. Res., 88, 3079, 1983.

Roux, A., S. Perraut, J. L. Rauch, C. de Villedary, G. Kremser, A. Korth, and D. T. Young, Wave-particle interactions near Ω_{He+} observed on board GEOS-1 and 2. 2. Generation of ion cyclotron waves and heating of He^+ ions, J. Geophys. Res., 87, 8174, 1982.

Roux, A., and R. Pellat, A theory of triggered emissions, J. Geophys. Res., 83, 1433, 1978.

Sgro A. G., and C. W. Nielson, Hybrid model studies of ion dynamics and magnetic field diffusion during pinch implosions, Phys. Fluids, 19, 126, 1976.

Shelley, E. G., R. D. Sharp, and R. G. Johnson, Satellite observations of an ionospheric acceleration mechanism, Geophys. Res. Lett., 3, 654, 1976.

Szucszewicz, E. P., and C. S. Lin, Ignition of the beam-plasma-discharge and its dependence on electron density, in Artificial Particle Beams in Space Plasma Studies, edited by B. Grandal, pp. 361-370, Plenum, New York, 1982.

Tanaka M, and C. C. Goodrich, Simulation study of heavy ion heating by electromagnetic ion cyclotron waves induced by proton temperature anisotropy, Research Report, HIFT-87, Hiroshima Univ., 1983.

Vomvoridis, J. L., Nonuniform whistler mode propagation, Ph. D. thesis, Northwestern Univ., Evanston, Ill., 1978.

Vomvoridis, J. L., T. L. Crystal, and J. Denavit, Theory and computer simulation of magnetospheric very low frequency emissions, J. Geophys. Res., 87, 1473, 1982.

Vomvoridis, J. L., and J. Denavit, Nonlinear evolution of a monochromatic whistler wave in a nonuniform magnetic field, Phys. Fluids, 23, 174, 1980.

Vomvoridis, J. L., and J. Denavit, Test particle correlation by whistler waves in a nonuniform magnetic field, Phys. Fluids, 22, 367, 1979.

Wandzura, S., and F. V. Coroniti, Nonconvective ion cyclotron instability, Planet Sci, 23, 123, 1975.

Young, D. T., S. Perraut, A. Roux, C. de Villedary, R. Gendrin, A. Korth, G. Kremser and D. Jones, Wave-particle interactions near Ω_{He+} observed on GEOS-1 and -2, 1. Propagation of ion cyclotron waves in He^+-rich plasma, J. Geophys. Res., 86, 6755, 1981.

Young, P. T., Ion composition measurements in magnetospheric modeling, in Quantitative Modeling of Magnetospheric Processes, Geophys. Monogr. Ser., vol. 21, edited by W. P. Olson, pp 340-363, AGU Washington, D.C., 1979.